Titre: Title:	Étude numérique de l'impact de la distribution de catalyseur sur les performances des filtres à particules catalytiques
Auteur: Author:	Igor Barnabé Belot
Date:	2020
Type:	Mémoire ou thèse / Dissertation or Thesis
Référence: Citation:	Belot, I. B. (2020). Étude numérique de l'impact de la distribution de catalyseur sur les performances des filtres à particules catalytiques [Ph.D. thesis, Polytechnique Montréal]. PolyPublie. https://publications.polymtl.ca/5303/

URL de PolyPublie: PolyPublie URL:	https://publications.polymtl.ca/5303/
Directeurs de recherche: Advisors:	François Bertrand, & David Vidal
Programme: Program:	Génie chimique

POLYTECHNIQUE MONTRÉAL

affiliée à l'Université de Montréal

Étude numérique de l'impact de la distribution de catalyseur sur les performances des filtres à particules catalytiques

IGOR BARNABÉ BELOT

Département de génie chimique

Thèse présentée en vue de l'obtention du diplôme de *Philosophiæ Doctor*

Génie chimique

Juin 2020

POLYTECHNIQUE MONTRÉAL

affiliée à l'Université de Montréal

Cette thèse intitulée :

Étude numérique de l'impact de la distribution de catalyseur sur les performances des filtres à particules catalytiques

présentée par **Igor Barnabé BELOT**

en vue de l'obtention du diplôme de *Philosophiæ Doctor*

a été dûment acceptée par le jury d'examen constitué de :

Robert LEGROS, président
François BERTRAND, membre et directeur de recherche
David VIDAL, membre et codirecteur de recherche
Jean-Philippe HARVEY, membre
Olivier BONNEFOY, membre externe

DÉDICACE

«All models are wrong, but some are useful.»

Georges Box

«Republicans buy sneakers, too.»

Mikael Jordan

«I never lose. I either win or learn.»

Nelson Mandela

À mes parents.

REMERCIEMENTS

Je remercie mon directeur de recherche, le professeur François Bertrand, pour m'avoir donné sa confiance tout au long de ce projet de doctorat. Mes échanges avec lui ont toujours été productifs et professionnels, mais aussi agréables et légers. Je remercie mon codirecteur de recherche, le professeur David Vidal, pour son travail incroyable, ses idées, et tout le temps qu'il a passé à m'accompagner dans ce projet. Mes deux directeurs ont été des mentors et des exemples, ils m'ont autant marqué par leurs connaissances scientifiques que par leurs personnalités.

Je remercie nos partenaires allemands de l'entreprise Umicore : Robert Greiner et le professeur Martin Votsmeier, avec qui nos échanges tout au long du projet ont été très intéressants et motivants. Danke schön. Je remercie le professeur Robert E. Hayes pour sa collaboration depuis l'université d'Alberta. Je remercie le groupe de recherche du professeur François Trochu, en l'incluant : Philippe Causse et Yixun Sun, pour leur aide précieuse dans la réalisation de l'Article 3. Ce travail n'aurait pas été possible sans les différents collaborateurs avec lesquels j'ai pu échanger tout au long de mon projet. Même dans le cadre d'un doctorat, l'ingénierie ne peut jamais être le fruit du travail d'une seule personne.

Je remercie ma famille : mes parents d'abord, Alain et Isabelle Belot, pour tout. Ma sœur, Léa Belot, qui m'inspire par sa créativité. Mes grands-parents Jean et Françoise Belot et Monique Humbert, pour leur amour. Je remercie aussi Pauline Belot, qui a été mon morceau de famille au Canada pendant ces années de doctorat.

Je remercie Clara Houtin, avec qui j'ai partagé ma vie et qui m'a soutenu de façon formidable. Mes amis de toujours : Gabriel Autier, Antoine Devillers, Antoine Abadia, Alice Ellenbogen, Célia Bocchi. Mes amis d'ici : Alexandre Al-Haiek et Alexandra Goupil qui sont mes frère et sœur du Québec.

Je remercie tous mes collègues de l'URPEI : Tiffany Bellanger, Shuli Shu, Rémi Demol, Olivier Bertrand, Christine Beaulieu, Serge Delacroix, Jean-Michel Tucny, Charlotte van Engeland, Asher Benchimol et Olivier Guévremont. L'ambiance dans le bureau a toujours été agréable et détendue, entre rigolades et discussions scientifiques.

Je remercie le professeur Bruno Blais pour son enseignement incroyable des méthodes numériques et son soutien tout au long de mon projet. Je remercie également les professeurs Sébastien Leclaire et Nick Virgilio, pour leur aide.

Je remercie Pauline Laurainne pour son soutien pendant ma période de rédaction.

RÉSUMÉ

Les moteurs essence à injection directe (EID) sont une technologie en vogue pour limiter les émissions de gaz à effet de serre, grâce à d'importantes économies de carburant comparé aux autres technologies d'essence. Cependant, d'autres polluants sont émis par les véhicules à combustion interne, comme les particules fines et les oxydes d'azote (NO_X) par exemple. Pour les traiter, des filtres à particules (FAP) et des chambres catalytiques (CC) sont appliqués aux systèmes de traitement des gaz d'échappement par les manufacturiers. Ces deux dispositifs sont constitués de monolithes fait de canaux rectangulaires. Dans le cas du FAP, les murs des canaux sont composés d'une céramique poreuse qui filtre les aérosols. Dans le cas des CC, les canaux sont imperméables à l'écoulement des gaz d'échappement et recouverts de catalyseur dans lequel les espèces chimiques à traiter diffusent. Afin d'abaisser les coûts et le volume de ces deux systèmes, il est possible d'intégrer le catalyseur directement dans la céramique qui forme les canaux du FAP. On parle alors de filtre à particule catalytique (FAPC). Cependant, cette déposition altère de façon significative les caractéristiques géométriques du FAPC à l'échelle du mur poreux. De plus en plus d'études s'intéressent ainsi à évaluer l'impact du dépôt de catalyseur sur les performances du FAPC en fonction, par exemple, de la quantité introduite, de la différence entre une déposition dans le mur ou sur le mur, ou encore d'un recouvrement par zones le long de chaque canal.

De façon expérimentale, une caractérisation globale des FAPC est possible et des valeurs caractéristiques peuvent être mesurées. Cependant ces études doivent être supportées par la simulation numérique à l'échelle microscopique. Ces modèles sont généralement multi-étapes : (1) reconstruction du milieu poreux, (2) calcul du champ d'écoulement des gaz d'échappement par une méthode de mécanique des fluides numérique (MFN), et (3) calcul du transport de quantité de matière des polluants par une approche eulérienne ou lagrangienne. Ils sont utilisés pour comprendre de façon générale l'impact d'un dépôt de catalyseur sur les performances microscopiques des FAPC. Cependant aucune étude n'a encore investigué l'impact spécifique de la distribution du catalyseur sur les performances du FAPC.

Pour pallier ce manque dans la littérature, l'objectif principal de cette thèse est de prédire l'impact de la distribution de catalyseur sur les performances globales d'un FAPC à l'échelle du milieu poreux qui forme ses canaux. Les performances globales d'un FAPC à l'échelle microscopique

sont définies par : (1) la perte de charge à travers le mur (ΔP), (2) l'efficacité de capture du mur (E_f), et (3) la conversion des espèces chimiques à travers le mur recouvert de catalyseur (X). Afin de mener à bien cet objectif, un modèle numérique multi-étape à l'échelle microscopique a été développé dans ce travail. Il consiste en : (1) la reconstruction digitale d'un domaine représentatif du mur de céramique composant les canaux d'un FAPC pour moteur EID, à partir d'images tomographiques, et la déposition artificielle de catalyseur dans celui-ci (2) le calcul du champ d'écoulement d'air à travers le milieu reconstruit à l'aide de la méthode de Boltzmann sur réseau (MBR), (3) le calcul des trajectoires des particules de suies à travers le champs d'écoulement par la résolution de l'équation de Langevin à l'aide du logiciel commercial GeoDict® et (4) le calcul du champ de concentration d'une espèce chimique hypothétique à l'aide de la MBR.

Le modèle ainsi assemblé a été utilisé pour réaliser une étude comparative entre deux séries de structures poreuses de FAPC présentant différents profils de distribution de catalyseur. La performance en filtration et en conversion catalytique des structures reconstruites a été systématiquement évaluée. Ainsi, il a été démontré qu'un mur de cordiérite recouvert d'un dépôt de catalyseur uniformément distribué peut atteindre un gain de 50% de performance en filtration par rapport à la même structure présentant une distribution non uniforme de catalyseur à quantité équivalente. Cette différence de performance en filtration entre les deux profils de distribution testés a pu être attribuée à un effet de renardage de l'écoulement d'air dans la structure poreuse. Cet effet de renardage est causé par le remplissage préférentiel des petits pores lorsque le catalyseur est déposé de façon non uniforme dans la céramique du FAPC. Dans ce cas, les particules de suies sont redirigées vers les canaux de plus gros diamètre où elles sont capturées moins efficacement. De la même façon, des meilleures performances en conversion catalytique pouvant aller jusqu'à 20% ont été évaluées, pour une réaction du premier ordre, en considérant une cinétique rapide, pour un une distribution uniforme de catalyseur comparée à une distribution non uniforme. Cette différence peut être attribuée à une plus faible surface de contact entre le catalyseur et l'espace poreux à travers lequel sont transportées les espèces chimiques, dans le cas d'un profil non uniforme, dû au remplissage préférentiel des petits pores. Cela rend le catalyseur moins accessible et dans le cas d'un régime limité par le transport des espèces chimiques, cela mène à une diminution des performances catalytiques du FAPC. Ces différents liens de cause à effet entre caractéristiques géométriques à l'échelle microscopique et performances du FAPC ont pu être déterminés à l'aide

d'outils numériques permettant une analyse détaillée des résultats : champ d'écoulement, champ de concentration des polluants et trajectoires des particules de suie.

Au cours de cette étude, chaque étape du modèle de prédiction des performances des FAPC a été vérifiée et validée. Pour valider l'étape (2), une nouvelle méthode expérimentale a été développée. Elle consiste à imprimer en 3D des structures digitales magnifiées de FAPC et de mesurer leur perméabilité à l'aide d'un montage expérimental à pression variable. La mesure de perméabilité se base sur une similarité cinématique entre le modèle digital à l'échelle microscopique et le modèle imprimé à échelle macroscopique. Un très bon accord entre les résultats numériques obtenus à partir de la MBR et les résultats expérimentaux ont confirmé la validité du modèle. Pour vérifier les étapes (3) et (4), des résultats de calculs sur des géométries simples ont été comparés à des solutions analytiques ou semi-empiriques et des résultats obtenus à l'aide d'autres logiciels commerciaux. L'étape (3) a été validée en reproduisant numériquement des résultats expérimentaux de filtration de filtres fibreux obtenus dans la littérature. Des calculs sur des géométries complexes et représentatives des FAPC ont également été comparés entre l'étape (4) et un logiciel commercial, afin d'évaluer la précision du calcul du champ d'écoulement par le modèle numérique.

Ayant ces données de confiance entre leurs mains, les industriels travaillant à l'amélioration des FAPC pourront prendre les bonnes décisions quant à l'investissement nécessaire rapporté au gain de performance pour l'uniformisation de la distribution du dépôt de catalyseur introduit dans les murs de céramiques de ces systèmes. Ainsi ces systèmes pourront être rendus plus performants et cela aura un impact direct sur la qualité de l'air dans les villes. Le modèle développé dans ce travail a donc été prouvé utile dans l'étude de la performance des FAPC à l'échelle microscopique. En continuant de développer ce modèle numérique afin de le rendre plus complet, par la prise en compte de plusieurs espèces et réactions chimiques par exemple, il pourra être utilisé dans d'autres études d'évaluation des performances des FAPC. Ce modèle numérique pourrait également servir dans d'autres contextes de milieux poreux réactifs comme dans l'étude du traitement des eaux, de l'absorbance des sols ou l'optimisation des matériaux de batteries lithium-ion pour ne citer que ces trois exemples.

ABSTRACT

Particulate filters (PF) have been used very successfully during the past decade to reduce particulate matter from the exhaust gas of modern vehicles. They consist in honeycomb monoliths made out of rectangular channels in most cases. These channels are alternatively plugged at the inlet or the outlet in order to force the exhaust gases to go through the porous material composing its walls. Catalytic chambers (CC) are open monoliths coated with precious metal composed catalysts. By diffusing in the catalyst, noxious gases as carbon monoxide (CO), nitrogen oxides (NO_X) and hydrocarbons (HC) are reduced or oxidized in armless components like CO_2, H_2O and N_2.

A relatively new technology consist in integrating the catalyst coating directly within the porous wall of the PF. The resulting system is called a coated particulate filter (c-PF). It possess both functionalities of filtering soot particles and treating noxious gases and it is expected to perform almost as well as the two concatenated separated systems. Nevertheless, the coating deposition impact on the performance of the PF and the catalyst itself is difficult to predict because of the complex structure of the c-PF. Indeed, the c-PF presents a multiscale nature. At the wall scale, its performance is defined by : (1) its pressure drop, (2) its capture efficiency and (3) its catalytic conversion through the coated walls of its channels. Experimentally, it is possible to study the performance of the c-PF at the whole monolith scale. This way, manufacturers can have global performance values of the whole filter and try to improve its geometry and physical properties.

Numerical simulation is a great tool to study c-PF at the microscopic scale. Thus numerous studies have investigated the impact of the washcoat deposition on the c-PF performance. These works make use of a three-step methodology consisting of : (1) the reconstruction representative elementary volume (REV) of a piece of porous wall, (2) the calculation of the flow field using a computed fluid dynamics (CFD) method, and (3) the calculation of either the soot particle trajectories or the chemical species concentrations within the wall. Doing so, it has been shown that the catalytic deposition can have a big impact on the performance of the c-PF at the microscopic scale. Nonetheless, the impact of the distribution uniformity of the catalyst has never been assessed.

In this work, a four step methodology is developed to shed light on the impact of the catalyst distribution in the porous wall of a PF on its global performance. It consists of: (1) digitally

reconstructing a representative domain of the ceramic wall composing the channels of a c-PF from tomographic images and artificially cover it with different catalyst profiles, (2) calculating the air flow field through the reconstructed medium using the lattice Boltzmann method (LBM), (3) calculating the trajectories of soot particles through the flow field by solving the Langevin equation using GeoDict software and (4) calculating the concentration field of a hypothetical chemical species using the LBM. Each step of this model was then verified by comparing calculation results on simple geometries with analytical or semi-empirical solutions or results obtained using other commercial software and validated by comparing with experience or results obtained using other commercial software on realistic geometries.

This model was then used to perform a comparative study between two catalyst distribution profiles in the cordierite wall of a c-PF. For this purpose, 9 structures with a non-uniform catalyst distribution profile with increasing amounts of catalyst and 4 structures with a uniform distribution profile with increasing amounts of catalyst were generated, to which a structure with no catalyst deposits was added. The filtration and catalytic conversion performance of these 14 structures was systematically evaluated. It was shown that a cordierite wall with a uniformly distributed catalyst deposition can achieve a 50% gain in filtration performance compared to the same structure with a non-uniform distribution of catalyst at equivalent coating amount. This difference in filtration performance between the two tested distribution profiles could be attributed to a channelling effect of the air flow in the porous structure. This channelling effect is caused by the preferential filling of small pores when the catalyst is deposited non-uniformly in the c-PF ceramic. In this case, the soot particles are redirected to the larger diameter pores where they are less efficiently captured. Similarly, better catalytic conversion performances of up to 20% have been evaluated, for a first order reaction, considering fast kinetics, for a uniform catalyst distribution compared to a non-uniform distribution. This difference can be attributed to a smaller interfacial area between the catalyst and the pore space through which the chemical species are transported, in the case of a non-uniform profile, due to the preferential filling of the small pores. This makes the catalyst less accessible and in the case of a transport-limited regime, this leads to a decrease in the catalytic performance of the c-PF. These different causal links between geometrical characteristics at the microscopic scale and the performance of the c-PF could be determined using numerical tools

allowing a detailed analysis of the results: flow field, pollutant concentration field and soot particle trajectories.

During this study, each step of the c-PF performance prediction model was verified and validated. To validate step (2), a new experimental method was developed. It consists in the 3D printing of digital c-PF structures and measuring their permeability using a variable pressure experimental set-up. The printed structures must first be magnified in order to make their manufacture possible and the permeability measurement is then based on a kinematic similarity between the digital model at the microscopic scale and the printed model at the macroscopic scale. A very good agreement between the numerical results obtained from the LBM and the experimental results confirmed the validity of the model. To verify steps (3) and (4), calculation results on simple geometries were compared with analytical or semi-empirical solutions and results obtained using other commercial software. Step (3) was validated by numerically reproducing experimental results of filtration of fibrous filters obtained in the literature. Calculations on complex and representative c-PF geometries were also compared between step (4) and commercial software to assess the accuracy of the flow field calculation by the numerical model.

With this reliable data in their hands, manufacturers working to improve c-PFs will be able to make the right decisions regarding the investment required in relation to the gain in performance in the uniformization of the distribution of the catalyst introduced into the ceramic walls of these systems. This way, these systems can be made more efficient and this will have a direct impact on air quality in cities. The model developed in this work has therefore proven useful in the study of the performance of c-PFs at the microscopic scale. By continuing to develop this numerical model to make it more complete, by taking into account several species and chemical reactions for example, it will be able to be used in other studies to evaluate the performance of c-PFs. This numerical model could also be used in other contexts of reactive porous media such as in the study of water treatment, soil absorbency or the optimization of lithium-ion battery materials, to name just a few.

TABLE DES MATIÈRES

LISTE DES TABLEAUX

LISTE DES FIGURES

LISTE DES SIGLES ET ABRÉVIATIONS

ADR	Advection-diffusion-réaction
CC	Convertisseur catalytique
CFD	*Computational fluid dynamics*
CPU	*Central processing unit*
CT	Tomographie
EID	Essence à injection directe
FAP	Filtre à particules
FAPC	Filtre à particules catalytique
MBE	Microscope à balayage électronique
MBR	Méthode de Boltzmann sur réseau
MDF	Méthode des différences finies
MEF	Méthode des éléments finis
MFN	Mécanique des fluides numérique
MPPS	*Most penetrating particle size*
MVF	Méthode des volumes finis
NS	Navier-Stokes
RAM	*Random access memory*
REV	*Representative elementary volume*
SRC	Système de réduction catalytique
TWC	*Three-way catalyst*
URPEI	Unité de recherche en procédés d'écoulements industriels

CHAPITRE 1 INTRODUCTION

1.1 Contexte de la recherche

Dans le contexte actuel de pandémie mondiale liée au covid-19, les chiffres semblent alarmants, avec une estimation de près de 500 000 morts dans le monde ('www.worldometers.info' Accessed June 26, 2020), 6 mois après l'identification des premiers cas dans la région de Wuhan en Chine. Selon un récent rapport de l'Organisation mondiale de la Santé, la pollution serait quant à elle responsable d'au moins 3 millions de morts par an dans le monde ("Ambient air pollution: A global assessment of exposure and burden of disease" 2016). Les polluants principalement visés par ce rapport sont les particules fines dont le diamètre aérodynamique est inférieur à 10 µm (PM_{10}) et à 2.5 µm ($PM_{2.5}$). Elles sont une menace grandissante pour la santé : problèmes pulmonaires et cancers (Lewtas 2007; Weichenthal et al. 2017; Weichenthal et al. 2019). Elles causent, dans de nombreuses grandes métropoles du monde, des phénomènes de *smog* ayant également un impact négatif sur l'environnement : notamment par le blocage de la photosynthèse des plantes recouvertes de particules (Penner, Chuang, and Grant 1998). Or, à Beijing en 2018 par exemple, 15 % des émissions de $PM_{2.5}$ étaient causés par le domaine des transports (Chang et al. 2019). Dans les dernières années, une partie active de la recherche s'attache donc à proposer des solutions pour des véhicules moins polluants. Dans ce contexte, les moteurs essence à injection directe (EID) sont une des technologies en vogue pour limiter la pollution. Diminution des gaz à effet de serre, en augmentant l'efficacité de carburant jusqu'à 25% par rapport à d'autres technologies d'injection d'essence (Zhao, Lai, and Harrington 1999). Diminution des particules fines, les émissions des moteurs EID représentant seulement 1% de celles des moteurs diesels : $1\text{-}10\times10^{12}$ #/km pour les moteurs EID contre $1\text{-}10\times10^{13}$ #/km pour les moteurs diesels. En 2016 les véhicules EID ont gagné 49% et 43% du marché des véhicules légers et des camions aux USA et en UE respectivement, 9 ans après leur introduction (Joshi and Johnson 2018; Davis et al. 2016; Mock 2017). Cependant, les moteurs EID ne sont pas totalement propres. Bien que leurs émissions de particules fines soient moindres comparées à celles des moteurs diesels, elles sont aussi très irrégulières sur un cycle moteur (Maricq et al. 2013) et peuvent atteindre des pics très élevés à des diamètres de l'ordre de 30 nm (Zhao, Lai, and Harrington 1999). Enfin, il a été récemment montré que les moteurs EID

émettent plus de particules fines que les moteurs diesels équipés de filtres (Platt et al. 2017). Outre les particules fines, d'autres polluants, émis par les véhicules modernes, sont à prendre en considération. Les oxydes d'azotes (NO_X), les hydrocarbures (HC) et le monoxyde de carbone (CO), participent aussi à la mauvaise qualité de l'air dans les zones urbaines (Maricq et al. 1999; Zhao, Lai, and Harrington 1999; Khalek, Bougher, and Jetter 2010). Les rejets de ces polluants sont encadrés par des normes dans différentes régions du monde. Ces normes contrôlent la masse de particules fines maximale tolérée ainsi que leur nombre et les concentrations maximales en gaz nocifs. Pour limiter les émissions des véhicules à moteur EID et respecter les normes environnementales, les industriels font face à deux options. La première est de travailler à l'amélioration continue de l'efficacité du moteur, afin qu'il rejette moins de polluants. La seconde est de développer des systèmes de traitement des gaz d'échappement de plus en plus efficaces.

Les filtres à particules (FAP) ont été développés et appliqués avec succès pendant les dernières décennies, dans le contexte des moteurs diesels. Ils présentent des efficacités de captures proches de 100 % dans certaines conditions (Konstandopoulos 2000). Ils consistent en des cylindres formés de canaux en nids d'abeilles extrudés, organisés en damier : ouverts à l'entrée et fermés à la sortie ou inversement. Ils sont formés par un matériau poreux qui est généralement une céramique. En plus du FAP, l'utilisation de catalyseur est nécessaire au traitement des gaz nocifs comme les NO_X. Cela se fait notamment à l'aide d'un ou plusieurs convertisseurs catalytiques (CC) placés en amont, en aval ou de part et d'autre du FAP. Afin de gagner en espace, en coût de matériel, mais aussi en perte de charge totale à travers le système de traitement des gaz d'échappement, de récentes techniques consistent à introduire le catalyseur directement dans l'espace poreux formant les canaux du FAP. On parle alors de FAP catalytique (FAPC).

1.2 Problématique des FAPC

La performance d'un FAPC se résume à trois principaux critères : (1) la perte de charge à travers le milieu filtrant (ΔP), le but est de minimiser la différence de pression entre l'entrée et la sortie du FAPC pour éviter un retour des gaz d'échappement vers le moteur, (2) l'efficacité de capture du filtre (E_f), le but étant de capturer le plus de particules de suie possible avant l'échappement des gaz dans l'atmosphère, (3) l'efficacité de conversion chimique du catalyseur (X), le but étant de réduire au maximum la concentration de NO_X, HC et CO en sortie du système d'échappement. La

technologie des FAPC étant relativement récente, encore peu d'études ont été menées pour déterminer l'impact que peut avoir un dépôt de catalyseur sur ses performances, notamment dans le cas des moteurs EID. Or selon la quantité et la localisation du dépôt, les performances du FAPC pourraient être impactées de façon significative. Faut-il alors accorder de l'importance à la façon dont est déposé le catalyseur dans le milieu poreux qui compose les canaux du FAP ?

Afin de répondre à cette problématique et fixer l'objectif de recherche de cette thèse, une revue de l'état de l'art sera entreprise dans le Chapitre 2.

CHAPITRE 2 REVUE DE LA LITTÉRATURE

Les FAP sont utilisés depuis plusieurs dizaines d'années et se sont prouvés très performants dans le contexte des moteurs diesels, avec des efficacités de capture allant de 20-30% pour un filtre propre à 100% pour un filtre encrassé (Tessier et al. 1980; Johnson 2004; Tandon et al. 2010; George and Heibel 2016). Les FAPC étant une technologie plus récente, notamment dans le contexte des moteurs EID, leurs performances sont moins étudiées et plus difficiles à prédire, plus de paramètres sont à prendre en compte. Pour comprendre les enjeux liés à l'étude des FAPC, l'état de l'art qui suit se propose de revenir sur des notions de base de la filtration des aérosols et de la conversion catalytique. Il sera ensuite présenté différentes études expérimentales et numériques du comportement des FAPC pour soulever les enjeux principaux auxquels font face les industriels pour améliorer ces systèmes. Le but de cet état l'art est de soulever les questions non résolues dans ce domaine, afin de se fixer un objectif dont la résolution pourra à la fois répondre à la problématique exposée en Section 12 et constituer un travail original, repoussant les limites des connaissances actuelles.

2.1 Les particules fines et autres polluants

Avant de s'intéresser au principe de fonctionnement des FAPC, il est important de bien comprendre les caractéristiques des particules à filtrer ainsi que des autres espèces chimiques à traiter à la sortie des moteurs diesels et EID. Comprendre les caractéristiques de ces aérosols est clé pour prendre la mesure de la problématique liée aux systèmes de traitement des gaz d'échappement tels que les FAPC. En plus des particules fines, les principaux polluants à traiter à travers le système d'échappement des véhicules modernes sont les oxydes d'azotes (NO_x) qui en plus d'être toxiques pour la santé humaine, sont également des gaz à effet de serre, les hydrocarbures (HC) et le monoxyde de carbone (CO). Enfin il faut savoir que d'autres polluants, tels que le benzène, le toluène ou les composés carbonylés, sont émis par les véhicules diesel ou essence, mais ne font pas l'objet de régulations, bien que pouvant être dangereux pour la santé et l'environnement (Martinet et al. 2017). Ces derniers ne seront pas étudiés dans ce travail.

2.1.1 Particules fines de moteurs diesels

Les particules émises par les moteurs diesels sont composées de plusieurs éléments qui résultent principalement de la combustion incomplète des carburants dans le moteur, voir Figure 2.1. Ces éléments et leur quantité varient selon les types de véhicules, l'étape du cycle du moteur, les conditions extérieures et la localisation dans le système d'échappement. On résume souvent cette composition à la dénomination de suie, bien qu'aucune définition stricte n'y soit associée.

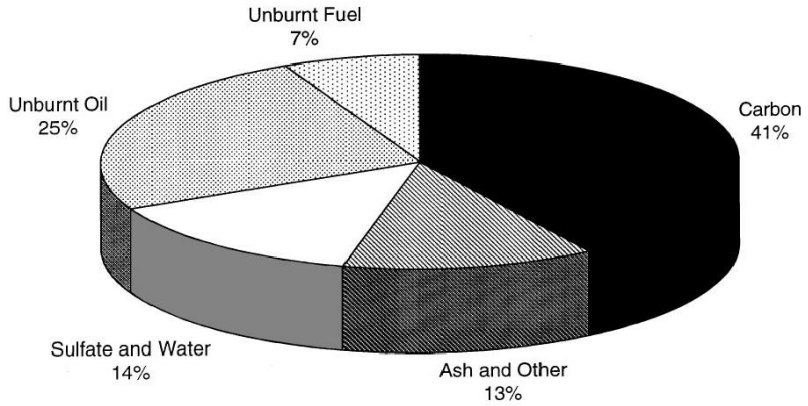

Figure 2.1 : Diagramme fromage de la composition des particules de suie de moteurs de véhicules diesels (Kittelson 1998). Les particules rejetées par les véhicules essence présentent la même composition dans d'autres proportions.

On peut distinguer trois modes de formation des particules de suie dans un véhicule à combustion. Premièrement, les noyaux, ou particules primaires, formées dans la chambre de combustion, dont la taille ne dépasse pas les 50 nm. Ces particules primaires, bien que ne contribuant que très peu à la masse totale des rejets, sont en très grand nombre. Plus loin dans le système d'échappement, les agglomérats ou agrégats se forment à partir de plusieurs particules primaires, comme illustré à la Figure 2.2. Leur taille est de l'ordre de 50 nm à 1 μm, et ils contribuent plus à la masse totale de suie qu'au nombre total de particules. Enfin les agglomérats peuvent former de plus gros groupes de particules d'une taille de 1 μm et plus, en se collant aux parois du système d'échappement puis en étant ré-entrainées par l'écoulement des gaz d'échappement. Pour les particules primaires ayant une sphéricité proche de 1, il est facile de définir une taille d'aérosol à partir de leur diamètre. Pour les plus gros agrégats, comme ceux montrés en Figure 2.2, il est beaucoup plus difficile de définir une taille de particule. Différentes définitions existent alors pour définir un diamètre équivalent de

particule, noté d_p. Ces dernières seront passées en revue dans la Section 2.2.1.4. La définition du diamètre utilisée dépend du domaine d'application et du phénomène physique à étudier. Dans le cas de la filtration à travers les FAP, le diamètre de mobilité, qui est défini comme le diamètre d'une particule sphérique ayant la même mobilité que la particule considérée, est généralement utilisé (Thomas et al. 2017).

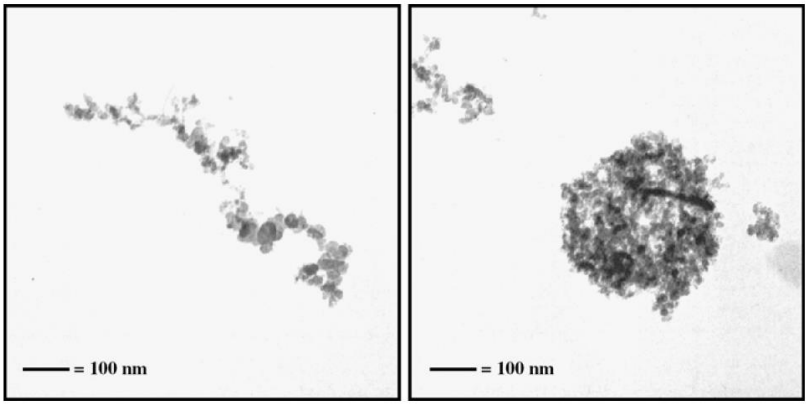

Figure 2.2 : Agrégats de particules de suie de moteur diesel avec un facteur de sphéricité de 0.04 à gauche, et de 0.15 à droite (Smekens et al. 2007).

La distribution de taille des particules émises par les moteurs diesels suit une loi log-normal qui présente un pique en nombre de particules autour de $d_p = 10\ nm$ à $d_p = 50\ nm$, qui correspond à la taille des particules primaires, et un pique en masse de particules autour de $d_p = 300\ nm$, correspondant à la taille moyenne des agglomérats, comme le montre la représentation schématique de la Figure 2.3.

Les caractéristiques des particules de suie émises par les moteurs diesels ont été étudiés plus en détail par (Kittelson 1998; Park, Kittelson, and McMurry 2004; Burtscher 2005).

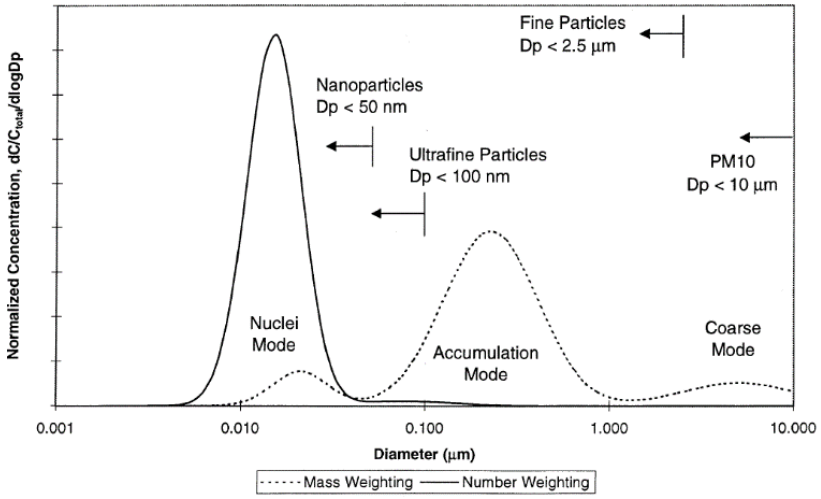

Figure 2.3 : Distribution typique de tailles de particules d'un moteur de véhicule léger diesel en masse (pointillés) et en nombre (trait plein) (Kittelson 1998).

2.1.2 Particules fines de moteurs essence à injection directe

Si les émissions de particules fines ont été d'abord pointées du doigt dans le cadre des véhicules diesel, les moteurs EID se sont prouvés non exempts de ces mêmes rejets. Comme pour les moteurs diesels, les caractéristiques des particules émises par les véhicules EID dépendent fortement du type de véhicule, du cycle moteur, des conditions extérieures et d'autres paramètres de conduite comme la vitesse notamment.

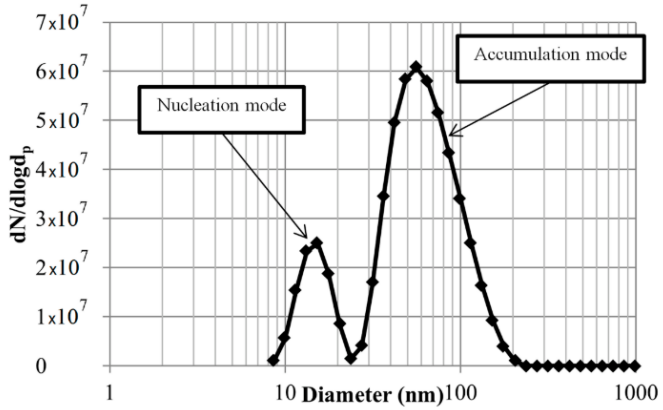

Figure 2.4 : Distribution de taille de particules de suie de moteur EID (Raza et al. 2018)

Il est à noter tout de même que la distribution de taille de particule est différente que pour les moteurs diesels. La principale différence à remarquer étant que la taille moyenne de particule se trouve autour de $d_p = 50\ nm$, ce qui est très inférieur au cas des moteurs diesels, comme le montre la Figure 2.4. Une quantité infime des particules émises par les moteurs EID présentent un diamètre supérieur à $d_p = 200\ nm$.

Les caractéristiques des particules de suie émises par les véhicules EID ont été étudiées plus en détail par (Maricq et al. 1999; Maricq, Podsiadlik, and Chase 1999; Zhao, Lai, and Harrington 1999; Khalek, Bougher, and Jetter 2010; Zinola et al. 2013; Platt et al. 2017; Raza et al. 2018). Dans le cas des moteurs essence comme diesel, la difficulté de la filtration des particules de suie vient de la distribution de leurs tailles, étendue sur plusieurs ordres de grandeur; les phénomènes physiques impliqués dans leur capture sont donc très variés. Une autre difficulté vient de la caractérisation de ces particules : taille, densité, forme, etc. rendant très difficile la prévision de l'efficacité de leur capture. Toutefois, plusieurs modèles analytiques ou empiriques ont été développés pour prédire par exemple la densité des particules de suie en fonction de leur diamètre équivalent d_p. Une relation régulièrement utilisée dans le domaine des suies et basée sur des valeurs empiriques est donnée par (Keskinen et al. 1998):

$$\rho_p = 1550 - (1550 - 155)\left(1 - \exp\left(-6.908\left(\frac{\log(d_p) - \log(0.03)}{-\log(0.03)}\right)^{4.28}\right)\right) \qquad (2.1)$$

Où ρ_p est la densité (exprimé en kg/m^3) d'une particule de suie de diamètre équivalent d_p. D'autres relations développées plus récemment peuvent être trouvées dans la littérature (Olfert and Rogak 2019; Baltzopoulou et al. 2018). Dans toutes ces relations, la densité des particules de suie est une fonction décroissante de leur diamètre. Comme le montre la Figure 2.2, les particules de suie se forment de façon dendritique et les plus grosses particules peuvent présenter des aspects très allongés qui mènent à une densité beaucoup plus faible que les particules primaires.

2.1.3 Régulation des émissions de particules fines

Les règles visant à réduire le nombre et la masse de particules fines rejetées dans l'atmosphère par les véhicules légers ont été introduites pour les moteurs diesels. Elles sont désormais également en

vigueur pour les moteurs essence dans de nombreuses régions du monde, en Europe et en Chine notamment. Ces règlementations tendent à devenir de plus en plus strictes au cours du temps, afin de diminuer l'impact de ces polluants, obligeant les constructeurs à une amélioration constante des moteurs et systèmes de traitement des gaz d'échappement. En Europe depuis 2017, la régulation Euro 6d-tmap limite les rejets de particules fines à 4.5 mg/km en masse ou 6.0×10^{-11} #/km en nombre (Inoda et al. 2017). Abaissant ainsi d'un ordre de grandeur le nombre maximal de particules rejetées autorisé par rapport à la précédente régulation datant de 2015. Pour respecter ces limites de pollution, deux possibilités s'offrent aux constructeurs. La première étant de modifier directement les moteurs ou les carburants pour réduire la formation des polluants à la source (dans la chambre de combustion). La seconde est de travailler sur des systèmes de traitement des gaz d'échappement tels que les FAP pour réduire les suies, ou les systèmes catalytiques pour réduire les gaz nocifs tels que les NO_x. Dans les dernières années, le développement de nouveaux systèmes tels que les FAPC vise à traiter tous ces polluants en même temps.

2.1.4 Autres polluants faisant l'objet de régulations

En plus des particules fines, d'autres polluants font l'objet de régulations. Dans le cas des véhicules EID les principales espèces chimiques à traiter à la sortie du système d'échappement sont le monoxyde de carbone (CO, 0.5% en volume), les hydrocarbures (HC, 350 ppmv) et les oxydes d'azote (NO_X, 900 ppmv) (Wang et al. 2014). La Figure 2.5 représente des exemples de limites d'émissions de ces différents composés en 2012 en Europe pour des véhicules à ignition par compression ou par étincelle.

		compression ignition vehicles	spark ignition vehicles
THC	mg / km	n.a.	100
NMHC	mg / km	n.a.	68
HC+NOx	mg / km	170	n.a.
NOx	mg / km	80	60
CO	mg / km	500	1000
particle mass	mg / km	4.5	4.5
particle number	# / km	$6.0\text{x}10^{11}$	TBD

Figure 2.5 : Exemples de valeurs limites pour différents polluants rejetés par les véhicules légers essence (Richter et al. 2012)

Dans le cas des moteurs diesels comme essence, ces polluants sont traités à l'aide de convertisseurs catalytiques (CC) utilisant le principe de réactions d'oxydo-réduction.

2.2 Les filtres à particules (FAP)

Les FAP ont été d'abord introduits pour satisfaire aux régulations en vigueur sur les rejets de particules fines, PM_{10} et $PM_{2.5}$, émis par des moteurs diesels. Ils sont désormais également appliqués aux moteurs EID dans certaines régions du monde. On distingue les FAP simples des FAP catalytiques (FAPC). Le principe de fonctionnement de ces deux systèmes sont développés dans les sous-sections qui suivent.

2.2.1 Les FAP non catalytiques

Bien qu'il existe plusieurs types de FAP (mousse ou flux radial, en autres), la technologie la plus largement utilisée, car prouvée comme étant la plus efficace (van Setten, Makkee, and Moulijn 2001), est le filtre en nid d'abeille extrudée. Elle fut introduite par (Howitt and Montierth 1981). Cette configuration présente l'avantage de maximiser la surface du collecteur tout en minimisant la perte de charge à travers le filtre.

2.2.1.1 Principe de fonctionnement

Les FAP en nid d'abeille extrudés prennent la forme de monolithes cylindriques d'environ 10 cm de longueur et 30 cm de diamètre, composés de milliers de canaux rectangulaires, d'environ 1 mm de largeur, organisés en damiers : ouverts à l'entrée et fermés à la sortie, ou schéma inverse. Ainsi, les gaz d'échappement transportant les particules de suie, traversent la paroi formée d'un matériau poreux entre deux canaux, pour ressortir de l'autre côté du FAP. Les particules transportées par l'écoulement sont alors capturées au passage du mur, lorsqu'elles entrent en collision avec le substrat poreux. Le principe de fonctionnement des FAP est présenté en Figure 2.6. Sur ce schéma descriptif, le mur poreux est représenté en trait plein jaune. Il existe plusieurs régimes de filtration à travers un milieu poreux tel que la céramique qui compose les canaux d'un FAP (Tien and Ramarao 2007). Le premier est la filtration profonde, elle a lieu lorsque le filtre est encore propre, les particules arrivent à pénétrer assez loin dans l'épaisseur du mur séparant deux canaux, et sont capturées à l'intérieur des pores. Après un certain temps, dépendant des caractéristiques du

véhicule, du régime moteur et du milieu poreux lui-même, l'encrassement du FAP amène les particules à s'accumuler en surface du mur poreux. Il peut alors se former un « gâteau » de suie à la surface du mur. Les particules dès lors très efficacement filtrées par cette couche de suie, c'est le second régime de filtration.

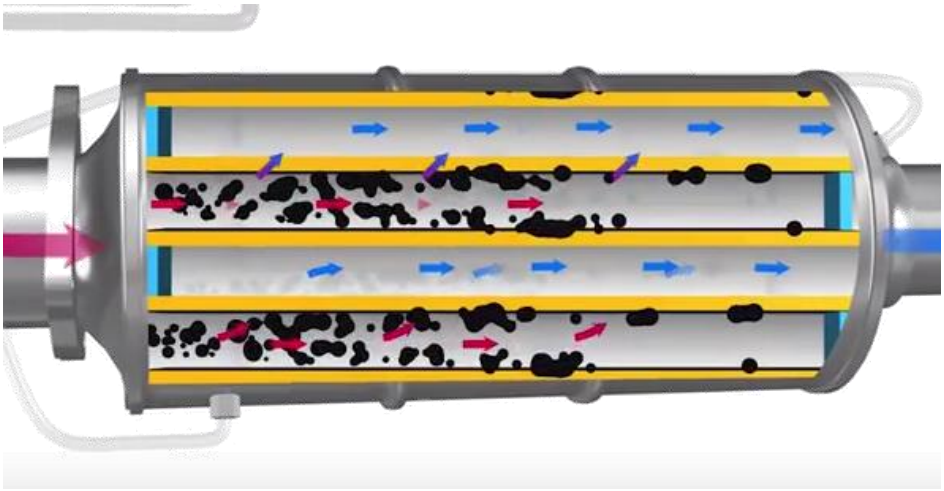

Figure 2.6 : Schéma du parcours des particules de suie à travers les canaux d'un FAP en plan de coupe. Le milieu poreux est représenté en trait plein jaune. Les particules de suie sont en noir. Le sens de l'écoulement est indiqué par des flèches rouges et bleues.

Le matériau poreux formant les murs des canaux du FAP est une céramique. On peut trouver plusieurs natures de céramiques dans les FAP, quelques-unes sont illustrées à la Figure 2.7. Les plus courantes étant le carbure de silicone (SiC) et la cordiérite dans le cas des moteurs EID, pour sa grande résistance thermique et son relativement faible coût. Ces céramiques ont l'avantage de maximiser la surface de solide par rapport à la porosité du matériau.

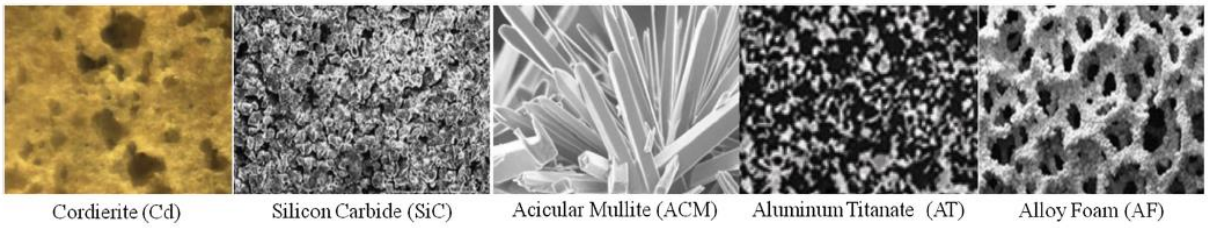

Figure 2.7 : Différents types de céramiques pour les FAP (Guan et al. 2015).

Deux caractéristiques mécaniques sont très importantes pour les FAP. La première est la perte de charge. Pour avoir un FAP performant, il faut minimiser la différence de pression (ΔP) à travers celui-ci, afin d'éviter un retour du flux des gaz d'échappement vers le moteur (Masoudi 2005). Mais cette caractéristique est à mettre en balance avec l'efficacité de capture des particules (E_f). De façon générale, il est difficile d'augmenter l'efficacité de capture sans impacter négativement la perte de charge. C'est l'enjeu de la conception des FAP. D'autres paramètres sont évidemment à prendre en compte pour juger de la qualité d'un FAP (Konstandopoulos 2000): résistance aux températures élevées et durabilité, par exemple. Ces caractéristiques ne seront cependant pas prises en compte dans ce travail, le but étant l'amélioration de la configuration géométrique des matériaux plutôt que leur nature.

La complexité de l'étude des FAP vient principalement de leur nature multiéchelle. Les différentes échelles du FAP seront détaillées en Section 2.3. L'échelle la plus critique pour l'étude des FAP est celle du mur poreux (quelques microns). Car c'est à cette échelle que la majorité des phénomènes physiques impliqués dans le principe de filtration ont lieu. Afin de mieux comprendre les caractéristiques mécaniques du FAP, il est donc essentiel d'évaluer ses caractéristiques géométriques à l'échelle microscopique.

2.2.1.2 Caractérisation du milieu poreux

De nombreuses caractéristiques géométriques des milieux poreux sont pertinentes dans l'évaluation ou la prédiction des performances du FAP. Deux catégories de descripteurs peuvent être distingués. Les descripteurs globaux, pour lesquels une valeur scalaire est attribuée à l'ensemble du milieu, et les descripteurs locaux pour lesquels une fonction ou vecteur est attribué à un volume élémentaire représentatif du milieu (*Representative Elementary Volume : VER*).

La première caractéristique, la plus utilisée pour la description des milieux poreux, est la porosité définie par (Dullien 1979):

$$\varepsilon = \frac{V_{por}}{V_{tot}} \tag{2.2}$$

où V_{por} est le volume de la phase poreuse et V_{tot} est le volume total du milieu poreux

Une autre caractéristique très importante pour les milieux poreux est la surface spécifique S_0 de la phase solide définie par (Dullien 1979):

$$S_0 = \frac{S}{V_{sol}} \tag{2.3}$$

où S est la surface interfaciale séparant la phase solide de la phase poreuse et V_{sol} est le volume de la phase solide. Enfin il est possible de définir un diamètre moyen de pore par (Dullien 1979):

$$d_w = \frac{2\varepsilon}{3(1-\varepsilon)}\frac{6}{S_0} \tag{2.4}$$

Ces trois descripteurs sont globaux et permettent une première caractérisation du milieu poreux. Cependant, une fois combinés, ils peuvent être des indicateurs des caractéristiques physiques du milieu poreux, comme il sera montré dans les deux sous-sections suivantes. Des caractéristiques vectorielles peuvent être également attribuées au milieu poreux afin de le caractériser plus précisément. Une catégorie très utilisée pour les descripteurs locaux est celle des fonctions de corrélation. La plus utilisée est le *two-point probability function*, qui est définie par (Torquato 2002):

$${S_2}^i(r) = \frac{n_i(r)}{n_t(r)} \tag{2.5}$$

où $n_i(r)$ et $n_t(r)$ sont respectivement le nombre de paires de points jetés aléatoirement dans le milieu et atterrissant tous deux dans la phase *i* et le nombre total de paires de points lancés aléatoirement, séparés par une distance *r*. Une autre fonction de corrélation importante dans un milieu poreux est le *lineal-path function*, donné par (Torquato 2002):

$$L^i(r) = \frac{m_i(r)}{m_t(r)} \tag{2.6}$$

où $m_i(r)$ et $m_t(r)$ sont le nombre de segments de longueur *r* inclus totalement dans la phase *i* lancés aléatoirement et le nombre total de segments lancés aléatoirement. Cette fonction de corrélation est représentative de la connectivité d'une phase (poreuse ou solide) dans le milieu. Ces

deux fonctions de corrélation, en plus d'être descriptives de la géométrie du milieu poreux, peuvent servir à des algorithmes de reconstruction des milieux poreux (Havelka, Kucerova, and Sykora 2016; Torquato 2002).

Des méthodes expérimentales existent afin de caractériser géométriquement un milieu poreux. Par exemple, la porosité peut être mesurée simplement par une méthode d'immersion (Harry and Johnson 2004; Zou and Malzbender 2016). La distribution de tailles de pore peut être évaluée par une intrusion au mercure (Abell, Willis, and Lange 1999). Le principe de cette méthode consiste à introduire du mercure liquide dans l'espace poreux du milieu par application d'une pression. Le diamètre de pore est alors donné par l'équation de Washburn:

$$d_{w,exp} = \frac{-4\gamma cos\theta}{\Delta P} \tag{2.7}$$

où ΔP est la pression appliquée, γ est la tension de surface du liquide et θ son angle de contact avec le solide. Les descripteurs locaux peuvent être plus difficilement évalués de façon expérimentale. L'une des méthodes les plus répandues pour la caractérisation des milieux poreux est l'analyse d'image, car elle offre la possibilité de définir une infinité de descripteurs à très petit coût.

2.2.1.3 Perte de charge

Le premier paramètre important, et le plus facile à étudier à priori, pour juger de la performance en filtration d'un FAP, est la perte de charge, définie par :

$$\Delta P = P_{in} - P_{out} \tag{2.8}$$

Où P_{in} et P_{out} sont les pressions à l'entrée et à la sortie du FAP respectivement. Expérimentalement elle peut se mesurer sur banc d'essai à l'aide de deux capteurs de pression en amont et en aval du filtre (Mikulic et al. 2010; Tsuneyoshi, Takagi, and Yamamoto 2011; Swanson et al. 2013; George and Heibel 2016). Cette mesure se fait en continu dans les véhicules modernes pour contrôler la régénération du filtre, c'est-à-dire le nettoyage du FAP. La perte de charge à travers un FAP se décompose en plusieurs contributions. Les principales contributions à la perte de charge totale à travers un FAP sont : les frictions le long des canaux, la contraction à l'entrée et l'expansion à la

sortie du cylindre, et finalement le passage à travers le mur poreux (Koltsakis et al. 2013). Expérimentalement il est impossible de différencier les contributions de chaque partie du FAP sans connaissance préalable de grandeurs locales telles que la perméabilité du milieu poreux qui constitue les canaux. C'est ce dernier paramètre qui est le plus difficile à évaluer parmi les performances en filtration du FAP, car il fait intervenir les caractéristiques microscopiques de l'écoulement à travers la géométrie complexe du milieu poreux. La perméabilité d'un milieu poreux est liée à la perte de charge à travers celui-ci via la loi de Darcy (Dullien 1979), qui est une expression de la conservation de la quantité de mouvement, valable pour des faibles nombres de Reynolds. Dans le contexte des milieux poreux, le nombre de Reynolds poreux est défini par (Bird, Stewart, and Lightfoot 2007):

$$Re_p = \frac{\rho U d_c}{\mu(1-\varepsilon)} \tag{2.9}$$

où U est la vitesse superficielle du fluide dans le milieu poreux, ρ et μ sont respectivement la densité et la viscosité dynamique du fluide, ε est la porosité du milieux poreux et d_c est le diamètre de collecteur du milieu poreux, qui sera défini plus en détail à l'Eq. (2.20).

À la loi de Darcy (premier membre de droite), peut s'ajouter, pour des plus hauts nombres de Reynolds ($Re_p \sim \geq 8$), le terme de Forchheimer (deuxième membre à droite) dans l'équation qui suit (Bird, Stewart, and Lightfoot 2007):

$$\Delta P = \frac{\mu U L}{k} + \beta \rho U^2 L \tag{2.10}$$

Où L est l'épaisseur de milieu poreux traversé par le fluide, k est la perméabilité au sens de Darcy du milieu poreux, μ est la viscosité dynamique du fluide, ρ est la masse volumique du fluide et β est le coefficient de Forchheimer déterminé expérimentalement. La vitesse de l'air dans le milieu poreux étant généralement faible dans le cadre des FAP ($U \approx 10^{-2}\ m/s$), l'écoulement se fait en régime laminaire, on peut donc négliger le terme de Forchheimer. Cette expression peut alors être utilisée pour calculer la perte de charge à travers un FAP propre, connaissant la vitesse superficielle du fluide et la perméabilité du milieu. L'ordre de grandeur de la perméabilité des milieux poreux formant les FAP est le μm^2 (Liu et al. 2018; Aleksandrova et al. 2018). La perméabilité du mur

poreux constituant un FAP peut être également exprimée en fonction des caractéristiques géométriques du milieu filtrant. Pour des écoulements laminaires, à travers des milieux semblables à des entassements de sphères, la perméabilité peut être décrite par la formule de Blake-Kozeny (Blake 1922; Kozeny 1927):

$$k_{BK} = \frac{1}{C_k}\frac{1}{S_0^2}\frac{\varepsilon^3}{(1-\varepsilon)^2} \tag{2.11}$$

Où $C_k = 4.16$ est la constante de Kozeny reliée à la tortuosité. Cette constante peut prendre d'autres valeurs selon la géométrie du milieu. Dans le cas des FAP, ΔP est une fonction croissante du temps, ou de l'accumulation des suies. La perte de charge est fortement influencée par le régime de filtration, comme évoqué plus haut. Lors de la filtration à travers un lit épais, c'est-à-dire à l'intérieur même du milieu poreux, l'évolution de la perte de charge est exponentielle en fonction du temps. Lors de la filtration par le gâteau de suie, l'évolution de la perte de charge est une fonction linéaire du temps ou de l'accumulation des suies. Ces deux tendances sont présentées dans les travaux de (Konstandopoulos 2000) notamment, qui ont comparé des résultats de simulation numérique d'un modèle de tranches d'un mur de cordiérite, avec des résultats expérimentaux sur un FAP de véhicule diesel, comme montré en Figure 2.8.

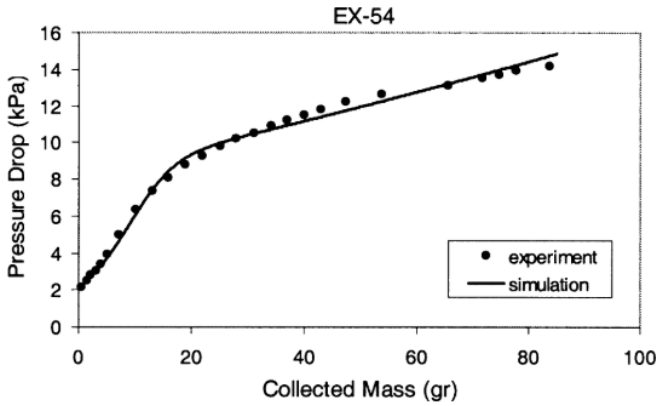

Figure 2.8 : Évolution de la perte de charge dans le temps, expérimentale et numérique dans un FAP pour moteur diesel (Konstandopoulos 2000)

Lorsque la perte de charge devient trop importante (plusieurs dizaines de kPa), le gâteau de suie étant devenu très épais (dans le cas des moteurs diesels principalement), il y a un risque de retour

de flux des gaz d'échappement vers le moteur. Il faut alors brûler les suies pour « nettoyer » le filtre. Ce procédé est appelé régénération et peut se faire principalement de deux manières (Konstandopoulos 2000). La première est dite active, par le biais du moteur : augmentation de la température des gaz d'échappement pour brûler les suies. Cette fonctionnalité étant maintenant automatique dans les véhicules les plus modernes. La deuxième est dite passive, par l'utilisation de catalyseur afin d'oxyder les suies en dioxyde de carbone (CO_2). Dans le cas des moteurs EID, dû à la plus faible concentration des suies et aux températures plus élevées, la formation d'un gâteau de suie est moins probable (Gong et al. 2018) et peut avoir lieu plus tard que dans le cas d'un moteur diesel.

2.2.1.4 Efficacité de capture

Après la perte de charge, le deuxième paramètre qui entre en compte dans l'évaluation de la performance en filtration d'un FAP est l'efficacité de capture du filtre, donnée par l'équation suivante :

$$E_f = \frac{N_{in} - N_{out}}{N_{in}} \tag{2.12}$$

où N_{in} est le nombre de particules entrant dans le filtre alors que N_{out} est le nombre de particules sortant du filtre. Expérimentalement, E_f peut se mesurer sur banc d'essai par la génération de particules à l'aide d'un moteur réel (Bogarra et al. 2017) ou artificiellement à l'aide d'un brûleur (Kazemimanesh et al. 2018). Les concentrations en suies à l'entrée et à la sortie du filtre peuvent ensuite être mesurées à l'aide d'un compteur de fumé ou d'un capteur photo-acoustique (Tandon et al. 2010). Ces mesures sont très sensibles à plusieurs paramètres : température, distribution de tailles de suie, vitesse de l'écoulement, etc., et aussi très coûteuses. Comme pour la perte de charge, l'efficacité de capture globale du FAP peut être décomposée en plusieurs contributions : effets d'entrée dans le cylindre du FAP, diffusion des aérosols le long des canaux et finalement passage à travers le milieu poreux constituant les canaux. Expérimentalement, il est encore une fois impossible de distinguer les différentes contributions à l'E_f des différentes échelles du FAP. Une solution est le développement de modèles analytiques, empiriques ou numériques.

Afin de minimiser le besoin en expérimentation, durant les dernières décennies, plusieurs modèles analytiques de filtration ont été développés pour prédire l'efficacité de capture des filtres, fibreux notamment. Ces modèles ont ensuite été portés à des géométries plus proches des céramiques formant les FAP, comme des entassements de sphères. Dans ces modèles, les aérosols sont également représentés par des sphères de diamètre équivalent d_p. Comme évoqué précédemment, le choix du diamètre équivalent de la particule n'est pas trivial et dépend notamment de ses caractéristiques géométriques ainsi que du phénomène physique à prendre en compte. La notion de diamètre équivalent permet de modéliser les particules de suie par des sphères possédant des propriétés physiques similaires aux particules de suie. Il existe, dans la littérature, plusieurs types de diamètres équivalents, selon la propriété physique à partager avec la particule de suie. Ceux-ci sont revus dans les travaux de (Thomas et al. 2017; Park, Kittelson, and McMurry 2004; Burtscher 2005; Smekens et al. 2007). Les trois principaux diamètres équivalents utilisés en pratique sont détaillés dans cette section. Premièrement, le diamètre équivalent de volume est le diamètre de la sphère de même volume que la particule considérée. Il s'exprime par:

$$d_V = \sqrt[3]{\frac{6m_p}{\pi\rho_p}} \tag{2.13}$$

où m_p est la masse de la particule et ρ_p sa masse volumique. Deuxièmement, le diamètre équivalent de mobilité (Tavakoli and Olfert 2014) est le diamètre d'une sphère partageant la même mobilité que la particule en considération:

$$d_{mo} = \frac{C_c(d_{mo})}{3\pi\mu B} \tag{2.14}$$

où μ est la viscosité dynamique du fluide. La mobilité B représente l'habilité d'une particule à se mouvoir dans le fluide en considération et est définie par :

$$B = \frac{\tau_p}{m_p} \tag{2.15}$$

où τ_p est le temps de relaxation de la particule. Cc est le facteur de correction de Cunningham dont la forme générale s'écrit :

$$C_c(d_p) = 1 + AK_n + BK_n \exp\left(\frac{-C}{K_n(d_p)}\right) \tag{2.16}$$

où A, B et C sont des constantes déterminées de façon expérimentale. K_n est le nombre de Knudsen de la particule définit par :

$$K_n(d_p) = \frac{2\lambda}{d_p} \tag{2.17}$$

où λ est le libre parcours moyen des particules de fluide à une température donnée. Enfin, le diamètre équivalent aérodynamique est le diamètre de la sphère de masse volumique standard $\rho_0 = 1000\ kg.m^{-3}$ et ayant la même vitesse terminale U_{ts} que la particule considérée :

$$d_{ae} = \sqrt{\frac{18\mu U_{ts}}{\rho_p C_c(d_{ae}) g}} \tag{2.18}$$

Dans d'autres domaines faisant intervenir des particules à l'échelle nanométrique, le diamètre de Feret, qui considère la distance entre deux tangentes à la particule dans un plan donné, est aussi régulièrement utilisé (Dražić, Sladoje, and Lindblad 2016). Dans le contexte des FAP, le diamètre équivalent le plus souvent utilisé est le diamètre de mobilité (Eq. (2.14)). La mesure de la mobilité d'un aérosol peut se faire à l'aide d'un analyseur de mobilité nanoélectrique (Tavakoli, Mitra, and Olfert 2011). Dans la suite de ce document, le diamètre équivalent des particules de suie, considéré comme étant leur diamètre de mobilité, sera simplement noté d_p.

La théorie de la filtration à travers un lit épais se base sur la théorie de filtration à l'aide d'un collecteur simple qui a été pour la première fois adaptée aux FAP diesels par (Konstandopoulos and Johnson 1989). Ces modèles ont été revus par (Tandon et al. 2010; Yang et al. 2016; Koltsakis et al. 2013) notamment. Dans ce modèle, l'efficacité globale du filtre est vue comme la somme des efficacités dues à différents mécanismes de capture des particules par un collecteur simple. Dans le cadre des FAP, plusieurs mécanismes de capture peuvent être négligés : gravité, électrostatique,

thermophorèse (Matte-Deschênes et al. 2016). Restent trois mécanismes de capture prépondérants. Le premier mécanisme de capture est la diffusion brownienne, il intervient pour les particules de très petites tailles ($d_p \leq 30\ nm$), dont les collisions dans des directions aléatoires avec les molécules de fluide les dévient des lignes de courant et les amènent à percuter le collecteur. Le deuxième mécanisme de capture est l'interception, il est prépondérant pour des tailles de particules moyennes ($30\ nm \leq d_p \leq 200\ nm$), lorsque le rayon de mobilité de la particule est inférieur à la distance entre le collecteur et le centre de la particule.

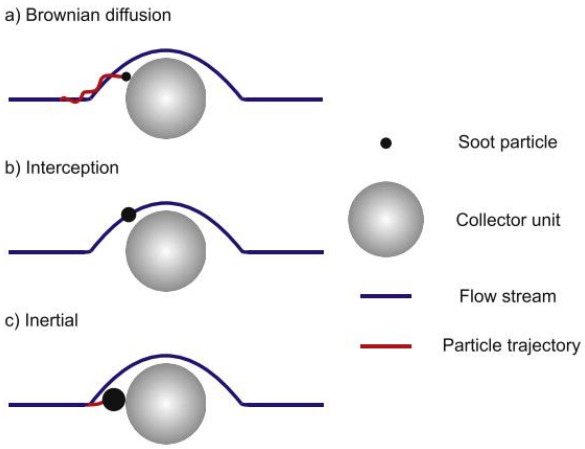

Figure 2.9 : Illustration des mécanismes de capture des particules de suie par un collecteur simple : a) diffusion brownienne, b) interception, c) impact inertiel. Tiré de (Serrano et al. 2016).

Enfin le troisième mécanisme de capture est l'impaction inertielle, pour des particules de taille plus importante ($d_p \geq 200\ nm$), les changements trop brusques de la direction des lignes de courant mènent à une déviation de la trajectoire des particules dont l'inertie est plus élevée. Elles en viennent alors à heurter le collecteur. Ces différents mécanismes de capture sont représentés de façon schématique à la Figure 2.9. Chaque mécanisme de filtration est décrit par un coefficient de collecteur simple η_i adimensionnel. L'efficacité totale de capture du filtre est alors donnée par la relation suivante (Lee and Gieseke 1979a) :

$$E_f = 1 - P_p = 1 - \exp\left(\frac{-3\eta(1-\varepsilon)L}{2\varepsilon d_c}\right) \tag{2.19}$$

où ε, d_c et L sont respectivement la porosité, le diamètre de collecteur et l'épaisseur du milieu filtrant considéré. Ces paramètres sont pris en compte dans P_p qui est le coefficient de pénétration du filtre. Le collecteur simple dans le cas des murs poreux de FAP est considéré comme une sphère de diamètre définit par :

$$d_c = \frac{3(1-\varepsilon)}{2\varepsilon} d_w = \frac{6}{S_0} \tag{2.20}$$

où d_w est le diamètre de pore moyen, qui peut être mesuré expérimentalement par des méthodes d'intrusion comme évoqué en Section 2.2.1.2. η est l'efficacité de capture globale du collecteur simple, définie comme étant la somme des contributions de chacun des mécanismes de capture :

$$\eta = \eta_D + \eta_R + \eta_I \tag{2.21}$$

Où η_D, η_R et η_I sont les efficacités de capture du collecteur simple par les mécanismes de diffusion, interception et impact inertiel respectivement. Plusieurs expressions pour les efficacités de capture du collecteur simple pour les différents mécanismes peuvent être trouvées dans la littérature pour des réseaux fibreux et des entassements de sphères. Dans un souci de concision, seuls les plus fréquemment utilisés dans le domaine des FAP seront rapportés ici. Pour la diffusion brownienne (Konstandopoulos and Johnson 1989) ont les premiers utilisé l'expression suivante dans le contexte des DPF:

$$\eta_D = C_D g_D(\varepsilon) {P_{e,p}}^{-2/3} \tag{2.22}$$

Où C_D est une constante qui varie selon plusieurs modèles (c.-à-d. 3.5 ou 4 dépendamment de la méthode d'analyse de la couche limite de diffusion), g_D est une fonction de la porosité, qui permet de tenir compte de la multiplicité du collecteur simple, qui est définie comme suit :

$$g_D(\varepsilon) = \sqrt[3]{\frac{\varepsilon}{2-\varepsilon-\frac{9}{5}(1-\varepsilon)^{\frac{1}{3}}-\frac{1}{5}(1-\varepsilon)^2}} \tag{2.23}$$

$P_{e,p}$ est le nombre de Péclet de la particule, qui rend compte du rapport entre les phénomènes d'advection et de diffusion et est défini par :

$$P_{e,p} = \frac{U_w d_c}{D_p} \tag{2.24}$$

Avec $U_w = \frac{U}{\varepsilon}$ la vitesse interstitielle définie comme étant la vitesse superficielle du fluide sur la porosité du milieu, et D_p est le coefficient de diffusion brownienne des particules de suie, défini par :

$$D_p = \frac{k_B T C_c}{3\pi\mu d_p} \tag{2.25}$$

Avec k_B la constante de Boltzmann, T la température, C_c le facteur de correction de Stokes-Cunningham défini à l'Eq. (2.16) et μ la viscosité dynamique du fluide. Pour modéliser l'interception (Lee and Gieseke 1979a; Konstandopoulos and Johnson 1989), l'expression suivante est utilisée:

$$\eta_R = \frac{3}{2} {N_r}^2 \frac{g_D(\varepsilon)^3}{(1+N_r)^S} \tag{2.26}$$

Avec $N_r = \frac{d_p}{d_c}$, le rapport entre le diamètre de particule et le diamètre du collecteur. Et le coefficient en exposant s dépendant de la porosité du filtre par la relation :

$$s = \frac{3-2\varepsilon}{3\varepsilon} \tag{2.27}$$

Enfin pour l'impaction inertielle (Rosner and Tandon 1995), l'expression suivante peut-être utilisée :

$$\eta_I = \frac{{S_t}^2}{(S_t + \frac{1}{4})^2} \tag{2.28}$$

où S_t est le nombre de Stokes de la particule de suie, définit comme le ratio de l'énergie inertielle de la particule sur l'énergie de frottement avec le fluide :

$$S_t = \frac{\frac{2}{9} C_c \rho_p U_w d_p^2}{2\mu d_c} \tag{2.29}$$

où ρ_p est la masse volumique des particules et C_c est le facteur de correction de Stokes-Cunningham (voir Eq. (2.16)).

Ainsi, chaque mécanisme de capture pris séparément contribue à l'E_f qui varie spécifiquement en fonction de la taille des particules. La sommation des E_f dues à chaque mécanisme résulte en la courbe d'E_f globale en fonction de la taille de particule, voir Figure 2.10. Le choix du diamètre des sphères servant à modéliser les particules est alors rendu très important et peu sensiblement influencer les résultats (Viswanathan et al. 2017).

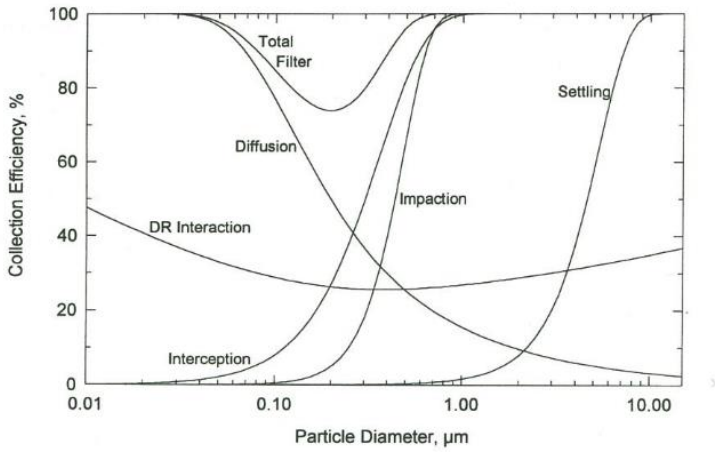

Figure 2.10 : Formes générales des efficacités de capture des particules incombant aux différents mécanismes de capture et leur sommation pour obtenir l'efficacité globale (Hinds 1999).

L'efficacité de capture peut être mesurée expérimentalement, sur banc d'essai, à l'aide d'un moteur réel ou par lancés de particules générées artificiellement (Yang et al. 2009; Mikulic et al. 2010; Tandon et al. 2010; Swanson et al. 2013; Joshi and Johnson 2018). Tout comme la perte de charge, l'efficacité de capture est influencée par l'accumulation des suies à l'intérieur puis à la surface du mur poreux. Pour un filtre propre, l'efficacité de capture dépend des conditions extérieures, des caractéristiques géométriques du filtre et des propriété des particules (Viswanathan et al. 2017). De manière générale, l'E_f est fortement dépendante de la taille des particules comme le montre l'étude

de (Joshi and Johnson 2018) sur des FAP pour moteurs EID, illustrée à la Figure 2.11, ou celle de (Liu et al. 2018).

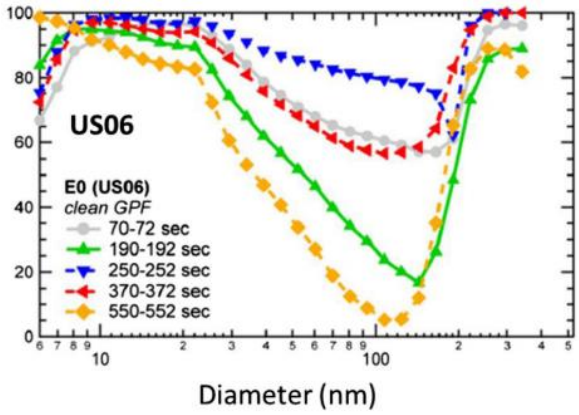

Figure 2.11 : Évolution de l'E_f en fonction du temps pour différents diamètres de particules sur un cycle de moteur US06 (Joshi and Johnson 2018).

Le diamètre auquel l'E_f est la plus basse est dénommée la taille de particule de pénétration maximale (*most penetrating particle size* : MPPS) et se situe, dans le cas des moteurs EID aux alentours de 200-300nm, comme le montre la Figure 2.11. Pendant le régime de filtration par le gâteau de suie, l'efficacité de capture est très proche de 100% pour tous les diamètres aérodynamiques de particules.

2.2.1.5 Facteur de qualité

Un FAP présentant de bonnes performances de filtration doit allier un faible ΔP et une haute E_f. Cependant, dans le cas général, la balance tend d'un côté ou de l'autre : un faible ΔP est associé à une faible E_f et inversement (Konstandopoulos 2000; Zuberi et al. 2008; Yang et al. 2009), ces deux valeurs étant inversement proportionnelles l'une par rapport à l'autre à la taille de pore moyenne dans le mur. Pour juger systématiquement des performances de filtration des FAP, l'utilisation d'un facteur de qualité du filtre (*quality factor* : Q_f), défini dans (Hinds 1999), est nécessaire. Il s'exprime par:

$$Q_f = \frac{-\ln(1 - E_f)}{\Delta P} \tag{2.30}$$

La propriété intéressante de cette grandeur est qu'elle est indépendante de l'épaisseur du milieu filtrant, voir les Eq. (2.10) et (2.19). Le Q_f est donc un critère de jugement de qualité des performances en filtration qui peut être utilisé à des fins de comparaison entre différents milieux filtrants.

2.2.2 Les FAP catalytiques (FAPC)

Dans le cas des moteurs diesels comme essence, les FAP sont habituellement associés à des chambres de conversion catalytiques (CC) pour réduire ou oxyder les gaz nocifs comme les NO_x, les HC ou le CO, qui sont transformés en composés moins nocifs tels que H_2O, CO_2 et N_2. Ces dernières prennent la forme de monolithes cylindriques composées de canaux, de façon similaire aux FAP, à la différence qu'ils ne sont bouchés ni à l'entrée ni à la sortie. Les gaz d'échappement circulent dans ses canaux et sont en contact avec le catalyseur déposé sur leurs parois. Ainsi les gaz d'échappement diffusent à travers le catalyseur et réagissent dans son volume. Dans le cas des moteurs diesels, on associe généralement le système de réduction catalytique (SRC) au FAP pour obtenir un FAPC. Son but est principalement de traiter les NO_X, pour les transformer en H_2O et N_2, la plupart du temps à l'aide d'urée. Dans le cas des moteurs essence, on associe le système de catalyseur à trois voies (*three-way catalyst : TWC*), dont le but est de traiter les NO_x, les HC et le CO, au FAP pour former le FAPC (Lee, Theis, and Kyriakidou 2019). Le TWC est généralement composé de mixtures de platine ou de palladium et d'alumine (Pd ou Pt/Al2O3) (Benjamin, Liu, and Roberts 2004), ce qui en fait un matériau relativement onéreux et donc à utiliser avec parcimonie. Dans un souci de gain de place, de réduction des coûts et de diminution de la perte de charge globale du système d'échappement, la tendance est de réduire ces deux systèmes en un (CC + FAP), par l'intégration du catalyseur au sein même du mur poreux du FAP. À la faible perte de charge et la grande efficacité de capture, il faut alors ajouter un haut taux de conversion du catalyseur pour résumer les caractéristiques d'un filtre à particules catalytiques (FAPC) haute performance.

2.2.2.1 Techniques de déposition de catalyseur

L'intégration du catalyseur dans la céramique du FAP peut se faire à l'intérieur du mur, à la surface du mur ou de façon combinée. La déposition se fait généralement par l'introduction d'une mixture de catalyseur et d'un fluide, sous pression, puis par succion et séchage du fluide, pour ne laisser qu'un dépôt de catalyseur sur les parois de la céramique du FAP (Shimrock, Taylor, and John M. Collins 1985; Aderhold et al. 1999; Foerster et al. 2000). Lorsqu'à l'intérieur du mur, cette déposition ne se fait pas forcément de façon uniforme, comme le montre la Figure 2.2.12. Des agglomérats de catalyseur se forment à certains endroits de l'espace poreux, alors que d'autres zones sont laissées vides de catalyseur. Les techniques de déposition de catalyseur sont donc sujettes à beaucoup d'amélioration et de nombreux paramètres peuvent être optimisés : pression, nature du fluide, concentration du catalyseur, etc.

La non-uniformité du dépôt de catalyseur peut poser plusieurs problèmes : une partie du catalyseur est susceptible de ne pas être utilisé pour la réaction et les caractéristiques de l'espace poreux vont être fortement altérées. Par exemple, la distribution de taille de pores peut être grandement modifiée, comme le montre les études de (Seong et al. 2019; Václavík et al. 2017). Cela peut avoir des conséquences importantes sur la performance en filtration et en conversion catalytique du FAPC.

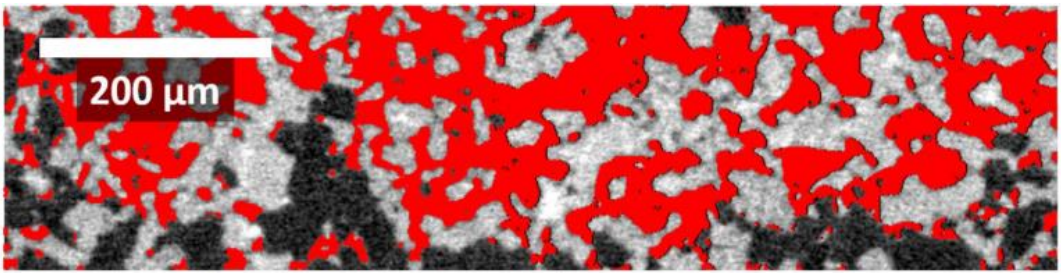

Figure 2.2.12: Image tomographique d'un dépôt de catalyseur (en rouge) dans l'espace poreux (gris foncé) d'un mur de cordiérite (gris clair) d'un FAP pour moteur essence (Václavík et al. 2017).

Ainsi plusieurs paramètres peuvent être ajustés afin d'améliorer la déposition de catalyseur dans l'espace poreux et la rendre plus uniforme. Cela reste une problématique industrielle importante et

le gain de performance obtenu par l'uniformisation du dépôt catalytique doit donc être bien évalué pour que les industriels prennent les meilleures décisions.

2.2.2.2 Performances en filtration

Les premiers paramètres sur lesquels la déposition de catalyseur peut avoir un impact sont ceux qui définissent la performance en filtration du FAPC (ΔP et E_f). Or cette performance est l'essence même du FAP avant qu'il soit rendu catalytique. Il est donc important pour les industriels de s'assurer que la déposition de va pas altérer négativement ces performances. (Tsuneyoshi, Takagi, and Yamamoto 2011) ont étudié l'évolution de la taille de pores, de l'efficacité de capture et de la perte de charge d'échantillons de SCR-FAP, dénotés de A à E, dans lesquels ont été introduits des quantités croissantes de catalyseur formé de particules d'alumine.

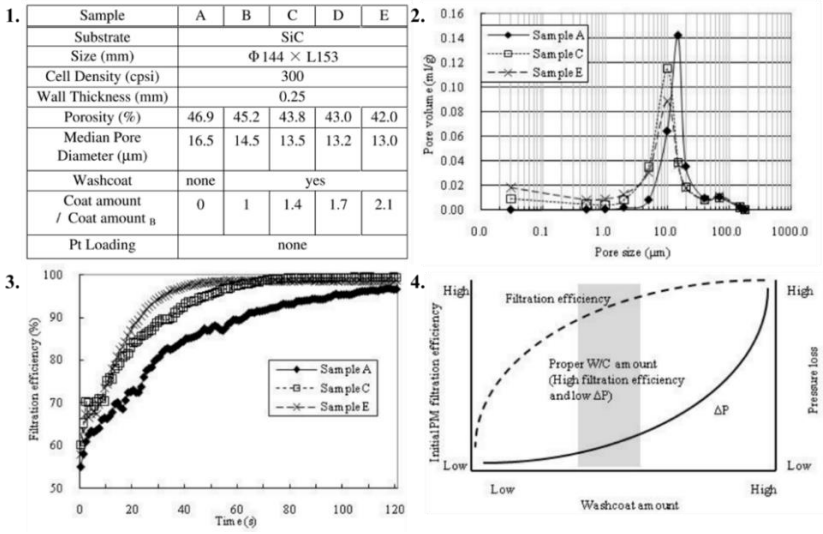

Sample	A	B	C	D	E
Substrate	SiC				
Size (mm)	Φ144 × L153				
Cell Density (cpsi)	300				
Wall Thickness (mm)	0.25				
Porosity (%)	46.9	45.2	43.8	43.0	42.0
Median Pore Diameter (μm)	16.5	14.5	13.5	13.2	13.0
Washcoat	none	yes			
Coat amount / Coat amount $_B$	0	1	1.4	1.7	2.1
Pt Loading	none				

Figure 2.13: Résumé des résultats de l'étude de (Tsuneyoshi, Takagi, and Yamamoto 2011). 1. Plan expérimental. 2. Évolution de la distribution de taille de pores pour trois échantillons. 3. Évolution de l'efficacité de capture pour trois échantillons. 4. Graphique résumé de l'évolution de la perte de charge et de l'efficacité de capture en fonction de la quantité de catalyseur dans un SCR-FAP.

Leurs résultats tendent à montrer qu'une augmentation de la quantité de catalyseur augmente la perte de charge ainsi que l'efficacité de capture à travers le FAPC, voir graphiques 3. et 4. en Figure

2.13. Cependant, comme mentionné dans cette étude, ce résultat est spécifique à un type de céramique et de distribution de catalyseur. Or les paramètres géométriques du dépôt ne sont pas caractérisés. Toutefois, les résultats du graphique 2. de la Figure 2.13 laissent présumer un dépôt uniforme. Il est tout de même à noter que cette étude souligne l'impact très important de la quantité de dépôt de catalyseur sur les performances en filtration des FAPC.

Le recouvrement d'un FAP pour moteur EID est d'autant plus avantageux que dans les cas des moteurs diesels, dû à la plus faible quantité de particules à filtrer et donc de la faible accumulation rendant le catalyseur plus accessible, car moins encrassé. (Inoda et al. 2017) ont comparé l'impact de dépôts de catalyseur sur les performances des FAPC pour moteurs EID. Dans ce cas, quatre profils étaient à l'étude pour deux types de dépositions: une déposition sur le mur et une déposition à l'intérieur du mur. L'étude rapporte des résultats similaires à ceux de (Tsuneyoshi, Takagi, and Yamamoto 2011). L'augmentation de la quantité de catalyseur tend à augmenter la perte de charge, voir Figure 2.14, ainsi que l'efficacité de capture des FAPC dans le cas des moteurs EID comme diesels. Cependant, une fois de plus, les caractéristiques géométriques du dépôt ne sont pas présentées. Un résultat notable est que l'impact d'un dépôt de catalyseur à la surface de la céramique est présenté comme plus important que pour un dépôt interne, en termes de performance de filtration.

Coated GPF	Substrate (Filter)	Coating Area	Coating Amount (relative value)
C	300cpsi 8mil φ118.4mm	On-the-wall	a (10%)
D			b (50%)
E			c (100%)
F			d (150%)
G		In-the-wall	a (10%)
H			b (50%)
I			c (100%)
J			d (150%)

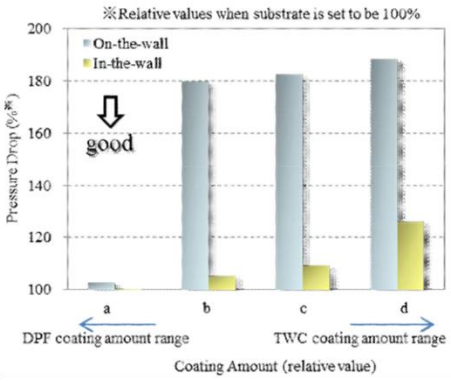

Figure 2.14 : Influence de la quantité de catalyseur sur la perte de charge à travers un FAPC pour EID (Inoda et al. 2017)

L'une des problématiques importantes soulevées par les deux précédentes études est la large possibilité de profils de déposition lorsque le catalyseur est introduit à l'intérieur du mur séparant les canaux du FAPC. Or aucune de ces études ne caractérise la distribution du dépôt à l'intérieur

du milieu poreux. Dépendamment du type de céramique et de ses caractéristiques géométriques, la distribution de catalyseur peut avoir des conséquences bien différentes sur les performances en filtration des FAPC. Il est donc difficile de penser pouvoir optimiser par essai erreur la déposition de catalyseur dans les FAPC. Une étude plus systématique et caractérisée doit être entreprise pour vraiment comprendre l'évolution des performances des FAPC.

2.2.2.3 Performances en conversion

En plus des performances en filtration, la caractérisation des performances des FAPC comprend également les performances catalytiques. Pour évaluer ces performances, la concentration des espèces chimiques dans le FAPC, qui sont régis par un problème d'advection-diffusion-réaction (ADR), doivent être monitorées. La performance en catalyse est traduite par la conversion des espèces chimiques à traiter. Cette conversion s'exprime pour une espèce chimique donnée, pouvant être le NO_X, HC ou CO présent dans les gaz d'échappement, par :

$$X = \frac{c_{in} - c_{out}}{c_{in}} \tag{2.31}$$

Où c_{in} et c_{out} sont les concentrations de l'espèce chimique à l'entrée et à la sortie du système catalytique, respectivement.

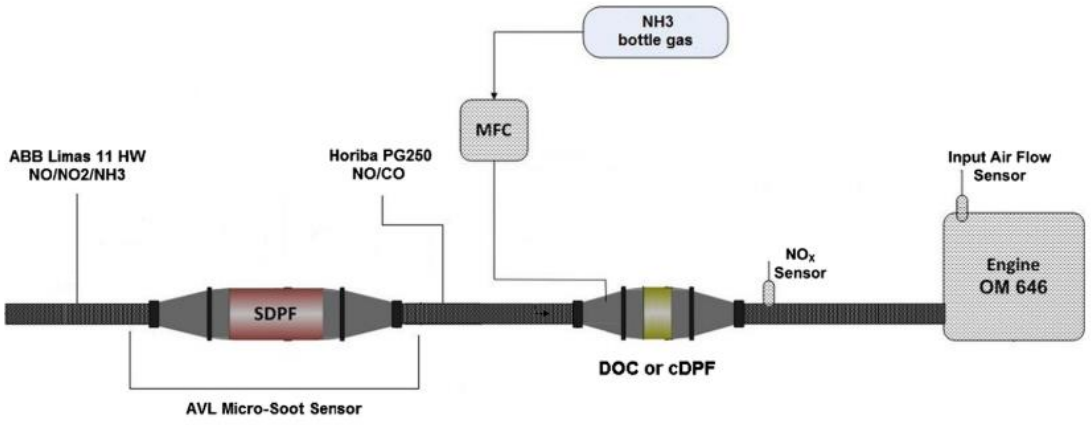

Figure 2.15: Montage expérimental pour la mesure de la conversion d'un DPF recouvert de catalyseur (Tronconi et al. 2015).

Expérimentalement la conversion d'un système catalytique peut se mesurer de plusieurs façons. Premièrement sur un échantillon (quelques canaux) de monolithe recouvert de catalyseur placé dans un réacteur (Tomašić and Gomzi 2004) dans lequel vont s'écouler des gaz d'échappement artificiels. Les produits de la réaction peuvent alors être analysés par chromatographie en phase gazeuse, afin de déterminer la conversion du système catalytique. Autrement à travers le monolithe au complet sur banc d'essai à l'aide de senseurs (Tronconi et al. 2015). La conversion catalytique dans un FAPC vise à être aussi élevée que pour un convertisseur catalytique en monolithe. Or elle peut atteindre 90% pour la réduction des NO_X notamment dans le cas d'un SRC (Czerwinski et al. 2015). L'une des principales difficultés dans le contrôle de ce procédé est que les réactions mises en jeux pour la réduction des NO_X, et l'oxydation du CO et des HC, sont interdépendantes, multi-étapes et faisant intervenir plusieurs composés chimiques (Olowojebutu and Steffen 2017; Ahmadinejad et al. 2015). Pour la réduction des NO_X notamment, les équations mises en jeu sont (Rappé 2014):

$$NH_2 - CO - NH_2 \rightarrow NH_3 + HNCO \quad (2.32.1)$$

$$HNCO + H_2O \rightarrow NH_3 + CO_2 \quad (2.32.2)$$

$$4NH_3 + 4NO + O_2 \rightarrow 4N_2 + 6H_2O \quad (2.32.3)$$

$$2NH_3 + NO + NO_2 \rightarrow 2N_2 + 3H_2O \quad (2.32.4)$$

$$4NH_3 + 3NO_2 \rightarrow 3.5N_2 + 6H_2O \quad (2.32.5)$$

Cela rend la prédiction des conversions atteintes en sortie de FAPC très difficile. Une autre difficulté de l'intégration du catalyseur dans le mur de céramique composant les canaux du FAP est la limitation en diffusion que cela peut induire. En effet, dans le cas des CC la diffusion se fait instantanément par la promiscuité entre l'écoulement des gaz d'échappement et le catalyseur. Dans le cas d'un FAPC, la structure tortueuse du milieu poreux ralentit le transport des espèces chimiques vers le catalyseur. Dans la littérature, la métrique rendant compte de cet effet est appelée l'efficacité du catalyseur et est définie par :

$$\eta = \frac{\bar{c}_{cat}}{\bar{c}_{por}} \tag{2.33}$$

Où $\bar{c}_{cat}$ et $\bar{c}_{por}$ sont respectivement la concentration moyenne dans le catalyseur et dans l'espace poreux. Une autre façon de quantifier les limites de transport des espèces chimiques dans l'espace poreux rempli de catalyseur est par le biais du module de Thiele (Aris 1957). Il est défini pour une réaction du premier ordre à travers le deuxième nombre de Damköhler (Da_{II}):

$$\Phi = \sqrt{Da_{II}} = \sqrt{\frac{k_1}{D_{cat}}} L_{cat} \tag{2.34}$$

pour lequel k_1 est la constante cinétique de la réaction prise en compte, D_{cat} est le coefficient de diffusion dans le catalyseur et L_{cat} est une longueur effective caractéristique dans le catalyseur, pouvant être interprétée par une demi-épaisseur moyenne du dépôt. Pour de faibles valeurs de Φ, la réaction est limitante, pour de grandes valeurs de Φ, le transport des espèces chimiques (advection et diffusion) est limitant. Ce nombre peut être approximé par des corrélations semi-empiriques. Ainsi dans la littérature, selon la forme géométrique du catalyseur on trouve plusieurs formules pour Φ (Papadias, Edsberg, and BjoKrnbom 2000; Hayes, Liu, and Votsmeier 2005; Hayes et al. 2007; Opitz and Votsmeier 2016; Greiner et al. 2019). Deux autres nombres adimensionnels sont importants pour la description d'un problème d'advection-diffusion, le premier nombre de Damköhler (Da_I), qui traduit le rapport adimensionnel entre la réaction et la convection se définit comme :

$$\mathrm{Da}_I = \frac{k_1 d_w}{U} \tag{2.35}$$

Enfin le nombre de Péclet, qui représente le rapport adimensionnel du transport par convection par rapport au transport par diffusion, se définit comme :

$$\mathrm{Pe} = \frac{d_w U}{D_{por}} \tag{2.36}$$

où dans ce cas, D_{por} est le coefficient de diffusion d'une espèce chimique considérée, dans l'espace poreux du FAPC.

Dans le contexte des moteurs diesels (Karamitros and Koltsakis 2017) proposent une étude comparative, à l'aide d'un modèle analytique, entre plusieurs profils de déposition de SRC dans un FAP recouvert de catalyseur par zone : un profil uniforme dans l'épaisseur du mur poreux, un profil présentant davantage de catalyseur à l'entrée du mur (2:1) ou à la sortie du mur (1:2), comme illustré à la Figure 2.16. Cette étude souligne les hautes performances pouvant être atteintes en conversion par les FAPC. Cependant la dépendance des résultats au profil de déposition global n'est pas très marquée dans ce cas d'étude.

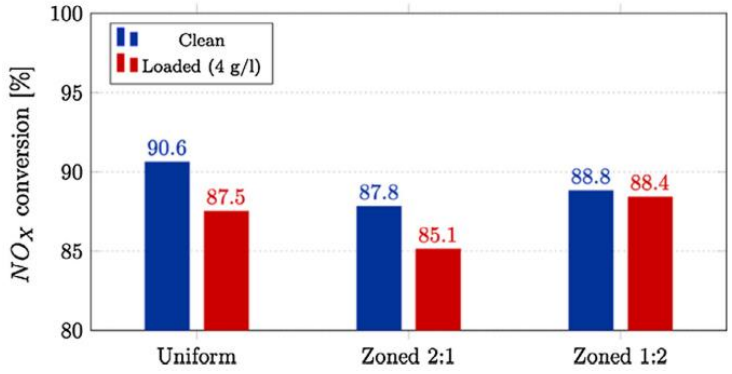

Figure 2.16 : Résultats de conversion des NO_X à 250°C pour différents profils de déposition de catalyseur dans le cas d'un filtre diesel propre (barres bleues) et encrassé (barres rouges) (Karamitros and Koltsakis 2017).

Plus d'études sur les performances des FAPC dans le contexte des moteurs diesels ont été menées par (Palmaa et al. 2013; Czerwinski et al. 2015; George and Heibel 2016), et plus généralement les technologies de FAPC pour moteurs diesels ont été revues par (van Setten, Makkee, and Moulijn 2001; Johnson 2004). Dans le contexte des moteurs EID, l'étude de (Inoda et al. 2017), mentionné dans la Section 2.2.2.2, est complétée par la comparaison entre deux profils de dépositions, par zone ou uniformément dans le mur du FAP, et leurs performances en conversion catalytique sur les concentrations de HC et de NO_X. Les résultats soulignent une meilleure performance pour les FAPC dont la déposition se fait par zone (plus grande densité de catalyseur proche de l'entrée ou de la sortie du mur poreux). Cela souligne encore une fois l'importance des caractéristiques du profil de déposition sur les performances en conversion du FAPC. Une autre étude mené par

(Tanaka, Miyoshi, and Sato 2018) propose une analyse complète des caractéristiques et performances de FAPC pour moteurs EID. Pour les performances en conversion, les résultats sont comparés à un TWC conventionnel. Dans le cadre de cette étude, la conversion des trois espèces visées par des réglementations est moindre dans le cas d'un FAPC par rapport à un TWC conventionnel, comme montré en Figure 2.16. Mais le dépôt n'est pas caractérisé. Pour être plus complet, les FAPC pour moteurs EID ont été revus en détail par (Richter et al. 2012) notamment.

De ces différentes études, deux résultats importants peuvent être dégagés. Le premier étant que les réactions mises en jeu au sein des FAPC sont complexes et très difficiles à contrôler de façon complète et prédictive. Le second étant que les caractéristiques géométriques de la déposition de catalyseur au sein des FAPC ont un impact important sur ses performances en conversion catalytique, comme sur ses performances en filtration.

2.3 Modélisation des FAPC

Comme entrevu dans les parties précédentes de cet état de l'art, l'étude des FAPC fait intervenir de nombreux phénomènes physico-chimiques complexes et plusieurs constituants matériels, dont la géométrie à un fort impact sur ses performances. Cela rend l'optimisation expérimentale des FAPC très couteuse et compliquée : matériaux onéreux, panel d'expérience multiple, difficulté de reproductibilité de la mesure. La modélisation numérique apparaît alors comme une alternative de choix pour l'étude de ces systèmes. Les enjeux de la modélisation des FAPC sont d'abord les enjeux de la modélisation des FAP. Or les FAP induisent des phénomènes physiques à plusieurs échelles bien distinctes comme le montre la Figure 2.17 : du filtre complet (quelques dizaines de centimètres), à un canal spécifique (quelques millimètres), au mur de matériaux poreux séparant les canaux (quelques centaines de microns), jusqu'au pore de taille caractéristique à l'intérieur du mur poreux (quelques dizaines de microns). En pratique la modélisation des FAP se fait principalement à deux échelles dans la littérature. La première et la plus courante est celle du canal, dont la répétition par milliers forme le cylindre du FAP.

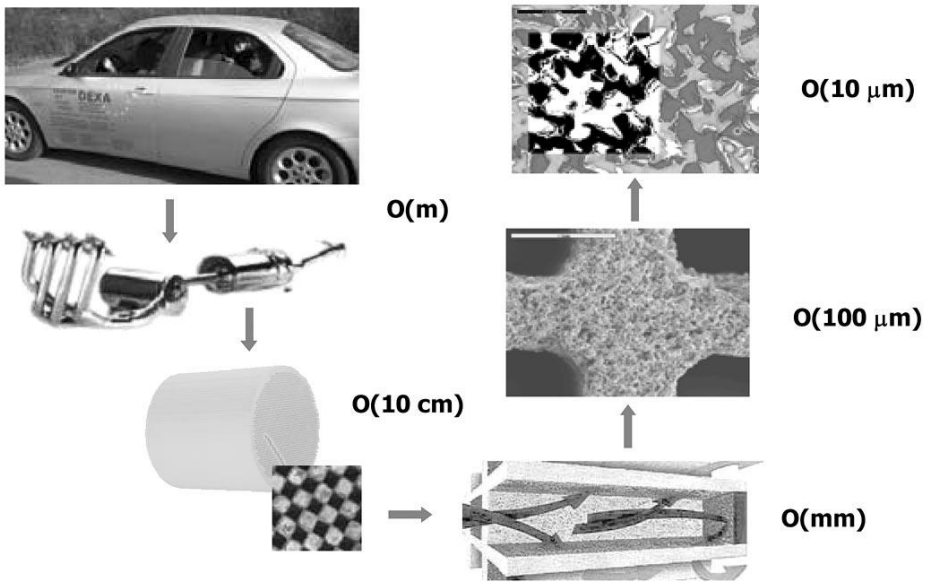

Figure 2.17: Les échelles spatiales induites par les FAP (Konstandopoulos, Kostoglou, and Vlachos 2006)

L'échelle du canal est de l'ordre du millimètre. Les modèles que l'on trouve à cette échelle dans la littérature sont principalement 1D ou 1D+1D. La deuxième échelle la plus courante est celle du mur poreux, de l'ordre de quelques centaines de micromètres. Ces simulations se font principalement en 2D ou 3D. Enfin, il est possible de modéliser le FAP dans son ensemble, échelle de quelques dizaines de centimètres. Cependant cette échelle est rarement utilisée dans la prédiction des performances en filtration ou en conversion catalytique des FAP, mais plutôt dans des études du champ de température ou de turbulence du champ d'écoulement en amont et en aval du monolithe (Bensaid, Marchisio, and Fino 2010; Cornejo, Nikrityuk, and Hayes 2020). De plus cette échelle ne permet pas d'étudier à elle seule l'impact des caractéristiques géométriques à des échelles plus faibles comme la distribution du dépôt de catalyseur dans l'espace poreux du FAP. L'échelle du FAP au complet ne sera donc pas développé dans cet état de l'art. Les différentes échelles de la simulation des FAP ont été revues notamment par (Konstandopoulos, Kostoglou, and Vlachos 2006; Yang et al. 2016).

2.3.1 Échelle du canal

La modélisation des FAP à l'échelle du canal en 1D a d'abord été introduite par (Bissett and Shadman 1985). Cette modélisation prend en compte deux canaux adjacents (numérotés 1 : entrée et 2 : sortie) séparés par un mur filtrant (substrat) sur lequel peut se former un gâteau de particules de suie comme illustré Figure 2.18. Cette géométrie est représentative de tous les canaux du FAP sous les hypothèses d'uniformité du flux de vitesse sur la section d'entrée du filtre et d'uniformité de la température et de la concentration des espèces radialement dans le filtre.

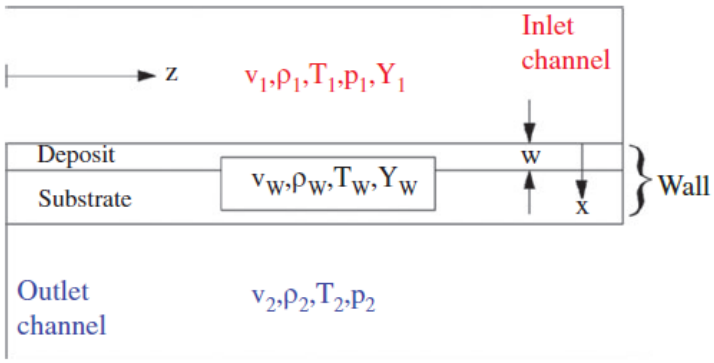

Figure 2.18 : Modèle de canal de Shadman et Bissett (1985) (Koltsakis et al. 2013)

Des équations bilans (quantité de mouvement, masse et énergie) sont ensuite établies pour déterminer les profils de vitesse, de concentrations des espèces chimiques et de température dans la direction perpendiculaire au mur poreux, ainsi que l'évolution de la taille du dépôt de particules. Par exemple, les équations bilans pour la quantité de mouvement s'écrivent (Koltsakis et al. 2013):

$$\frac{\partial p_1}{\partial z} + \frac{\partial(\rho_1 {u_1}^2)}{\partial z} = -F\frac{\mu u_1}{d^2} \tag{2.37.1}$$

$$\frac{\partial p_2}{\partial z} + \frac{\partial(\rho_2 {u_2}^2)}{\partial z} = -F\frac{\mu u_2}{d^2} \tag{2.37.2}$$

Où u_i représente la vitesse de l'écoulement, p_i la pression et ρ_i la masse volumique du fluide dans le canal i, d est une longueur caractéristique liée à la taille de la section du canal. Pour un écoulement laminaire dans un canal à section rectangulaire, une corrélation relie le coefficient F à la différence de pression locale qui peut être exprimée à partir de la loi de Darcy. Ces équations

peuvent ensuite être adimensionnalisées et résolues à l'aide d'un solveur algébrique différentiel ou par méthode des différences finies (MDF). Les évolutions du modèle de canal 1D de (Bissett and Shadman 1985) ont été revues par (Konstandopoulos et al. 2005; Konstandopoulos, Kostoglou, and Vlachos 2006; Koltsakis et al. 2013). Ce modèle 1D et ses évolutions sont largement utilisés dans la littérature pour calculer la perte de charge à travers le mur poreux séparant deux canaux (Masoudi 2005; Charbonnel and Opris 2009; Tandon et al. 2015; Xuereb and Farrugia 2016; Watling et al. 2017), calculer la dynamique d'accumulation des suies sur un cycle moteur (Wanker et al. 2004; Khan and Shamim 2008; Lupše, Campolo, and Soldati 2016) ou encore calculer la conversion des espèces chimiques comme les NO_X (Premchand 2013; Karamitros and Koltsakis 2017) dans des modèles très complets et prédictifs pour un type de FAP ou de FAPC caractérisé et à géométrie connue. Dans des cas bien déterminés, ces modèles offrent une représentation très précise des résultats expérimentaux, notamment pour la perte de charge comme le montre la comparaison de résultats expérimentaux et numériques à la Figure 2.19, tirés de la revue de (Koltsakis et al. 2013). Il est possible d'étendre le modèle de canal 1D en pseudo 2D ou 1D+1D dans des modèles compartimentaux permettant une meilleure description des caractéristiques géométriques du milieu poreux séparant deux canaux (Torregrosa et al. 2011; Wurzenberger et al. 2016; Gong et al. 2017; Gong et al. 2018). Cela se fait par un découpage de la géométrie dans les directions x et z (voir orientation des axes à la Figure 2.18). Enfin l'extension peut également se faire en pseudo 3D par la prise en compte des variations des grandeurs physiques de façon radiale dans le filtre complet et le long des canaux et par la multiplication des canaux représentés (Yang et al. 2016). Les modèles qui se basent sur une représentation à l'échelle du canal permettent donc une bonne prédiction des performances en filtration et en conversion des FAP. Ils présentent l'avantage d'être simples à implémenter, faciles à comprendre et à exploiter. De plus ils donnent des résultats quasi instantanés une fois le modèle établi, grâce à des temps de calcul faibles étant donné la simplicité de la géométrie. Cependant ce type de modèle est incapable de prédire l'impact de variations locales des caractéristiques géométriques des FAP ou FAPC sur leurs performances. Pour être précis, ils nécessitent la connaissance de caractéristiques microscopiques du milieu filtrant telles que la perméabilité ou la porosité du mur poreux. Or ces caractéristiques doivent être obtenues par la résolution d'équations bilans à plus petite échelle, prenant en compte la variation locale des caractéristiques du milieu filtrant, ou par l'expérience. Pour ces raisons, ces modèles ne

sont pas adaptés à l'étude de l'impact de la distribution de catalyseur sur les performances des FAPC. Ces modèles doivent être associés ou remplacés par des études à l'échelle microscopique.

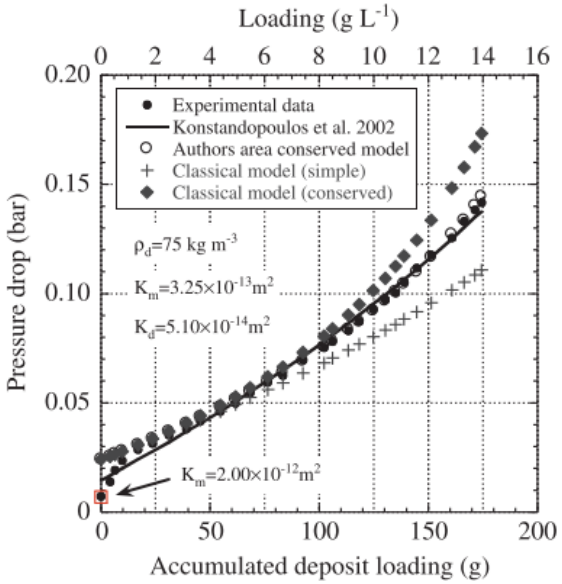

Figure 2.19: Modèle 1D amélioré par les auteurs pour la perte de charge en fonction de la masse de suie accumulée (cercles), comparé au modèle classique (croix) et à des résultats expérimentaux (disques) (Koltsakis et al. 2013)

2.3.2 Échelle du mur poreux

Pour mesurer l'impact des caractéristiques géométriques d'un dépôt de catalyseur sur les performances en filtration et en conversion catalytique du FAPC, il est indispensable de se placer à l'échelle du mur poreux séparant ses canaux. Les ordres de grandeur sont de quelques nanomètres pour la modélisation des particules de suie, de quelques dizaines de micromètres pour la taille des pores du mur filtrant, jusqu'à plusieurs centaines de micromètres pour l'épaisseur totale du milieu poreux. Les simulations dans ce paradigme nécessitent donc plus de ressources de calculs : domaines complexes multiéchelles (millions de cellules), grand nombre de particules à considérer dans le cas d'un modèle lagrangien (dizaines de milliers). Ces ressources sont rendues disponibles par l'amélioration continue de la puissance de calcul des unités centrales de traitement (central process unit : CPU) (Moore 1965) et de la mémoire vive (*random access memory* : RAM) (Kinoshita et al. 2017). De ce fait, dans les dernières décennies, de plus en plus de travaux se sont

intéressés à la modélisation des FAP à l'échelle microscopique. La méthodologie classique de calcul de performances des FAP pour ces modèles se décompose en 3 étapes selon les grandeurs physiques à calculer: (1) la reconstruction du milieu poreux, (2) le calcul du champ d'écoulement et (3) le calcul des trajectoires des particules et/ou du transport des espèces chimiques et/ou du profil de température à travers le milieu.

2.3.2.1 Reconstruction et caractérisation du milieu poreux

La modélisation des FAPC à l'échelle du mur poreux permet de nombreuses possibilités en termes de configuration, de géométrie et de conditions expérimentales. Cet éventail de possibilités est mis en valeur si la précision du milieu poreux numérisé est grande. Les premiers modèles microscopiques de FAP à avoir été développés ont employé des techniques de cellules unitaires (Konstandopoulos and Johnson 1989), qui représentent des collecteurs caractéristiques (sphères dans le cas des céramiques) sur lesquels se fait l'accumulation des suies. Ces modèles ont notamment été améliorés et utilisés dans les dernières années afin de mener des études de performances des FAP (Serrano et al. 2016). Quelques années après l'introduction de ce concept, des méthodes de reconstruction des milieux poreux de plus en plus poussées se basant sur des algorithmes avancés ont été développées pour une représentation plus précise des caractéristiques réelles du filtre. Ces techniques se basent sur des algorithmes de Monte Carlo, comme la technique de déplacement du point médian ou la technique du recuit simulé (Kikkinides and Burganos 2000; Brandstätter et al. 2005; Matte-Deschênes et al. 2016).

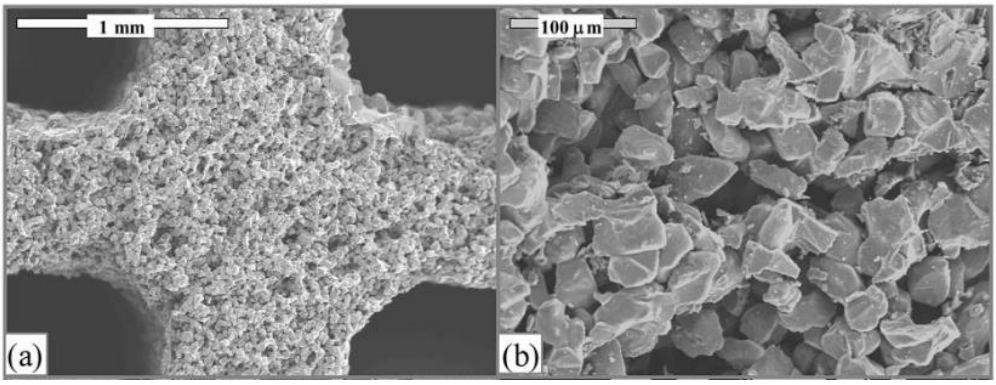

Figure 2.20 : Images MBE de FAP de SiC à différentes magnitudes (Konstandopoulos, Kostoglou, and Vlachos 2006)

Plus récemment encore, les techniques d'imagerie telle que le microscope à balayage électronique (MBE) (Konstandopoulos, Kostoglou, and Vlachos 2006) ou la tomographie (CT) (Stewart et al. 2004; Lindquist and Venkatarangan 1999) ont permis une représentation encore plus précise des milieux poreux composant les filtres, voir Figure 2.20. Une fois les images traitées et segmentées, afin de différencier les phases solides et fluides, les milieux reconstruits offrent une précision de l'ordre du micron à la centaine de nanomètres. Une fois acquises, les images doivent être traitées afin de réduire le potentiel bruit, et segmentées afin de distinguer les différentes phases qui la composent (Otsu 1979). Cependant ce type d'acquisition est coûteux et nécessite de vrais milieux poreux provenant de FAPC à disposition. Des techniques de reconstruction basées sur des algorithmes numériques apparaissent alors comme des méthodes de choix pour contourner les contraintes en coût et accessibilité des vrais milieux poreux. Ces méthodes se basent sur des caractéristiques des milieux réels obtenues dans la littérature, par analyse d'image ou par techniques expérimentales (Rouquerol et al. 2011). De plus, ces techniques peuvent être autosuffisantes ou se combiner à des méthodes d'imagerie de vrais milieux poreux afin d'augmenter la variabilité ou d'étudier plus de configurations géométriques. La problématique principale des milieux poreux est leur géométrie complexe. Cependant, plusieurs grandeurs ou corrélations géométriques permettent de les caractériser. Enfin, dans le cas des céramiques utilisées pour former les FAP, les domaines étant relativement homogènes et isotropes il est possible de trouver un volume élémentaire représentatif (*representative elementary volume* : REV). La caractérisation du REV permet la caractérisation du milieu au complet.

Les méthodes stochastiques permettant de reconstruire un REV du FAPC se basent sur la reconstruction de milieux poreux numériques visant à atteindre des caractéristiques représentées par des fonctions géométriques cibles. Dans un premier temps, l'utilisation d'un champ gaussien corrélé et normalisé permet de reconstruire des milieux 3D en se basant sur des fonctions morphologiques du milieu réel telles que l'autocorrélation de masse (Levitz 1998). Cependant cette méthode est peu adaptée aux milieux poreux complexes. D'autres méthodes plus efficaces sont utilisées dans ce domaine. La méthode de recuit simulé est directement définie par son nom : elle simule un processus de recuit de métal évoluant vers un minimum d'énergie. Elle utilise en fait une pseudo-énergie construite sur des fonctions géométriques caractéristiques du milieu à reconstruire.

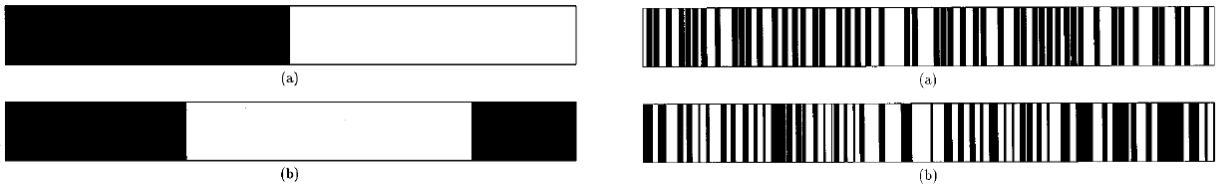

Figure 2.21 : (a) structures de référence, (b) structure reconstruite. Systèmes de 1000 pixels et fraction volumique de 0.5 (Yeong and Torquato 1998a)

En théorie, la méthode de recuit simulé peut prendre en compte une infinité de fonctions géométriques pour construire sa fonction de pseudo-énergie. En pratique, les deux fonctions les plus utilisées sont le *two-point-probability function* et le *lineal-path* (Haile, Massobrio, and Torquato 1985). (Yeong and Torquato 1998b, 1998a) ont par exemple développé des algorithmes de reconstruction de milieux 1D ou 2D possédant les mêmes caractéristiques géométriques (fonctions de corrélation) que les structures de référence, comme illustré à la Figure 2.21. De la même façon, (Matte-Deschênes et al. 2016) ont utilisé le recuit simulé pour reconstruire des milieux de cordiérite représentant la céramique de FAP pour moteurs diesels. Les résultats mènent à une grande précision dans les structures reconstruites. Ces techniques peuvent être également adaptées à des milieux non homogènes (Quintanilla and Torquato 1997; Patelli and Schuëller 2009). Le principal désavantage de ces méthodes est qu'elles nécessitent de grandes ressources CPU et un temps de calcul qui augmente exponentiellement en fonction de la taille des structures. Cependant différentes techniques sont proposées dans la littérature pour paralléliser le recuit simulé afin d'augmenter son efficacité de calcul et pouvoir travailler sur des structures de tailles plus importantes (Chen et al. 2007; Gonçalves-e-Silva, Aloise, and Xavier-de-Souza 2018; Wang, Zhao, et al. 2018).

Dans le domaine de l'apprentissage profond, (Mosser, Dubrule, and Blunt 2017) ont utilisé une approche de réseaux de neurones (*neural network* : NN) convolutifs pour reconstruire des milieux poreux 3D. Cette méthode fait appel à deux NN différents : un générateur, dont le rôle est de créer des structures aux caractéristiques géométriques proches de la structure de référence, et un discriminateur, dont le rôle est de différentier les structures réelles ou reconstruites. En proposant différentes structures, originales ou reconstruites, le générateur essaye de tromper le discriminateur. Ainsi par ce processus, le générateur améliore son algorithme de reconstruction.

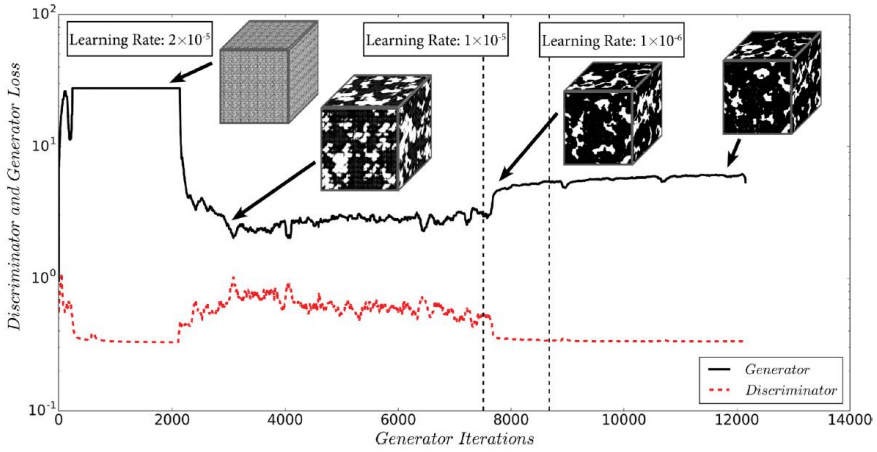

Figure 2.22 : Schéma de reconstruction par une méthode de réseaux de neurones (Mosser, Dubrule, and Blunt 2017)

Ce processus est illustré à la Figure 2.22. Un autre travail mené par (Wang, Arns, et al. 2018) présente une méthode de reconstruction de milieux poreux en 3D à l'aide d'images CT dont la résolution a été amélioré par NN se basant sur des sections d'images MBE. Cette technique permet d'allier la reconstruction 3D continue des images CT avec la résolution plus raffinée des images MBE. Mais ce processus se fait section par section. L'étape limitante est l'alignement des sections MBE avec les sections correspondantes de l'image CT. Les méthodes neuronales présentent l'avantage de minimiser grandement le temps de calcul par rapport aux méthodes stochastiques classiques, une fois que le NN est entrainé. La principale limitation de ces méthodes réside dans la dépendance aux données : qualité, quantité, représentativité.

2.3.2.2 Calculs du champ d'écoulement dans le milieu poreux

Une fois le milieu reconstruit, il est possible de calculer le champ d'écoulement à travers celui-ci par des méthodes de mécanique des fluides numériques (MFN). Les méthodes les plus adaptées pour ce type de simulation en milieu poreux sont la méthode des volumes finis (MVF), la méthode des éléments finis (MEF), la méthode des différences finies (MDF) ou la méthode de Boltzmann sur réseau (MBR). La grande majorité des méthodes de MFN procèdent au calcul du champ d'écoulement dans une géométrie par résolution d'un schéma numérique d'approximation des équations de Navier-Stokes (NS). Pour un fluide newtonien, isotherme et incompressible, qui sont les hypothèses classiques faites en milieu poreux microscopique, les équations de NS s'écrivent :

$$\frac{\partial \boldsymbol{u}}{\partial t} + \boldsymbol{u}.\boldsymbol{\nabla}\boldsymbol{u} = -\frac{1}{\rho}\boldsymbol{\nabla}p + \frac{\mu}{\rho}\boldsymbol{\nabla}^2\boldsymbol{u} + \boldsymbol{F}$$
$$\boldsymbol{\nabla}.\mathbf{u} = \mathbf{0} \tag{2.38}$$

Dans le cas de la MDF, les opérateurs de dérivées partielles sont discrétisés à l'aide d'approximations faisant appel aux développements de la fonction $\boldsymbol{u}(\boldsymbol{x}, t)$ en séries de Taylor. À partir d'une équation aux dérivées partielles, on obtient alors un système matriciel à résoudre ou un système d'équations de récurrence évoluant dans le temps.

La MVF approxime les équations de NS par des bilans mésoscopiques sur chacun des éléments de discrétisation de la géométrie. Cette méthode fait appel au théorème de Green-Ostrogradski.

La MEF utilise le concept de formulation faible des équations de NS, à l'aide de fonctions d'interpolation et par intégration de la forme forte présentée dans l'Eq. (2.38).

Ces trois différentes MFN sont particulièrement matures et décrites dans plusieurs ouvrages de la littérature (Blazek 2005; Larson and Bengzon 2013; Ferziger and Peric 2002). La MDF possède l'avantage de la simplicité d'implémentation et de parallélisation, mais fait appel à un maillage cartésien de la géométrie qui peut induire un effet de crénelage du champ de vitesse calculé. La MEF et la MVF nécessitent quant à elle un maillage non cartésien de la géométrie. Dans le contexte de milieux poreux à géométrie très complexe, cette étape peut devenir limitante. Elle pourrait induire de plus grand temps de calcul, un prétraitement lourd et des capacités de parallélisation amoindries par rapport à une méthode « sans maillage ».

La MBR est la méthode la plus largement utilisée dans le contexte des FAP dans la littérature, car très bien adaptée aux milieux poreux, aucun maillage du domaine n'étant nécessaire, et à des possibilités de parallélisation très importantes (Vidal, Roy, and Bertrand 2010a, 2010b; Krüger et al. 2017). La particularité de cette méthode est qu'elle ne résout pas directement les équations de NS, mais l'équation de Boltzmann qui s'écrit :

$$\frac{\partial f}{\partial t} + \mathbf{u} \cdot \boldsymbol{\nabla}_{\boldsymbol{x}} f + \frac{\boldsymbol{F}}{\rho} \cdot \boldsymbol{\nabla}_{\boldsymbol{\xi}} f = \Omega(f) \tag{2.39}$$

Plusieurs études utilisent la MBR pour simuler l'accumulation des particules de suie sur des entassements de sphères, combinant la microfluidique numérique au modèle du collecteur unitaire (Hayashi and Kubo 2008; Lee et al. 2018). Une étude de (Stewart et al. 2010), propose une comparaison de l'accumulation de suie sur plusieurs types de substrats, sous différentes conditions d'écoulement, en utilisant la MBR. Également en utilisant la MBR, (Kong and Yamamoto 2018) ont étudié l'impact sur les performances de filtration des FAPC pour moteur diesel, de plusieurs dépositions de catalyseurs, dans le mur ou à la surface du mur, en comparaison avec un FAP non catalytique. Les résultats tendent à démontrer qu'une déposition à l'intérieur de l'espace poreux induit une perte de charge plus importante et une efficacité de capture moindre que dans le cas d'une déposition à la surface du mur. Cependant les deux dépositions ne sont pas caractérisées géométriquement dans cette étude. On peut enfin trouver dans la revue de (Konstandopoulos, Kostoglou, and Vlachos 2006), une analyse comparative de la perméabilité, calculée supposément par la MBR, de FAPC présentant deux profils de dépositions, un profil uniforme et un profil non uniforme, illustré Figure 2.23. Les résultats démontrent une perméabilité décroissante des FAPC pour une fraction croissante de volume poreux remplie de catalyseur. Encore une fois, les dépôts ne sont pas caractérisés et la technique de déposition artificielle n'est pas expliquée.

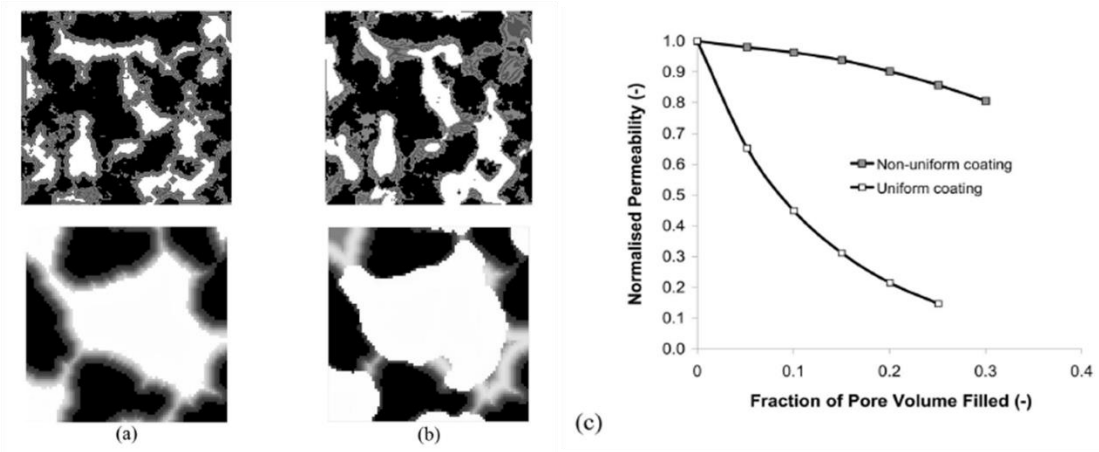

Figure 2.23 : Influence de l'uniformité du dépôt de catalyseur sur la perméabilité du mur poreux d'un FAP (Konstandopoulos, Kostoglou, and Vlachos 2006)

Bien que la majorité des travaux sur la modélisation des FAP à l'échelle microscopique se fassent à partir de la MBR pour le calcul du champ d'écoulement, d'autres méthodes de MFN sont parfois utilisées, notamment la MVF à partir du logiciel libre OpenFOAM par exemple (Allouche et al.

2017; Kočí et al. 2019). Cette méthode présente l'avantage d'être plus mature et propose des logiciels plus avancés que la MBR.

2.3.2.3 Calculs de performance dans le milieu poreux

Une fois le milieu poreux reconstruit et l'écoulement fluide calculé par une méthode de MFN, d'autres phénomènes physiques peuvent y être simulés, comme la filtration des suies, le traitement des espèces chimiques gazeuses ou l'évolution du profil de température.

Pour prédire l'efficacité de capture des particules de suie, deux principales classes de méthodes peuvent être utilisées. La première classe de méthodes consiste à résoudre l'advection-diffusion des suies à travers le champ d'écoulement, de façon eulérienne. Cette technique est entreprise notamment par (Tsushima et al. 2010; Yamamoto and Ohori 2012) qui résolvent par la MBR le champ d'écoulement et le transport des particules de suie dans des milieux poreux de FAP pour moteur diesel. La déposition des particules se fait alors à l'aide d'un modèle probabiliste considérant les trois principaux mécanismes de capture évoqués à la section 2.2.1.3. Le principal inconvénient de cette méthode vient de la paramétrisation du procédé de déposition qui laisse place à un large éventail de possibilité et donc de résultats.

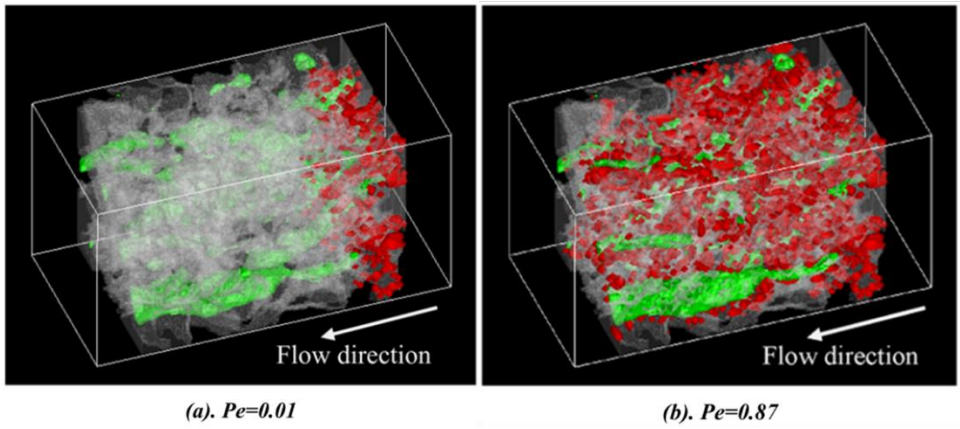

Figure 2.24: Trajectoires des particules de suie dans le mur de cordiérite d'un FAP pour moteur diesel, simulé par MBR (Tsushima et al. 2010).

La deuxième classe de méthodes, plus repandue dans la littérature, consiste à calculer les trajectoires des particules de suie dans le champ d'écoulement à l'aide d'un bilan de forces, de façon lagrangienne (Vadeiko and Drolet 2009; Becker et al. 2016; Wiegmann, Rief, and Latz

2006). Ainsi la seconde loi de Newton est résolue pour chaque particule en considérant un terme stochastique qui représente la diffusion brownienne. Ce terme est calculé en utilisant le coefficient de diffusion D et un processus de Wiener 3D $\boldsymbol{w}$. L'ajout de ce terme mène à l'équation de Langevin qui suit:

$$\frac{d\boldsymbol{v}(t)}{dt} = \frac{3\pi\mu d_p}{mC_c}\left(\boldsymbol{u}(\boldsymbol{x}) - \boldsymbol{v}(t) + \sqrt{2D}\frac{d\boldsymbol{w}(t)}{dt}\right)$$
$$\frac{d\boldsymbol{r}(t)}{dt} = \boldsymbol{v}(t) \tag{2.40}$$

où $\boldsymbol{r}$ et $\boldsymbol{v}$ sont, respectivement, la position et la vitesse de la particule, $\boldsymbol{u}$ est la vitesse du fluide obtenue préalablement par une méthode de MFN, μ est la viscosité dynamique du fluide, d_p est le diamètre équivalent de la particule et m est sa masse, et C_c est le facteur de correction de Cunningham, voir Eq. (2.16).

Trois principaux modèles de collision peuvent alors être envisagés. Le premier et le plus répandu (*caught on first touch*) considère une particule capturée lorsque sa distance entre son centre et le collecteur est inférieure à son rayon équivalent. Dans le modèle de Hamaker, la vitesse de la particule est considérée lorsqu'elle touche le collecteur. Pour être considérée comme capturée, la vitesse de la particule doit respecter la condition suivante (Krupp 1967):

$$\boldsymbol{v}^2 < \frac{H}{\pi\rho_p a_0 d_p^2} \tag{2.41}$$

où H représente l'adhésion (constante de Hamaker), a_0 est la distance d'adhésion. Enfin dans le modèle de Sieving, les particules sont capturées si et seulement si elles ne se mouvent plus dans le filtre.

Dans le contexte des moteurs EID, les hautes températures et la faible concentration des particules rendent l'accumulation des suies négligeable et l'on peut considérer le FAPC comme propre tout au long du cycle moteur.

Outre la simulation de la capture des suies, l'un des principaux phénomènes à simuler dans le cadre des FAPC est la conversion des espèces chimiques. Ce phénomène est la fonction principale du

catalyseur introduit dans le mur poreux du FAPC. La méthodologie utilisée dans les travaux qui visent à simuler ce processus à l'échelle microscopique en 3D consiste à la résolution de l'équation d'advection-diffusion-réaction (ADR) pour calculer le champ de concentration des espèces chimiques dans l'espace poreux et à travers le catalyseur de façon analytique ou numérique (Yamamoto et al. 2010). Un bilan de matière mésoscopique sur un élément de volume permet de traduire ce problème par l'équation d'ADR suivante :

$$\frac{\partial c}{\partial t} + \boldsymbol{u} \cdot \boldsymbol{\nabla} c = D \boldsymbol{\nabla}^2 c + r \tag{2.42}$$

où c est la concentration de l'espèce chimique considérée, $\boldsymbol{u}$ est le champ de vitesse, D est le coefficient de diffusion de l'espèce considérée dans le milieu considéré et r est un taux de réaction. Dû à la complexité du problème : géométrie non triviale, nombreuses espèces chimiques et réactions à considérer. Pour pallier ce problème, des modèles de réaction simplifiés ont d'abord été introduits dans la littérature (Konstandopoulos et al. 2012). Ils remplacent la résolution de l'ADR par celle d'une forme fermée de solution. Cependant ces modèles sont incapables de prendre en compte les caractéristiques géométriques locales des céramiques du FAPC et doivent être ajutés par l'expérience ou par des modèles plus précis.

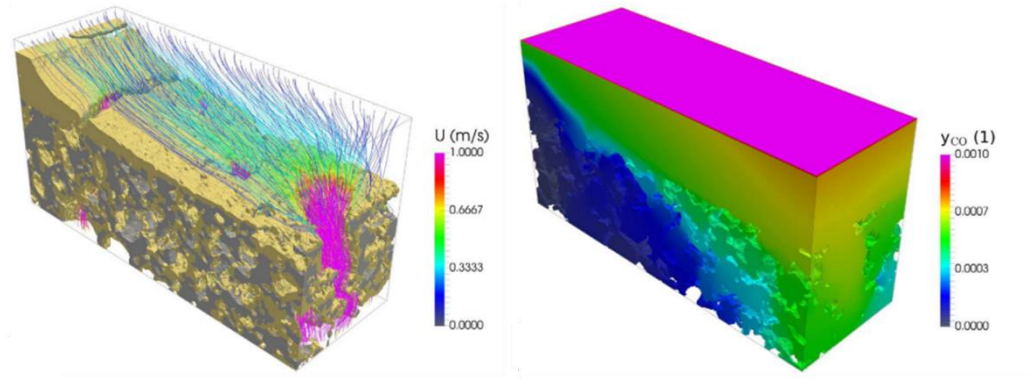

Figure 2.25 : Simulations 3D par MVF pour le calcul du champ d'écoulement (à gauche) et du champ de concentration (à droite) dans le mur poreux d'un FAPC (Kočí et al. 2019)

Parmi les rares travaux à avoir entrepris la résolution de l'ADR au niveau microscopique en 3D, (Kočí et al. 2019) ont comparé les performances en perte de charge et en conversion catalytique du

CO de FAPC présentant trois types de dépositions. Une déposition à l'intérieur du mur poreux et deux combinaisons de dépositions à la surface et à l'intérieur du mur poreux. Les équations de Navier-Stokes a été résolues à l'aide du solver OpenFOAM, puis un solver maison a permis de résoudre l'ADR. Les résultats donnent l'avantage en perte de charge à une déposition à l'intérieur du mur, alors que la conversion est largement améliorée par une déposition en surface de l'espace poreux. Des visualisations de ces simulations sont présentées en Figure 2.25. Dans cette étude, une seule espèce chimique est considérée ainsi qu'une seule réaction. De plus les distributions des dépositions de catalyseur à l'intérieur du milieu poreux ne sont encore une fois pas caractérisées. Or dans le cas d'un dépôt en surface comme à l'intérieur du milieu poreux, l'effet de canalisation est souligné. L'écoulement tend à se produire principalement à travers de gros passages poreux dans la céramique aux dépens des plus petits espaces. Cela est particulièrement visible en Figure 2.25 (image de gauche). Or cet effet de canalisation est largement dépendant de la géométrie du milieu poreux du FAPC. Cela met en évidence, une fois de plus, la nécessité de la caractérisation géométrique des milieux poreux dans la compréhension de l'évolution des performances des FAPC.

Cependant ces modèles, une fois développés, ne doivent pas être considérés comme une fin. Le rôle d'un modèle est de fournir des prédictions. Or dans le monde industriel, ces prédictions doivent être les plus précises possible en nécessitant le moins de ressources possible. Ainsi l'un des débouchés des simulations en 3D à l'échelle microscopique est la réduction de modèle. Dans le travail de (Greiner et al. 2019), un modèle 1D d'ADR à travers le mur de céramique d'un FAPC est développé. Ce modèle, basé sur des équations bilans, de façon similaire aux modèles à l'échelle du canal complet, se différencie de la littérature par la prise en compte d'un facteur limitant dans l'advection des espèces chimiques. Cela s'explique par les caractéristiques géométriques de la structure poreuse : l'écoulement à lieu dans des canaux préférentiels alors qu'une fraction du volume de l'espace poreux ne contribue quasiment pas à celui-ci. Or ce facteur est calculé à partir de résultats de simulation en 3D à l'échelle du microscopique. Cet exemple illustre ce vers quoi les modèles 3D doivent tendre.

2.3.3 Résumé des différentes échelles de modélisation des FAP

La modélisation numérique semble être un outil de choix pour l'étude des FAPC : réduction des coûts et de la quantité de matériel et d'instruments, multiples possibilités de combinaison géométriques, analyse poussée des phénomènes physiques. Cependant, la problématique de la modélisation des FAPC tient dans leur caractère multiéchelle. Aucun modèle n'étant parfait, il est important de choisir celui le plus adapté au type de physique à représenter et au niveau de détails des résultats souhaités.

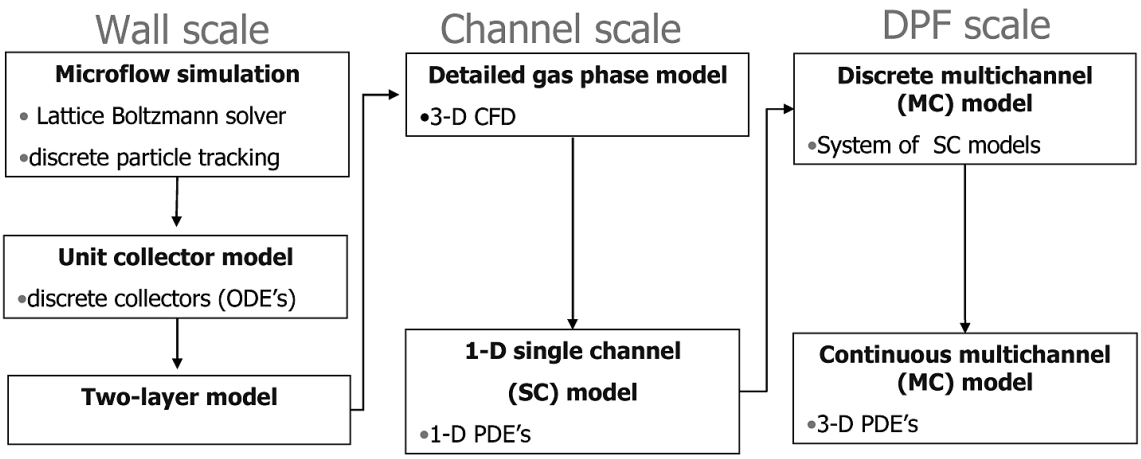

Figure 2.26 : Lien entre les différents modèles de FAP aux trois échelles les plus courantes dans la littérature (Konstandopoulos, Kostoglou, and Vlachos 2006)

L'échelle du canal est souvent utilisée pour obtenir des corrélations simples pouvant lier deux grandeurs physiques caractérisées : l'épaisseur du gâteau de suie en fonction de la vitesse d'écoulement par exemple dans le cas des FAP pour moteurs diesels. Dans le contexte des FAPC, l'impact du dépôt de catalyseur se fait à l'échelle microscopique. Un modèle qui rend compte de la géométrie de l'espace poreux et des phénomènes physiques s'y déroulant est alors indispensable. La modélisation à l'échelle microscopique nécessite une méthodologie en trois étapes auxquelles peuvent s'ajouter des sous-étapes ou des boucles de couplage. Pour la première étape, la reconstruction du milieu poreux, de nombreuses possibilités s'offrent aux chercheurs grâce aux nouvelles techniques d'imagerie de plus en plus précises, mais aussi aux puissances de calcul permettant de développer des algorithmes de reconstruction de plus en plus performants. Ces différentes techniques seront revues dans la suite de cet état de l'art. Pour la deuxième étape, le

calcul du champ d'écoulement d'air à travers le milieu filtrant, la MBR est la méthode numérique la plus répandue dans la littérature et semble la plus adaptée pour résoudre les équations bilans en milieu poreux à l'échelle microscopique. De plus, d'autres études en dehors du domaine des FAP ont montré qu'il est possible de résoudre l'équation d'advection-diffusion-réaction avec la MBR (Xu et al. 2018). Un logiciel pouvant résoudre le champ d'écoulement et le champ de concentration des espèces chimiques à travers le filtre en utilisant la même méthode numérique semble particulièrement prometteur. Les principes qui font de la MBR une méthode de choix pour résoudre ces deux phénomènes et en tirer de l'information intéressante pour l'optimisation des FAPC seront également revus dans la suite de cet état de l'art. Enfin un développement des principes de la théorie de la filtration permettra de mieux comprendre les enjeux de la capture des aérosols afin de choisir la méthode la mieux adaptée à sa modélisation. Ce dernier développement permettra de finir le recouvrement des différentes étapes de la modélisation des FAPC à l'échelle microscopique. Ceci dans le but d'entrevoir une réponse à la problématique exposée plus haut : bâtir une méthode de prédiction des performances des FAPC capable de mesurer l'impact de la distribution de catalyseur.

2.4 Conclusions de l'état de l'art et enjeux du domaine des FAPC

L'état de l'art proposé plus haut a permis de mettre en évidence la complexité du domaine des FAPC. De nombreux constituants physico-chimiques à plusieurs échelles interviennent et il est alors très compliqué de bâtir des études d'évaluation systématique des performances de ces systèmes. Si plusieurs études montrent que la déposition de catalyseur à un impact important sur les performances du FAPC, aucune ne s'attache à montrer l'importance de la distribution du catalyseur dans l'espace poreux sur ces mêmes performances. De plus, les techniques de déposition actuelles semblent mener à des résultats de déposition non uniforme et donc potentiellement non optimale. Une amélioration de l'uniformité du dépôt pourrait mener à une grande amélioration de la performance des FAPC. Pour s'en assurer, des méthodes d'évaluation et de prédiction des performances des FAPC sont nécessaires. Expérimentalement, des valeurs caractéristiques de performances des FAPC peuvent être déterminées et servir de guides aux modèles. Cependant des études de caractérisation complètes des performances des FAPC de cette façon sont trop complexes, trop couteuses et trop chronophages. Numériquement, les travaux proposés pour la modélisation des FAPC offrent de bonnes performances de prédictibilité, mais sont souvent trop

restreints, ne s'intéressant pas à un grand nombre d'échantillons et n'englobent pas toutes les contraintes et tous les objectifs de performances de ces systèmes de traitement des gaz d'échappement. De plus, ces études doivent être multiéchelle. L'échelle du mur poreux semble toutefois la plus déterminante. Cependant, à ce jour, la littérature est vacante d'études comparatives et caractérisées de différentes géométries des FAPC où l'évaluation globale des performances en filtration et en catalyse sont entreprises à l'échelle microscopique. Or les techniques pouvant permettre de réaliser ces études sont en pleine croissance et restent à être exploitées à travers des méthodologies à 3 étapes permettant la prédiction des performances globales des FAPC. Pour la première étape, la reconstruction d'un VER du mur poreux d'un FAPC, plusieurs possibilités sont envisageables : formation de géométries simples comme des entassements de sphères, reconstructions à l'aide de méthodes stochastiques, techniques d'imageries MBE ou CT. Pour la deuxième étape, le calcul du champ d'écoulement à travers le VER de mur poreux, la MBR est largement plus utilisée et semble la méthode de choix pour contourner la complexité des milieux poreux représentés. Enfin pour la troisième étape, la modélisation des phénomènes physiques comme la capture des suies et le traitement des espèces chimiques, deux types de méthodes sont utilisées. Les méthodes eulériennes de calculs de profils de concentrations sont utilisées efficacement pour obtenir des tendances. Dans le contexte des FAP, la MBR a été utilisée pour calculer l'accumulation des suies, mais n'a jamais été encore adaptée au calcul du champ de concentration des espèces chimiques tels que les NO_X. Enfin, les méthodes lagrangiennes de suivit de trajectoires sont utilisées dans le cas des filtres fibreux, mais leur application aux FAPC pour moteurs EID à des échelles microscopiques et des concentrations faibles en particules semble prometteuse et doit permettre une grande précision dans le calcul des performances. Ces différentes méthodes numériques restent donc à exploiter pour bâtir un modèle de prédiction complet des performances des FAPC à l'échelle microscopique. À la lumière de ces informations, l'objectif de cette thèse ainsi que la méthodologie employée pour l'atteindre seront présentés dans les prochains chapitres.

CHAPITRE 3 OBJECTIFS DE LA THÈSE

La revue de la littérature, développée dans le Chapitre 2, nous a permis de prendre la mesure de la difficulté de prédire les performances des FAPC. La modélisation numérique semble l'outil le mieux adapté pour évaluer l'impact d'un dépôt de catalyseur sur les performances globales du FAPC. Mais elle doit se faire à l'échelle microscopique du mur poreux séparant deux canaux. Plusieurs études ont ainsi évalué l'impact d'un dépôt de catalyseur, par exemple entre un dépôt à l'intérieur et en surface du mur. Mais aucune étude ne s'est intéressée à l'impact de la distribution locale de catalyseur. À la lumière de ces éléments, l'objectif de cette thèse sera formulé dans cette section afin de répondre à la problématique exposée en Section 1.2.

3.1 Cadre industriel du projet

Dans un contexte industriel automobile de développement de systèmes de traitement des gaz d'échappement les plus performants possibles, la compagnie Umicore AG (Hanau, Allemagne), représentée par le professeur Martin Votsmeier, l'Université d'Alberta (Edmonton (AB), Canada), représentée par le professeur Robert E. Hayes et Polytechnique Montréal (Montréal (QC), Canada), représenté par le professeur François Bertrand, se sont associés pour la réalisation d'un projet industriel commun dont le but est le développement de FAPC à technologie avancée. Pour cela, une étude expérimentale et numérique multi-échelle doit être réalisée afin de mener à l'amélioration de la déposition de catalyseur dans les FAP pour moteur EID afin d'augmenter leurs performances globales. Cela doit passer par une meilleure compréhension des phénomènes physiques ayant lieu dans ces systèmes, à différentes échelles et pour plusieurs critères de performance. Le diagramme organisationnel du projet est illustré Figure 3.1. L'entreprise Umicore, qui développe une technologie de dépôt de catalyseur pour les FAPC est dans la mesure de fournir des images de FAPC par des technologies MBE et CT. En plus de fournir ces données, Umicore travaille depuis plusieurs années sur des modèles 1D et 2D de prédiction des performances des FAPC. Ces modèles simplifiés permettent des calculs rapides de valeurs de références en utilisant des paramètres qui doivent être ajustés à partir de simulations à l'échelle microscopique. L'université d'Alberta, qui possède des bancs d'essai pour les mesures de performances de FAP est dans la mesure de réaliser des expériences de validation en perte de charge et en efficacité de

capture, en plus de développer un modèle de MFN à l'échelle macroscopique d'un canal de FAP. Enfin Polytechnique Montréal, au sein de l'unité de recherche en procédés d'écoulements industriels (URPEI, http://www.urpei.polymtl.ca/fr/), qui possède des outils et des connaissances numériques avancés applicables aux milieux poreux, est dans la mesure de développer un modèle numérique complet de prédiction des performances des FAPC à l'échelle microscopique. Ainsi l'objectif de cette thèse, énoncé dans la section qui suit, est défini dans le cadre industriel et académique précédemment décrit, mais se suffit à lui-même dans la définition d'un projet doctoral et se doit de pouvoir répondre à la problématique énoncée à la section 1.2.

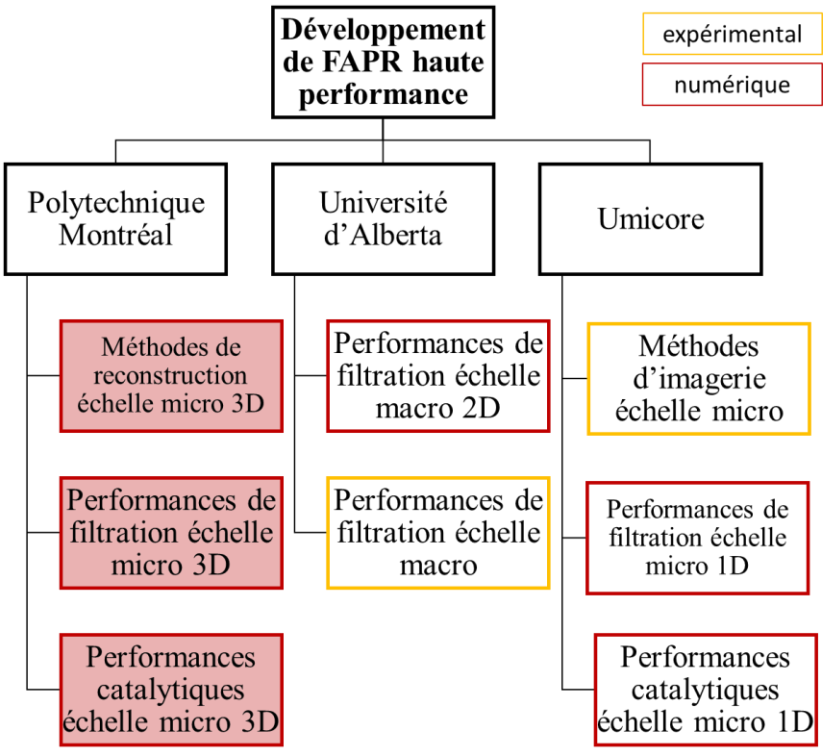

Figure 3.1: Organigramme du projet global de développement de FAPC haute performance. Les cadres pleins en rouge sont les parties inhérentes au projet doctoral présenté dans ce document.

3.2 Objectif général

L'état de l'art précédent a permis de mettre en évidence le fait qu'un dépôt catalytique peut avoir un impact important sur les performances des FAPC à l'échelle microscopique définies par : (1) la

perte de charge (ΔP), (2) l'efficacité de capture (E_f) et (3) la conversion catalytique (X). Mais aucun travail ne s'est encore intéressé de façon globale à l'impact de la distribution du dépôt de catalyseur. Pour répondre à la problématique énoncée à la Section 1.2, l'objectif général de ce travail est d'évaluer numériquement l'impact de la distribution de catalyseur sur les performances globales des FAPC pour moteurs EID à l'échelle microscopique.

3.3 Objectifs spécifiques

Pour atteindre l'objectif général de ce travail, et en se basant sur l'état de l'art réalisé précédemment, les objectifs spécifiques suivants devront être atteints :

1) Développer des techniques numériques permettant la reconstruction d'un volume élémentaire représentatif (VER) d'une paroi poreuse composant les canaux d'un FAPC.
2) Créer artificiellement deux profils de distribution de catalyseur dans le VER précédemment reconstruit, un uniforme et un non uniforme, à différentes quantités de catalyseur.
3) À l'aide d'outils numériques précédemment mis au point (Vidal, Roy, and Bertrand 2010a, 2010b; Vadeiko and Drolet 2009) et des structures de parois poreuses reconstruites en 1), réaliser une étude systématique de l'impact de la quantité et de l'uniformité du dépôt de catalyseur sur la performance en filtration des FAPC.
4) Développer un modèle de prédiction de la performance en conversion catalytique des FAPC et ainsi compléter l'étude comparative réalisée en 3) afin d'évaluer de façon globale la performance des FAPC à l'échelle microscopique.
5) Valider les modèles de prédiction des performances en filtration et catalytique des FAPC développés respectivement dans les sous-objectifs 3) et 4).

3.4 Organisation de la thèse

L'objectif général énoncé à la Section 3.2 devra être atteint à travers le développement cette thèse. Pour cela, la méthodologie générale employée sera présentée dans le Chapitre 4.

Dans le chapitre 5 (Article 1), l'assemblage d'un modèle numérique 3 étapes de prédiction de la performance en filtration d'un FAPC à l'échelle microscopique est présenté. Ce modèle est

appliqué à une étude comparative entre deux profils de déposition uniforme et non-uniforme au sein du mur poreux constituant les canaux du filtre. Ce chapitre vise donc à atteindre les objectifs spécifiques 1 et 2.

Dans le chapitre 6 (Article 2), le développement d'un modèle 3 étapes de prédiction de la performance en conversion d'un FAPC à l'échelle microscopique est présenté. Ce chapitre vise donc à atteindre l'objectif spécifique 3.

Dans le chapitre 7 (Article 3), la validation du modèle 3 étapes de prédiction de la performance en filtration des FAPC est présenté. Ce chapitre vise donc à atteindre l'objectif spécifique 4.

Tout au long des Chapitres 5-7, des cas de vérification et validation sont présentés. Dans les Annexes A-C, des cas de vérification supplémentaires sont présentés pour les différentes étapes du modèle numérique. Toutes les parties de cette thèse ayant aspect à la vérification et la validation de la méthodologie numérique utilisée, sont résumées dans la Section 4.3.

CHAPITRE 4 MÉTHODOLOGIE

Dans ce chapitre, la méthodologie employée pour mener à bien l'objectif général de cette thèse sera brièvement présenté. Le modèle 4-étapes assemblé pour prédire la performance globale des FAPC à l'échelle microscopique sera décrit de façon générale, tout comme la stratégie de vérification et de validation (V&V) employée. La contribution de l'auteur à chaque partie de ce modèle sera illustrée par un graphique. Par ailleurs, la méthodologie plus spécifique à chaque chapitre (correspondant à chaque article) est présentée dans le chapitre même et n'est donc pas abordée ici afin d'éviter toute redondance.

4.1 Modèle en quatre étapes

Pour atteindre l'objectif général de prédiction de l'impact de la distribution de catalyseur sur les performances globales des FAPC, un modèle numérique à l'échelle microscopique 4-étapes a été assemblé. Ce modèle est illustré en Figure 4.1.

Il consiste en : (1) la reconstruction d'un volume élémentaire représentatif (REV) du milieu poreux constituant les canaux d'un FAPC, (2) le calcul du champ d'écoulement d'air à travers ce REV, (3) le calcul des trajectoires des particules de suie dans le champ d'écoulement précédemment calculé à travers la structure et (4) le calcul du champ de concentration d'une espèce hypothétique, à travers le REV reconstruit. L'étape (1) se décompose en deux sous-étapes. Premièrement, des images tomographiques, acquises à l'aide d'un *Phoenix Nanotom M* de General Electric, d'un REV de mur de cordiérite séparant deux canaux du FAPC sont rassemblés en une image 3D. Cette image contient de l'information sous forme de voxels (pixels en 3 dimensions) en niveau de gris, et est donc segmentée pour différencier les trois phases du milieu : cordiérite, catalyseur et espace poreux. Deuxièmement, le dépôt de catalyseur original, issu de l'image tomographique, est modifié afin de créer plusieurs profils de distributions. Ainsi une série de 9 structures présentant une distribution non uniforme de catalyseur et 4 structures présentant une distribution uniforme de catalyseur sont créées. À ces 13 structures est ajoutée une structure sans catalyseur. La procédure permettant de mener à ces 14 structures est décrite en détail dans l'Article 1 (Chapitre 5).

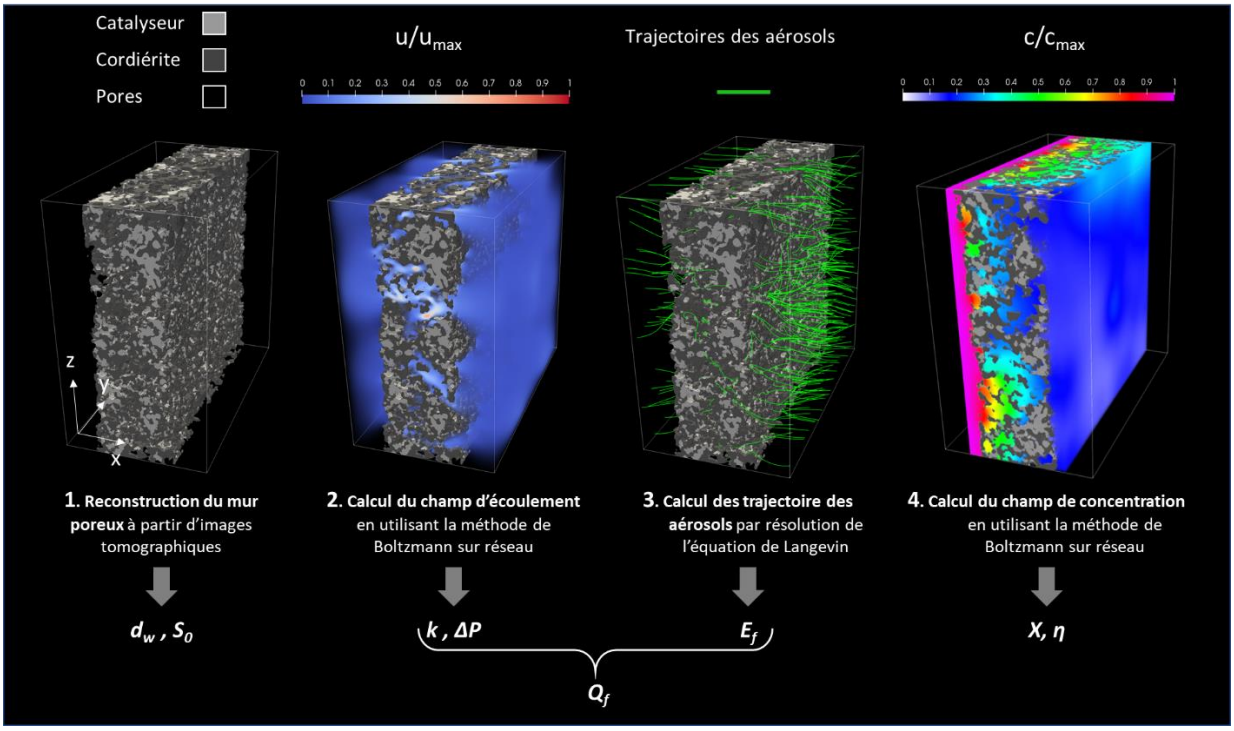

Figure 4.1 : Illustration du modèle 4-étapes de prédiction des performances globales des FAPC à l'échelle microscopique.

La contribution de l'auteur à chaque partie du modèle est décrite en Figure 4.2.

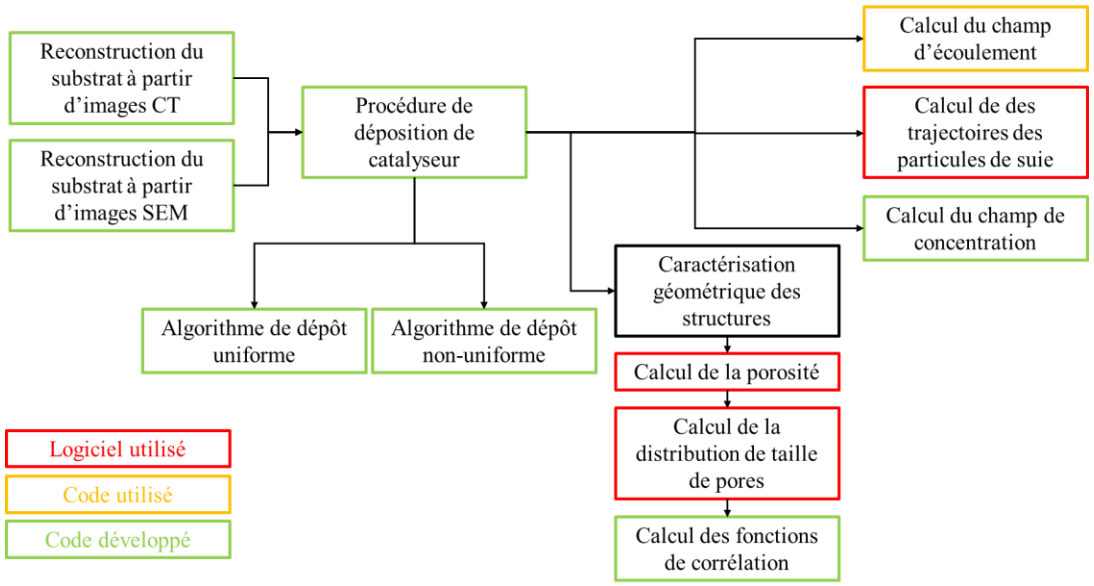

Figure 4.2 : Schéma descriptif des liens entre les différents composants du modèle numérique 4-étapes et des types de solveurs utilisés.

4.2 Choix des solveurs

Différentes méthodes numériques sont envisageables pour la complétion des étapes (2)-(4) du modèle de prédiction de la performance des FAPC. L'étape (2) nécessite l'utilisation d'un logiciel de MFN capable de résoudre des écoulements laminaires en milieu poreux. Les méthodes envisageables sont : la méthode des différences finies (MDF), la méthode des éléments finis (MEF), la méthode des volumes finis (MVF) ou la méthode de Boltzmann sur réseau (MBR). La MEF et la MVF souffrent principalement de la nécessité d'un maillage de la géométrie. Or dans un milieu aussi complexe que celui de la céramique qui forme les canaux du FAPC, cette étape pourrait être limitante. La MDF et la MBR présentent l'avantage de pouvoir utiliser directement la voxélisation du milieu poreux issu des images tomographiques comme grille de calcul. Cependant la MDF amène à calculer les grandeurs macroscopiques telles que la vitesse du fluide, directement sur cette grille, et peut donc induire un effet de crénelage du champ d'écoulement. Finalement, un code développé par le groupe de l'URPEI s'est déjà montré très performant dans le calcul de champs d'écoulement à travers des milieux poreux (Vidal 2008). L'étape (3) nécessite la résolution des trajectoires des particules de suie par un calcul lagrangien (suivit de chaque particule individuellement) ou eulérien (suivit du champ de concentration des particules). La résolution de façon lagrangienne permet d'éviter l'utilisation de fonctions probabilistes semi-empiriques liées à la capture des particules comme dans les travaux de (Yamamoto et al. 2009; Yamamoto and Ohori 2012). Les méthodes lagrangiennes sont donc plus précises, mais aussi plus couteuses en temps de calcul. Cependant, étant donné la faible concentration des suies dans le cas des FAPC pour moteurs EID, ainsi que l'absence d'effet d'accumulation de ces dernières, le coût d'une méthode lagrangienne est abordable. Deux options sont donc envisageables, un code commercial GeoDict® ("GeoDict" 2018) ou un code développé au sein du groupe de recherche de l'URPEI (Vadeiko and Drolet 2009). Après des essais de calculs à travers les deux programmes, la résolution des images tomographiques ($dx = 1.25\ \mu m$) nous a conduit à nous tourner vers le logiciel commercial GeoDict®. Enfin, l'étape (4) nécessite la résolution d'un problème d'ADR des espèces chimiques devant être traités par le catalyseur du FAPC. Pour résoudre ce problème, comme pour l'étape (2), plusieurs méthodes numériques sont envisageables : MEF, MVF, MDF et MBR.

4.3 Vérification et validation du modèle

Une étape importante de la méthodologie d'une étude numérique est la vérification et la validation (V&V). Ainsi chaque partie du modèle numérique assemblée doit être vérifiée et validée. La vérification d'un modèle consiste à s'assurer de la bonne implémentation des schémas numériques et de l'accord entre la solution numérique et la solution du modèle mathématique. La validation consiste à s'assurer de la validité du modèle physique. Il s'agit donc de comparer la solution numérique avec l'expérience.

4.3.1 V&V de la reconstruction : étape (1)

Une façon simple pour valider en première approximation la procédure de segmentation des images tomographiques utilisées pour reconstruire le milieu poreux est de mesurer leur porosité expérimentalement et de comparer avec la porosité de l'échantillon numérique. Ceci a été vérifié dans le travail de (Greiner et al. 2019) avec une porosité nominale du FAP avant dépôt de catalyseur de l'échantillon mesuré comme celle de la structure numérique à 65%.

Les méthodes de déposition artificielle de catalyseur ont été vérifiées par procédure inverse. En partant d'une déposition non uniforme à grande quantité de catalyseur, obtenue par dilatation de la phase de catalyseur de l'image d'origine, une procédure d'érosion a permis de retomber sur de plus faibles quantités de catalyseur. La perméabilité de ces milieux a ensuite été comparée avec celle de ceux issus d'une simple procédure d'érosion de la phase de catalyseur des images d'origine. Les résultats de cette analyse sont présentés en Annexe C.

4.3.2 V&V du calcul du champ d'écoulement : étape (2)

Le calcul du champ d'écoulement a été validé à l'aide d'une méthode d'impression 3D et de mesure de perméabilité à l'aide d'un perméamètre. Cette procédure est l'objet de l'entièreté du Chapitre 7. Elle consiste à (1) imprimer des sections de parois poreuses agrandies par la fabrication d'additifs pour filaments fondus ; et (2) caractériser leur perméabilité en utilisant un dispositif de mesure de la perméabilité à la tête tombante et une procédure d'essai modifiés. Une approche détaillée est également proposée pour sélectionner le facteur d'échelle approprié pour produire les échantillons par impression 3D. Une comparaison entre les prédictions numériques, Blake-Kozeny, et

expérimentales de l'impact de la quantité de revêtement et du degré d'uniformité sur la perméabilité des parois est présentée. Malgré la sensibilité inhérente de la perméabilité aux caractéristiques de l'espace poreux, un très bon accord est signalé entre les simulations et les expériences avec un écart moyen de 19,3 % pour les sept structures agrandies testées.

Des cas de vérification du calcul du champ d'écoulement par comparaison à des corrélations de la littérature sont également présentés en Section 5.3.2.1.

4.3.3 V&V du calcul des trajectoires des particules : étape (3)

Il est très difficile en pratique de valider des calculs numériques de l'efficacité de capture des FAP à l'échelle microscopique, étant donné leur nature multiéchelle. En effet, les différentes contributions à l'efficacité de capture totale du filtre sont difficilement différenciables par l'expérience. Afin d'isoler l'efficacité de capture du mur poreux, il faudrait ainsi découper une surface de matériaux et le placer sur banc d'essai. Or, étant donné la finesse des murs constituant les canaux du FAP (quelques centaines de microns), cette procédure nécessite des appareils extrêmement minutieux et donc couteux.

Pour valider cette étape du modèle, une campagne d'expériences a été réalisée à l'université d'Alberta. Les résultats sont présentés en Annexe D. Les autres cas de V&V pour cette étape du modèle sont présentés en Section 5.3.3.1.

4.3.4 V&V du calcul du champ de concentration : étape (4)

Le champ de concentration a été vérifié contre des solutions analytiques et les logiciels commerciaux COMSOL Multiphysics® sur des cas simples et GeoDict® sur un cas réaliste. Ces cas de V&V sont présentés en Section 6.3. Un test additionnel est présenté en Annexe A. La validation de cette étape du modèle numérique est la seule étape de validation à compléter dans ce projet. Cependant les résultats de l'Article 2 (Chapitre 6), montrent un excellent accord entre les prédictions du modèle et la théorie du module de Thiele. Cela permet, à défaut de valider le modèle, de s'assurer de sa précision et de son accord avec la théorie semi-empirique.

CHAPITRE 5 ARTICLE 1 : NUMERICAL INVESTIGATION OF THE IMPACT OF WASHCOAT DISTRIBUTION ON THE FILTRATION PERFORMANCE OF GASOLINE PARTICULATE FILTERS

Igor Belot, David Vidal, Martin Votsmeier, Robert E. Hayes and François Bertrand

Published in Chemical Engineering Science

Abstract : A three-step numerical model sheds light on the impact of three-way catalyst washcoat distribution within the cordierite porous wall of a clean gasoline particulate filter on its filtration performance. The model relies on (1) the numerical reconstruction of porous wall sections with various washcoat distributions and coating amounts, generated using a novel set of erosion/dilation-based procedures applied on segmented X-ray computed tomography data, (2) the computation of the flow field using the lattice Boltzmann method, and (3) the prediction of soot capture efficiency by solving the Langevin equation. The impact of washcoat distribution and amount on the pressure drop, permeability, filtration efficiency, and filter quality factor is systematically investigated. For a non-uniform washcoat distribution, an unexpected decrease in filtration efficiency with an increase in washcoat amount is explained and this highlights the complexity of the effects generated by the deposition of washcoat within the porous wall of the filter.

5.1 Introduction

With up to 25% improved fuel efficiency and performance as well as reduced greenhouse gas emissions compared to traditional gasoline port fuel injection engines (Zhao, Lai, and Harrington 1999), gasoline direct injection (GDI) engines have been rapidly adopted by automotive manufacturers and consumers. This technology has captured over 50% and 43% of the gasoline passenger car market share as of 2016 in the USA and EU, respectively, only nine years after its worldwide introduction (Joshi and Johnson 2018; Davis et al. 2016; Mock 2017). Although GDI engine particulate emissions account for only about 1% of the total particle number emitted by diesel engines, they are not as benign as they seem since they often peak at diameters around 30 nm (Braisher, Stone, and Price 2010; Platt et al. 2017; Zinola et al. 2013). At these particle sizes, soots

are much more difficult to remove from exhaust gases and can penetrate much more deeply into the lungs (Lewtas 2007). In addition to soot particles, nitrogen oxide (NO_X), hydrocarbon (HC), and carbon monoxide (CO) emissions are also of particular concern to OEMs (Zhao, Lai, and Harrington 1999). To comply with increasingly stringent pollutant emission regulations such as Euro 6 (Richter et al. 2012; Inoda et al. 2017), automotive OEMs must develop improved exhaust gas aftertreatment devices.

Particulate filters (PF) were originally introduced to reduce diesel engine particulate matter (PM) emissions. PFs consist of a honeycomb structure of parallel channels alternately closed at the inlet and outlet. Their walls are made of a porous material such as cordierite or silicon carbide (SiC) (Guan et al. 2015), as shown in Figure 5.1. In parallel, catalytic converters have been developed to reduce NO_X, CO, and HC gas emissions (Wang et al. 2014). They consist of a monolith containing open channels covered with a catalytic washcoat.

In recent years, researchers have become increasingly interested in combining the two units into a catalyst-coated PF (CPF), which consists of depositing a catalytic washcoat directly on or within the porous wall of the filter. Many techniques have been reported in the literature to achieve this result. The most common method involves injecting a dispersion coating into the PF and then drying the catalyst carrier afterwards (Shimrock, Taylor, and John M. Collins 1985; Aderhold et al. 1999; Foerster et al. 2000). CPFs have the advantage of removing soot particles at the same time as CO, HC, and NO_X gases, while gaining space, improving effectiveness, and reducing costs and overall pressure drop. In the case of a diesel particulate filter (DPF), a selective catalytic reduction (SCR) coating (Thomas et al. 2019), is usually applied to the filter wall.

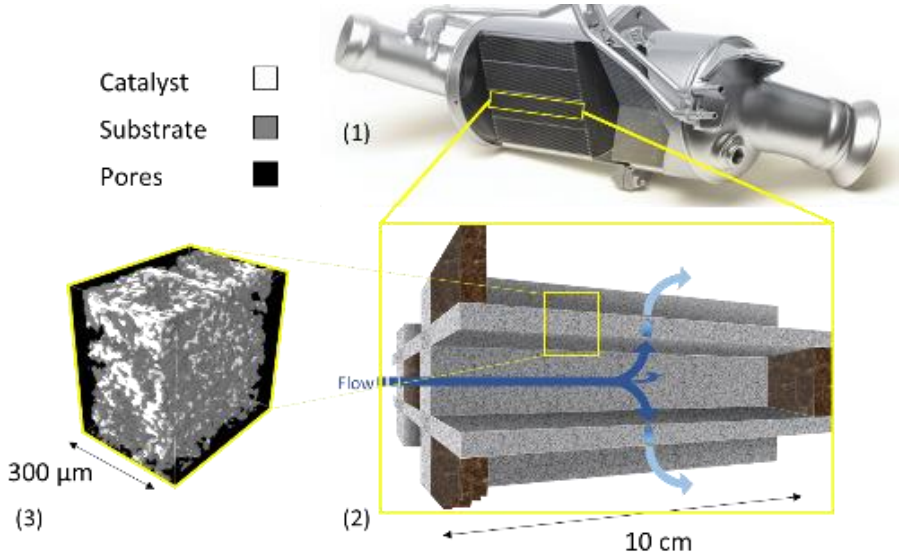

Figure 5.1 : Illustration of the three scale levels of coated PF: (1) whole filter scale (~10 cm long), (2) channel scale (~1 mm wide), and (3) porous wall scale (~10 µm pore size).

Numerous studies have compared the effect of different substrates and/or amounts of coating on pressure drop, filtration efficiency and NO_X reduction of a SCR-DPF combination. A study on the performance of cordierite-based wall-flow filters coated with an SCR catalyst at different densities revealed that the impact of the catalyst coating on the pressure drop of the filter was negligible compared to the effect of soot accumulation (Rappé 2014). On the other hand, it was shown that variable catalyst coating amounts in different substrates can multiply the pressure drop through the wall up to 20 times compared to a bare filter (Swanson et al. 2013). In another study, various amounts of washcoat deposited on an SiC-based DPF were compared in terms of pressure drop and filter efficiency (Tsuneyoshi, Takagi, and Yamamoto 2011). The general conclusion was that higher catalyst coating amounts usually result in an increase in both filtration efficiency and pressure drop. In the case of gasoline particulate filters (GPF), a three-way catalyst (TWC) containing platinum group metals is usually used in the catalytic washcoat (Thomas et al. 2019). Studies similar to those on SCR-DPFs have been conducted on TWC-GPFs (Inoda et al. 2017; Lopez-Gonzalez et al. 2015; Richter et al. 2012), most of which concluded that, like SCR-DPFs, washcoat deposition increases both the pressure drop and the capture efficiency. This can be explained by the loss of pore space caused by the deposition of the catalyst. Contrariwise, it has

also been proposed that increased washcoat loadings can lead to decreased filter capture efficiency due to higher gas flow velocities and thus lower residence time (Joshi and Johnson 2018; Liu et al. 2018). A complete understanding of this issue is lacking in the literature and further work is needed to explain the impact of the amount of washcoat and its distribution in the pore space. Such an investigation would be very complex if conducted experimentally.

Therefore, in addition to experimental work, many studies have explored CPFs using numerical simulations. This approach has the advantage of being less costly, easier to manage, and less intrusive than bench experiments. Three different numerical PF modelling scales have been reported in the literature. Figure 5.1 illustrates the various PF scales usually modeled numerically. The largest is the whole filter scale. Models at this scale are, however, rarely used to predict the overall filtration performance of PFs except through semi-empirical or analytical expressions developed at smaller scales at which soot capture takes place. For more details on this modelling scale, the reader is referred to more exhaustive reviews (Konstandopoulos and Papaioannou 2008; Koltsakis et al. 2013). The middle scale refers to the channel scale, the modelling of which was pioneered by Bisset and Shadman (Bissett and Shadman 1985) and improved later by Watling et al. (Watling et al. 2017), among others. The related modelling and improvements have been reviewed in recent years (Koltsakis et al. 2013; Xuereb and Farrugia 2016), and usually consider 1D, 2D, or 1D+1D domains using a compartmental approach for the channel length and the wall thickness (Wurzenberger et al. 2016), and solving macroscopic conservation equations of mass, momentum, and energy in two adjacent channels of the PF. This modelling scale has the advantage of being simple and efficient for predicting back pressure and filter efficiency behaviour over time for well-characterized filters (Torregrosa et al. 2011; Gong et al. 2018). Filter cake evolution over driving cycles and time is often considered at this modelling scale (Bensaid et al. 2009; Lupše, Campolo, and Soldati 2016; Karamitros and Koltsakis 2017). The major drawback of this model, as with the largest scale, is that it is not able on its own to predict the impact of smaller-scale features of the porous wall medium on the performance of the filter. Indeed, in this approach, porous wall resistance to the flow is usually accounted for through the resolution of the Brinkman equations. For example, the prediction of the impact of washcoat distribution uniformity in the porous wall on pressure drop and filtration efficiency is not possible without prior knowledge of small-scale structural properties such as permeability, tortuosity, and pore size distribution.

In recent years, advances in high-performance computing (HPC), improvements in computational memory and power, and the development of new imagery techniques such as tomography have made the numerical study of PF structures at the micron scale possible. They have also made it possible to represent the porous wall of the filter in greater detail. As such, considerable research interest has been directed toward porous media modelling. The review of Konstandopoulos et al. (Konstandopoulos, Kostoglou, and Vlachos 2006), one of the earliest studies, reported permeability predictions for two different washcoat distributions in the porous wall of an SiC-based DPF. The washcoat distribution was varied at the pore scale level by erasing washcoat voxels from a segmented scanning electron microscope (SEM) image using an unreported procedure. The results showed that a non-uniform distribution profile leads to higher permeability than a uniform one in the 0-30% range of pore volume filled with washcoat. However, neither the detailed characteristics of the two washcoat distributions nor their soot capture efficiency were reported by the authors, limiting the conclusions regarding the overall filtration performance of such washcoat depositions. More recently, an investigation of the impact of on-wall and in-wall depositions of catalyst on the filtration performance of the porous wall of an SCR-DPF reported better results with the on-wall deposition in terms of pressure drop, soot capture, and contact ratio between the deposited soot and the catalyst (Kong and Yamamoto 2018). However, the authors did not report any details with respect to the distribution uniformity of the in-wall deposited catalyst or the quantitative results of capture efficiency. Similarly, in the context of TWC-GPFs, other studies compared the filtration and catalyst performance of three cordierite filter structures with different in-wall and on-wall coating distributions (Tanaka, Miyoshi, and Sato 2018; Kočí et al. 2019) and reported that in-wall depositions were more permeable than mixed in- and on-wall depositions. Although these studies showed that detailed investigations of PF performance at the micron scale are feasible, a systematic parametric investigation of various coating distributions on filtration and catalytic performance was not done and capture efficiency was not considered. In all the aforementioned papers, the researchers employed a multi-step approach that appears to be well-suited for tackling PF modelling. First, a representative filter medium was generated using geometrical reconstructions such as spherical particle packing algorithms (Hayashi and Kubo 2008; Lee et al. 2018), simulated annealing (Matte-Deschênes et al. 2016), or real sample images from SEM images (Stewart et al. 2010) or computed tomography scans (Tsushima et al. 2010). Once the structure is reconstructed,

computational fluid dynamics (CFD) methods such as the well-established finite volume method (FVM) (Kočí et al. 2019) or the well-suited lattice Boltzmann method (LBM) (Konstandopoulos, Kostoglou, and Vlachos 2006; Yamamoto et al. 2006; Stewart et al. 2010; Matte-Deschênes et al. 2016; Kong and Yamamoto 2018; Lee et al. 2018) can be employed to compute the flow field through the filter porous wall and thus calculate the medium permeability and/or the pressure drop. These CFD methods can also be used to retrieve other fields such as the temperature across the filter wall (Yamamoto and Nakamura 2011). Once the flow field has been computed, filter capture efficiency can also be obtained by tracking individual particle trajectories using Lagrangian approaches (Wiegmann, Rief, and Latz 2006; Vadeiko and Drolet 2009; Becker et al. 2016; Stewart et al. 2004) or solving mass transport equations using the Eulerian approach and using probabilistic models of soot deposition (Yamamoto and Ohori 2012; Tsushima et al. 2010). Physical phenomena at the micron scale can thus be studied using this multi-step methodology. However, to date, no study has been able to provide an overall and systematic understanding of the impact of the structural characteristics of catalytic washcoat deposition on both the filtration performance and the catalytic conversion of a CPF. To achieve this, a complete set of numerical models at the wall scale must be developed to predict the overall performance of a CPF. In particular, artificial washcoat deposition techniques must be developed to generate different catalyst coating distributions in the porous wall and predict its performance.

To pave the way for this ultimate goal, two specific objectives are pursued. The first is to develop modelling tools able to predict both the filtration and catalytic conversion performance of a catalyst-coated GPF at the microscopic scale. The second is to demonstrate the usefulness of these modelling tools by applying them to determine the most appropriate catalyst distribution profile in a cordierite porous wall of a GPF by comparing the performance of uniform and non-uniform washcoat distribution profiles. More specifically, the aim of the present investigation was to quantify the possible benefits of uniform catalyst deposition versus non-uniform deposition within the porous wall of the filter in terms of GPF performance. The present article focuses on filtration performance as defined by pressure drop and soot capture efficiency, while an upcoming companion paper will compare catalytic conversion performance (Belot, Vidal, Greiner, et al. 2020). Soot and ash accumulation and the resulting filter clogging will be neglected here as a filter cake formation is less likely on the porous wall of GPFs due to lower soot concentrations, soot

oxidation by TWC and higher exhaust gas temperatures than in a DPF (Gong et al. 2018; Mikulic et al. 2010; Lambert et al. 2017) and because ash accumulation occurs mainly over extended use (Lambert et al. 2016; Joshi and Johnson 2018).

The remainder of the paper is organized as follows. In Section 2, the three-step numerical model developed in the present investigation and relying on the lattice Boltzmann method is examined in detail. In Section 3, the quality of the model predictions is assessed, and a detailed analysis of the impact of catalytic deposition uniformity on pressure drop, permeability, capture efficiency and, thus, overall filtration performance is presented. Lastly, Section 4 provides concluding remarks and the prospects of the present work for achieving the general objective of building a wall-scale model for predicting overall CPF performance.

5.2 Three-step methodology

To achieve the two specific objectives mentioned in the Introduction, the three-step methodology shown in Figure 5.2, which was partly inspired by the methodology proposed in (Matte-Deschênes et al. 2016), was developed and is presented in this section. It consists of (1) the numerical reconstruction of a representative elementary volume (REV) of the coated porous wall with various washcoat distributions (i.e., uniform and non-uniform) and coating amounts, generated using a novel set of erosion/dilation-based procedures, (2) the computation of the flow field using the lattice Boltzmann method (LBM) to obtain the back pressure (hereafter referred to as pressure drop or ΔP) across the wall, and (3) the calculation of soot particle trajectories by solving the Langevin equation to obtain the capture efficiency (E_f) of the porous wall. Knowing the ΔP and E_f of the reconstructed GPF wall, it is possible to compute the filter quality factor (Q_f), which is a criterion often used in air filtration by fibrous filters and employed here to compare the overall filtration performance of the different washcoat distributions within the porous wall. Here, the catalyst coating was assumed to be impermeable as its permeability (~10^{-15} m^2 according to (Kočí et al. 2019)) is at least two orders of magnitude lower than that of the resulting substrates studied and, therefore, its pore network was not resolved and thus accounted for.

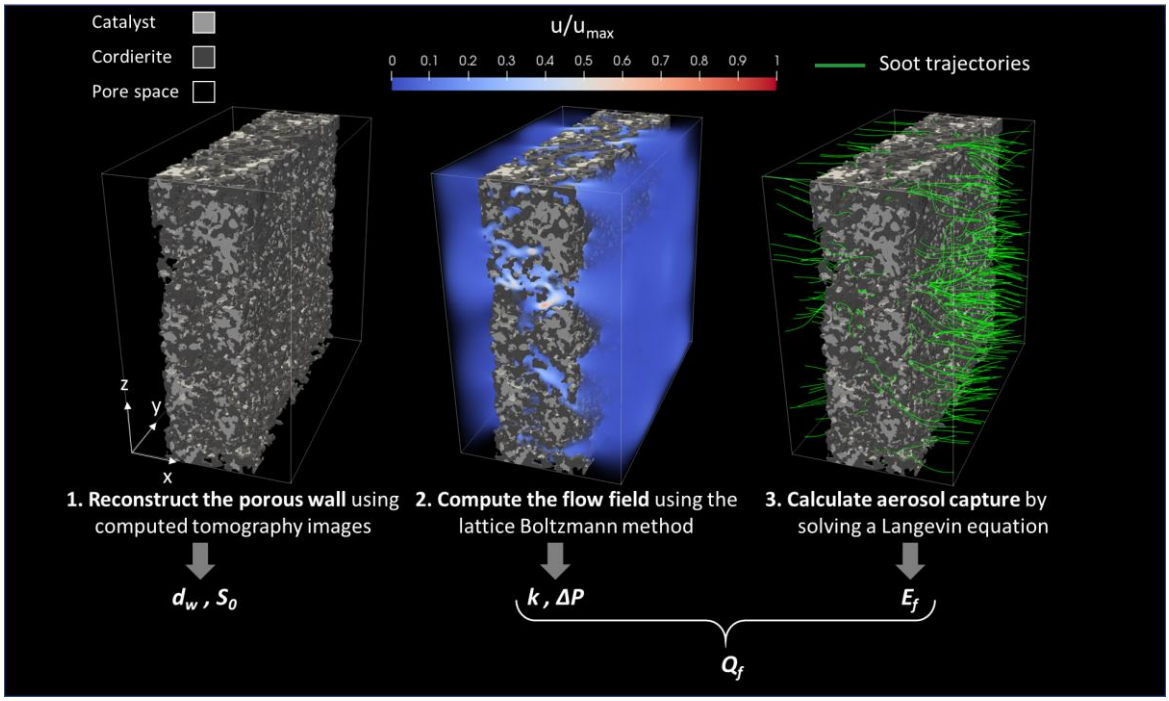

Figure 5.2 : Illustration of the three numerical steps leading to the prediction of the filtration performance of a GPF porous wall at the microscopic scale.

5.2.1 Reconstruction and characterization of the porous wall

The first step in the development of a model able to predict the performance of a filter is the reconstruction of a piece of the porous wall that divides two adjacent channels of a coated GPF. The wall is composed of three phases: the pore space, the substrate (here cordierite), and the catalyst coating (also called washcoat). To generate a good numerical representation of the porous walls and their washcoat distribution profiles, multiple reconstruction methods can be considered. They all require different levels of information about the original base structure and the washcoat distribution profiles. One approach, the simulated annealing technique, uses stochastic algorithms (Matte-Deschênes et al. 2016). In this case, geometrical characteristics such as the phase correlation functions of a real substrate and coating deposition are needed but are not readily available. A second approach simulates the physical phenomena or processes involved in manufacturing catalyst-coated filters. The main drawback of this approach is that it can be very complicated and time consuming in the case of complex industrial processes. It also requires a great deal of

information about the manufacturing process itself, which is often not readily available. A good compromise and computationally efficient solution for achieving better precision and a more realistic reconstruction of the porous wall is to start from an actual numerical image of a coated GPF sample at the pore scale on which digital operations can be performed to reconstruct filter structures virtually. In the present study, an X-ray computed tomography (CT) image of a 3×3×1.5 mm^3 piece of a 1.16-mm wide channel of a cordierite-based GPF coated with a TWC washcoat was acquired using a General Electric *Phoenix Nanotom M*. The lab sample used, hereafter referred to as the original R&D sample (OS), was non-uniformly coated throughout the wall thickness, with 23.2% of the cordierite pore volume filled with washcoat. A stack of 256 images, each composed of 801×779 pixels representing a section of the porous wall, was extracted from the 3D raw image of the OS sample. This stack of images was then reconstructed into a 3D image, as shown in Figure 5.3. The voxel resolution in every direction was $dx = 1.246\ \mu m$. The raw data were encoded using an 8-bit grey scale, and the image was segmented into pore space, cordierite, and catalyst phases based on a thresholding algorithm (Greiner et al. 2019).

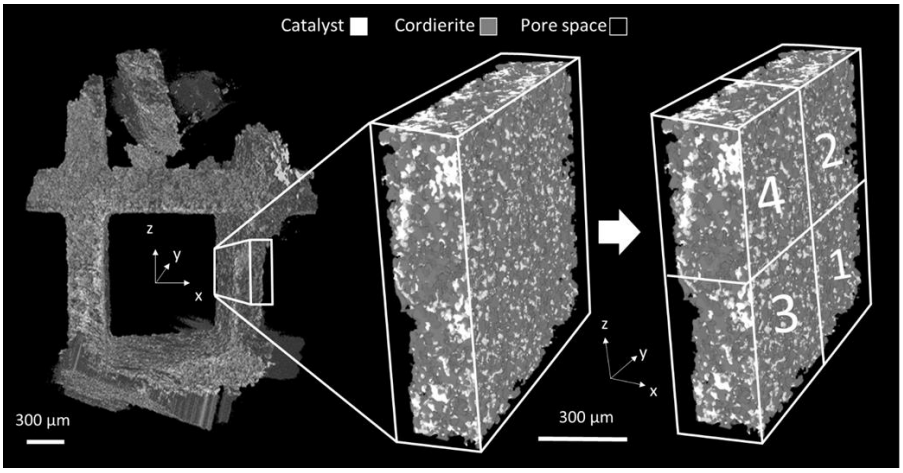

Figure 5.3 : Representation of the 3D image of a section of the porous wall (middle) extracted from the raw data of a channel piece from the OS sample of a specially prepared TWC-GPF (left), and the later splitting of this wall section into subdomains used for the computations (right).

Once the wall section was segmented, a novel artificial washcoat deposition method applied to the resulting three-phase image and relying on classical morphological dilation and erosion algorithms

used in image analysis (Young 1983) was devised to modify the original washcoat distribution profile. This method is based on a set of three independent procedures depending on the type of washcoat distribution profiles to be reconstructed, which are illustrated using 2D slices in Figure 4. The first procedure of the artificial deposition method created a uniform distribution profile, i.e., completely different from the non-uniform distribution profile of the OS sample. To obtain a uniform distribution profile, the original coating deposition (white pixels in Figure 5.4) was digitally erased and was replaced by pore space pixels. Next, the substrate (grey pixels in Figure 5.4) was dilated from its surface using a sphere of a specific diameter as a 3D structuring element by means of a custom-written MATLAB program based on the MATLAB Central File Exchange routine STREL3D (version 1.1.0.0) (Xie 2014). The added voxels resulting from this morphological dilation of the substrate were converted into washcoat voxels (white pixels in Figure 5.4), creating a uniform washcoat deposition within the porous wall, the coating amount of which was determined by the size of the sphere used as a structuring element. Here, the sphere diameters used varied from 2 to 9 times the voxel size.

The second and third procedures of the artificial deposition method aimed at creating non-uniform distribution profiles that follow from the OS sample non-uniformity and differ depending on whether the amount of washcoat is larger or smaller than that of the OS sample. Specifically, the two procedures were devised to either (1) increase the coating amount of the OS sample while accentuating its non-uniformity using a dilation-based technique, or (2) decrease the coating amount of the OS sample while decreasing its non-uniformity using an erosion-based technique. To increase the coating amount, the catalyst phase was dilated using spherical structuring elements of increasing diameter (from 2 to 9 times the voxel size) as previously described for the uniform coating profile creation procedure. Note that the dilation procedure only takes place within the pore space and not the substrate. To decrease the coating amount, the procedure was slightly more complex and is detailed in the insert of Figure 5.4. The substrate phase was first merged with the original catalyst phase to form a solid phase (white pixels in frame (b) of the insert in Figure 5.4). The new solid phase was then eroded using a spherical structuring element of a specific diameter (from 2 to 9 times the voxel size), with higher diameters resulting in lower coating amounts. Lastly, the original substrate phase was overlaid on the resulting catalyst and pore phases as shown in

Figure 5.4. This technique prevented the creation of gaps between the catalyst and substrate phases that occur when a direct erosion of the original catalyst phase is performed.

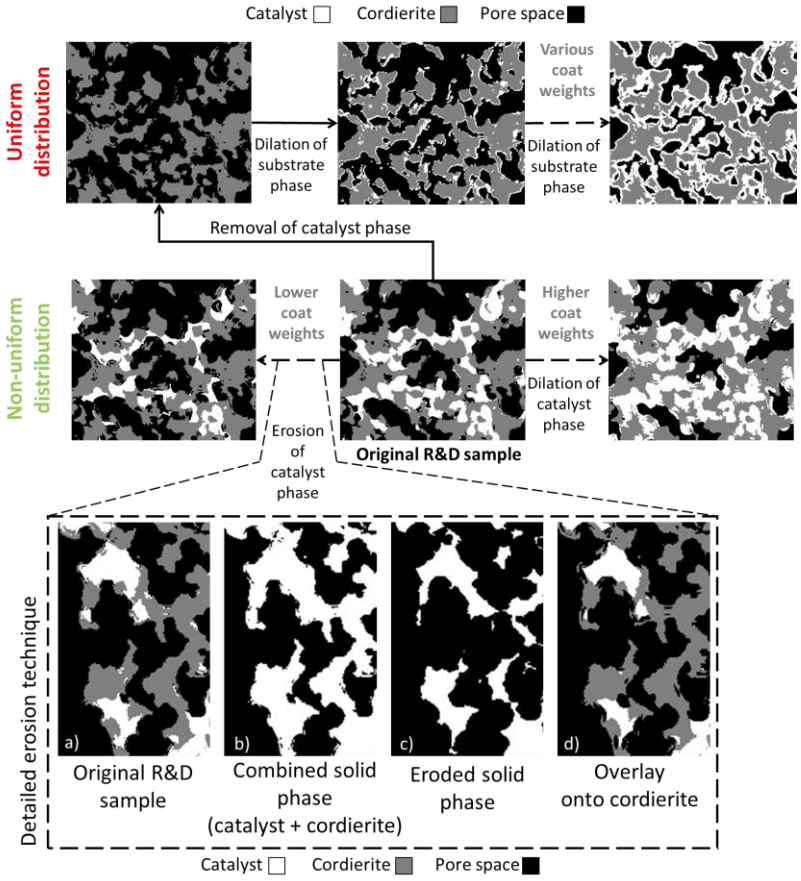

Figure 5.4 : 2D illustrations of the different deposition procedures used to obtain the uniform and non-uniform distribution profiles from the OS sample image. The insert at the bottom illustrates the more complex erosion technique employed to obtain a thinner non-uniform catalyst deposition from the OS sample distribution profile.

Following these two procedures, four and eight structures of increasing coating amount with, respectively, uniform and non-uniform washcoat distribution profiles (hereafter denoted as U1 to U4 and N1 to N8, respectively) were created. In addition to these 12 structures, two other structures were considered: (1) the OS sample, which can be considered as part of the non-uniform structure

series, and (2) the bare wall (BW) structure (i.e., the OS structure from which the catalyst phase was completely removed), which can be considered as a limiting case with the coating amount equal to zero for both the uniform and non-uniform structure series. This brought the total number of structures studied to 14. The dimensions of all the structures were 256×801×779 voxels at the tomographic image resolution (i.e., $dx = 1.246\ \mu m$). For ease of computation, each of these structures was split into four 256×400×389-voxel subdomains, as shown in Figure 5.3, resulting in a total of 56 structures. The accuracy of the permeability predictions with respect to the subdomain size chosen is assessed in detail in Appendix A.

Once reconstructed, the characterization of the porous structures is an essential step for an in-depth understanding of the difference in filtration performance between the two washcoat distribution profiles. The most obvious metrics is the volume fraction of the pore space (i.e., the porosity), denoted as ε, defined as:

$$\varepsilon = \frac{V_{por}}{V_{tot}} \tag{5.1}$$

where V_{por} is the volume of the pore space and V_{tot} is the total volume of the porous medium. This value can be calculated by dividing the number of pore voxels by the total number of voxels. Knowing the porosity of the reconstructed structures, the fraction of pore volume filled with catalyst can be calculated as:

$$f_w = 1 - \frac{\varepsilon}{\varepsilon_{BW}} \tag{5.2}$$

where ε_{BW} is the porosity of the bare wall. The specific surface area S_0 is another important characteristic of a porous medium as it is strongly related to permeability and capture efficiency, as we shall see later, and is linked to the interfacial area S between the two phases per unit volume of the solid phase through:

$$S_0 = \frac{S}{(1-\varepsilon)V_{tot}} \tag{5.3}$$

Here, the specific surface area of each digitized structure was calculated using the PoroDict® module of the commercial software GeoDict® (version 2018, Math2Market GmbH, www.geodict.com) using a statistical method (Ohser and Mücklich 2000). Both ε and S_0 can be used to evaluate the mean pore diameter d_w of the wall given by:

$$d_w = \frac{2\varepsilon}{3(1-\varepsilon)}\frac{6}{S_0} \tag{5.4}$$

Lastly, pore size distribution is a sensitive metric for characterizing the pore space and for differentiating one porous medium from another. Although there is no strict and unambiguous definition of a pore, many methods exist in the literature to evaluate this characteristic function. In the present study, the PoroDict® module of the commercial software GeoDict® was used to compute the pore size distribution of the reconstructed structures based on a granulometry technique (Soille 1999). Additional statistical structural descriptors, namely the two-point probability function and the lineal path, are also provided in Appendix B. They may help reconstruct these structures using the simulated annealing technique (Matte-Deschênes et al. 2016), for instance, to enable future use of these structures by any interested reader.

5.2.2 Computation of the flow field through the porous wall

The second step in the development of a model able to predict filter performance is the calculation of the flow field through the porous wall. Although several other CFD methods (particularly Explicit-Jump, SIMPLE-FFT, and LIR methods as well as the FVM) implemented in commercial or open-source software packages (such as GeoDict® ("GeoDict" 2018) or OpenFOAM® ("OpenFOAM")) could also have been well suited in this context (Azimian, Cheng, and Wiegmann 2017; Kočí et al. 2019), the lattice Boltzmann method (LBM) was here chosen as it is particularly effective for porous media due to the several reasons: (1) its ease in dealing with complex geometries and the associated mesh generation (Vidal et al. 2009), (2) its parallel efficiency on large-scale parallel and distributed computer systems due to the inherent locality of its explicit scheme (Vidal, Roy, and Bertrand 2010a, 2010b), (3) its relative simplicity of implementation, and (4) its capability to solve partial differential equations, making an LBM scheme a generic partial differential equation solver for porous media (Krüger et al. 2017). Furthermore, although the

present study only required steady state flow computations, the LBM is an intrinsically transient solver (as opposed to current GeoDict® flow solvers using Explicit-Jump, SIMPLE-FFT, and LIR methods), a feature which will be used in future studies related to the present investigation. We did, however, use the SIMPLE-FFT GeoDict® flow solver to assess the quality of the LBM code predictions for steady state flows.

Assuming an isothermal incompressible flow, the LBM does not tackle the problem at a continuum mechanics scale, which would require solving the incompressible Navier-Stokes equations as classical CFD methods do, but rather at a mesoscopic scale using statistical mechanics following the Boltzmann equation in which the probability distribution function is discretized in the time, space, and velocity domains using a set of microscopic velocities (Krüger et al. 2017). The LBM scheme has been shown to satisfactorily recover the transient Navier-Stokes equations for incompressible flows in the limits of lower Mach and Knudsen numbers (Krüger et al. 2017). In this work, a D3Q15 velocity set and a single-unit dimensionless relaxation time were here used for the sake of computational and memory usage efficiencies, as explained in (Vidal, Roy, and Bertrand 2010b).

The LBM code developed in (Vidal, Roy, and Bertrand 2010a, 2010b) was used to calculate the flow velocity field of each of the 56 reconstructed media and the reader is referred to these papers for more details about the LBM and its implementation. No mesh generation was needed for these calculations as the LBM scheme uses directly the voxelization of the reconstructed geometries as a computational grid or lattice, with a lattice spacing being equal to the CT image resolution, i.e., $dx = 1.246\ \mu m$. The LBM implementation only retains the pore voxels and, as such, probability distribution functions arriving at a wall (solid voxel) are bounced back to the pore space using the half-way bounce back boundary condition (Vidal, Roy, and Bertrand 2010a). The flow here is driven by a pressure drop implemented through an added body force in the discretized Boltzmann equations in the flow direction (here the wall thickness, i.e., *x* direction) at each lattice site and each time step (see (Bertrand et al. 2012) or (Krüger et al. 2017), for detailed implementations). The outside domain boundary conditions used in these simulations were periodic for the probability distribution functions in the direction of the flow (x) and symmetric in the directions perpendicular to the flow (*y*,*z*). Lastly, two buffers of 100 fluid voxels were added upstream and downstream

from the structures to prevent too large edge effects and facilitate the implementation of the periodic flow boundary condition. The size of the buffer zones can influence the uniformity of the velocity profiles at the inlet and outlet, but their influence on the permeability has been evaluated to be much lower than 1% at the size selected here. The effective dimensions of the 56 structures studied were thus 456×400×389 voxels. It must be mentioned that even if the flow was driven by a pressure drop, and as long as the flow regime remained laminar, the resulting velocity field could be linearly rescaled afterward such that the targeted superficial velocity U was obtained and ΔP was corrected accordingly as a result. The physical parameters used for these LBM calculations of gas flow through the 56 porous structures studied are summarized in Table 5.1, in which it is assumed that the exhaust gases have the same properties as air.

Table 5.1: Physical parameters used for flow field calculations with the LBM.

Parameter	**Symbol**	**Value**
Fluid density ($kg.m^{-3}$)	ρ	0.543
Fluid dynamic viscosity ($kg.m^{-1}.s^{-1}$)	μ	3.18×10^{-5}
Superficial velocity ($m.s^{-1}$)	U	0.055
Temperature (K)	T	650

Once the velocity field was obtained using the LBM for each of the 56 structures and ΔP was calculated, it was possible to retrieve a key macroscopic property of the porous medium, i.e., which is the hydraulic Darcy's permeability using Darcy's law for laminar flows (Dullien 1979) given by:

$$k_D = -\frac{\mu U L}{\Delta P} \tag{5.5}$$

where L is the wall thickness. This physical property is a material characteristic when calculated using pore-based Reynolds numbers lower than 10. In the present study, the pore-based Reynolds

number Re_p lay in the laminar Darcy's regime for all the conditions investigated (Bird, Stewart, and Lightfoot 2007):

$$0.03 \leq Re_p = \frac{\rho U d_c}{\mu(1-\varepsilon)} \leq 0.3 < 10 \tag{5.6}$$

where d_c is the diameter of the spherical collectors constituting a packed bed having the same specific surface area as the PF wall and is defined by (Dullien 1979):

$$d_c = \frac{3(1-\varepsilon)}{2\varepsilon} d_w = \frac{6}{S_0} \tag{5.7}$$

For accuracy assessment purposes and despite being more appropriate for packed beds of spherical particles, the computed permeability was compared to the Blake-Kozeny (BK) correlation (Blake 1922; Kozeny 1927) given by:

$$k_{BK} = \frac{1}{4.1\overline{6}\, {S_0}^2} \frac{\varepsilon^3}{(1-\varepsilon)^2} \tag{5.8}$$

Lastly, note that while the ΔP and k_D of the 56 reconstructed structures were computed using our own LBM code, the same calculations could have been performed with the FlowDict® module of the commercial software GeoDict® as these calculations only require steady state solutions. However, as already mentioned, the LBM makes efficient parallelization possible on massively parallel computer clusters. Because of this, launching the simulations on dedicated computer clusters on several tens of cores resulted in very short computational times, i.e., in the order of minutes (see Section 3.2.1). Moreover, the LBM solved the transient flows through the structures, which provided additional information on flow behaviour through the structures over time that could be used in later analyses. Nevertheless, the initial LBM calculations within the OS structure were assessed using calculations made with the SIMPLE-FFT solver of FlowDict® and with predictions from the Blake-Kozeny equation (see Section 3.2.1).

5.2.3 Computation of soot particle trajectories in the porous wall

The last step in the development of a model able to predict the behaviour of filter performance is the calculation of the soot capture efficiency of the porous wall of a GPF. Two modes of filtration occur in a PF. The first is deep-bed filtration when the filter is still clean and the particles can penetrate deeply into the porous walls. Over time, ash/soot can accumulate and form a soot cake layer at the inlet surface of the channel wall. Clean filter capture efficiency was calculated using the FilterDict® module of GeoDict®. The approach consists of launching a large number of soot particles, represented by spheres with equivalent mobility diameters (Thomas et al. 2017), into the flow passing through the 56 previously reconstructed structures. For each particle diameter under investigation (with $d_p(\mu m) \in$ (1.00, 0.500, 0.375, 0.325, 0.275, 0.225, 0.175, 0.125, 0.090, 0.03)), 25000 particles were launched from locations evenly distributed on the domain entry plane. Soot capture efficiency was then calculated for a given particle size as given by:

$$E_f = \frac{N_{in} - N_{out}}{N_{in}} \tag{5.9}$$

where N_{in} and N_{out} are, respectively, the number of particles launched at the inlet and the number collected at the outlet of the filter. In the packed bed model, the filter efficiency for a specific particle size can be linked to the efficiency of a single collector through the single collector theory as given by (Lee and Gieseke 1979b):

$$E_f = 1 - P_p = 1 - e^{-\beta\,\eta(1-\varepsilon)L} \tag{5.10}$$

where P_p is the particle penetration, η is the single collector efficiency, L is the thickness of the filter, and β is a constant or a function of porosity linked to the surface area of the collector for which many approximate expressions exist that are either derived analytically or obtained empirically (e.g., $\beta = \frac{4}{\pi d_c \varepsilon}$ for fibrous filters (Lee and Liu 1981) or $\beta = \frac{3}{2\varepsilon d_c}$ for spherical pack beds (Konstandopoulos 2000)). As larger soot particles are made of dendritic clusters of smaller primary particles, the density of the soot particles is a function of their diameter, which was chosen based on the diameter reported in (Keskinen et al. 1998), and is given by:

$$\rho_p = 1550 - (1550 - 155)\left(1 - \exp\left(-6.908\left(\frac{\log(d_p) - \log(0.03)}{-\log(0.03)}\right)^{4.28}\right)\right) \tag{5.11}$$

where d_p is the soot particle mobility diameter. A Lagrangian method was then used to follow each particle trajectory independently throughout the filter. To do so, Newton's second law of motion is solved for each particle considering the drag force and a stochastic term representing Brownian diffusion. This term is calculated using the diffusion coefficient of soot particles $D = \frac{k_B T}{\gamma}$ (where k_B is the Boltzmann constant and $\gamma = 6\pi\mu\frac{d_p}{2C_c}$ is the friction coefficient of a spherical particle in Stokes flow), and a 3D Wiener process $\boldsymbol{w}$ for a Brownian diffusion force in a way similar to that in (Vadeiko and Drolet 2009). Adding this term gives the following Langevin equation:

$$\begin{gathered}\frac{d\boldsymbol{v}(t)}{dt} = \frac{3\pi\mu d_p}{mC_c}\left(\boldsymbol{u}(\boldsymbol{x}) - \boldsymbol{v}(t) + \sqrt{2D}\frac{d\boldsymbol{w}(t)}{dt}\right) \\ \frac{d\boldsymbol{r}(t)}{dt} = \boldsymbol{v}(t)\end{gathered} \tag{5.12}$$

where $\boldsymbol{r}$ and $\boldsymbol{v}$ are, respectively, the position and velocity of the particle, $\boldsymbol{u}$ is the previously obtained flow velocity, μ is the dynamic viscosity of the fluid, d_p is the equivalent soot diameter of the particle, m is the mass of the particle, and C_c is the Cunningham correction factor given by (Thomas et al. 2017):

$$C_c = 1 + A\,Kn + B\,Kn\,\exp\left(\frac{-C}{Kn}\right) \tag{5.13}$$

where $A \approx 1.17$, $B \approx 0.525$, and $C \approx 0.78$ are empirical parameters given in (Crowe 2005). Kn is the particle Knudsen number given by:

$$Kn = \frac{2\lambda}{d_p} \tag{5.14}$$

where λ is the mean free path of the fluid molecules. Other forces such as electrostatic attraction, thermophoresis, or gravity could have been considered but were excluded here because of their

insignificant impact (Hinds 1999; Matte-Deschênes et al. 2016). A one-way coupling between the calculated flow field and the Langevin equation was considered in this work because the soot concentration was low and the flow disturbance caused by the motion of soot particles could be overlooked. This calculation takes into account three main particle capture mechanisms, namely Brownian diffusion, interception, and inertial impaction (Hinds 1999). The addition of these three capture mechanisms results in a capture efficiency relationship as a function of particle size that is typically shaped like a "smile", as reported in the literature for GPF and for fibrous filters (Joshi and Johnson 2018; Gervais et al. 2015). If a soot size distribution would be available, a composite capture efficiency could be calculated from this capture efficiency relationship, but soot coalescence/breakage cannot be account for in the current model. The soot diameter for which the capture efficiency is the lowest is usually taken as a reference value known as the capture efficiency of the most penetrating particle size (or MPPS). In the context of GPF, this diameter is usually around 200-300 nm (Joshi and Johnson 2018). Therefore, the range of soot diameters tested in the present study was mainly centred on this range, which is actually close to the upper limit of soot size encountered in GPFs (Graves, Koch, and Olfert 2017). A particle was considered captured when the distance between its centre and an inner wall surface voxel was smaller than its radius. Once captured, it was assumed that the particles stick to the solid wall due to short-range electrostatic forces and cannot be reentrained by the flow. This approximation is valid for low particle Reynolds numbers (Hinds 1999), which is the case here:

$$8 \times 10^{-5} \leq Re = \frac{\rho U d_p}{\mu} \leq 3 \times 10^{-4} \ll 1 \tag{5.15}$$

5.2.4 Calculation of the porous wall quality factor

Knowing the ΔP and E_f values of a PF, it is possible to calculate a filter quality factor (Q_f) (sometimes also called a figure of merit) that is a relevant criterion for judging the overall filtration performance of a porous medium and that has been more commonly employed in the field of fibrous filters. The Q_f is defined as (Hinds 1999):

$$Qf = \frac{-log\,(1 - E_f)}{\Delta P} \tag{5.16}$$

The main advantage of this metric is that it is independent of the wall thickness that can be regarded as the filtration performance achieved with respect to the energy input into the system.

5.3 Results and discussion

The presentation of the results is divided into four parts. First, the 56 numerical structures reconstructed for the present investigation are characterized using the statistical and global structural descriptors described in Section 2. Then, the flow properties of the various porous walls predicted by the LBM are given and compared with predictions from the correlation mentioned in Section 2. Next, the results of filtration efficiency obtained by the resolution of the Langevin equation are presented and analyzed in detail. Lastly, the filter quality factor is calculated for every structure to compare the filtration performance of uniform and non-uniform deposition profiles at different coating amounts. The advantage of a uniform deposition profile compared to a non-uniform deposition profile is then assessed.

5.3.1 Characterization of the reconstructed structures

Once the 56 porous walls with varying amounts of washcoat and degrees of uniformity were numerically reconstructed, the global and statistical structural descriptors described in Section 2 could be calculated to characterize the structures. The porosities and the corresponding fractions of pore volume filled with catalyst (i.e. f_w calculated using Eq. (5.2)) for all the structures studied

in the present investigation are presented in Table 5.2 and Table 5.3, respectively, for the non-uniform and uniform washcoat distribution profiles.

Table 5.2: Porosity values (ε) and corresponding fractions of pore volume filled (f_w) by the catalyst for all reconstructed non-uniform washcoat distribution profiles.

Sample ID:	**BW**	**N1**	**N2**	**N3**	**OS**	**N4**	**N5**	**N6**	**N7**	**N8**
Section	**Porosity (%)**									
1	68.3	60.4	58.6	56.1	54.6	52.0	48.8	46.4	42.7	36.7
2	67.2	58.3	56.3	53.7	52.2	49.5	46.4	44.0	40.3	34.6
3	69.8	60.6	58.6	55.8	54.2	51.5	48.1	45.7	41.9	36.0
4	67.8	55.4	53.1	50.2	48.5	45.7	42.3	39.9	36.2	30.7
Average	68.3	58.7	56.7	54.0	52.4	49.7	46.4	44.0	40.3	34.5
	Pore volume filled with washcoat (%)									
Average	0.0	14.0	17.0	20.9	23.2	27.2	32.0	35.6	41.0	49.4

[a] BW: bare wall without washcoat, OS: original R&D sample, N: reconstructed non-uniform washcoat distribution profiles

Table 5.3: Porosity values (ε) and corresponding fractions of pore volume filled (f_w) by the catalyst for all reconstructed uniform washcoat distribution profiles.

Sample ID:	**BW**	**U1**	**U2**	**U3**	**U4**
Section	**Porosity (%)**				
1	68.3	59.4	50.5	39.9	33.0
2	67.2	57.7	48.6	38.0	31.2
3	69.8	61.1	52.4	42.0	35.2
4	67.8	58.4	49.2	38.4	31.4
Average	68.3	59.2	50.2	39.6	32.7
	Pore volume filled with washcoat (%)				
Average	0.0	13.3	26.4	42.0	52.1

[a] BW: bare wall without washcoat, U: reconstructed uniform washcoat distribution profiles

In addition to porosity, another very important global descriptor for porous media revealed by the Blake-Kozeny correlation (see Eq. (5.8)) is the specific surface area S_0 defined in Eq. (5.3). The specific surface area decreases when the catalyst coating amount increases for both the uniform and non-uniform washcoat distribution profiles as shown in Figure 5.5. In addition, the specific surface area decreases more rapidly for a structure with a non-uniform washcoat distribution profile than for one with a uniform washcoat distribution profile for the same amount of washcoat. As

expected, this trend suggests that small pore channels are more impacted as the pore space is filled with a non-uniform distribution than with a uniform one, since they usually contribute much more to the specific surface area. Knowing the specific surface area and the porosity, the mean pore diameter could be evaluated using Eq. (5.4), as shown in Figure 5.6. A gradual decrease in the mean pore diameter is observed as the coating amount increases for a uniform distribution profile since adding more catalyst over the entire substrate tends to uniformly reduce the pore sections. On the other hand, the behaviour of the mean pore diameter as the coating amount increases for the non-uniform distribution profile is non-linear and non-intuitive. The mean pore diameter reaches a maximum when $f_w \leq$ ~30%. This can be explained by the fact that non-uniform filling of the pore volume closes the small pores first, which corroborates the findings for the specific surface area. As a result, the larger pores make a greater contribution to the mean value of the remaining pores, and the mean pore size increases up to a certain filling degree, after which the remaining large pores are gradually filled, leading to a gradual decrease in the mean pore size. The pore size distributions plotted in Figure 5.7 clearly confirm this explanation by showing that when $f_w \leq$ ~30%, only the small pores (i.e., those with diameters smaller than 20 μm) of the non-uniform profiles are impacted. On the other hand, all pore sizes are affected to a similar extent by the addition of washcoat in the case of the uniform profiles.

The structural properties of some of the virtual porous walls generated, particularly the non-uniform ones, thus behave non-linearly as the pore space is filled. This suggests that nonintuitive effects on ΔP and E_f may result from these characteristics. We shall return to this when we describe how filtration performance is affected by the addition of uniformly or non-uniformly distributed washcoat.

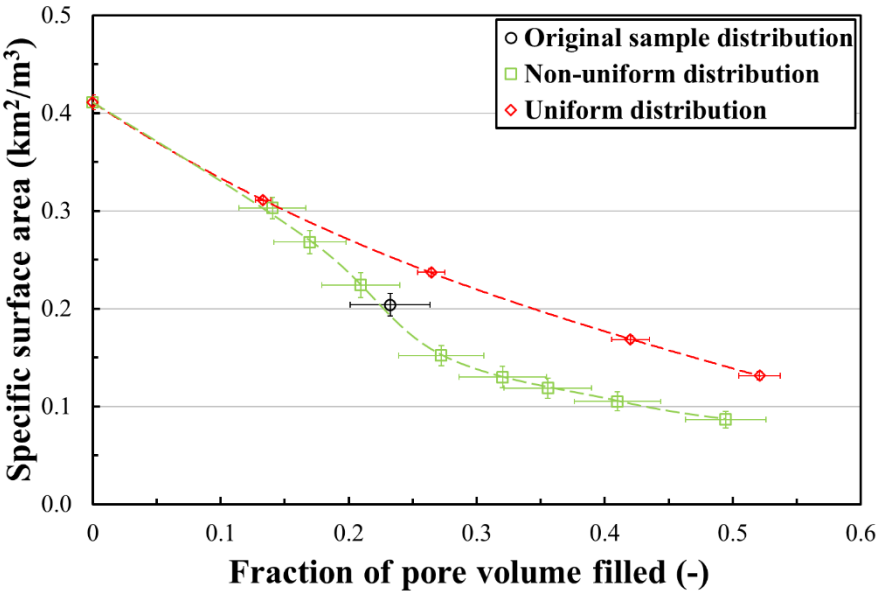

Figure 5.5: Comparison of specific surface areas (S_0) of the digitized structures as a function of the amount of washcoat (f_w) for the two washcoat distribution profiles, for all the reconstructed GPF porous wall structures. The dashed lines are a guide for the eye, and the error bars represent the standard deviations of the reported mean values for the four wall subdomains.

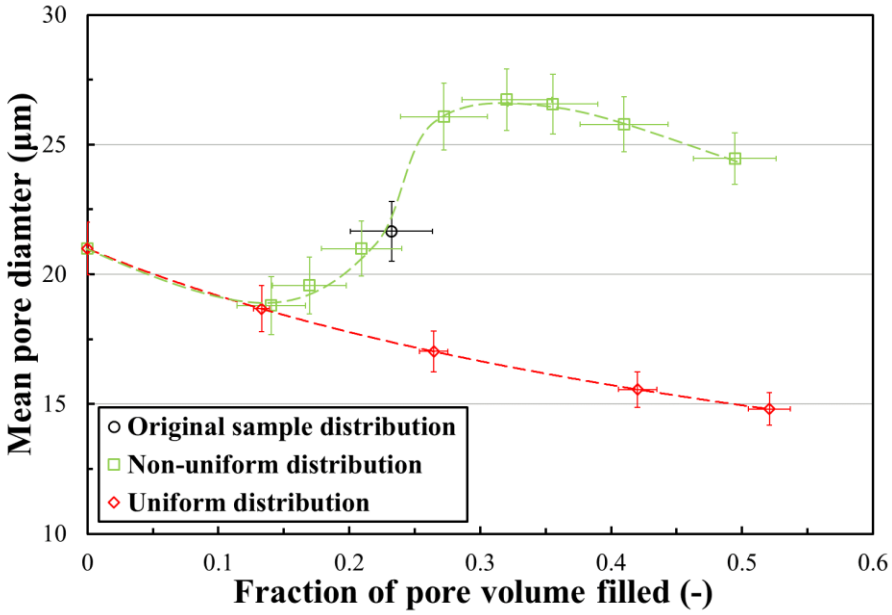

Figure 5.6: Comparison of mean pore diameters (d_w) as a function of the amount of washcoat (f_w) for the two washcoat distribution profiles, for all the reconstructed GPF porous wall structures. The dashed lines are a guide for the eye, and the error bars represent the standard deviations of the reported mean values for the four wall subdomains.

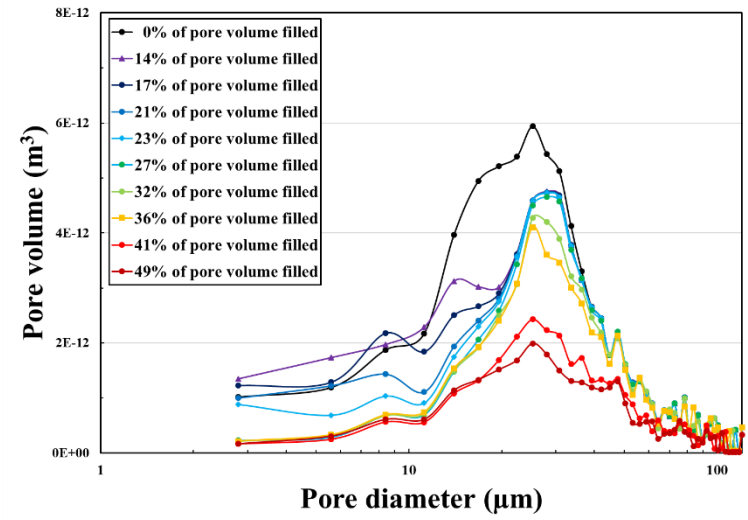

(a)

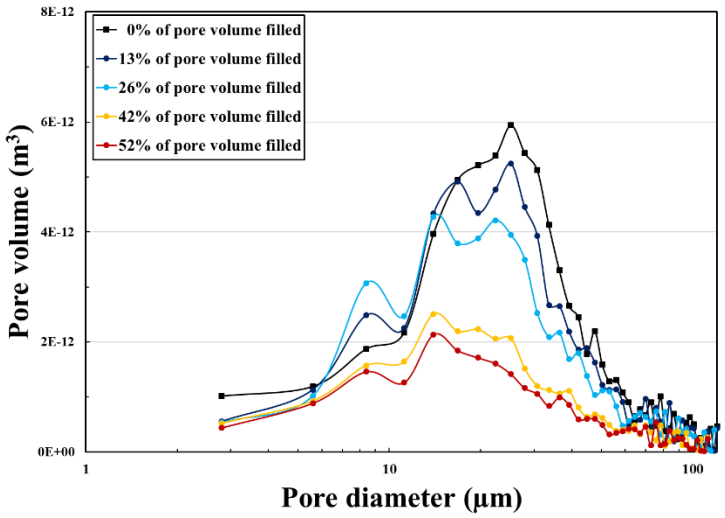

(b)

Figure 5.7: Comparison of pore size distributions calculated by the granulometry technique (using GeoDict®, (Soille 1999)) for a (a) non-uniform and (b) uniform washcoat distribution profiles in Subdomain 1 of the reconstructed GPF porous wall structures.

For the sake of completeness, we also provide in Appendix B two other statistical structural descriptors, namely the two-point probability and the lineal-path functions, for the two series of distribution profiles and all coating amounts.

5.3.2 Gas flows through the reconstructed structures

In this section, the accuracy and performance of the LBM code used to compute the flow field in the OS sample is first assessed. Then, the impact of various washcoat distribution profiles on the flow properties of the reconstructed porous walls is examined in detail.

5.3.2.1 Model assessment and computational performance

To assess the computations of the flow field through the reconstructed structures using the LBM code, the permeability of the four sections of the OS sample were compared to the results obtained with the FlowDict® module of the GeoDict® software using the SIMPLE-FFT Stokes solver and the predictions from the Blake-Kozeny correlation (i.e., Eq. (5.8)). The results are shown in Figure 5.8.

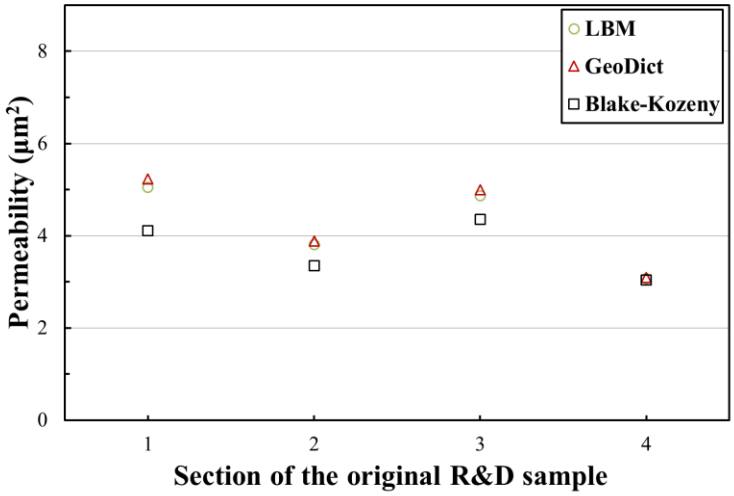

Figure 5.8: Comparison of permeability predictions by the LBM code, GeoDict® software, and the Blake-Kozeny correlation for the four subdomains (Figure 5.3) of the OS sample.

Keeping in mind that permeability is an extremely sensitive material property, there is good agreement between the different methods. The LBM code and GeoDict® give very similar permeability results, which lead to slightly higher permeability values than the predictions from the Blake-Kozeny correlation for three of the four porous wall subdomains analyzed. A detailed validation study of the LBM predictions reported here is provided in (Belot et al. Submitted (2020)).

The computational time of our LBM code for a 456×400×389-voxel porous wall subdomain was approximately 6 hours on 8 cores (2.67 GHz Intel Xeon X5650 Westmere processor). The simulations used approximately 3.5 GB of RAM. As permeability calculations only require steady state flow fields and as the LBM is intrinsically a transient flow solver, GeoDict® steady state flow solvers are efficient alternatives to the LBM in this context as the computational time of the SIMPLE-FFT Stokes solver was approximately 12 hours on 2 cores (2.5 GHz Intel Xeon E5-2430V2 processor) and used only 0.8 GB of RAM. However, the LBM code has effective distributed parallelization capabilities that allow it to tackle very large domains in a reasonable computational time. For example, Figure 5.9 presents the steady state flow field computed by the LBM code on the whole OS sample. The CPU time was only 2 hours on 100 cores for the 456×801×779-voxel domain size. It was not possible, however, to evaluate the parallel capabilities

of GeoDict® because of the limitations of our license. The LBM code was used for the reminder of the study.

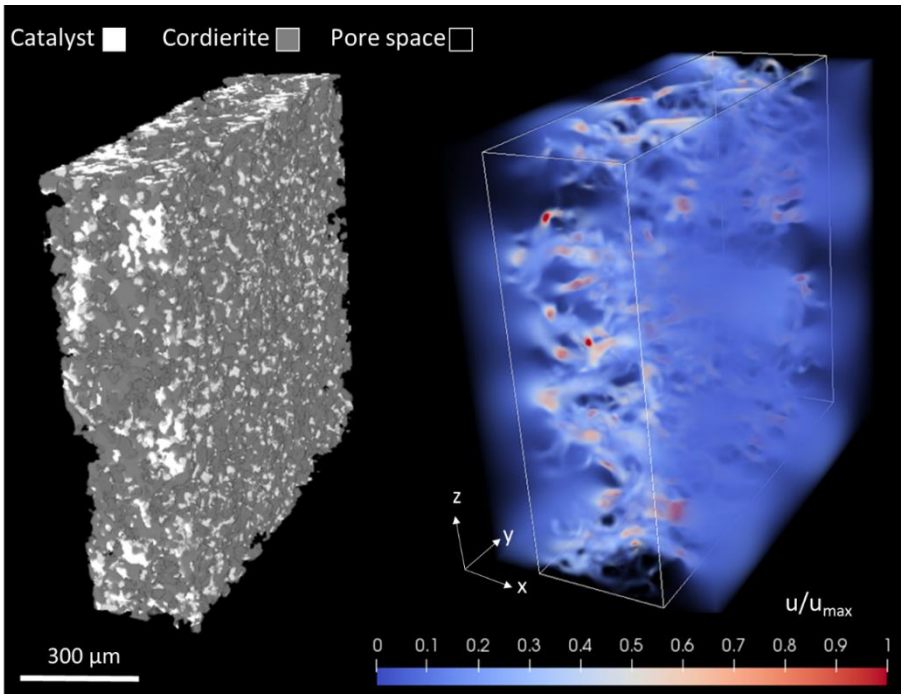

Figure 5.9: Structure (left) and flow field (right) in the original 456×801×779-voxel OS sample computed with the LBM code. The color scale represents the normalized gas velocity.

5.3.2.2 Permeability predictions

Having assessed the quality of our flow computations using the LBM code, we next explored the impact of the washcoat distribution profiles on permeability and pressure drop using the 56 structures characterized in Section 3.1. The average permeabilities of the four wall subdomains are plotted in Figure 5.10 for the uniform and non-uniform distribution profiles at the various coating amounts investigated.

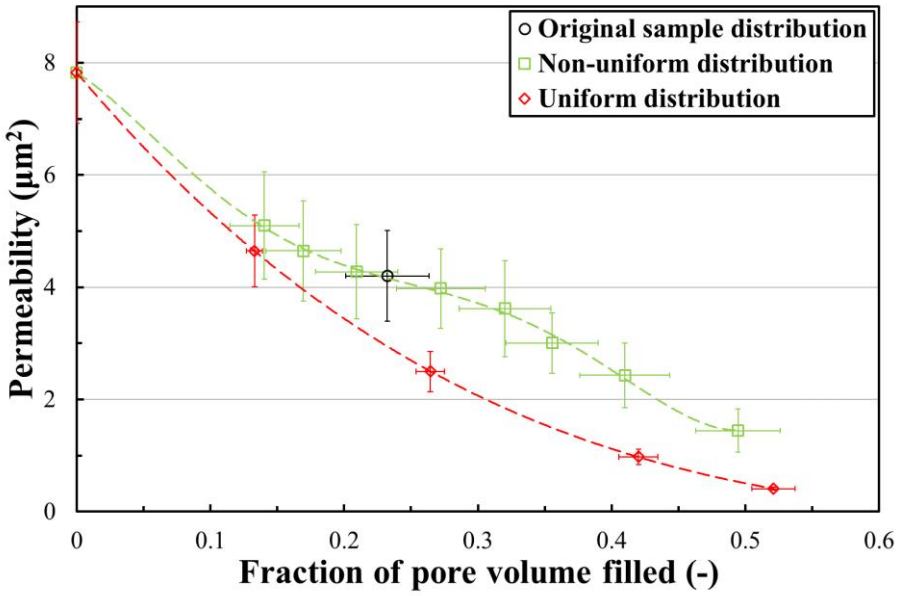

Figure 5.10: Comparison of the permeabilities (k) predicted by the LBM-based numerical model as a function of the amount of washcoat (f_w) for the two washcoat distribution profiles in the reconstructed GPF porous wall structures. The dashed lines are a guide for the eye, and the error bars represent the standard deviations of the reported mean values for the four wall subdomains.

As the pore volume was filled with an increasing amount of washcoat, the permeability decreases for both the uniform and the non-uniform distribution profiles, as expected. The addition of catalyst is detrimental to the gas flow, but this is to the benefit of better noxious gas conversions, which will be evaluated in a future work. A quadratic decrease in permeability as a function of the pore volume filled by the catalyst is found for the uniform distribution profile, whereas the decrease is less pronounced but more non-linear for the non-uniform distribution profile. The relative difference in permeability between the uniform and non-uniform catalyst profiles is up to 125% when $f_w \approx 50\%$. In the case of the uniform distribution, all flow pathways in the porous wall are affected by an increasing amount of washcoat so that they all narrowed to a similar extent. In the case of the non-uniform distribution, the relation between pore volume filled with catalyst and mean pore diameter is not linear, as seen in Figure 5.6. Initially, as more and more catalyst is added to the pore space, the small pores are plugged preferentially, as seen in Figure 5.7(a), leaving more

big pores and preferential pathways untouched such that the permeability is less affected by an increasing amount of catalyst. Interestingly, the trend for the non-uniform distribution profiles exhibited an inflection point near the OS data point (black open circle in Figure 5.10). In Appendix C, a comparison is made between the permeability predictions obtained in the present study and the ones from (Konstandopoulos, Kostoglou, and Vlachos 2006), showing that both the substrate and the type of washcoat non-uniformity can lead to somewhat different impacts on permeability.

5.3.2.3 Pressure drop predictions

For the sake of completeness and because it is of more practical use than permeability, Figure 5.11 presents the pressure drops through the reconstructed structures.

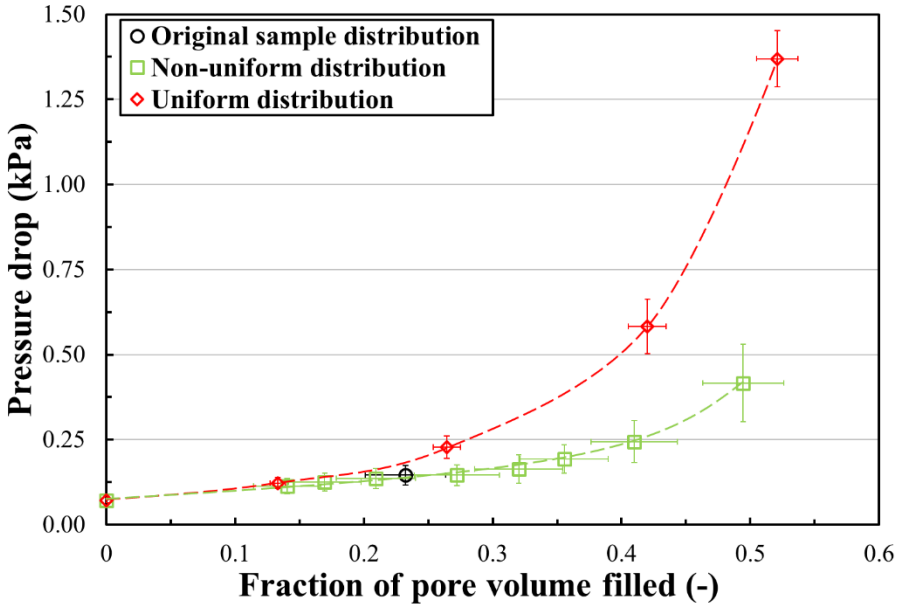

Figure 5.11: Comparison of the pressure drops (ΔP) predicted by the LBM-based numerical model as a function of the amount of washcoat (f_w) for the two washcoat distribution profiles in the reconstructed GPF porous wall structures. The dashed lines are a guide for the eye, and the error bars represent the standard deviations of the reported mean values for the four wall subdomains.

Results show a near-exponential increase in the pressure drop as the pore volume is filled with catalyst. Significant differences in pressure drop between the two sets of washcoat profiles are only

noticeable when f_w > ~20-25%, which corresponds roughly to amounts of washcoat greater than that used for the OS sample. When $f_w \approx 50\%$, a roughly 3-fold higher pressure drop is predicted with the uniform profile.

5.3.3 Soot capture by the reconstructed structures

In this section, the accuracy and performance of the commercial software GeoDict®, which was used for this part of the work, is first assessed. Then, the impact of various washcoat distribution profiles on the capture efficiency of the reconstructed porous walls is examined in detail.

5.3.3.1 Model assessment and computational performance

Obtaining appropriate capture efficiency data for the GPF porous wall alone is not an easy task as: (1) the overall capture efficiency of a GPF is a sum of several contributions from different origins (e.g. entrance effects, capture into channels through diffusion, porous wall microstructure,…) which are difficult to isolate independently of each other and are intrinsically multiscale, and (2) experimental work reported in the literature often lacks details regarding the exact geometry of these different parts of the GPF and/or the exact operating conditions (e.g. precise soot size and shape distributions), making it difficult to carry out detailed model validation at the wall scale. The validity of the predictions of the FilterDict® module was therefore here assessed using the detailed fibrous filter data published by Lee and Liu (Lee and Liu 1981) and the analytical correlations for fibrous filters provided in Gervais et al. (Gervais et al. 2015).

In the experiments of Lee and Lie (1981), moderately monodisperse aerosols were generated by dissolving a low vapour pressure substance such as DOP (di-octyl phthalate) in a volatile solvent such as alcohol. The mixture was heated and then cooled to obtain monodisperse spherical particles whose diameter could be controlled by adjusting the DOP concentration. An electrical particle detector was used to measure the aerosol concentration upstream and downstream from the filter and to thus retrieve E_f. Two types of fibrous filters were produced for these experiments: filter A, which was made of uniform 11.0 ± 1.06-µm diameter Dacron fibers, and filter B, which was made of uniform 12.9 ± 1.06-µm diameter Dacron fibers. Data from filters A and B, which had porosities within the range of porosities used for the GPF study, are here reported with three air velocities, i.e., 0.01, 0.03, and 0.1 m/s. Since the original filter structures were not readily available but there

was sufficient data to recreate them with a good degree of fidelity, corresponding 3D random fiber network structures were created using the FiberGeo® module of GeoDict®. The in-plane dimensions of the computational domain were 500 µm × 500 µm, and the filter thickness was adjusted to fit the reported values (i.e., 183 µm and 243 µm, respectively, for filters A and B). In addition, 200-µm and 100-µm buffers, respectively, were added upstream and downstream from the filter. The voxel resolution was set at 0.5 µm.

Figure 5.12 compares the numerical capture efficiency predictions as a function of particle diameter with the experimental data from Lee and Liu (1981) and analytical correlation predictions from Gervais et al. (2015). Although no information was provided on the experimental uncertainty, overall the trends predicted are all in relatively good agreement with those observed experimentally and analytically with respect to the effect of air velocity and soot particle diameter. Nonetheless, numerical simulations tend to overestimate, by a constant bias, the capture efficiency obtained from experimental data and analytical correlations. A detailed analysis is carried out in Appendix D to determine this bias and a corresponding correction is proposed, although it is not applied in the remaining of this paper.

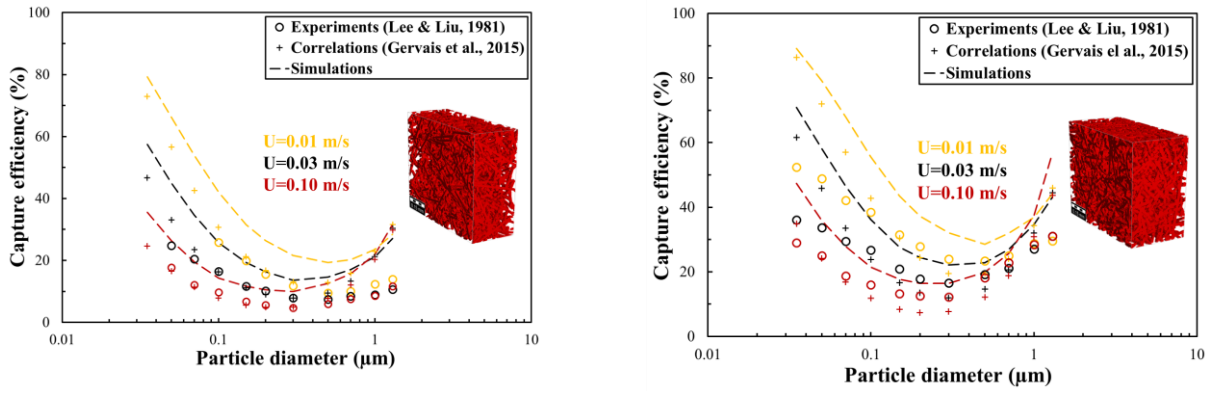

(a) (b)

Figure 5.12: Comparison between our numerical predictions and experimental data from Lee and Liu for the capture efficiency of (a) fibrous filter A (ε=70.1%, L=183 µm) and (b) fibrous filter B (ε=58.0%, L=243 µm). The insert in each graph represents the reconstructed fibrous structures used for the simulations.

Despite the reported discrepancy in capture efficiency, the overall trends appear to be well predicted, which is satisfactory in the context of a study that focuses on the relative differences between clean porous wall microstructures. In fact, the actual magnitude of the capture efficiency can be affected by many factors. In the case of soot particles in a cordierite-based particulate filter, the capture efficiency is actually expected to be underestimated by the current methodology for two main reasons: (1) as soots are non-spherical clusters of primary particles, assuming spherical particles will tend to underestimate capture, and (2) as shown recently by (Kočí 2019), substantial soot capture by inertial impaction may take place at the wall surface due to the sudden 90° change in flow direction going from the channel into the wall. Assuming a flow perpendicular to the wall surface can indeed misrepresent the inlet flow condition and thus potentially reduce the capture efficiency, although most of the soot sizes in a GPF are generally less than 200 nm and therefore the number of inertial particles may in fact be limited. A measurement campaign is currently being carried out to validate the model in the PF context.

Lastly, in terms of computational requirements, the computational time for each simulation done with GeoDict® on the 456×400×389-voxel domains for tracking 250 000 particles (25 000 particles for each of the 10 particle diameters investigated) was approximately 6 hours on 2 cores (2.5 GHz Intel Xeon E5-2430V2 processor).

5.3.3.2 Soot capture efficiency predictions

The soot capture efficiency of the 56 generated structures for various soot sizes was computed using the FilterDict® module of the commercial software GeoDict®. Noticeable differences in the impact of increasing coating amount between the two washcoat uniformity profiles on the capture efficiency can be seen in Figure 5.13.

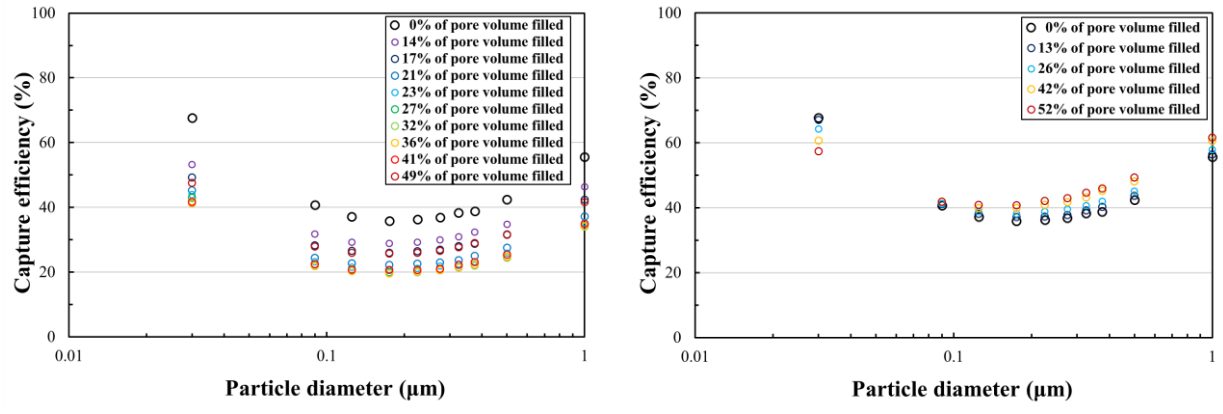

(a) (b)

Figure 5.13: Soot capture efficiency (E_f) as a function of soot particle diameter (d_p) for a (a) non-uniform and (b) uniform washcoat distribution profiles in Subdomain 4 of the reconstructed GPF porous wall structures.

In the case of a non-uniform profile, capture efficiency is degraded more or less evenly throughout the range of particle diameters while increasing coating amount in the range 0% $\leq f_w \leq$ 41%. This decrease in capture is somewhat surprising and will be explained in more detail later in this section. Beyond this amount of washcoat, the capture starts to increase sharply (as evidenced by the data points at f_w= 49%). For the uniform deposition, the capture efficiency of the very small particles is degraded by an increasing coating amount, whereas a reverse trend is observed for larger particles. The results of Figure 5.13 show also a minimum capture efficiency at a particle mobility diameter of approximately 200 nm, which is a common value in the PF context (Joshi and Johnson 2018).

For the remainder of the paper, unless stated otherwise, the results are reported in terms of the minimum capture efficiency (i.e., at the most penetrating particle size or MPPS), hereafter referred to as E_f for conciseness. Figure 5.14 presents the variation of E_f averaged over the four subdomains (Figure 5.3) for the two sets of profiles, as a function of the pore volume filled.

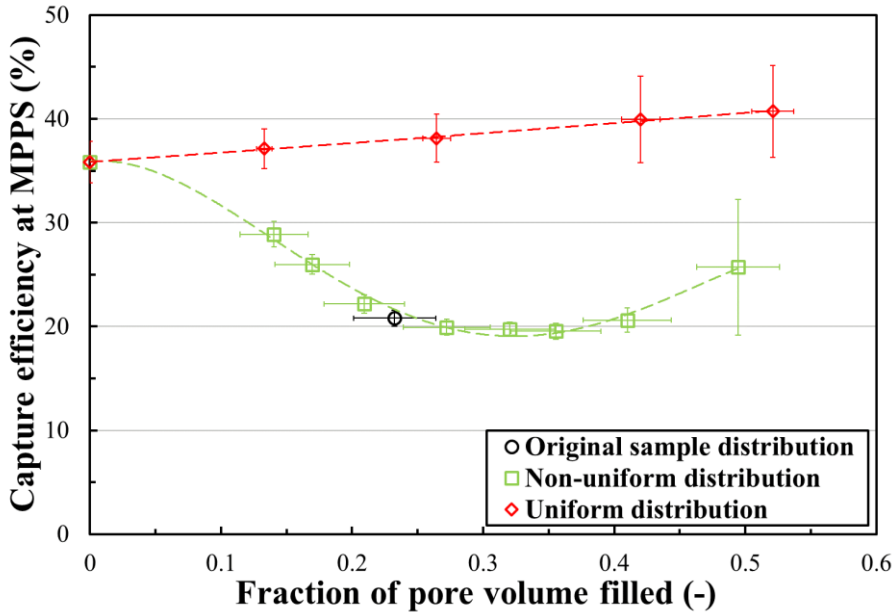

Figure 5.14: Comparison of soot capture (E_f) at MPPS as a function of the amount of washcoat (f_w) for the two washcoat distribution profiles in the reconstructed GPF porous wall structures. The dashed lines are a guide for the eye, and the error bars represent the standard deviations of the reported mean values for the four wall subdomains (Figure 5.3).

The range of efficiency values is comparable to those in the literature for clean coated GPFs (Joshi and Johnson 2018). Nonetheless, similarly to what has been reported in Figure 5.13, two different soot capture efficiency behaviours can be observed at MPPS as the pore space is filled with increasing amounts of washcoat depending on the uniformity of the washcoat distribution profile. In the case of a uniform distribution, as expected, E_f increased gradually as more and more catalyst is added to the pore space. This behaviour can be explained by the gradual decrease in all pore diameters as shown by the mean pore diameter and pore size distribution variations in Figure 5.6 and Figure 5.7(b). As each channel being smaller, the soot particles transported by the air flow through the filter wall are more easily captured by interception. At the same time, as evidenced by the decrease in capture at small particle sizes in Figure 5.13(b), the capture by diffusion slightly decreases as a result of the increase of interstitial velocity (as the superficial velocity is kept constant). Now, for a non-uniform coating profile, similarly to what has been reported in Figure 5.13(a) and again somewhat surprisingly, the soot capture efficiency at MPPS decreases when f_w

is increased from 0% to ~30%, and then begins increasing beyond this point. At first glance, this result appears to be counter-intuitive as higher soot capture is normally expected when filter porosity decreases (see (Lee and Gieseke 1979b; Lee and Liu 1981)), although some contradictory results have also been reported by others (Liu et al. 2018). To date, no comprehensive explanation for this phenomenon can be found in the literature, but this will be clarified in the following.

The great advantage of numerical simulations is that they can be used to correlate filtration performance with the flow and structural characteristics of the porous medium in a way that is much more detailed than what can be achieved experimentally. To determine the detailed mechanisms involved in the decrease in filtration performance with an increase in the amount of washcoat, visualizations of the flow field through the same porous wall section but with two different amounts of washcoat (low and high coating amounts) for the uniform and non-uniform distribution profiles are presented in Figure 5.15, including a region of particular interest circled in yellow dashes. The flow pathways through this region are very similar, ranging from a low coating amount to a high coating amount when a uniform distribution of washcoat is used. Only the magnitude of the velocity increases as the pores are filled with more washcoat because every pore channel section decreases with an increasing amount of catalyst. In the case of the non-uniform distribution profile, the velocity magnitude is also affected by an increasing amount of washcoat, so are the flow paths, as shown by the disappearance of many small flow channels in the area of interest. This is caused by the complete obstruction of a large number of smaller channels as the amount of catalyst increases, redirecting the flow to larger channels that are not completely clogged and reinforcing the flow channelling effect inherent to such complex porous structures. This observation can provide a good explanation for the decrease in soot capture in the range $0\% \leq f_w \leq$ ~30% for the non-uniform profiles in Figure 5.14. Indeed, as the amount of washcoat increases in the range $0\% \leq f_w \leq$ ~30%, the flow is redirected to larger pore channels in which interstitial velocities are increasing (as the superficial velocity is kept constant and ε is decreasing). As a result, the transported soot particles have less chance to collide with the solid surface of the porous medium both by interception and diffusion, leading to a decrease in E_f. This is also evidenced in Figure 5.13(a) by the decrease in both diffusion- (below the MPPS) and interception-driven (above the MPPS) capture efficiency values. Beyond these coating amounts, as all small channels are

finally clogged, the size of the remaining larger channels gradually decreases, leading to a sharp increase in capture efficiency through the interception mechanism.

Furthermore, a close examination of the pore size distributions in Figure 5.7 confirms the explanation provided by the visual inspection of the flow fields. As mentioned in Section 3.1, the pore size distributions showed that when $0\% \leq f_w \leq 30\%$, the small pores (i.e., with diameters lower than 20 µm) of the non-uniform profiles are preferentially affected leading to a redirection of the flow to larger, but less capture-efficient channels, whereas all pore sizes are reduced to a similar degree by the addition of washcoat in the case of uniform profiles and thus leading to a gradual increase in soot capture in this case. In addition, when $f_w > 30\%$, larger pores also begin to be affected, which can be seen by the corresponding decrease in the mean pore diameter shown in Figure 5.6. This corresponds precisely to the onset of the gradual increase in soot capture observed beyond this point in Figure 5.14. These findings clearly show that there is a very close relationship between filtration performance and the structural characteristics of the porous medium and the impact of the non-uniform washcoat distribution investigated in the present study. However, caution should be exercised in over-generalizing the results in Figure 5.14, as they have been obtained in specific conditions, i.e. in a clean filter for a given type of non-uniform washcoat distributions under constant flow rate conditions. In fact, in light of these results, the contradictory results reported in the literature regarding the trend in capture efficiency for a non-uniform profile may be explained by different factors: 1) the structural characteristics of the base substrate, 2) the coating non-uniformity and 3) the conditions under which the experiments were carried out (e.g. constant flow velocity or constant pressure drop, presence of soot clogging,…). Here, the numerical experiments were conducted at constant flow rate, which leads to a decrease in capture by diffusion as the interstitial velocity increases for an increasing amount of washcoat. At the same time, experiments conducted at constant pressure drop are expected to result in greater capture by diffusion while they may not show an overall decrease in capture efficiency.

On the basis of capture efficiency results discussed above, it follows that the uniform profiles deposited on the cordierite are up to twice as efficient as the non-uniform profiles, particularly when $f_w \leq 30\%$. However, to be able to judge the intrinsic performance of a filter medium, it is

common in the field of air filtration to relate capture efficiency to the pressure drop using the quality factor. This is what we will analyze next.

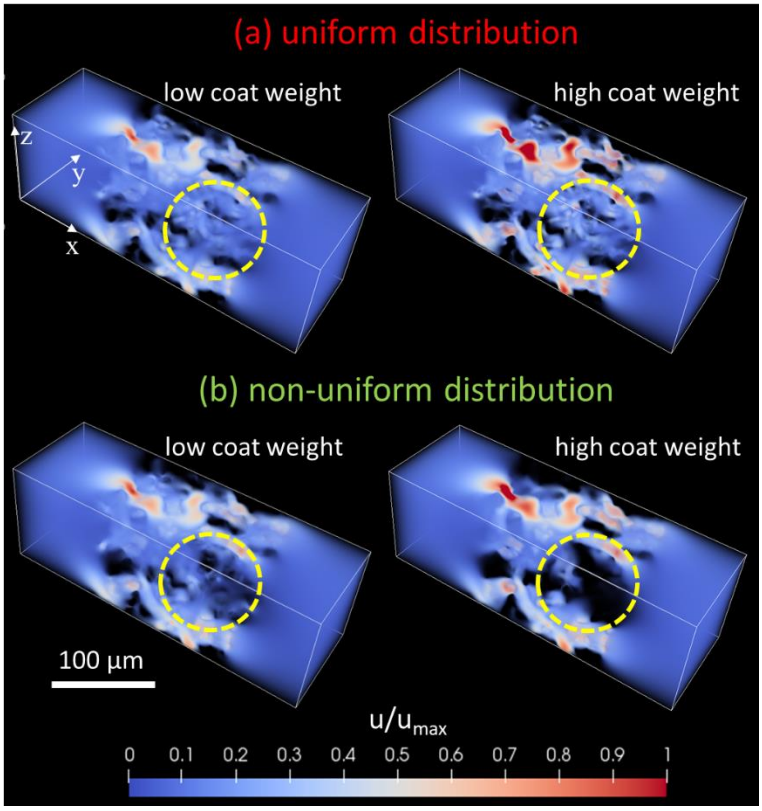

Figure 5.15: Close-up visualizations of the normalized flow field for the same 456×100×100-voxel porous wall section with two different coating amounts (low and high) and for the two washcoat distribution profiles (uniform and non-uniform). Low and high coating amounts correspond to f_w = 14.0% and 27.2% and f_w = 13.3% and 26.4% for the non-uniform and uniform distribution profiles, respectively. The dashed yellow circles represent regions of interest, in which a significant change in flow pathways takes place as the washcoat profile is changed.

5.3.3.3 Overall filtration performance of the reconstructed structures

As previously seen, on the one hand, structures with a non-uniform washcoat distribution presented a lower pressure drop than structures with a uniform washcoat distribution at every washcoat amount studied. On the other hand, soot capture was greater for all structures with a uniform

washcoat distribution at a given coating amount. Comparing the two distribution profiles in terms of filtration performance is thus not straightforward if one does not resort to the quality factor as defined in Eq. (5.16). Figure 5.16 presents variations of Q_f as a function of coating amount for the two washcoat distribution profiles.

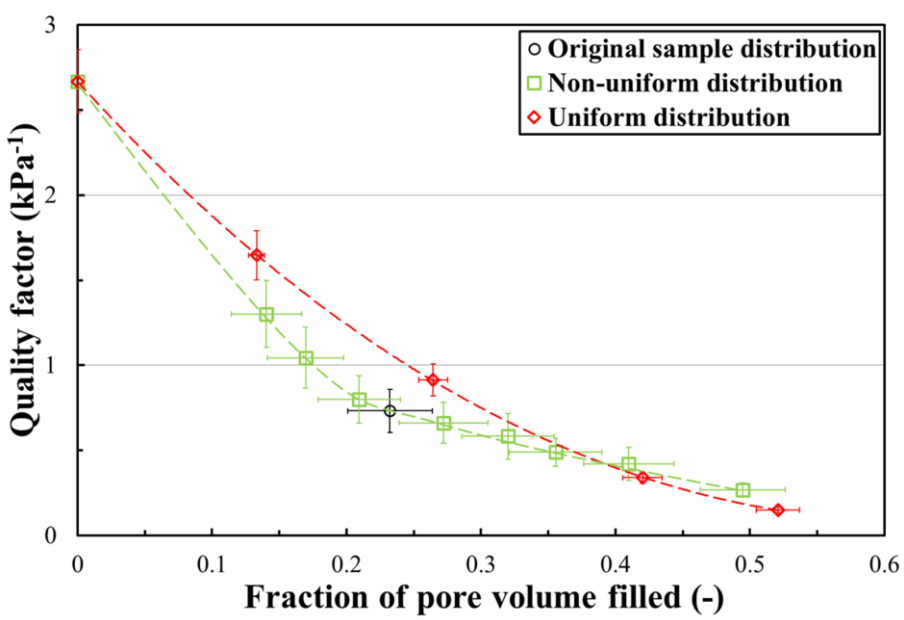

Figure 5.16: Comparison of quality factors (Q_f) as a function of the amount of washcoat (f_w) for the two washcoat distribution profiles in the reconstructed GPF porous wall structures. A higher Q_f corresponds to a better filtration performance. The dashed lines are a guide for the eye, and the error bars represent the standard deviations of the reported mean values for the four wall subdomains (Figure 5.3).

The first striking result is that the filtration performance of the porous wall decreases for both washcoat profiles investigated as the coating amount is increased, meaning that the addition of a catalyst for reducing noxious gases is detrimental to the filtration performance of the cordierite substrate. This decrease is quadratic for the uniform deposition profiles throughout the coating amount range investigated. On the other hand, the decrease for the non-uniform deposition profiles is also quadratic, albeit only when $f_w \leq$ ~20% (i.e., up to approximately the OS washcoat profile) and is initially significantly steeper than the trend for the uniform deposition profiles but becomes linear thereafter. Overall, the uniform washcoat deposition profile gives a better filtration

performance than the non-uniform deposition profile when $f_w \leq$ ~40%. Beyond this level, no significant advantage to using a uniform deposition is observed and, in fact, the non-uniform deposition profile tested performed slightly better. The greatest relative difference between the two deposition profiles peaks at 50% when $f_w \approx 20\%$. In addition, a 30% improvement in Q_f could be expected if the OS structure had been manufactured with a uniform washcoat deposition profile. In this regard, these predictions demonstrate how this type of modelling may help GPF manufacturers determine an optimum trade-off between coating amount, filtration performance and catalytic conversion, and help design filters with the best washcoat distribution profile.

5.4 Conclusion

To shed light on the impact of the amount of catalyst and deposition uniformity of the porous wall on the filtration performance of clean catalyst-coated GPFs, a three-step numerical model was developed to (1) reconstruct representative volumes of a GPF porous wall based on X-ray computed tomography data and to create artificial uniform and non-uniform catalyst depositions in its pore space using novel erosion-dilation procedures, (2) compute the permeability and pressure drop of the reconstructed structures by solving the flow field using the LBM, and (3) predict the soot capture efficiency of the reconstructed structures by solving the Langevin equation using GeoDict® software. The accuracy of the model predictions and thus the soundness of the numerical methodology was also assessed using data and correlations from the literature. The impacts of the amount of washcoat and the deposition profiles on permeability, pressure drop, soot capture efficiency, and quality factor of the filter medium were investigated in a systematic way and were correlated to the structural characteristics of the reconstructed media (particularly the mean pore diameter and the pore size distribution). To our knowledge, this is the first time that such a detailed investigation has been conducted.

Despite a significantly higher pressure drop, it was found that a uniform washcoat distribution throughout the clean GPF wall resulted in significantly better filtration performance than a non-uniform washcoat distribution in terms of soot capture efficiency (up to 100% improvement) and quality factor (up to 50% improvement) for up to 40 % of pore volume filled with catalyst. Interestingly, as previously reported by some literature data (Liu et al. 2018; Joshi and Johnson 2018), our numerical results showed that increasing the amount of washcoat can counter-intuitively

result in a decrease in soot capture if it is non-uniformly deposited in the pore space as this leads to a strengthening of flow channeling. This was revealed by detailed visualizations of the flow field and analysis of the pore size distribution. However, caution should be exercised when extrapolating the findings reported here to all non-uniform washcoat deposition profiles and to all ceramic substrates. These findings call for a more thorough investigation of various forms of non-uniform and ceramic substrates with a focus on structures, for which a process or device exists to produce them.

Lastly, the present study is a first step toward building a more comprehensive model that not only predicts GPF wall filtration performance but also the chemical conversion of noxious gases by the catalyst, and that will ultimately provide more information on the effectiveness of washcoats. A more comprehensive model that makes use of an LBM scheme for solving an advection-diffusion-reaction equation for the GPF porous wall will be presented in an upcoming paper (Belot, Vidal, Greiner, et al. 2020). Once fully developed, the model will become a valuable design tool that will provide guidance to catalyst-coated GPF manufacturers as well as insights into why specific catalyst coatings perform better than others.

5.5 Acknowledgements

This research was supported by the Natural Sciences and Engineering Research Council of Canada through a Strategic Partnership Grant (STPGP-493797-16) and a Grant from the Collaborative Research and Training Experience (CREATE-481695-2016) program in Simulation-based Engineering Science (Génie Par la Simulation). The authors would also like to thank Calcul Québec/Compute Canada for the computational resources and support provided.

5.6 Appendix A – Definition of a representative elementary volume for the reconstructed structures

To ensure that the domain size is large enough so as to not influence the permeability predictions and that it can thus be considered as a Representative Elementary Volume (REV) of the pore space, the Brinkman screening length, defined as the distance over which velocity disturbances caused by an individual flow obstacle decay to the bulk fluid velocity, is commonly used (Clague and Phillips

1997). This length scale is equal to the square root of Darcy's permeability (i.e., $\sqrt{k_D}$). To determine a permeability measurement independent of the domain size, the Brinkman screening length criterion prescribes that $\ell \gg \sqrt{k_D}$, where ℓ is the domain characteristic dimension. For all the structures investigated, knowing that $0.4\ \mu m^2 \leq k_D \leq 8\ \mu m^2$, $\ell \gg \sim 3\ \mu m$ would thus be required according to this criterion. Partitioning the OS sample wall structure into four subdomains (as in Figure 5.3) and up to 16 subdomains would thus easily fulfill this requirement as 16 subdomains would result in $\ell \cong 200\ dx \approx 250\ \mu m$. To further verify that the number of subdomains does not influence permeability, a comparison between the mean permeability computed on 4, 9, and 16 subdomains with the mean permeability computed over the entire wall structure has been carried out and is presented in Figure 5.17. The results show a slight increase in the discrepancies with respect to the number of subdomains, i.e., 2.6%, 7.5%, and 11.0% for 4, 9 and 16 subdomains, respectively, as well as an increase in the variability from subdomain to subdomain, as shown by the standard deviations plotted as error bars. The increase in discrepancies can be attributed to the symmetric boundary conditions added at the lateral boundaries of the subdomains created. The increase in variability from subdomain to subdomain can be attributed to the large-scale heterogeneity of the cordierite structure, which is well above the Brinkman screening length. As such, this result clearly underlines the fact that the Brinkman screening length criterion is a necessary condition but not a sufficient one for guaranteeing the domain size independence of the flow computation for such heterogenous porous media. Another important criterion that should be taken into consideration is the mean pore size, which in this study ranges from 10 to $30\ \mu m$ (see Figure 5.6). Also, every partition considered for this REV study resulted in subdomains that were at least one order of magnitude larger than the mean pore size. Nevertheless, the partition of the OS sample domain into four subdomains seems to be a good trade-off between ease of computation and accuracy, which is why it was chosen in the present study.

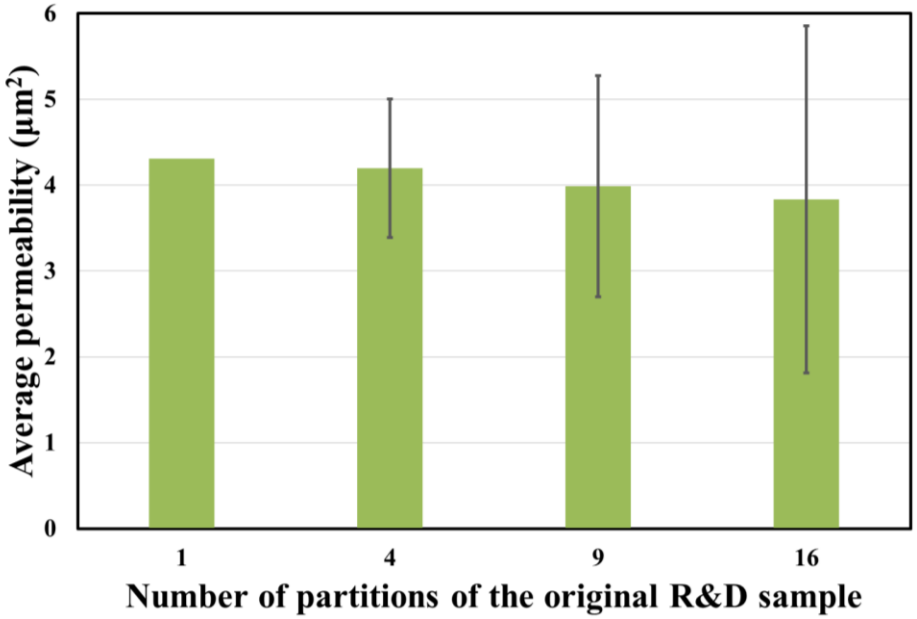

Figure 5.17: Comparison of the average permeabilities obtained for different partitioning schemes of the whole OS sample. The error bars represent the standard deviations of the permeability values computed on all the partitions for a given partitioning scheme.

5.7 Appendix B - Correlation functions of the reconstructed structures

Additional statistical structural descriptors, namely the two-point probability function and the lineal path, are provided here. They may help reconstruct the artificial structures created in this work using the simulated annealing technique (Matte-Deschênes et al. 2016), for instance, to enable future use of these structures by any interested reader. Both correlation functions were computed on the solid phase (i.e., cordierite + catalyst) of each structure reconstructed from Subdomain 1 of the OS sample.

The probability that n points at positions $(x_1, x_2, \ldots, x_n)$ in the medium are in phase i is denoted by ${S_n}^i$. Here, we only considered two phases, i.e., the solid phase (cordierite + catalyst, with $i = 1$) and the void phase (with $i = 0$). Based on this definition, for an isotropic medium, the two-point probability function is given by:

$$S_2{}^i(r) = \frac{n_i(r)}{n_t(r)} \tag{5.17}$$

where $n_i(r)$ and $n_t(r)$ are, respectively, the number of pairs of phase *i* voxels and the total number of pairs of voxels of any phase separated by distance *r*. Interestingly, both global descriptors ε and S_0 can be obtained from the two-point probability function for any 3D digitized porous medium as $\varepsilon = S_2{}^0(0)$ and $S_0 = -6\frac{dS_2{}^0}{dr}(0)$ (Yeong and Torquato 1998b, 1998a). In addition to the two-point probability functions, another spatial correlation function that is very useful for characterizing porous media is the lineal-path function given by (Torquato 2002):

$$L^i(r) = \frac{m_i(r)}{m_t(r)} \tag{5.18}$$

where $m_i(r)$ and $m_t(r)$ are the number of segments of length *r* wholly fitting in phase *i* when randomly thrown into the sample and the total number of fitting attempts, respectively. This correlation function provides interesting information on the connectiveness of phase *i* in the structure and can serve for reconstruction algorithms (Havelka, Kucerova, and Sykora 2016; Torquato 2002). In the present study, the $S_2{}^i(r)$ and $L^i(r)$ functions were calculated using a custom-written program based on a procedure described in the literature (Torquato 2002).

The two-point probability and lineal-path functions calculated in a direction perpendicular to the flow in the GPF porous wall structures reconstructed from Subdomain 1 for the uniform and non-uniform deposition profiles with various amounts of washcoat are presented in Figure 5.18 and Figure 5.19.

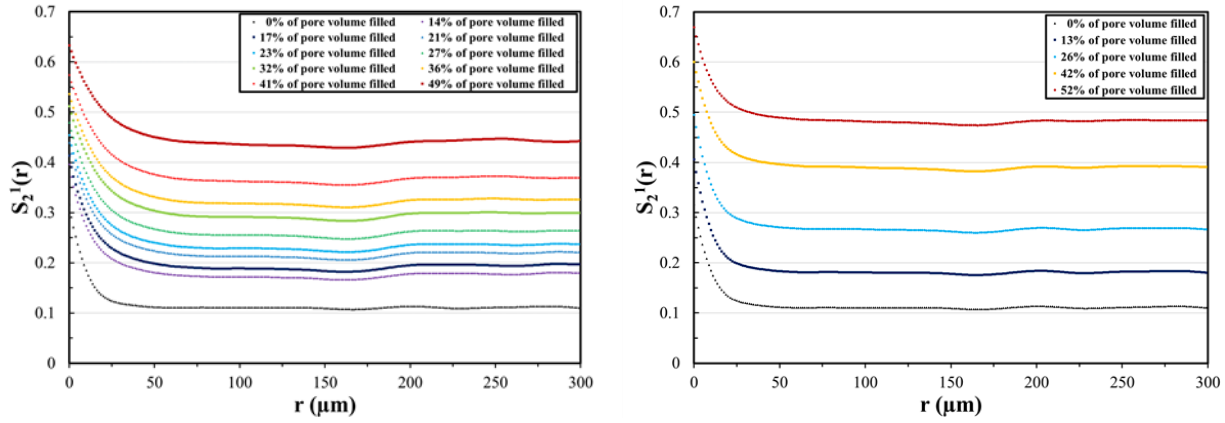

(a) (b)

Figure 5.18: Two-point probability functions calculated for a (a) non-uniform and (b) uniform washcoat distribution profiles of the GPF porous wall structures reconstructed from Subdomain 1 of the OS sample.

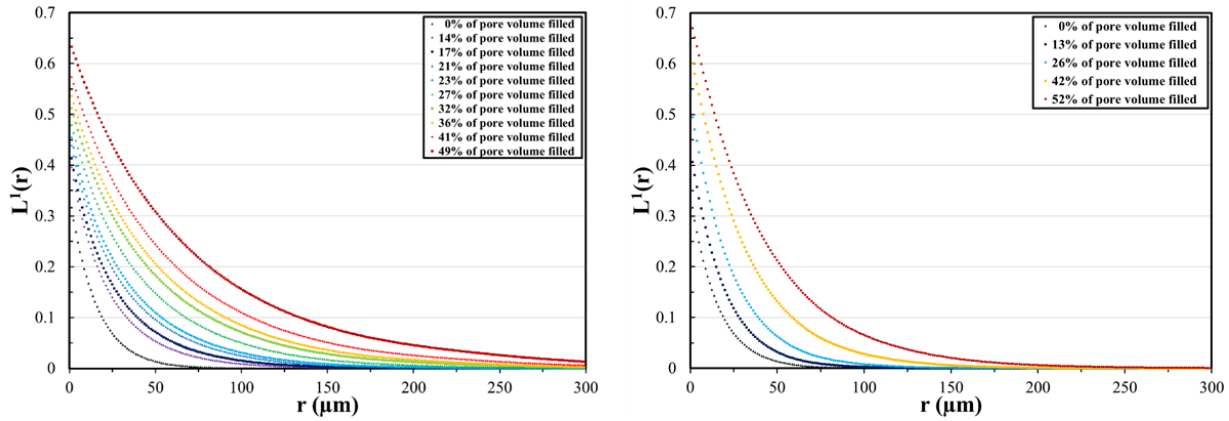

(a) (b)

Figure 5.19: Lineal-path functions calculated for a (a) non-uniform and (b) uniform washcoat distribution profiles of the GPF porous wall structures reconstructed from Subdomain 1 of the original OS sample.

5.8 Appendix C - Comparison of the obtained permeability trends with literature data

Although the SiC-based ceramic substrate used by Konstandopoulos et al. (Konstandopoulos, Kostoglou, and Vlachos 2006) was structurally different, and although the characteristics of the non-uniform washcoat depositions were not reported, a qualitative comparison with their results was attempted in Figure 5.20, which presents the trends obtained in terms of normalized permeability as a function of the amounts of washcoat for the uniform and non-uniform distribution profiles reported together with those presented in Figure 5.10. The SiC-based structures with uniform distributions of washcoat displayed similar quadratic decreases in permeability as a function of the amount of washcoat deposited on the bare ceramic. Note that while the trends are similar, they are not identical as the bare substrate can obviously play a determining role. In addition, while both studies reported a smaller decrease in permeability as a function of the amount of washcoat for the non-uniform washcoat profiles than for the uniform ones, the difference between the uniform and non-uniform distribution profiles reported by Konstandopoulos et al. is much more pronounced than the one obtained in the present study. In comparison, the decrease in permeability for the non-uniform profiles with respect to the permeability of the bare substrate was actually more limited (~ 20 % at $f_w = 30$ %) whereas it is approximately 50% in our numerical experiments for the same amount of washcoat. This difference can be attributed to the nature of the non-uniformity created, which unfortunately was not reported by the authors. Indeed, while there is only one uniform profile at a given coating amount on a given ceramic substrate, there is a quasi-infinite number of possible non-uniform profiles. Some might be better than others, although not all of them are necessarily achievable in practice. It should be remembered that, in the present study, the non-uniformity of the OS sample was decreased or amplified using an erosion-dilation algorithm. This created non-uniform profiles that were more permeable that their uniform counterparts. However, other types of non-uniformity could possibly have more or less impact. As already suggested, in addition to the nature of the non-uniformity, the magnitude of the impact may be also strongly influenced by the ceramic structure used as a substrate.

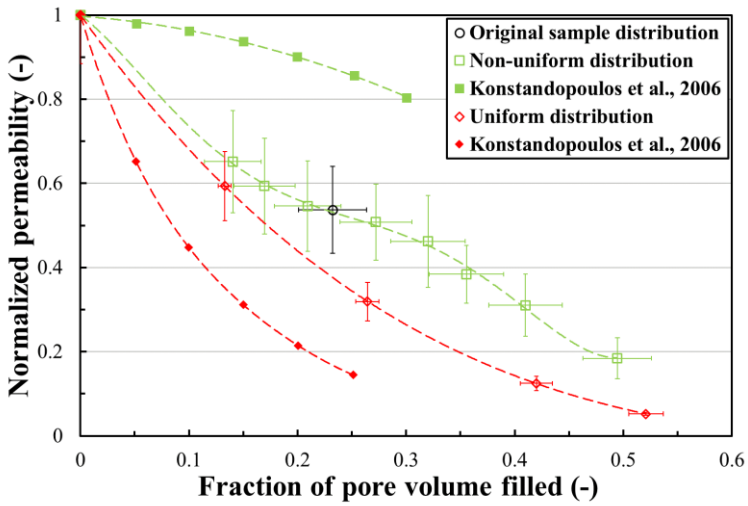

Figure 5.20: Comparison of permeabilities (normalized to the permeability of the bare wall) as a function of the amount of washcoat for the two washcoat distribution profiles as predicted by the proposed model and by (Konstandopoulos, Kostoglou, and Vlachos 2006). The dashed lines are a guide for the eye, and the error bars represent the standard deviations of the reported mean values for the four wall sections.

5.9 Appendix D – Discrepancy in filtration efficiency predictions between experiments and simulations

As noted in Section 3.3.1, there appears to be a constant bias between experimental and numerical predictions of capture efficiency for the partial experimental data set presented (i.e., for filters having porosities in the range of porosities used in the GPF study). In this appendix, an attempt is made to determine this bias for the entire data set from Lee and Liu (1981). It is possible to show that the following simple expression can be used to correct the capture efficiency predictions for a constant bias:

$$E_{f,corr} = 1 - P_{p,sim}^{\alpha} = 1 - \left(1 - E_{f,sim}\right)^{\alpha} \tag{5.19}$$

where $E_{f,corr}$ and $E_{f,sim}$ are, respectively, the corrected and originally computed capture efficiencies, $P_{p,sim}$ is the corresponding particle penetration and α is the correction factor. A minimization of the mean square difference between numerical and experimental data for the 11 filter configurations and operating conditions reported in Lee and Liu (1981) is carried out by varying systematically the correction factor through a list of possible fractions defined as $\alpha \in \left\{\frac{1}{2}, \frac{4}{7}, \frac{8}{13}, \frac{2}{3}, \frac{8}{11}, \frac{4}{5}, 1\right\}$. Figure 5.21 shows that a correction factor of $\frac{2}{3}$ leads to the best agreement between simulations and experiments bringing the mean relative difference for the entire data set from 40.7 % down to 17.0 %. Figure 5.22 shows the excellent improvement in the agreement between numerical, experimental and analytical predictions once the $\frac{2}{3}$ correction factor is applied.

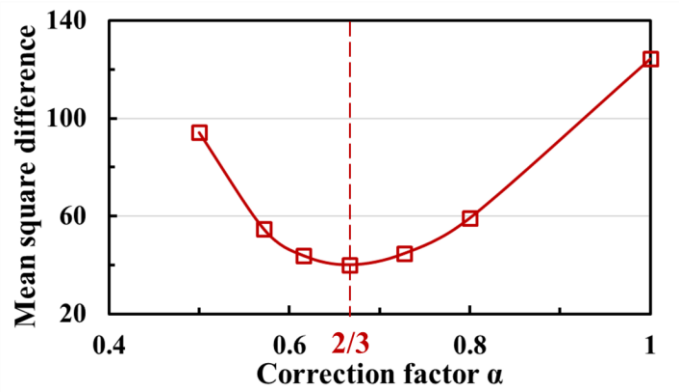

Figure 5.21: Mean square difference between numerical calculations using GeoDict® and experimental data from Lee and Liu (1981) and calculated on the 11 filter configurations.

Although further simulations and experiments would be required to identify the exact cause of this correction factor, it is interesting to point out that Yeong and Torquato (Yeong and Torquato 1998b, 1998a) reported an inherent overestimation of S_o for a voxelized porous structure, such as the ones used in this study, by a constant factor of $\frac{3}{2}$ because of the staircase-like fractal nature of such surface representation. As the single collector efficiency (i.e. $\beta\eta$ in Eq. (5.10)) is proportional to

S_o (through d_c), an overestimation of $\frac{3}{2}$ of the single collector efficiency could be expected and a correction of analytical predictions by a $\frac{2}{3}$ factor would thus be required. However, it is not yet clear how the fractal nature of the pore space would influence the numerical solution of the Langevin problem such that a constant bias would result, and this could be the result of a mere coincidence.

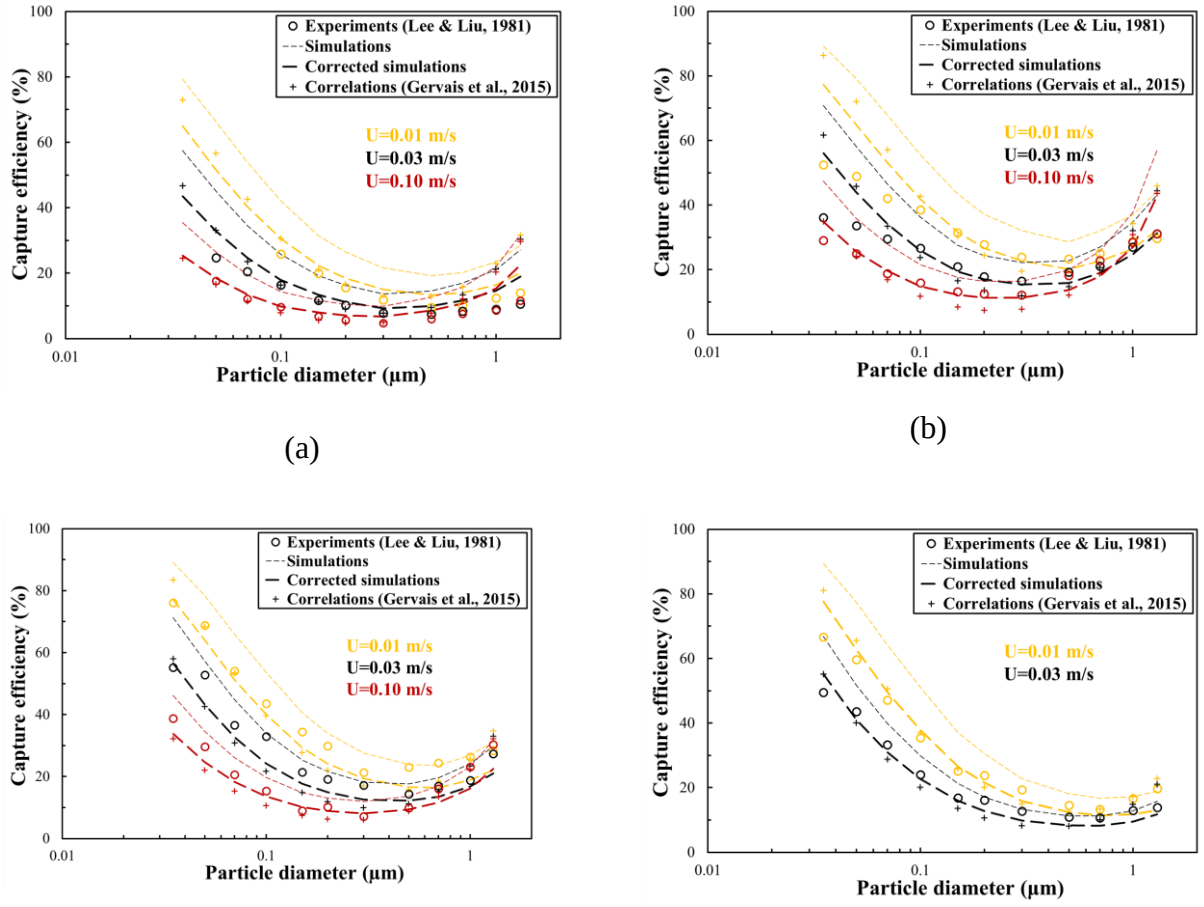

Figure 5.22: Comparison between the numerical predictions using $\alpha = 1$ (uncorrected) and $\alpha = \frac{2}{3}$ (corrected), experimental data from Lee and Liu (1981) and correlations from Gervais et al. (2015) for the capture efficiency at various superficial velocities of (a) fibrous filter A with ε=70.1% and L=183 µm, (b) fibrous filter B with

ε=58.0% and L=243 μm, (c) fibrous filter B with ε=72.9% and L=368 μm, and (d) fibrous filter B with ε=90.4% and L=1029 μm.

CHAPITRE 6 ARTICLE 2 : IMPACT OF WASHCOAT DISTRIBUTION ON THE CATALYTIC PERFORMANCE OF GASOLINE PARTICULATE FILTERS AS PREDICTED BY LATTICE BOLTZMANN SIMUALTIONS

Igor Belot, David Vidal, Martin Votsmeier, Robert Greiner, Robert E. Hayes and François Bertrand

Submitted to Chemical Engineering Journal

Abstract : The impact of catalyst distribution within the porous wall of a coated gasoline particulate filter on its catalytic performance is investigated. Sections of catalyzed filter wall with different amounts of washcoat and different levels of uniformity are digitally reconstructed from tomography data. A coupled problem involving the exhaust gas flow and the transport and reaction of a dilute species in the reconstructed structures is solved using the lattice Boltzmann method. The resulting model is verified and its accuracy is assessed for first-order reactions and those with inhibition kinetics. Computed washcoat effectiveness values agree well with the Thiele modulus theory. Improvements in catalytic conversion and washcoat effectiveness of uniform washcoat distribution are observed with increased washcoat loading. These effects are quantified and the benefits are found to be limited to the transitional regime. The uniform washcoat distribution is shown to be beneficial for both filtration and conversion performance.

6.1 Introduction

A World Health Organization survey reported an alarming 3 million deaths in 2016 due to poor air quality ("Ambient air pollution: A global assessment of exposure and burden of disease" 2016). Part of this air pollution is caused by the exhaust gases of internal combustion engines of heavy and light duty vehicles (Zhang and Batterman 2013). To reduce the negative impact of the transportation sector on air quality, manufacturers have added two devices to the exhaust gas aftertreatment system of modern vehicles. The first is the particulate filter (PF), which is customarily used for diesel vehicles (known as DPF for diesel particulate filter), but has recently been introduced to the gasoline direct injection (GDI) vehicle market (known as GPF for gasoline particulate filter) (Guan et al. 2015). It is aimed at capturing fine soot particles resulting from the

incomplete burning of fuel in the engine combustion chamber that are carried in the exhaust gas. The second device is the catalytic converter (CC), which can be placed upstream and/or downstream from the PF. It is aimed at converting pollutants that are threats to human health and the environment such as carbon monoxide (CO), nitrogen oxides (NO_X), and hydrocarbons (HC) into benign gaseous products such as CO_2, N_2 and H_2O.

There are different types of catalytic converters depending on the type of vehicle and the gases that have to be treated. Both the PF and the CC are honeycomb monoliths with typically square 1-2-mm-wide channels. In the case of the PF, the channels are alternatively plugged at the inlet or the outlet to force the exhaust gas to pass through the porous wall separating them. The fine particles carried by the gas flow are captured when they collide with the solid structure of the porous wall through electrostatic interactions. In the CC, the gas simply travels along the catalyst-coated channels such that the pollutants diffuse and react in the catalyst coating when passing through the device (Ozhan, Fuster, and Da Costa 2014). In recent years, manufacturers have developed catalyst-coated PFs (c-PF) by depositing catalyst coating, called washcoat, within the porous wall of the PF to create a single device that combines the catalytic conversion and filtration functionalities. This multifunctional device has the advantage of being more compact and less costly, easing heat up during a vehicle cold start, lowering the overall pressure drop of the exhaust gas aftertreatment system, and easing soot combustion (Richter et al. 2012). At the reactor scale, it also facilitates contact between the catalyst coating and the chemical species through the advection of the exhaust gas into the tortuous porous wall as opposed to the simple gas diffusion that takes place in a classical CC reactor (Ricca et al. 2017). For diesel engine applications, the selective catalytic reduction (SCR) functionality is usually integrated into the PF (van Setten, Makkee, and Moulijn 2001; Lorentzou, Pagkoura, Konstandopoulos, et al. 2008). For GDI engine applications, the three-way catalyst (TWC) functionality is now more often integrated into the PF (Richter et al. 2012). TWC is designed to handle simultaneously the three aforementioned pollutants (NO_X, CO, HC) using oxidation and reduction reactions (Wang et al. 2014). The TWC coating consists of a porous material containing the precious group metals platinum, palladium and rhodium (Benjamin, Liu, and Roberts 2004; Lorentzou, Pagkoura, Konstandopoulos, et al. 2008; Lorentzou, Pagkoura, Zygogianni, et al. 2008), which need to be used sparingly for cost reasons. The efficiency of c-PFs is very promising, as a single SCR-DPF displays the same deNO_X efficiency as two SCR-CC

systems in series (Czerwinski et al. 2015). However, even if the combination of these two aftertreatment devices (i.e., PF and CC) is expected to achieve an almost equivalent performance as the two separate units, the performance is not guaranteed and can certainly be optimized. Indeed, the distribution uniformity and the amount of catalyst deposited within the porous space of the PF can alter its pore size distribution (Václavík et al. 2017). This can have a significant impact on its overall performance characterized by (1) its pressure drop (ΔP), (2) its filter efficiency (E_f), and (3) its catalytic conversion (X), with the objective being to have the highest X and E_f at the lowest possible ΔP.

To gain a better understanding of the impact of washcoat distribution on the performance of a c-PF, numerous recent studies have endeavored to evaluate the filtration and catalytic performance of different c-PF configurations. In the context of c-DPF, an experimental study proposed to find the optimal $CuFe_2O_4$-based catalyst load in the PF to lower ΔP and the soot oxidation temperature at the same time using scanning electron microscopy (SEM), energy dispersive spectroscopy (EDAX), mercury porosimetry, TG-DTA analysis, H2-TPR measurements, and bending strength tests (Palmaa et al. 2013). Another study experimentally underscored the importance of wall-surface coating location in the channels of the PF, specifically by comparing depositions at the inlet and at the outlet of the channel wall of a SCR-DPF and by measuring ΔP and NO_X conversion using an FTIR spectrometer (Rappé 2014). The results showed that, in a diesel context, the impact of soot accumulation surpasses the impact of washcoat distribution and location on c-PF performance. In the context of a coated gasoline particulate filter (c-GPF), soot accumulation is expected to have a minor impact due to lower particle concentrations and higher gas temperatures (Lambert et al. 2016; Fiano 2017; Lambert et al. 2017; Joshi and Johnson 2018). An experimental comparison of numerous catalyst configurations within the porous wall of a PF in terms of filtration and catalytic conversion performance showed that the best configuration is a filter with an SiC filtration membrane coated with a catalyst layer (Lopez-Gonzalez et al. 2015). In addition, experimental testing of different coating locations within the porous walls of a GPF showed that an in-wall coating improves the catalytic performance of the TWC whereas an on-wall coating improves the filtration efficiency of the c-GPF (Inoda et al. 2017). Other experimental studies on the impact of washcoat distribution on the performance of c-PFs can be found in the literature (Tsuneyoshi, Takagi, and Yamamoto 2011; Czerwinski et al. 2015; Mitsouridis, Karamitros, and

Koltsakis 2019). The general conclusion is that a catalyst coating of a PF results in higher filtration performance but lower catalytic performance than a sequential treatment through a CC and a PF. This can be partly explained by (1) the reduction in the pore space, leading to better capture efficiency in general, and (2) the mass transfer limitation in a wall-flow configuration of a c-PF (Greiner et al. 2019). Overall, these studies did not precisely characterize the washcoats tested, and a limited number of cases were studied.

Numerically, several methods have been reported in the literature to evaluate the filtration and catalytic performance of a c-PF. Although the multiscale nature of these systems offers a wide range of possibilities for researchers to develop predictable models, they are faced with numerous difficulties. All the different scales of c-PF modelling, namely the whole filter scale, the channel scale, and the porous wall scale, as illustrated in Figure 6.1, have been presented in a number of exhaustive reviews (Ozhan, Fuster, and Da Costa 2014; Konstandopoulos, Kostoglou, and Vlachos 2006; Koltsakis et al. 2013). The whole device scale is often used to investigate the conversion performance of a classical catalytic monolith converter (Ozhan, Fuster, and Da Costa 2014; You et al. 2019) or the energy and filtration performance of a PF (Hajireza et al. 2010), but is not suited to investigate the impact of washcoat distribution on the overall performance of a c-PF. At the channel scale, numerous 1D or 2D models have been developed over the years. For the prediction of catalytic performance, (Premchand 2013) developed a 1D model to assess the oxidation of soot and NO_X using experimental data for the calibration of kinetic parameters. (Benjamin and Roberts 2014) presented a 1D porous medium approach that represents a SCR-DPF as a continuum medium. (Mitsouridis, Karamitros, and Koltsakis 2019) proposed a channel scale model to predict ΔP, filtration, soot oxidation. and ash effects. These models are based on balance equations for mass, momentum, and energy in two adjacent channels of the PF (Wurzenberger et al. 2016; Olowojebutu and Steffen 2017; Hayes, Liu, and Votsmeier 2005; Hayes et al. 2007). The advantage of such volume-averaged models is the low computational cost while their main drawback remains the tuning of parameters using other smaller scale models or experiments. Still, these models can be useful for providing general trends for optimizing the global parameters of a c-PF, as was done in a recent study for catalyst zoning in a c-DPF (Karamitros and Koltsakis 2017). However, channel scale models are not precise enough to reveal the impact of washcoat distribution within the porous wall on the performance of the filter.

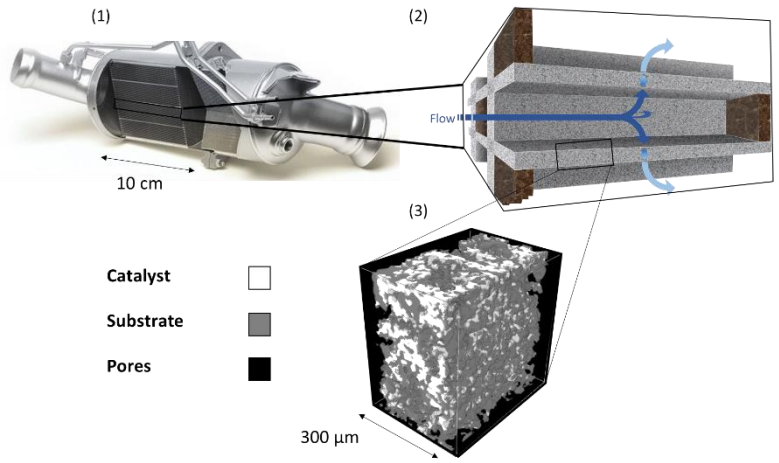

Figure 6.1: Schematic presenting the multiscale nature of a coated particulate filter (c-PF): (1) whole filter scale (~10 cm long), (2) channel scale (~1 mm wide), and (3) porous wall scale (~10 µm pore size).

At the microscopic scale, the main difficulties in modelling the conversion of pollutants in a c-PF are the large number of species and concurrent reactions (Lee, Theis, and Kyriakidou 2019) in combination with the complexity of the catalyst and substrate structures involved. To overcome these difficulties, simplified reaction models have been introduced for SCR-DFP that replace the solution of partial differential equations (PDEs) with a closed-form solution. The basic rules of these models, which are known as kinetics splitting schemes, have been described in an exhaustive review (Konstandopoulos et al. 2012). However, in a recent study, it was shown that these volume-averaged models usually overestimate the conversion performance of c-PFs by not considering transport limitations. This has been underscored by a recent 3D study at the pore scale (Greiner et al. 2019). New 1D models have thus been proposed that take these limitations into consideration and that show very good agreement with 3D simulations at the wall scale. To fully understand the impact of a catalyst coating on the performance of a c-PF and to feed larger-scale model inputs, simulations that directly solve partial differential equations at the microscale are needed. The methodology used by such models is usually multi-step and makes it possible to predict the filtration or catalytic performance of the c-PF. The first step involves the reconstruction a representative elementary volume (REV) of the porous structure of the c-PF. This can be done using geometrical reconstructions such as spherical particle packing algorithms (Hayashi and Kubo 2008; Lee et al. 2018), stochastic techniques such as simulated annealing (Matte-Deschênes et al.

2016), real sample images such as SEM images (Stewart et al. 2010), or computed tomography scans (Tsushima et al. 2010). The second step is to calculate the flow field through the pore space by solving the Navier-Stokes (NS) equations. For this purpose, several CFD methods can be employed, including the well-known finite volume (FVM), finite element (FEM) and lattice Boltzmann methods (LBM). The last step is to calculate the capture efficiency or chemical conversion of the c-PF by solving the Langevin equation for every soot particle or an advection-diffusion-reaction (ADR) equation for the soot and/or chemical species concentrations. (Kočí et al. 2006; Kočí et al. 2019; Kočí et al. 2007; Kočí et al. 2010; Dudák et al. 2014) used a three-step methodology to (1) reconstruct the porous wall using tomographic images of real c-PFs or washcoat depositions, (2) compute the flow field with FVM using open source OpenFOAM® software, and (3) solve the ADR equation in the porous medium using another in-house FVM solver. Similarly, in a previous study, the filtration performance of a series of REV of a c-GPF for various washcoat amounts and uniformity degrees was investigated with a 3D wall-scale model using LBM (Belot, Vidal, Votsmeier, et al. 2020). For the operating conditions and substrate investigated, it was found that, for the same amount of washcoat, a uniform washcoat distribution profile results in a higher capture of soot particles than a non-uniform distribution, partly due to flow channeling effects that deteriorate filtration efficiency in the latter case. In (Allouche et al. 2017), a non-isothermal model of a channel of a c-DPF developed using open source OpenFOAM® software showed that isothermal models are adequate for representing these systems. (Yamamoto et al. 2010; Yamamoto and Yamauchi 2013; Yamamoto and Sakai 2015) used LBM to develop a model to predict soot filtration as well as soot and NO_X oxidation by the platinum catalyst within the catalyst-coated DPF. They investigated where the reactions take place to better understand the evolution of the NO/NO_2 ratio in the thickness of the porous PF wall.

Lastly, an even smaller scale can also be considered. This is the pore scale of the catalyst itself as it is a porous material. Simulations of diffusion-reaction processes have been conducted using ANSYS FLUENT® software by (Karakaya et al. 2016) at the scale of the washcoat microstructure obtained from focused ion beam scanning electron microscope images of a rhodium alumina catalyst-coated monolith. They predicted catalyst performance as a function of the pore-scale microstructure and quantified pore effectiveness and reaction-diffusion limitations as a function of

the Damköhler number. Simulations at this scale can thus be used, for example, to retrieve effective diffusion coefficients of chemical species in the catalyst coating.

Various numerical methods, including FVM, LBM, and FDM, have been used in the context of c-PF to solve the NS and ADR equations at the microscale. Of these, LBM has been reported to be more accurate than classical FDM schemes (explicit Euler and implicit Crank-Nicolson) for advection-dominated mass transport problems (Hekmatzadeh et al. 2018) and makes possible higher time steps for the same space discretization (Krüger et al. 2017).

Although the feasibility of building predictable and relevant microscale models is possible, to our knowledge, no study on the impact of the distribution of the catalyst in the porous space of the c-PF walls on both its filtration and catalytic performance has ever been conducted. (Belot, Vidal, Votsmeier, et al. 2020) recently numerically studied such an impact on filtration performance for a cordierite substrate of a GPF. It would thus be natural to extend this study to catalytic performance. In this context, and following on from (Belot, Vidal, Votsmeier, et al. 2020), the objective of the present study was to evaluate the impact of uniform and non-uniform washcoat distributions and amounts in the porous wall of a c-GPF on catalytic performance. Together with the filtration performance reported in (Belot, Vidal, Votsmeier, et al. 2020), a uniform washcoat distribution compared with a non-uniform washcoat distribution in terms of the potential gain or loss in overall performance was assessed.

The remainder of this paper is organized as follows. In Section 2, the three-step numerical model developed to study the impact of washcoat amount and uniformity on the catalytic performance of a c-GPF is detailed. In Section 3, the LBM code implemented to solve the ADR problem is verified against an analytical solution, and its accuracy is assessed with commercial software using simpler and realistic test cases. In Section 4, the catalytic performance results for 14 reconstructed porous wall structures presenting two different degrees of catalyst distribution uniformity with several amounts of catalyst are presented. An example of how the proposed approach can be used to provide guidance in improving washcoat deposition is then provided. Lastly, Section 5 provides concluding remarks and guidelines for improving washcoat distribution in a c-GPF and for extending this work in future investigations.

6.2 Three-step methodology

To predict the catalytic performance of a c-GPF at the microscale and compare washcoat distribution uniformities within its porous wall, a three-step methodology was developed. It consisted of (1) numerically reconstructing a representative elementary volume (REV) of the GPF porous wall coated with a uniform or a non-uniform catalyst deposition with several amounts of washcoat, (2) computing the flow field, and (3) computing the concentration field of a hypothetical chemical species carried by the flow through the previously reconstructed porous wall structures by solving a one-way coupled problem involving the Navier-Stokes (NS) equations and an advection-diffusion-reaction (ADR) equation using the lattice Boltzmann method (LBM). This procedure is illustrated in Figure 6.2.

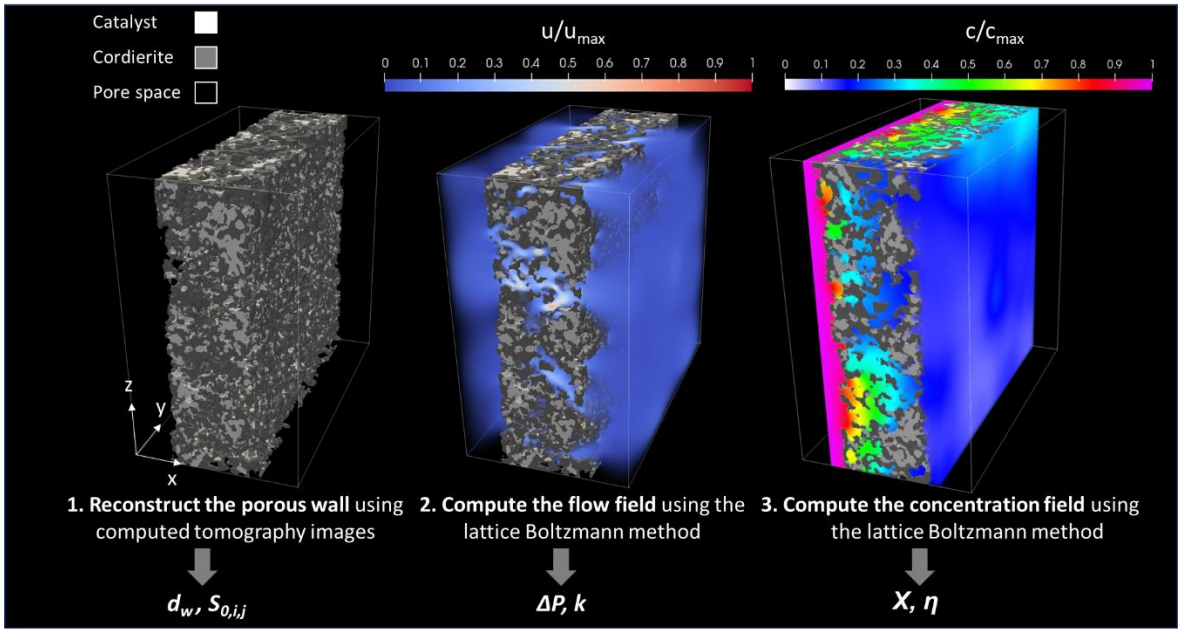

Figure 6.2: Illustration of the three-step numerical model used to predict the catalytic performance of a c-GPF porous wall at the microscopic scale level.

Given the large number of chemical species and the concurrent reactions that take place in a c-GPF, evaluating the catalytic performance in a comprehensive way would require solving as many ADR equations throughout the domain as there are chemical species involved in those reactions. To reduce the computational load and considering that the goal here was to determine whether or

not the catalyst is optimally distributed throughout the structure for a given washcoat deposition, a single first-order reaction of a hypothetical chemical species was mainly considered. Furthermore, it must be mentioned that this three-step methodology is in fact part of a four-step methodology that can predict the overall performance of a c-GPF at the microscale involving both filtration and catalytic conversion aspects. The additional step of this methodology, which involves the prediction of filtration efficiency, is presented in (Belot, Vidal, Votsmeier, et al. 2020) as are steps (1) and (2), which are also necessary for computing filtration efficiency. In this section, step (1) is first recalled, then the LBM used in steps (2) and (3) is presented in detail. This is followed by a description of the computational and physical assumptions that were used.

6.2.1 Porous wall reconstruction and characterization

To predict the catalytic performance of a c-GPF at the wall scale, the first step is to reconstruct a representative elementary volume (REV) of the porous wall that separates adjacent channels within the c-GPF monolith and that is taken here as the smallest volume over which the permeability measured is representative of the whole porous wall (see (Belot, Vidal, Votsmeier, et al. 2020)). The accuracy of the prediction of the catalytic performance of the system is highly dependent on the accuracy of the reconstruction of the structure. For example, the interfacial surface area between the catalyst and the pore space must be accurately digitally retrieved.

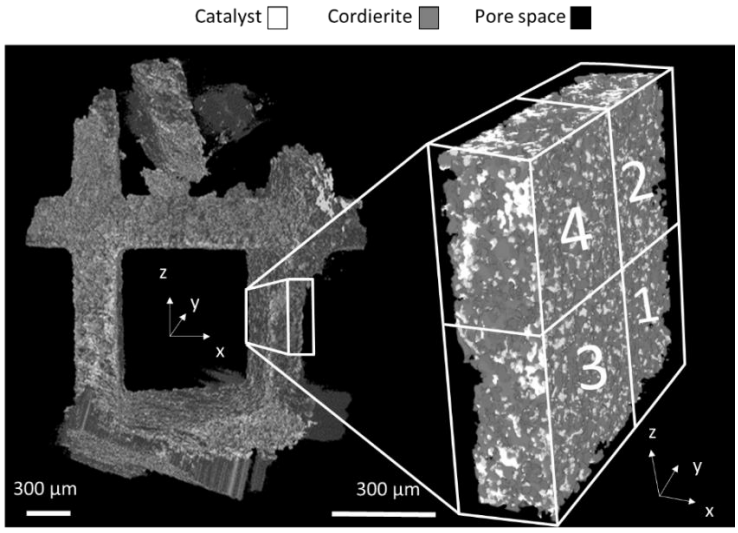

Figure 6.3: Visualization of the 256×779×801-voxel image segmented and partitioned into four subdomains (right) and extracted from the original tomographic image of the R&D sample (left).

For this purpose, a computed tomography (CT) scan of a 3×3×1.5-mm^3 piece of a 1.16-mm-wide channel of a c-GPF was acquired using a General Electric *Phoenix Nanotom M* apparatus, the preparation of which is detailed in (Greiner et al. 2019). A rectangular cuboidal 256×801×779-voxel domain of cordierite wall covered with a TWC washcoat was extracted from this scan and is depicted in Figure 6.3. This 8-bit grey scale image was segmented to distinguish between the washcoat, cordierite and pore space phases using the MATLAB Image Processing Toolbox™. The voxel resolution of this domain in every direction imposed by the digital resolution of the CT scanner was $dx = 1.25\,\mu m$. This cuboidal domain is referred to as the original R&D sample (labelled OS). From this OS structure, in which the catalyst is non-uniformly distributed within the cordierite porous structure, two series of structures presenting two different catalyst distributions were created using a set of morphological image processing operations applied on the segmented X-ray computed tomography data, as proposed by (Belot, Vidal, Votsmeier, et al. 2020). This resulted in a non-uniform washcoat distribution series consisting of 9 structures with increasing amounts of catalyst labelled N1 to N8, as well as the OS structure, and a uniform washcoat distribution series consisting of 4 structures with increasing amounts of catalyst labelled U1 to U4. A bare wall (BW) structure presenting no catalyst deposition was added to these 13 structures,

bringing the total number of structures studied to 14. For ease of computation, each of these 14 structures was partitioned into four 256×389×400-voxel subdomains, the size of which is an REV of the porous wall described in (Belot, Vidal, Votsmeier, et al. 2020). This is illustrated in Figure 6.3. This last operation brought the number of reconstructed domains to 56.

More details on the set of morphological image processing operations employed to deposit washcoat artificially within the cordierite structure (BW) are given in (Belot, Vidal, Votsmeier, et al. 2020). A 200×100-pixel cross-sectional visualization of each of the 14 structures investigated in the present study is presented in Figure 6.4.

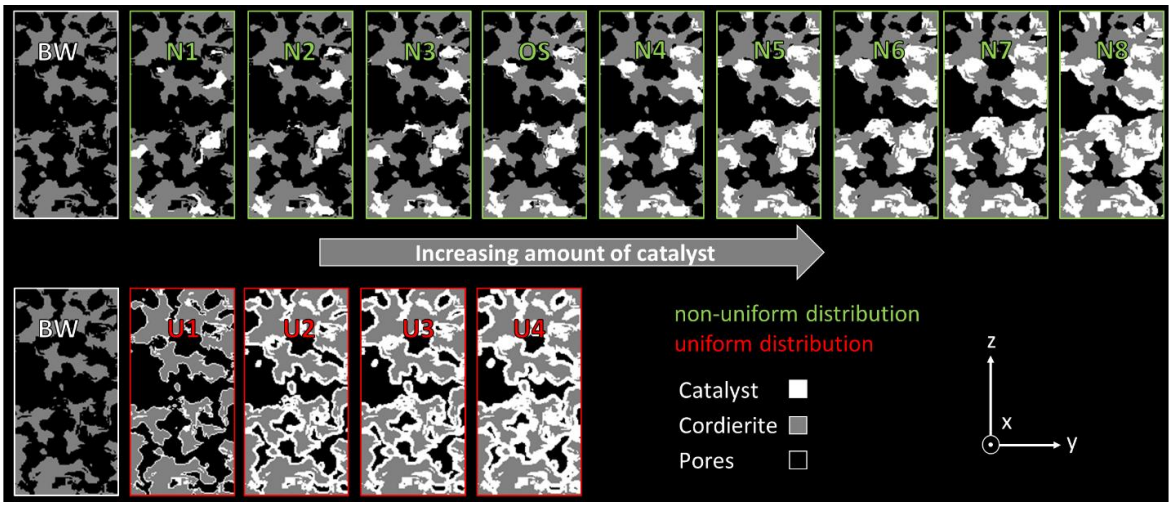

Figure 6.4: Close-up cross-sectional 200×100-pixel visualizations (with *dx*=1.25 µm) for each of the 14 structures reconstructed in (Belot, Vidal, Votsmeier, et al. 2020) and investigated in the present study, i.e., the non-uniform series (N1-N8) containing the original R&D sample (OS), the uniform series (U1-U4), and the bare wall (BW) structures.

For the numerical study presented herein, the three phases of the structures were encoded as follows: 0 for the pore space, 1 for the cordierite, and 2 for the catalyst phase. The volume fraction of phase i is denoted as ϕ_i. For the combined solid phase (catalyst + substrate), ϕ_{1+2} is simply denoted as ϕ and is commonly referred to as the solidity. For the porous phase, ϕ_0 is denoted ε and is thus commonly referred to as the porosity. Having the porosity of the reconstructed structures, the fraction of pore volume filled by the catalyst can be calculated as:

$$f_w = 1 - \frac{\varepsilon}{\varepsilon_{BW}} \tag{6.1}$$

where ε_{BW} is the porosity of the BW structure. This descriptor is representative of the amount of washcoat introduced into the BW substrate and will be used to report the results in Section 4. The surface area between phases *i* and *j* in the porous medium can be defined as:

$$S_{0,i,j} = \frac{S_{i,j}}{V_{tot}} \tag{6.2}$$

where $S_{i,j}$ is the interfacial area between phase *i* and *j*, and V_{tot} is the total volume of the porous medium. In the present study, the surface areas $S_{i,j}$ were calculated using a statistical method described in (Ohser and Mücklich 2000) and corrected by a factor $\frac{2}{3}$ to account for the inherent surface area overestimation due to the staircase-like fractal nature of a voxelized surface representation, as pointed out in the literature (Yeong and Torquato 1998b, 1998a). This property is a critical metric for the catalytic and filtration performance of a c-GPF. For overall c-GPF performance, it is generally beneficial to maximize (1) the surface area of the catalyst with respect to the pore space for chemical reactions, and (2) the surface area of the whole solid phase with respect to pore space for soot capture.

A characteristic length for the catalyst phase, which can be interpreted as the average thickness of the catalyst deposition, can then be defined by:

$$L_{cat} = \frac{\phi_2}{S_{0,2,0}} = \frac{f_w \varepsilon_{BW}}{S_{0,2,0}} = \frac{V_{cat}}{S_{2,0}} \tag{6.3}$$

where $S_{0,2,0}$ is the surface area between the pore space and the catalyst phase per unit volume of porous medium, and V_{cat} is the volume of the catalyst phase. The surface area of the solid phase $S_{0,(1+2),0}$ is also linked to the mean pore diameter, denoted d_w, as in (Dullien 1979):

$$d_w = \frac{2\varepsilon}{3} \frac{6\varepsilon}{S_{0,(1+2),0}} \tag{6.4}$$

The geometrical descriptors listed above serve two purposes. The first is to understand better the causal relation between the geometrical parameters of the reconstructed porous structures and catalytic performance. The second is to allow other researchers to replicate our experiments. Additional geometrical descriptors calculated on the structures generated for the present study can be found in (Belot, Vidal, Votsmeier, et al. 2020).

6.2.2 The Lattice Boltzmann Method

In the context of porous media, the lattice Boltzmann method (LBM) has received increasing attention from researchers over the last two decades because of its ease of implementation, its great potential for parallelization (Vidal, Roy, and Bertrand 2010a, 2010b) and its ability to deal with complex geometries (Vidal et al. 2009). It is not only a CFD solver but also a partial differential equation (PDE) solver (Krüger et al. 2017). It is thus possible to solve both the NS and ADR equations in a coupled way using the same overall numerical scheme. Although LBM is intrinsically a transient PDE solver that can be used to study the response to temporal fluctuations in concentration, only the steady-state solutions resulting from steady boundary conditions are analyzed here. For these reasons, LBM is particularly well adapted to the prediction of catalytic performance in porous media. It consists of solving any PDE using the Boltzmann equation from the kinetic theory of gases given by:

$$\frac{\partial f}{\partial t} + \boldsymbol{e}.\boldsymbol{\nabla}_{\boldsymbol{x}} f + \boldsymbol{F}.\boldsymbol{\nabla}_{\boldsymbol{e}} f = \Omega(f) \tag{6.5}$$

where Ω is an appropriate collision operator and f represents a probability distribution function of finding a quantity of interest or "population" traveling at a microscopic velocity $\boldsymbol{e}$, being at position $\boldsymbol{x}$ at time t, and being driven by an external force $\boldsymbol{F}$. Although derived from the kinetic theory of gases, this equation, which was originally used to describe the micro-dynamical evolution of a population of molecules in a gas, can also be used to evolve any given population (e.g. populations of molecules in a liquid, quanta of energy, a chemical species in a medium) and thus model any transport phenomena. To solve this equation, the discretizations of the partial derivatives in space and time are carried out by the voxelization of the domain (in which phases are eventually encoded

in a Boolean manner) using a Cartesian grid (also called lattice) and by a classic Euler explicit scheme, respectively.

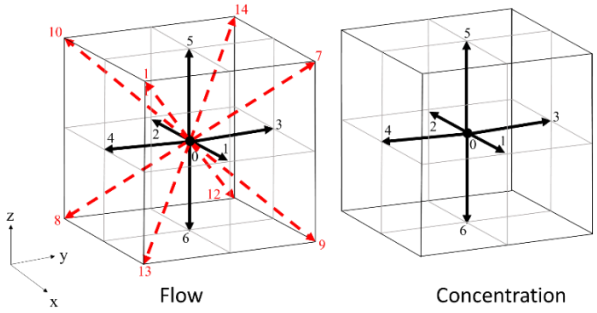

Figure 6.5: D3Q15 (left) and D3Q7 (right) velocity vector sets used for the discretization of the microscopic velocity domain, respectively, in flow and mass transport problems.

The discretization of the microscopic velocity domain is accomplished by projecting the distribution functions on a set of discrete velocities e_i denoted by *DnQm*, where *n* is the number of spatial dimensions and *m* the number of discrete velocities used. The sets of velocities used in the present study were *D3Q15* and *D3Q7* for solving the NS and ADR problems, respectively, as shown in Figure 6.5. In the case of an ADR problem involving isotropic diffusion with zero off-diagonal coefficients and a linear behavior, a simpler set of microscopic velocities such as D3Q7 as well as simpler equilibrium functions have been found to be sufficient to solve such phenomena (Toffoli and Margolus 1990; Krüger et al. 2017). In this work, LBM was employed to compute the flow field through the reconstructed porous wall structures using the second-order accurate computer code developed in (Vidal, Roy, and Bertrand 2010a, 2010b) as well as the concentration field using a custom-written program developed specifically for the present study. Assuming that the low concentration of the chemical species does not affect the gas flow field, a one-way coupling of these two solvers was used to evaluate the catalytic performance of the c-GPF. First, the flow field was solved and the flow properties through the structure were obtained. Then, taking the previously computed flow field as input data, the mass transport of a hypothetical species was solved to obtain its concentration field throughout the domain. From this, the catalytic performance of the structures was obtained. Details about the LBM schemes used for solving both the NS and ADR equations are provided in the following subsections to make it possible to compare the

implementations. For additional information about LBM, the reader is referred to the studies by (Guo and Shu 2013; Krüger et al. 2017).

6.2.2.1 Flow field computation

Instead of directly solving the NS equations, LBM solves a discretized Boltzmann equation in the time, space, and velocity domains, and reads as:

$$f_i(\boldsymbol{x} + \boldsymbol{e_i}dt, t + dt) = f_i(\boldsymbol{x}, t) + \Omega_i(\boldsymbol{x}, t) + \boldsymbol{F_i} \tag{6.6}$$

where $\boldsymbol{F_i}$ is an external body force and f_i represents here populations of gas molecules with microscopic velocity $\boldsymbol{e_i}$ (with $i \in (0,1,2,3,4,5,6,7,8,9,10,11,12,13,14)$ propagating at every time step dt from a lattice node to its nearest neighbor in the direction of the microscopic velocity. The collision operator Ω_i is approximated using a single relaxation procedure toward a local equilibrium state proposed by Bhatnager-Gross-Krook (Bhatnagar, Gross, and Krook 1954), which is commonly used due to its simplicity and accuracy. It reads as:

$$\Omega_i(\boldsymbol{x}, t) = -\frac{1}{\tau_f}\left(f_i(\boldsymbol{x}, t) - f_i^{eq}(\boldsymbol{u}, \rho)\right) \tag{6.7}$$

where τ_f is a dimensionless relaxation time (here, $\tau_f = 1$ is used). In addition, according to the kinetic theory of gases, the equilibrium population f_i^{eq} follows a Maxwell-Boltzmann distribution that can be approximated by a second-order expansion in velocity such that:

$$f_i^{eq}(\boldsymbol{u}, \rho) \approx \omega_i \rho \left(1 + \frac{\boldsymbol{e_i} \cdot \boldsymbol{u}}{c_s^2} + \frac{(\boldsymbol{e_i} \cdot \boldsymbol{u})^2}{2c_s^4} - \frac{\boldsymbol{u} \cdot \boldsymbol{u}}{2c_s^2}\right) \tag{6.8}$$

which depends on the local macroscopic fluid velocity $\boldsymbol{u} = \boldsymbol{u}(\boldsymbol{x}, t)$ and density $\rho = \rho(\boldsymbol{x}, t)$, where ω_i is a weight associated with velocity $\boldsymbol{e_i}$ (with $\omega_0 = \frac{2}{9};\ \omega_{1-6} = \frac{1}{9};\ \omega_{7-14} = \frac{1}{72}$) and c_s represents the speed of sound in the lattice space defined by:

$$c_s = \frac{dx}{\sqrt{3}dt} \tag{6.9}$$

where dx is the lattice spacing. The dimensionless relaxation time is related to the fluid kinematic viscosity ν through:

$$\nu = c_s^2 dt \left(\tau_f - \frac{1}{2}\right) \tag{6.10}$$

Summing zeroth- and first-order moments of the populations f_i, the macroscopic fluid properties ρ and $\boldsymbol{u}$ at every position and time can be retrieved:

$$\rho(\boldsymbol{x}, t) = \sum_i f_i(\boldsymbol{x}, t) \qquad \rho \boldsymbol{u}(\boldsymbol{x}, t) = \sum_i \boldsymbol{e_i} f_i(\boldsymbol{x}, t) \tag{6.11}$$

Lastly, to enforce the quasi-incompressibility and to obtain the pressure field p, the following equation of state is used (Bertrand et al. 2012):

$$p(\boldsymbol{x}, t) = \left(\rho(\boldsymbol{x}, t) - \overline{\rho(\boldsymbol{x}, t)}\right) c_s^2 - \frac{\|\Delta P\|}{L}\left(x_f - L\right) \tag{6.12}$$

for $0 \leq x_f \leq L$, where x_f and L are, respectively, the position and the domain thickness in the direction of the flow and ΔP is the pressure drop through the filter thickness. The second term on the right-hand side of Eq. (6.12) represents the static pressure that needs to be added when periodic boundary conditions combined with a body force are used to impose a ΔP through the thickness, as is the case in this study. This body force is added as a source term in the right-hand side of the LBM scheme (i.e., Eq. (6.6)) (see (Bertrand et al. 2012)). For the flow calculation, only two phases are considered: the solid phase (cordierite + washcoat) and the fluid phase (pore space). Once calculated, being strictly in a laminar regime, the flow field can be rescaled *a posteriori* to match the actual targeted superficial velocity U, and the ΔP is then rescaled accordingly.

6.2.2.2 Concentration field computation

To compute the concentration field of a chemical species, the most common procedure consists of solving the ADR equation. For a chemical species in a specific medium and a constant diffusion coefficient D, it reads as:

$$\frac{\partial c}{\partial t} + \boldsymbol{u} \cdot \boldsymbol{\nabla} c = D \boldsymbol{\nabla}^2 c + r \tag{6.13}$$

where c is the concentration of the chemical species and r is a reaction rate. Instead of directly solving the ADR equation, as for the NS equations, LBM solves a discretized Boltzmann equation in time, space, and velocity domains $\boldsymbol{e_i}, i \in (0,1,2,3,4,5,6)$, which reads as:

$$g_i(\boldsymbol{x} + \boldsymbol{e_i} dt, t + dt) = g_i(\boldsymbol{x}, t) + \Omega_i'(\boldsymbol{x}, t) + \gamma_i r \tag{6.14}$$

where g_i is used here to represent the corresponding populations and distinguish them from the gas molecule populations f_i. They thus represent populations of the chemical species propagating at velocity $\boldsymbol{e_i}$ along the lattice and colliding according to:

$$\Omega_i'(\boldsymbol{x}, t) = -\frac{1}{\tau_g}\left(g_i(\boldsymbol{x}, t) - {g_i}^{eq}(\boldsymbol{u}, c)\right) \tag{6.15}$$

in which τ_g is the dimensionless relaxation time towards an equilibrium state represented by ${g_i}^{eq}$ defined as:

$${g_i}^{eq}(\boldsymbol{x}, t) = \gamma_i c \left(1 + \frac{\boldsymbol{e_i}.\boldsymbol{u}}{c_s^2}\right) \tag{6.16}$$

where $\boldsymbol{u}$ and c are, respectively, the macroscopic velocity and the concentration of the chemical species, and γ_i is the weight related to the velocity $\boldsymbol{e_i}$ ($\gamma_0 = \frac{1}{4}$; $\gamma_{1-6} = \frac{1}{8}$). As for the flow calculation, c_s represents the speed of sound in the lattice space as expressed by Eq. (6.9). The time step dt, the diffusion coefficient of the species D, and the dimensionless relaxation time τ_g are related through the following equation:

$$D = c_s^2 dt \left(\tau_g - \frac{1}{2}\right) \tag{6.17}$$

The value of the time step dt and, as a result, that of c_s are different from those in the flow simulations. Summing all the populations g_i, it is possible to retrieve the macroscopic physical value of c at every position and time as in (Krüger et al. 2017):

$$c(\boldsymbol{x},t) = \sum_i g_i(\boldsymbol{x},t) + \left(1 - \frac{1}{2\tau_g}\right)\gamma_i r(\boldsymbol{x},t) \tag{6.18}$$

A first-order reaction was considered in the present study. It is expressed as $r(\boldsymbol{x},t) = -k_1 c(\boldsymbol{x},t)$, where k_1 is the rate constant. It made it possible to compare the catalytic performance of the two distribution profiles investigated. However, to extend the results presented in Section 4 to more realistic reaction rates, an inhibition kinetics (LHHW type) was also considered (Vollz et al. 1973). It can be expressed as $r(\boldsymbol{x},t) = -\frac{k_1 c(\boldsymbol{x},t)}{(1+Kc(\boldsymbol{x},t))^2}$, where k_1 and K are the kinetics and inhibition constants, respectively.

6.2.2.3 Boundary conditions

For the flow simulations, 100-voxel buffers were added at the inlet and outlet in the flow direction (*x*) of the structures studied, resulting in 456×400×389-voxel computational domains. This aimed to facilitate the imposition of the periodic boundary conditions in the flow direction and to avoid an edge effect at the entrance of the porous structure. For the ADR simulations, 20-voxel buffers were added at the inlet and outlet in the flow direction (*x*), resulting in 296×400×389-voxel computational domains. Contrary to other classical methods, boundary conditions for LBM are not applied directly on the macroscopic values but on the microscopic populations f_i or g_i instead. For the computation of the flow field, periodic boundary conditions were applied in the flow direction (*x*), and symmetric boundary conditions were applied in the directions perpendicular to the flow (*y,z*) at the outer domain boundaries. As previously mentioned, the periodic boundary conditions combined with a body force were used to impose a ΔP through the thickness direction (*x*). At the interface between the fluid and solid voxels, a half-way bounce-back boundary condition was applied to make the solid phase impermeable to the flow. More details on the implementation and the characteristics of these conditions can be found in (Vidal, Roy, and Bertrand 2010a, 2010b). For the concentration field at the inlet ($x=0$), a Dirichlet boundary condition in concentration, $c=c_0$, was applied, which translates at the microscopic scale into:

$$g_1(\boldsymbol{x},t+dt) = c_0 - \sum_{i\neq 1} g_i(\boldsymbol{x},t+dt) \tag{6.19}$$

At the outlet ($x=296\times dx$), a Neumann-type boundary condition was used for the concentration. This condition, commonly called outflow, forces a null diffusive flux at the outlet (i.e., $D\frac{\partial c}{\partial x}=0$), which reads, at the microscopic scale, as:

$$g_2(x,y,z,t+dt)=c(x-\boldsymbol{e_i}dt,y,z,t+dt)-\sum_{i\neq 2}g_i(x,y,z,t+dt) \tag{6.20}$$

Lastly, at the outer domain boundaries perpendicular to the flow direction, symmetric boundary conditions were implemented, meaning that no concentration flux was going through the boundaries: $\mathrm{D}\frac{\partial \mathrm{c}}{\partial \mathrm{y}}+u_y c=0$ or $\mathrm{D}\frac{\partial \mathrm{c}}{\partial \mathrm{z}}+u_z c=0$, where u_α is the component of the flow velocity in direction α. In the case of the ADR equation resolution with LBM, the symmetric boundary conditions corresponded to the classical half-way bounce-back boundary condition (Krüger et al. 2017), which read, respectively, as:

$$g_4(x,y,z,t+dt)=g_3(x,y,z,t)\ or\ g_6(x,y,z,t+dt)=g_5(x,y,z,t) \tag{6.21}$$

For the local boundary conditions, i.e., at the interface between two phases *i* and *j* inside the structure, two different treatments were needed. A half-way bounce-back boundary condition was used at the pore-cordierite and catalyst-cordierite interfaces to make the cordierite phase impermeable to the hypothetical chemical species considered, similar to Eq. (6.21). At the pore-catalyst interface, no specific boundary condition was applied, but the diffusion coefficient was different across the interface: D_{cat} and D_{por} for the catalyst and pore phases, respectively. The choice of $\tau_{g,por}=1$, for stability reasons, led to the two following dimensionless relaxation times in the domain (see Eq. (6.17)) for the calculation of the concentration field:

$$\tau_{g,por}=1;\ \tau_{g,cat}=\frac{1}{2}\left(1+\frac{D_{cat}}{D_{por}}\right) \tag{6.22}$$

6.2.3 Model assumptions

To proceed to the flow and concentration field calculations, several physical assumptions were made:

1. An isothermal, Newtonian, and incompressible air flow is considered for the flow field calculations. It only takes place in the pore phase, meaning that the catalyst and substrate phases are totally impermeable to the air flow. As washcoat permeability is about ~10^{-15} m^2 (Kočí et al. 2019), i.e., two orders of magnitude lower than that of the cordierite substrate, this is a highly reasonable assumption.
2. The concentration of the hypothetical chemical species is assumed to be very low such that it does not impact the fluid properties.
3. The reaction of the hypothetical species occurs exclusively in the catalyst phase and is isothermal.
4. The diffusion of the hypothetical species occurs at different rates in the pore and catalyst phases. The corresponding diffusion coefficients typical for such systems are provided in Table 6.1. The pore space at the washcoat scale is neglected so that an effective diffusion coefficient is considered for this phase.
5. The cordierite phase is also impermeable to chemical species diffusion and thus no reaction takes place in the cordierite.

Additional parameters used for the simulations through all the reconstructed structures are listed in Table 6.1. They are based on the parameters used in (Greiner et al. 2019) and are typical values for such a system (Zhang, Hayes, and Kolaczkowski 2004; Fuller, Schettler, and Giddings 1966). Note that the kinetics constant was varied from 1 to 10^6 s^{-1} in an additional study to verify the impact of the rate constant on the trends obtained. Results from this additional study are also reported in Section 4.

Table 6.1 : Physical parameters used in the calculations of the flow and concentration fields with LBM, considering air as a carrying fluid and a hypothetical chemical species

Parameter	**Symbol**	**Value**
Fluid density ($kg.m^{-3}$)	ρ	0.543
Fluid dynamic viscosity ($kg.m^{-1}.s^{-1}$)	μ	3.18×10^{-5}
Superficial velocity ($m.s^{-1}$)	U	0.055
Temperature (K)	T	650
Diffusion coefficient in pores ($m^2.s^{-1}$)	D_{por}	6.5×10^{-5}
Effective diffusion coefficient in catalyst ($m^2.s^{-1}$)	D_{cat}	10^{-6}
First-order reaction rate constant (s^{-1})	k_1	10503
Inhibition kinetics constant (m^3/mol)	K	2
Inlet concentration (mol/m^3)	c_0	1

The parameters listed in Table 6.1 led to the following Peclet number for the ADR problems investigated, which is well below the stability condition ($Pe \leq 1$) of the LBM scheme reported in the literature for such a problem (Hosseini et al. 2018; Suga 2009):

$$0.01 \leq \mathrm{Pe} = \frac{d_w U}{D_{por}} \leq 0.03 \ll 1 \tag{6.23}$$

Damköhler numbers can also be calculated for characterizing the prevalence of reaction through convection in the pore space (Da_I) or through diffusion in the washcoat (Da_{II}) They are respectively defined and bounded for the 14 structures studied in this work as:

$$\sim 2 \leq \mathrm{Da}_I = \frac{k_1 d_w}{U} \leq \sim 6$$
$$\sim 5 \times 10^{-3} \leq \mathrm{Da}_{II} = \frac{k_1}{D_{cat}} {L_{cat}}^2 = \Phi^2 \leq \sim 2 \tag{6.24}$$

These values show that the ADR problems investigated took place for the most part within a transitional regime, that is between a reaction-limited regime and a transport-limited regime. The second Damköhler number (Da_{II}) is related to an important dimensionless number, called the Thiele modulus Φ (Aris 1957), which can be used to characterize the transport limitation of the chemical species into the pore space and thus determine the effectiveness of a catalyst pellet or coating. It is shown in the literature that the catalyst effectiveness follows a specific relationship as a function of the Thiele modulus for a given catalyst shape or coating (Hayes, Liu, and Votsmeier 2005; Hayes et al. 2007; Deutschmann 2014; Greiner et al. 2019; Hayes and Mmbaga 2012). The agreement of the simulation results with the Thiele modulus theory is verified in Section 4.

Once the concentration field $c(\boldsymbol{x}, t)$ has been calculated, two important catalytic performance metrics can be extracted from the results, i.e., chemical conversion X and catalyst coating effectiveness η. Because of the Dirichlet boundary condition combined with the buffer zone at the inlet of the computational domain, it is practical to define chemical conversion as:

$$X = \frac{q_{tot,in} - q_{tot,out}}{q_{tot,in}} \tag{6.25}$$

where $q_{tot,in}$ and $q_{tot,out}$ are, respectively, the molar flux in the direction of the flow (x) at the inlet and the outlet of the computational domain, as defined by:

$$q_{tot} = \mathrm{D} \frac{\partial \mathrm{c}}{\partial \mathrm{x}} + u_x c \tag{6.26}$$

The second metric is more specific to the washcoat context and is an indicator of how effective the catalyst coating is to the reaction. Catalyst effectiveness can be calculated through (Greiner et al. 2019):

$$\eta = \frac{1}{n_x} \sum_{i=1}^{n_x} \frac{\bar{c}_{cat,i}}{\bar{c}_{por,i}} \tag{6.27}$$

where $\bar{c}_{cat,i}$ and $\bar{c}_{por,i}$ are, respectively, the mean concentrations in the catalyst and the pore space in slice *i* of the computational domain (see Section 2.2.3), and $n_x = 256$ is the number of slices in the *x* direction in the computational domain, without taking into account the added buffers. These two catalytic performance metrics of washcoat deposition were calculated for each of the 14 reconstructed structures.

6.3 LBM code Verification and Accuracy assessment

In this section, a verification of the LBM code implemented to solve the ADR equation is carried out by comparing the results obtained from an analytical solution and from commercial COMSOL Multiphysics® software, for a relatively simple test case. A comparison with the concentration field in the OS structure obtained with GeoDict® software ("GeoDict" 2018), as reported in (Greiner et al. 2019), is then provided to assess the accuracy of our implementation for a complex porous structure. Note that an exhaustive validation of the LBM code implemented for flow simulations in the reconstructed porous wall structures can be found in (Belot et al. Submitted (2020)).

6.3.1 Verification

To verify the calculation of the concentration field of a hypothetical chemical species using the LBM code implemented for the present study, three test cases were performed. One test case is presented in this section while the other two are detailed in Appendix A.

The first verification test case illustrated in Figure 6.6 consisted of a hypothetical pseudo-3D advection-diffusion problem of a species in a cuboidal domain split into two equal parts having a ratio of diffusion coefficients of the species into their respective medium of $D_2/D_1=20$. The transport velocity of the species was uniform throughout the domain, pointing in the *x*-direction and set to $U=L/t_1$ m/s, where *L* is the length of the rectangular domain in the direction of the flow and t_1 is a time period of 1. Furthermore, the diffusion coefficient in Medium 1 was defined such that $D_1=L^2/t_2$ with $t_2=t_1/20$. The outer domain boundary conditions were set to be symmetric in the

directions perpendicular to the flow (y,z). Two Dirichlet boundary conditions were used at the inlet ($c = 0$ mol/l) and outlet ($c = c_0 = 1$ mol/l) of the domain and periodic boundary conditions were used in the directions perpendicular to the direction of the flow.

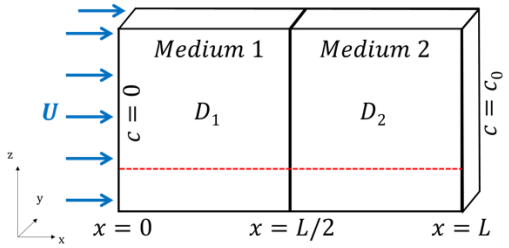

Figure 6.6: Schematic of the cuboidal domain and operating conditions employed for the pseudo-3D advection-diffusion test case used to verify the LBM code implemented for the present study. The red dashed line represents the direction along which the concentration data were gathered.

The results presented in Figure 6.7 and obtained with LBM for different grid spacings (*dx*) were compared to an analytical solution reported in (Karani and Huber 2015) as well as to the solution obtained using commercial COMSOL Multiphysics® software (version 5.2a) at the finest mesh possible.

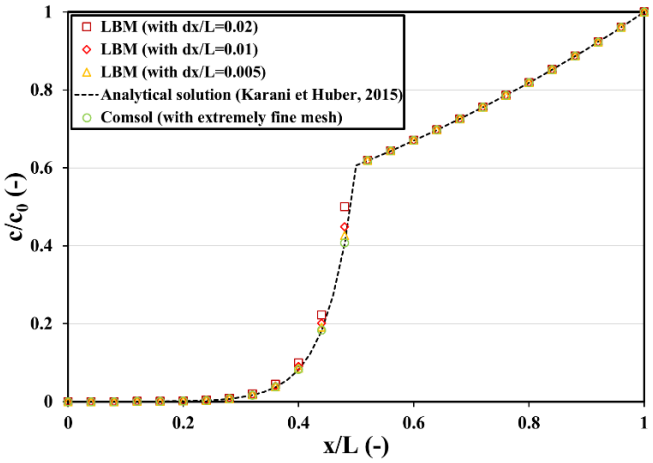

Figure 6.7: Concentration profile at steady state along the red dashed line of Figure 6.6 for different grid spacings using LBM compared to the analytical solution found in (Karani and Huber 2015) and the solution obtained using COMSOL Multiphysics® software.

Very good agreement between all the approaches used to solve this verification test case was found. The mean relative discrepancies for the three LBM grid resolutions with respect to the analytical solution were 3.5%, 1.6% and 0.7%, respectively. Only a slight discrepancy is apparent in the quadratic sharp variation region just before the transition between the 2D media, for which sufficient LBM grid spacing was required to achieve an accurate solution. This gives confidence in the accuracy of the advection-diffusion LBM solver implemented in the present study. An L_2-error first-order convergence was obtained for the LBM implementation, which is consistent with the results reported in (Krüger et al. 2017) for this LBM implementation in the case of an ADR equation.

6.3.2 Accuracy assessment

To evaluate the coupled LBM implementation in the context of an ADR problem for a first-order reaction through a complex porous structure, the 256×801×779-voxel OS structure shown in Figure 6.3, the concentration field of a hypothetical chemical species was computed and was compared with results reported in (Greiner et al. 2019) and obtained using the finite volume PoreChem simulation tool combined with the GeoDict® SimpleFFT flow solver. The physical parameters used for these simulations are those reported in Table 6.1. The grid spacing (dx) used here for the

comparison was 1.4 µm. The performance metrics are compared in Table 6.2. A relative difference of 0.8% for X and 3.8% for η were obtained. This small discrepancy can be attributed to the difference in buffer size used upstream and downstream from the structure (20 voxels in the present simulation vs. 100 voxels in (Greiner et al. 2019)).

Table 6.2 : Comparison of conversion and catalyst efficiency in the OS structure as calculated with LBM and GeoDict®.

	LBM (current work)	PoreChem/GeoDict® Greiner et al. (2019)
X	0.743	0.749
η	0.495	0.477

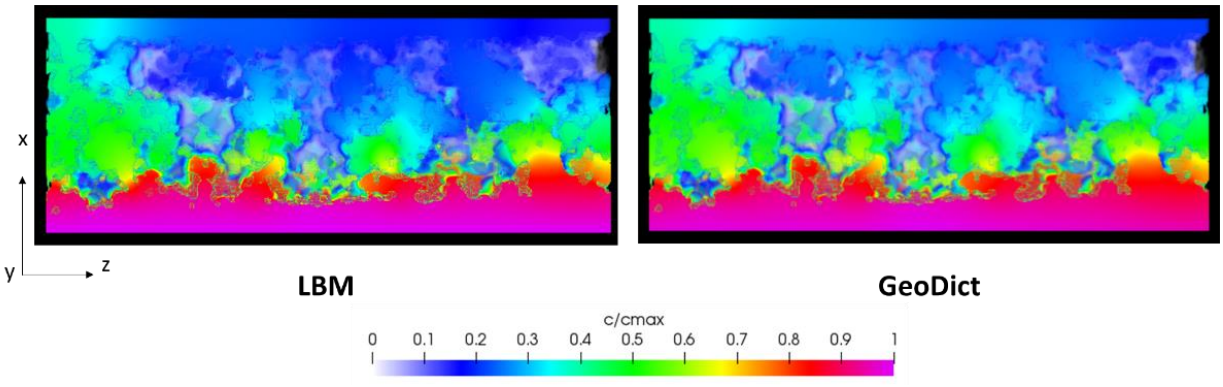

Figure 6.8: Comparison of the concentration field of a 2D slice obtained through the OS structure as computed using the LBM implementation (left) and PoreChem/GeoDict® (right).

A visualization of the two concentration fields in the top section of the computational domain (y=779×dx) is also provided in Figure 6.8. Two similar profiles were obtained, which gives confidence in the concentration field computations implemented in the present study.

6.3.3 Computational performance

The overall computational time for the LBM flow calculations on a 456×400×389-voxel porous wall subdomain was approximately 6 hours on 8 cores of a 2.67 GHz Intel Xeon X5650 Westmere

processor computer. The simulations used approximately 3.5 GB of RAM. For the concentration field calculations on a 296×400×389-voxel porous wall subdomain, the computational time was approximately 30 hours on 12 cores of 2.67 GHz Intel Xeon X5650 Westmere processor computer. The relative long computational time for the transient solution of the concentration field could be reduced by further code optimization. The simulations used approximately 15 GB of RAM.

6.4 Results and discussion

The presentation of the results is divided into five parts. A characterization of the structures using the geometrical descriptors presented in Section 2.1 is provided. The flow properties of the structures presenting a uniform distribution compared to those with a non-uniform distribution is illustrated by flow field visualizations. The results for chemical conversion and catalyst coating effectiveness made it possible to assess the impact of washcoat amount and distribution uniformity on catalytic performance. The results for catalytic performance were combined with those for filtration performance reported in (Belot, Vidal, Votsmeier, et al. 2020) to assess the impact of the washcoat on the overall performance of the c-GPF at the microscale for two distribution profiles investigated in the present study.

6.4.1 Reconstructed structure characterization

For every reconstructed structure, the fraction of pore volume filled f_w, defined in Eq. (6.1), is reported as an average over the four subdomains (see Fig. 3) of the whole 256×801×779-voxel structures along with its standard deviation σ, for the non-uniform and the uniform catalyst distribution series, in Table 6.3.

Table 6.3 : Fraction of pore volume filled by the catalyst (f_w) for all reconstructed non-uniform and uniform washcoat distribution profiles averaged over the four subdomains and the corresponding standard deviation σ.

Sample ID*	**BW**	**N1**	**N2**	**N3**	**OS**	**N4**	**N5**	**N6**	**N7**	**N8**
f_w	0.000	0.140	0.170	0.209	0.232	0.272	0.320	0.356	0.410	0.494
σ	0.00	0.026	0.028	0.031	0.031	0.033	0.034	0.034	0.034	0.032

Sample ID*	BW	U1	U2	U3	U4
f_w	0.000	0.133	0.264	0.420	0.521
$\sigma\ (\times 10^2)$	0.00	0.60	0.11	0.15	0.16

* BW: bare wall without washcoat, OS: original R&D sample, N: reconstructed non-uniform washcoat distribution profiles, U: reconstructed uniform washcoat distribution profiles.

The mean pore diameter (d_w) averaged over the four subdomains for each of the 14 structures investigated, as calculated using Eq. (6.4) from the surface area $S_{0,1+2,0}$ of the solid phase (i.e., catalyst + substrate) with respect to pore space, is reported in Figure 6.9.

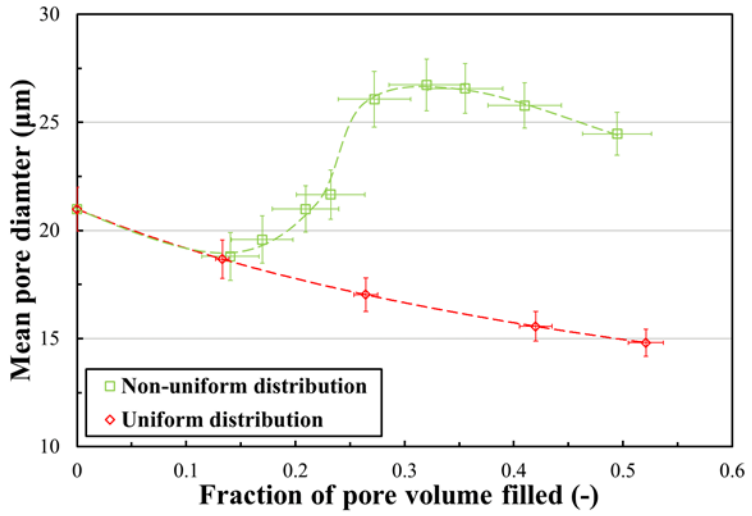

Figure 6.9: Evolution of the mean pore diameter (d_w) as a function of the amount of washcoat (f_w) for the two washcoat distribution profiles in the reconstructed GPF porous wall structures. The dashed lines are a guide for the eye, and the error bars represent the standard deviations of the reported mean values for the four wall subdomains.

These results show that, for a uniform distribution profile, as every pore section is impacted by an increasing amount of washcoat, the mean pore diameter decreases gradually with an increasing f_w, as intuitively expected. In the case of a non-uniform distribution profile, counter-intuitively, the average mean pore diameter increases with increasing amounts of washcoat in the $f_w \leq \sim 30\%$ range. This result suggests that small pores are preferentially filled up as the amount of washcoat is initially increased in the case of a non-uniform coating. At higher amounts of washcoat, the mean pore diameter decreases, proving that larger pores are in turn impacted by washcoat deposition.

This insight was confirmed by the pore size distribution analysis presented in (Belot, Vidal, Votsmeier, et al. 2020). These two different behaviors in the evolution of the mean pore size of the porous structure with the increase in the amount of washcoat had a significant impact on the evolution of c-GPF flow paths and catalytic performance, as presented in the following subsections.

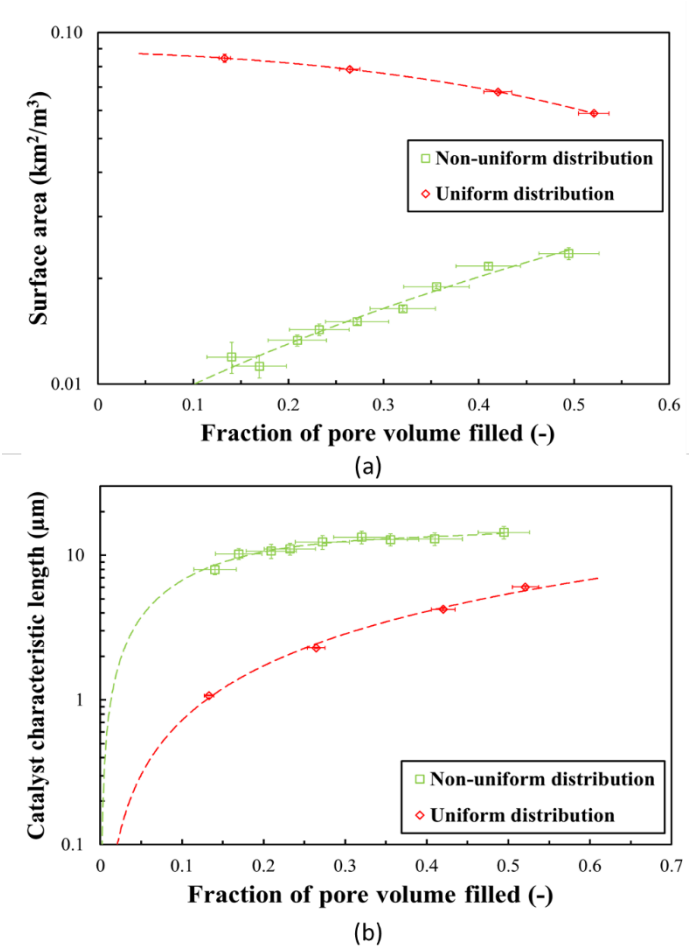

Figure 6.10: Evolution of the (a) surface area ($S_{0,2,0}$) and (b) the corresponding characteristic length (L_{cat}) of the catalyst phase with respect to the pore space phase, as a function of the amount of washcoat (f_w) for the two washcoat distribution profiles in the reconstructed GPF porous wall structures. The dashed lines are a guide for the eye, and the error bars represent the standard deviations of the reported mean values for the four wall subdomains.

Based on the visualizations in Figure 6.4, it appears that the interfacial area between the washcoat and the pore space gradually decreases as the amount of washcoat increases for reconstructed

structures with a uniform washcoat distribution. On the other hand, for reconstructed structures with a non-uniform washcoat distribution, catalyst lumps appear to grow, leading to an increase in interfacial area and the clogging of small pores as the amount of washcoat increases. This observation was confirmed by a surface area analysis of the two distribution profiles. The surface area of the catalyst phase with respect to the pore phase ($S_{0,2,0}$) and the corresponding characteristic length (L_{cat}) averaged over the four subdomains for 13 of the 14 structures investigated are reported in Figure 6.10.

The first observation is that $S_{0,2,0}$ is significantly higher for a uniform distribution profile than for a non-uniform distribution profile for all the amounts of washcoat investigated. In the case of a uniform washcoat distribution, $S_{0,2,0}$ gradually decreases as the amount of washcoat increases due to the uniform filling of the pore volume and the resulting decrease in the interfacial area between the catalyst and the pore space. In the case of a non-uniform distribution, $S_{0,2,0}$ is constrained to much lower values because of a preferential clogging of small pores as a non-uniform distribution removes a great deal of interfacial area between the washcoat and the pore space. However, as the non-uniform amount of washcoat is increased, the gradual but limited increase in surface area between the catalyst and the pores results from the significant growth of catalyst lumps, leading to an increase in the interfacial area despite further clogging of small pores, as can been seen in Figure 6.4. From Figure 6.10 (b), it appears that the corresponding L_{cat} increases gradually for the uniform washcoat distribution as the amount of washcoat is increased, whereas for the non-uniform case, after an initial increase at lower amount of washcoat ($f_w \leq \sim 30\%$) , L_{cat} reaches a more or less constant value of ~ 15 µm.

These two different trends in both the evolution of $S_{0,2,0}$ and thus L_{cat} lead to a different accessibility of the washcoat volume, which had a significant impact on the catalytic performance of the two distribution profiles, as will be presented in Sections 4.3 and 4.4.

6.4.2 Gas flow

Once the flow field has been computed using the LBM, the flow properties of the structures, like pressure drop (ΔP) and permeability (k), can be calculated. The flow properties of the 14 structures investigated in the present study are reported in (Belot, Vidal, Votsmeier, et al. 2020). For the sake

of concision, the reader is referred to this article for a detailed description of these properties. Here, only a comparison between two flow field visualizations is presented in Figure 6.11 to highlight some important differences between uniform and non-uniform structures. These visualizations show the different gas flow profiles for a uniformly coated structure (one subdomain of structure U2) and a non-uniformly coated structure (one subdomain of the OS structure), with amounts of washcoat that are as similar and typical as possible (i.e., $f_w \approx 23\%$). It can be seen that the diameters of the flow pathways in the uniformly coated structure are globally smaller than those in the non-uniformly coated structure. This can be explained, based on the mean pore diameter results in Figure 6.7, by (1) the uniform narrowing of the pore paths in the case of a uniform distribution and (2) the preferential filling of the small pores leading to a redirection of the flow through the bigger pores in the case of a non-uniform distribution. This channeling of the flow in favor of the bigger pores in the latter case have consequences on the filtration performance of a c-GPF at the micro-scale, as highlighted in (Belot, Vidal, Votsmeier, et al. 2020). We will get back to this when the catalytic performance of the structures is analyzed.

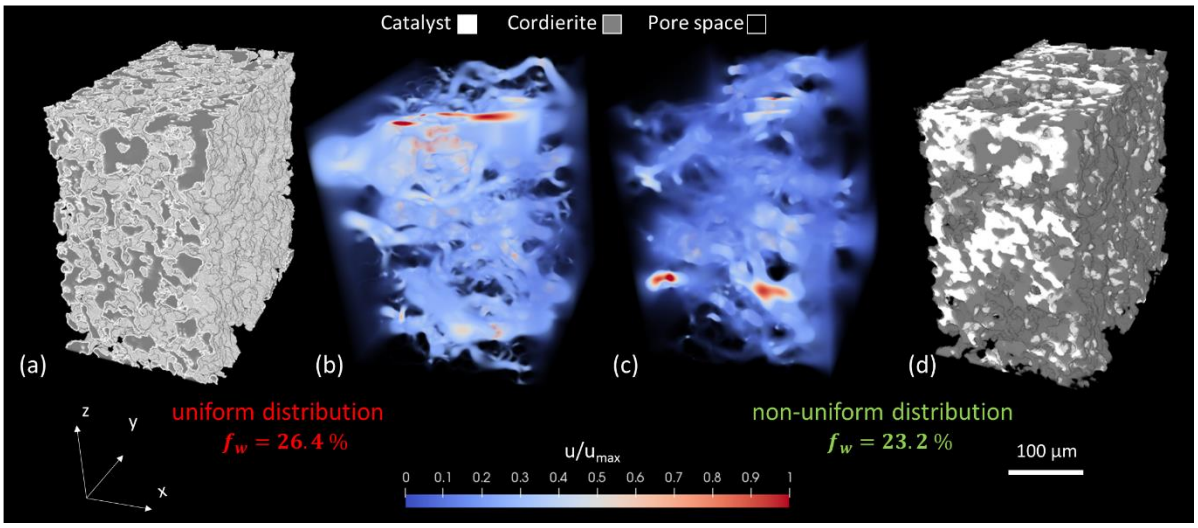

Figure 6.11: Visualizations of the reconstructed U2 (a) and OS (d) structures for one 256×389×400-voxel subdomain, and their corresponding flow fields (respectively (b) and (c)) obtained from LBM simulations.

6.4.3 Catalytic conversion

Once the concentration field has been computed using the LBM for each of the 14 reconstructed structures, catalytic conversion can be calculated from the data using Eq. (6.25). Following (Greiner et al. 2019), the present study investigated a first-order reaction of a hypothetical chemical species with a kinetic rate constant k_1 (see Table 6.1), the magnitude of which implies a fast reaction and thus a transitional regime close to a mass transport-limited regime. The conclusions set out in the following paragraphs are thus valid for this specific regime only. Nonetheless, the effect of different rate constants was also assessed. The catalytic conversion values obtained for the two distribution profiles are presented in Figure 6.12. As expected, catalytic conversion increases as the amount of washcoat increases for both the uniform and non-uniform distribution profiles, because more washcoat is available to the chemical species for conversion. The overall trend is similar for both distribution profiles, from a relatively sharp initial increase to a gradual flattening of the curves towards 100% conversion at high amounts of washcoat.

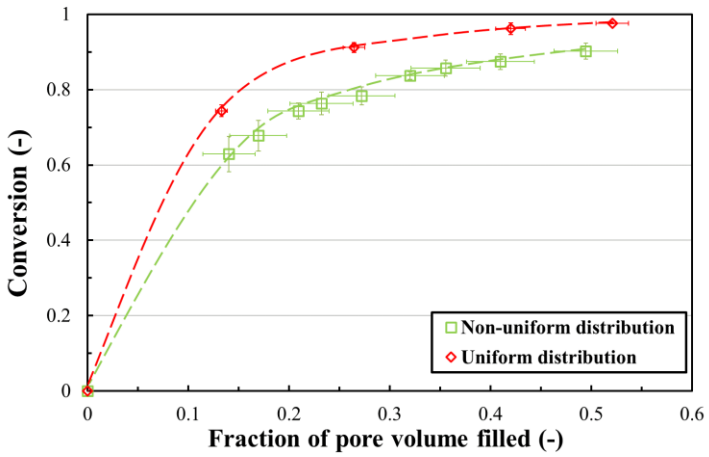

Figure 6.12: Evolution of catalytic conversion (X) for a fast first-order reaction as a function of the amount of washcoat (f_w) for the two washcoat distribution profiles and all the reconstructed GPF porous wall structures. The dashed lines are a guide for the eye, and the error bars represent the standard deviations of the reported mean values for the four wall subdomains.

However, the conversion for the uniform distribution series is systematically higher than for the non-uniform counterparts, for this first-order reaction. A uniform distribution profile can reach up to 20% better chemical conversion than a non-uniform distribution profile in the range $f_w < \sim 30\%$. At low amounts of washcoat, adding catalyst markedly increases the conversion of the chemical species for a uniform distribution. For a non-uniform distribution, the preferential filling of the small pores, which have a larger proportion of surface area than the larger pores, as can be deduced from Figure 6.10, leads to a lower increase in chemical conversion because of the lower availability of the catalyst due to transport limitations.

It is interesting to note that the amount of washcoat needed for a uniform deposition to obtain the same conversion as the OS structure (i.e., a non-uniform distribution at $f_w \approx 23\%$) is close to half that of the OS structure (i.e., $f_w \approx 12\%$). Substantial catalyst reduction could thus be achieved if the uniformity of the washcoat could be improved in the case of a transitional regime close to the transport-limited regime.

Figure 6.13 shows the concentration fields in one subdomain of the U2 and OS structures with the fast first-order reaction. These two structures have relatively similar amounts of washcoat (i.e., $f_w = 26.4\%$ and $f_w = 23.2\%$, respectively). Large differences in the concentration field profiles are observed, which can be attributed to the difference in coating uniformity. For the uniform distribution, conversion is gradual along the wall thickness whereas, for the non-uniform distribution, conversion is degraded by the presence of larger pores, which are open to the flow, devoid of catalyst, and through which most of the chemical species is transported (see Figure 6.11). The metric that quantifies this observable result is catalyst coating effectiveness (see Eq. (6.27)), the results of which are presented in the next subsection.

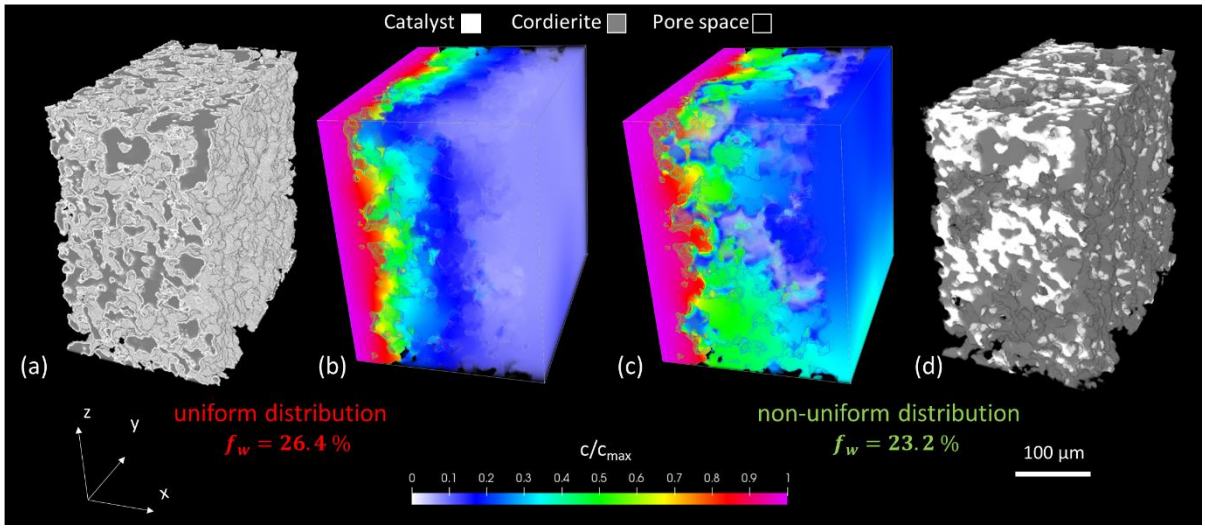

Figure 6.13: Visualizations of the reconstructed U2 (a) and OS (d) structures for one 256×389×400-voxel subdomain and their corresponding concentration fields (respectively (b) and (c)) as obtained from LBM simulations considering a fast first-order reaction.

To understand the impact of the reaction rate on the differences in conversion between uniform and non-uniform catalyst distributions, additional simulations on one subdomain of the N8 and U4 structures were conducted for different values of the rate constant k_1. Considering the two structures with the highest amounts of washcoat, as done here, maximizes the differences in uniformity between the two distributions and is expected to enhance the impact on conversion. Conversion as a function of the rate constant k_1 is reported in Figure 6.14. The results show that the impact of the washcoat distribution profiles on conversion becomes apparent for $\sim 10^2\ \text{s}^{-1} \leq k_1 \leq \sim 2 \times 10^4$

s^{-1}, i.e., for a transition between the kinetics-limited and the transport-limited regimes, more precisely here for Damköhler numbers in the range $\sim 0.01 \leq \mathrm{Da}_{II} \leq \sim 5$. At lower k_1 values, conversion is low and there is virtually no difference in catalytic conversion as the catalytic regime becomes kinetics-limited. The uniformity of the catalyst coating is not an issue in this case as relatively fast diffusion makes the catalyst available no matter how uniform it is. At the other end of the spectrum, at $k_1 = 10^5$ s^{-1}, the reaction rate is so fast that only a small amount of washcoat is required and its uniformity is unimportant. Thus, generalization of the results in Figure 6.12 is limited to the transport-limited regime at the one superficial velocity investigated ($U = 0.055$ $m.s^{-1}$).

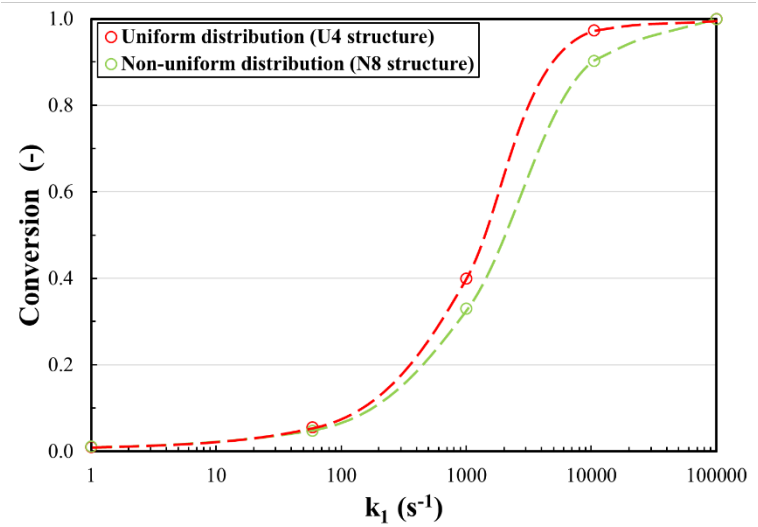

Figure 6.14: Evolution of the conversion (X) for a first-order reaction as a function of the rate constant (k_1) for a uniform washcoat distribution profile (one subdomain of the U4 structure with $f_w = 52.1\%$) and a non-uniform distribution profile (one subdomain of the N8 structure with $f_w = 49.4\%$) in the reconstructed GPF porous wall. The dashed lines are a guide for the eye.

The chemical conversion results of the two washcoat uniformity distribution series indicate, as expected, that the uniform distribution is more efficient than the non-uniform distribution, but only in the transition between the kinetics- and transport-limited regimes. Conversion is also highly dependent on the amount of washcoat and the reaction rate considered.

To assess the sensitivity of X to the type of reaction chosen, additional simulations were conducted on the two washcoat distribution series and an inhibition kinetics instead of a first-order reaction. The results are reported in Figure 6.15.

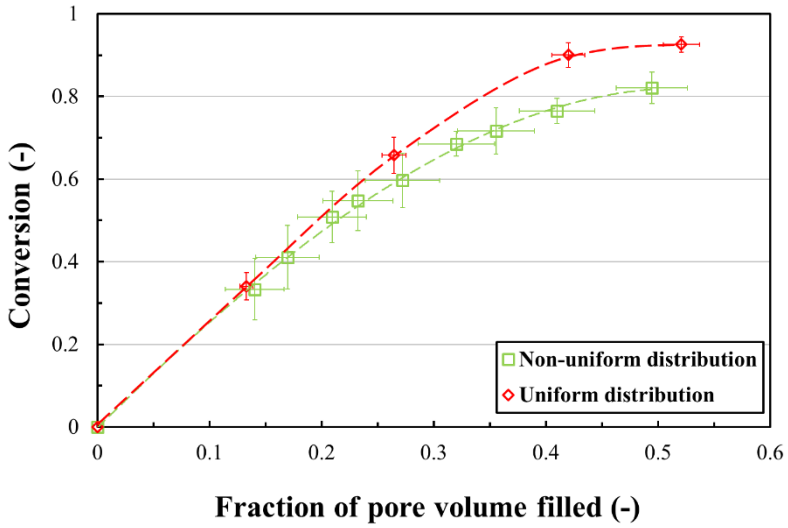

Figure 6.15: Evolution of catalytic conversion (X) for an inhibition kinetics as a function of the amount of washcoat (f_w) for the two washcoat distribution profiles in the reconstructed GPF porous wall structures. The dashed lines are a guide for the eye, and the error bars represent the standard deviations of the reported mean values for the four wall subdomains

The first observation is that lower conversions were reached for inhibition kinetics than for the first-order reaction studied for all washcoat amounts and levels of uniformity. The trends between the first-order reaction (Figure 6.12) and the one tested with the inhibition kinetics (Figure 6.15) were generally similar, i.e. an increase in conversion as the amount of washcoat is increased, but the increase is more gradual with the inhibition kinetics and the difference between a uniform and a non-uniform distribution is less important at low washcoat amount, but higher at large loadings. As a matter of fact, a mere improvement of 5% in conversion is obtained by improving the washcoat uniformity with inhibition kinetics at $f_w \approx 23\%$ (i.e. for the OS structure), whereas it is a 20% improvement for the first-order reaction. This result is obviously only valid for the kinetic constants investigated in this work (see Table 6.1). Nonetheless, this result shows that the use of a

uniform washcoat distribution can also be advantageous in the case of a more complex reaction kinetics, yet the overall performance still depends on the flow and properties of the catalyst.

6.4.4 Catalyst coating effectiveness

Chemical conversion is a good indicator of the efficiency of a specific catalytic deposition for treating harmful gases. Nonetheless, this value does not take the quantity of catalyst used to obtain such a chemical conversion performance into account. To gain a better idea of how useful the catalyst is to the conversion of the chemical species, catalyst coating effectiveness must be evaluated (see Eq. (6.27)). If a low concentration of chemical species is found in the catalyst, this means that only a low proportion of the catalyst contributed to the reaction, which reduces catalyst coating effectiveness. On the other hand, if a high concentration of chemical species is found in the catalyst, this means that the whole volume of catalyst contributed to the reaction, which increases catalyst coating effectiveness.

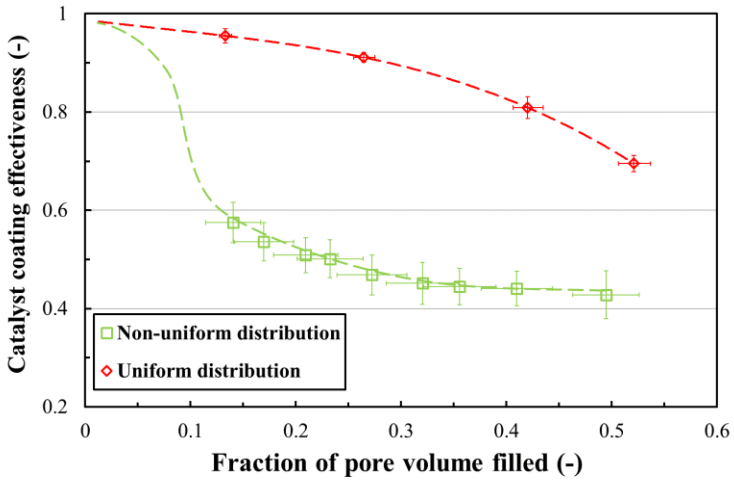

Figure 6.16: Evolution of catalyst coating effectiveness (η) for a fast first-order reaction as a function of the amount of washcoat (f_w) for the two washcoat distribution profiles in the reconstructed GPF porous wall structures. The dashed lines are a guide for the eye, and the error bars represent the standard deviations of the reported mean values for the four wall subdomains.

Catalyst coating effectiveness (η) values for the two washcoat distribution profiles are shown in Figure 6.16 for a fast first-order reaction, i.e., conditions corresponding to the transitional regime close to the transport-limited regime. Figure 6.16 shows that η decreases in tandem with an increase in the amount of washcoat for both distributions. This first observation is very intuitive, given that a greater proportion of the washcoat volume is less easily accessible by the chemical species as the amount of catalyst is increased. In the case of a uniform distribution, η decreases more gradually from the 100% effectiveness obtained with a very thin catalyst coating. This is due to the homogeneous incrementation of the thickness of the catalyst, which gradually increases the catalyst volume while the interfacial area between the washcoat and the pore space decreases (as can be seen in Figure 6.10). This drives additional catalyst volumes further and further from the interface with the pore space, making them harder to access by a chemical species.

In the case of a non-uniform distribution, the trend is different. From the initial few catalyst nuclei that grow as more catalyst is non-uniformly added (as can be seen in Figure 6.4), η rapidly drops to a value of $\sim$50%. The growth of catalyst lumps, as already discussed, results in a larger

proportion of the catalyst becoming less accessible to the chemical species and more affected by transport limitations. This phenomenon takes place despite the gradual but limited growth of the interfacial area between the catalyst and the pores (see Figure 6.10), which results from the expansion of the catalyst lumps. Above $f_w \approx 20\%$, η decreases only marginally because the lower accessibility of washcoat volumes is almost counterbalanced by the growth of the interfacial area and, as a result, η levels off to a plateau at $\eta \approx 45\%$. Moreover, results in Figure 6.16 show that for the fast first-order reaction, up to a 80% gain in catalyst coating effectiveness is obtained for a uniform distribution compared to a non-uniform distribution (notably at $f_w \approx 23\%$, which corresponds to the amount of washcoat of the OS structure). This result is consistent with that of Section 4.3 showing that a $\sim$50% increase in the amount of washcoat is required to reach the same conversion when going from a uniform to a non-uniform distribution.

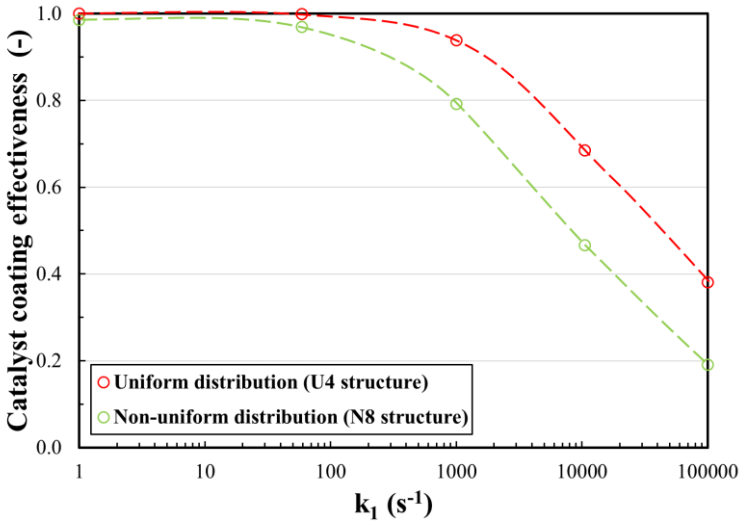

Figure 6.17: Evolution of catalyst coating effectiveness (η) for a fast first-order reaction as a function of the rate constant (k_1) for a uniform washcoat distribution profile (one subdomain of the U4 structure with $f_w = 52.1\%$) and a non-uniform distribution profile (one subdomain of the N8 structure with $f_w = 49.4\%$) in the reconstructed GPF porous wall. The dashed lines are a guide for the eye.

As for chemical conversion, η was evaluated on one subdomain of the N8 and U4 structures (see Figure 6.14) as a function of the kinetic constant k_1. Figure 6.17 shows that, in the kinetics-limited regime, for which the overall conversion is very low, as shown in Figure 6.14 (i.e., for $k_1 \leq$

$\sim 10^2$ s^{-1}), η is similar for both washcoat distributions and is close to 100%. Beyond this threshold, i.e., from the transitional to the transport-limited regime, η decreases with the same slope for both washcoat distributions as k_1 increases. Although it was not simulated, it is expected that η would eventually go asymptotically to zero for both washcoat distributions in the case of hypothetical reaction rates $k_1 \gg 10^4$ s^{-1}, for which conversion would reach 100% (see Figure 6.14), and for which only a small amount of catalyst would be required, making the thick coatings used for the U4 and N8 structures very inefficient.

To further assess the validity of our numerical predictions and compare the results with the Thiele modulus theory, the η data points presented in both Figure 6.16 and Figure 6.17 are plotted in Figure 6.18 as a function of the Thiele modulus $\Phi = \mathrm{Da}_{II}^{1/2}$ (see Eq. (6.24)). Apparent master curves were obtained for both the uniform and non-uniform washcoat distribution profiles in accordance with the Thiele modulus theory. They were fitted through weighted non-linear regressions, giving four times as much weight to the mean values (data from Figure 6.16) as to the data point of a single subdomain (data from Figure 6.17), by means of the following single-parameter relationship adapted from (Hayes and Mmbaga 2012; Leung and Hayes 1996):

$$\eta = \left(\frac{1}{1+\Phi^n}\right)^{1/n} \tag{6.28}$$

where n is a fitted parameter that is expected to depend on the "shape" of the washcoat deposition and is found to vary within a relatively limited range for the structures studied, i.e. from $n = 1.28 \pm 0.03$ to 1.10 ± 0.01 for the uniform and non-uniform washcoat distribution series, respectively (with $R^2 = 0.988$ and 0.990 for the corresponding regressions, and p-value $= 3.75 \times 10^{-11}$ and 4.97×10^{-19} for the corresponding fitted parameters, respectively). The fitted relationships are compared with theoretical ones reported for spherical pellets and slab-shaped catalyst layers (see e.g. (Hayes and Mmbaga 2012) for these classical expressions), both plotted as a function of a generalized Thiele modulus defined in terms of a characteristic length calculated as the catalyst surface-to-volume ratio. Interestingly, the single-parameter correlation used here can also represent very well data generated by the classical expressions for spherical pellets and slab-shaped catalyst layers using $n = 1.80 \pm 0.01$ and $n = 2.43 \pm 0.02$, respectively (with $R^2 = 1.00$ for both regressions). As one would

expect, the Thiele modulus threshold at which the decay of the catalyst coating effectiveness takes place, when mass transport limitation starts to become dominant, slightly varies with respect to the coating uniformity, in a way similar to a change of catalyst shape, i.e. going from sphere (blue dashed curve in Figure 6.18) to slab (orange dashed curve). As a matter of fact, washcoats with a more rounded or spherical shape, i.e. non-uniform coatings (see Figure 6.4), yield for a given Φ slightly lower η values than uniform coatings that can be regarded as a collection of slabs. A similar trend is obtained for spherical catalyst pellets and slab-shaped catalyst layers. It is also observed that the numerical data in Figure 6.18 converge towards $1/\Phi$ for large Thiele moduli, as expected, and without the need of any other adjustable parameters. This agreement with the Thiele modulus theory is concrete evidence of the soundness of the proposed numerical approach.

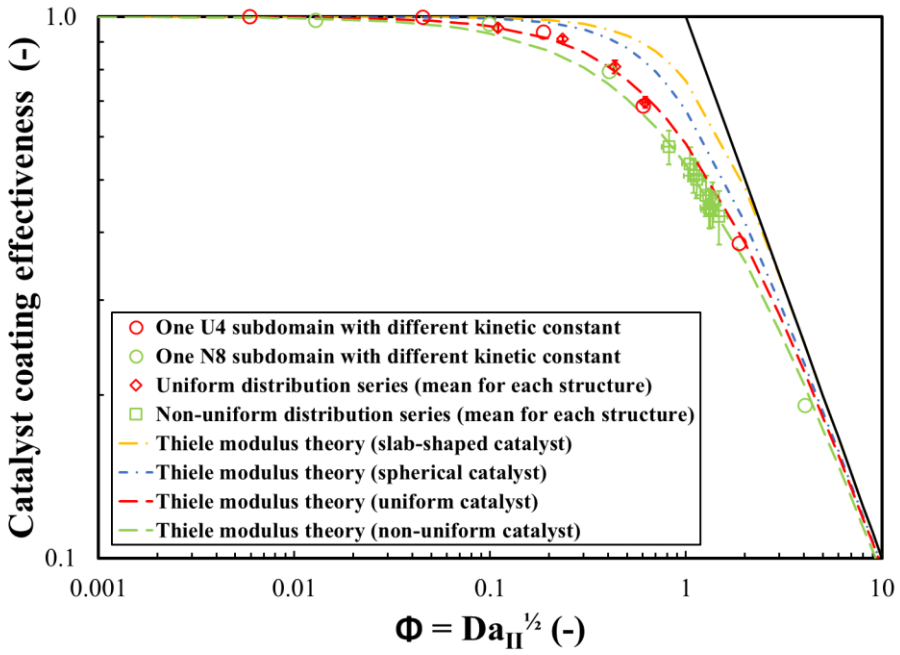

Figure 6.18: Evolution of catalyst coating effectiveness (η) for a first-order reaction as a function of the Thiele modulus (Φ) for uniform (red symbols) and non-uniform (green symbols) washcoat distribution profiles in the reconstructed GPF porous wall (combined data from both Figures 6.16 and 6.17), fitted through weighted non-linear regressions with Eq. (6.28) (red and green dashed curves respectively) and compared with relationships from the Thiele modulus theory for slab-shaped and spherical catalyst pellets (Liu 2017; Doran 2013). The black line represents the theoretical $1/\Phi$ relationship expected at high Thiele moduli.

Overall, these results underline that the chosen characteristic length, which is defined as the ratio of the volume of the catalyst phase to the open surface of the catalyst and appears in the expression for the Thiele modulus Φ, provides an excellent descriptor of the catalyst coating effectiveness. In addition, parameter n in Eq. (6.28) can be interpreted as a "washcoat shape factor" that is required to fit the data accurately. Using this characteristic length and this shape factor, the result suggests that the effectiveness can be quantitatively predicted for a given form of washcoat non-uniformity using a standard analytical formula. While more work would be needed to understand better how n varies with the shape of the washcoat, the correlation obtained for the uniform washcoat distribution may serve as an upper bound for the coating effectiveness. Alternatively, one may use the average value $n = 1.19 \pm 0.02$, which provides a good fit for all the current data with $R^2 =$

0.984 (not shown in Figure 6.18 for clarity). Using this n value, the correlation fits all our numerical data for the different washcoat distributions with a maximum relative deviation of 2.8%. Given the wide range of catalyst structure represented in our study, the good fit to all the data suggests that our correlation provides a good description for general washcoat distributions. Overall, these results are important as they provide a tool for catalyst design and guidance for the optimization of the catalyst deposition process. They are also relevant for the simulation community, since they show that a quantitative description of the reactive flow in the wall can be achieved by means of a homogeneous wall model without the need of further detailed pore scale simulations. The required catalyst washcoat effectiveness could be determined directly from the washcoat geometry, through desorption characteristics measurements for instance to identify the active surface area (Shen et al. 2020), without the need for pore-scale simulations or conversion measurements.

6.4.5 Overall performance

As reported in the present work, structures with a uniform washcoat distribution displayed a better catalytic performance than structures with a non-uniform washcoat distribution investigated here. In a previous study (Belot, Vidal, Votsmeier, et al. 2020), it was also shown that uniformly coated structures perform better in terms of filtration performance as measured by a filter quality factor (Q_f), which is an intrinsic filter property independent of filter thickness and is defined as $Q_f = -\log(1 - E_f)/\Delta P$, with E_f being soot capture efficiency and ΔP being pressure drop through the filter. The numerical models developed in the present study and in a previous study (Belot, Vidal, Votsmeier, et al. 2020) are able to quantify the advantage in terms of overall c-PF performance, i.e., in terms of both filtration and catalytic performance, of specific washcoat distributions compared to others. The proposed combined model appears to be a useful approach to assess the overall performance of a catalyst coating deposition in the porous wall of any PF system and thus provide guidance for optimizing its distribution. To illustrate this, Figure 6.19 provides a comparison of both the filter quality factor (reported in Figure 6.16 from (Belot, Vidal, Votsmeier, et al. 2020)) and catalytic conversion between the uniform and non-uniform washcoat distributions investigated in the present study. For example, one can see that the quality factor improves by 50% (corresponding to a $\sim 10\%$ relative decrease in ΔP and relative capture efficiency improvement

by ~ 70%, as shown in Figures 6.11 and 6.14, respectively, in (Belot, Vidal, Votsmeier, et al. 2020)). In addition, catalytic conversion can be enhanced by 20% by improving the uniformity of the catalyst coating distribution of the N3 sample ($f_w = 20.9\%$). Such precise quantifications of possible improvements obtained by refining washcoat uniformity represents valuable information for researchers interested in optimizing the overall performance of a c-PF.

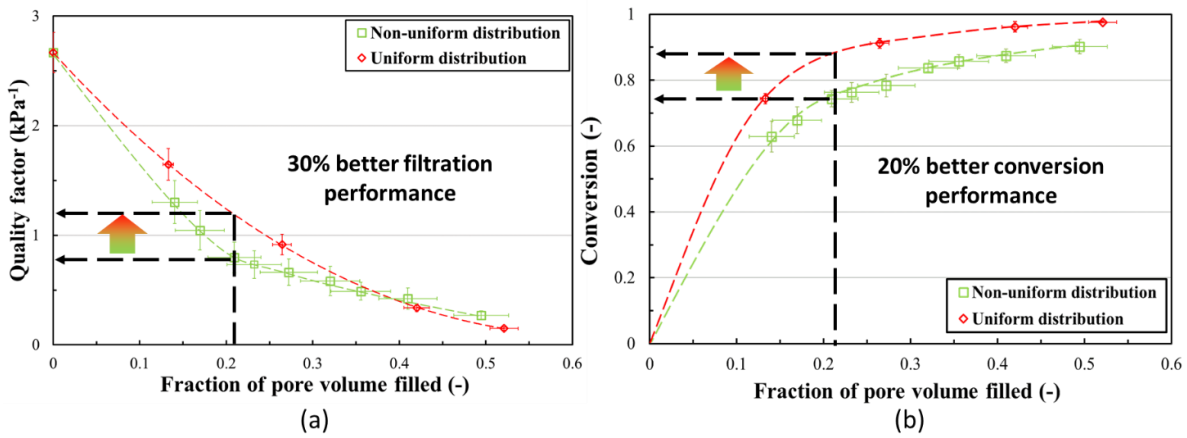

Figure 6.19: Example of the quantification of possible improvements in filtration (a) and catalytic (b) performance by changing from a non-uniform to a uniform washcoat distribution for the N3 structure ($f_w = 20.9\%$) as predicted by the results presented both in the present study (b) and in (Belot, Vidal, Votsmeier, et al. 2020) (a).

6.5 Conclusion

Following a previous study by (Belot, Vidal, Votsmeier, et al. 2020), which studied the impact of washcoat amount and uniformity on the filtration performance of a catalyst-coated gasoline particulate filter (c-GPF) at the wall scale, a three-step numerical model is proposed here to predict the catalytic performance of a c-GPF. It consists of (1) reconstructing representative elementary volumes of the porous walls of the c-GPF using tomographic images processed by a set of morphological image operations, and of (2) computing the flow field and (3) the concentration field following a fast first-order reaction of a hypothetical chemical species within the c-GPF wall using in-house LBM solvers. This approach can be used to predict and compare the catalytic conversion

and catalyst coating effectiveness of a c-GPF wall with a uniform or a non-uniform washcoat distribution and different washcoat amounts. Although caution should be exercised when generalizing the findings reported here to all non-uniform washcoat depositions and to all c-GPF wall substrates, the following conclusions can be drawn from the present study:

- For the cordierite substrate investigated, catalytic conversion increases markedly for both the uniform and non-uniform washcoat distributions with up to 30% of the pore volume filled with washcoat. However, the uniform coating provides up to ~20% better conversion for a fast first-order reaction. Beyond these amounts of washcoat, only a marginal improvement can be obtained.
- The difference in catalytic conversion between the two types of washcoat uniformity is mainly apparent within the transitional regime, that is, between the kinetics- and transport-limited regimes, for Damköhler numbers in the range $\sim 0.01 \leq \mathrm{Da}_{II} \leq \sim 5$. This difference can be explained by the lower specific surface area between the catalyst and the pores for the non-uniform distribution, which results from the clogging of the small pores, making a large fraction of catalyst unavailable for reaction.
- Catalyst coating effectiveness for a fast first-order and reaction gradually decreases as the amount of washcoat is increased for a uniform deposition, whereas catalyst coating effectiveness drops sharply for a non-uniform deposition with a low amount of washcoat. The latter trend can be explained by the nature of the non-uniformity studied, which consists of catalyst lumps expanding in size as the amount of washcoat is increased and which makes initially deposited volumes of washcoat less and less accessible because of chemical species transport limitations. Up to an 80% gain in catalyst coating effectiveness for a uniform distribution can be obtained compared to a non-uniform distribution for this reaction.
- The computed catalyst coating effectiveness data can be fitted to a single-parameter correlation that agrees with the Thiele modulus theory. This correlation underlines the importance of both the characteristic length, defined as the ratio of the volume of the catalyst phase to the open surface of the catalyst, and of parameter *n* that is related to the overall shape of the catalyst within the structure. The agreement with the Thiele modulus theory is concrete evidence of the soundness of the proposed numerical approach.

Using results from (Belot, Vidal, Votsmeier, et al. 2020), a case study demonstrated how the proposed numerical model can be a valuable and quantitative approach that can provide insights into whether and why specific catalyst coatings perform better than others in terms of filtration and catalytic performance, and thus provide guidance for particulate filter researchers and manufacturers for improving exhaust gas aftertreatment devices. This case study showed that a uniform washcoat distribution outperforms the non-uniform washcoat distribution studied in terms of both filtration and catalytic functionalities. Although this result could have been anticipated, the proposed model makes it possible to quantify the improvements that can be expected.

Lastly, it is interesting to note that, as the LBM approach used here is an intrinsically transient and highly parallelizable computational method, we believe that the proposed approach would be well-suited to study the time evolution of many concurrent reactions under varying conditions, such as for studying the impact of catalyst oxygen storage on NOx, CO, and HC emissions. This would require solving as many ADR problems as there are species involved in these reactions and deploying the resulting coupled computations on a high-performance GPU cluster, a solution that is capable of substantially accelerating the computations (Leclaire et al. 2018; Calore et al. 2016). This will be the subject of a future study.

6.6 Acknowledgements

This research was supported by the Natural Sciences and Engineering Research Council of Canada through a Strategic Partnership Grant (STPGP-493797-16) and a Grant from the Collaborative Research and Training Experience (CREATE-481695-2016) program in Simulation-based Engineering Science (Génie Par la Simulation). The authors would also like to thank Calcul Québec/Compute Canada for the computational resources and support provided.

.

6.7 Appendix A – Additional LBM code verifications

In this appendix, two additional test cases are presented to verify the LBM code used to solve the ADR equation in the present study. First, an advection-diffusion-first-order reaction is considered, then a simpler case with an inhibition kinetics is studied.

6.7.1 A.1 First-order reaction in concentric square materials

This verification test case consists of a channel with a square section presenting two hypothetical media labeled 1 and 2, as shown in Figure 6.20. The ratio between the two diffusion coefficients is $D_1/D_2=65$, and the velocity is uniform in Medium 1 and set to $U=L/t_1$ m/s, with $t_1=1$ s, $D_1=L^2/t_2$, and $t_2=t_1/20$. A first-order reaction exclusively takes place in Medium *2*. Dirichlet boundary conditions are set at the inlet ($c = 0$ mol/l in Medium 2 and $c = c_0 = 1$ mol/l in Medium 1) and an outflow boundary condition at the outlet (i.e., $D\frac{\partial c}{\partial x} = 0$).

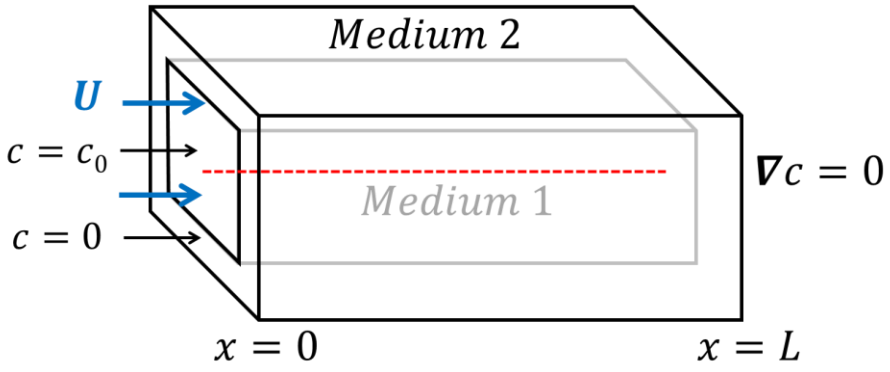

Figure 6.20: Schematic of the concentric square material test case. The red dashed line represents the direction along which the concentration data were gathered for the comparison.

The results were compared to those obtained using commercial COMSOL Multiphysics® software. Figure 6.21 shows that there is very good agreement between the results of the two programs.

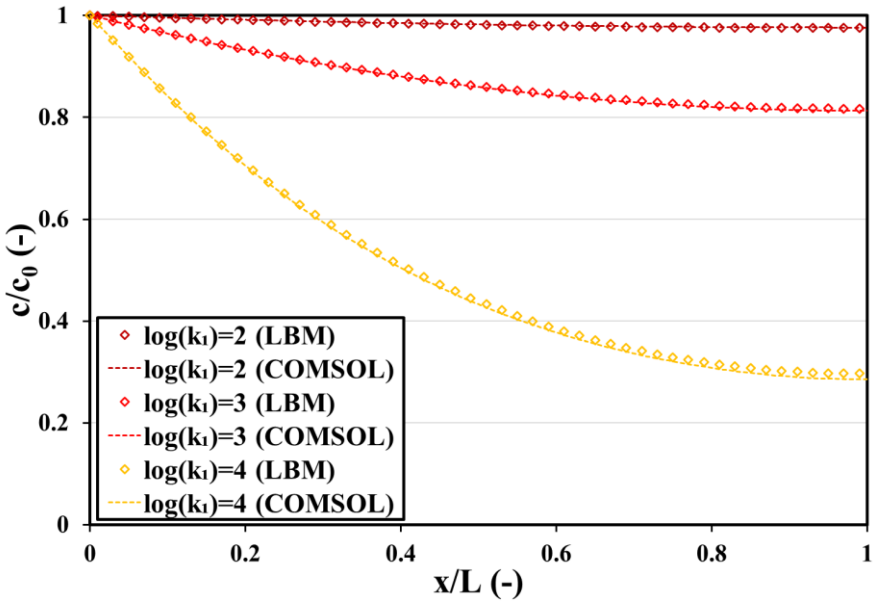

Figure 6.21: Concentration profile along the red dashed line of Figure 6.20 for different values of the kinetics constant k_1 (in s^{-1}) using the LBM code compared to the solutions obtained using COMSOL Multiphysics® software.

6.7.2 A.2 Inhibition kinetics reaction test case

This test case consists of a square channel of one phase as shown in Figure 6.22 where the inhibition kinetics reaction takes place. The velocity is uniform and is set to $U=L/t_1$ m/s, with $t_1=1$ s. A Dirichlet boundary condition is set at the inlet ($c = c_0 = 1$ mol/l) and an outflow boundary condition at the outlet (i.e., $D\frac{\partial c}{\partial x} = 0$). The diffusion coefficient is set to $D_1=L^2/t_2$ with $t_2=t_1/20$.

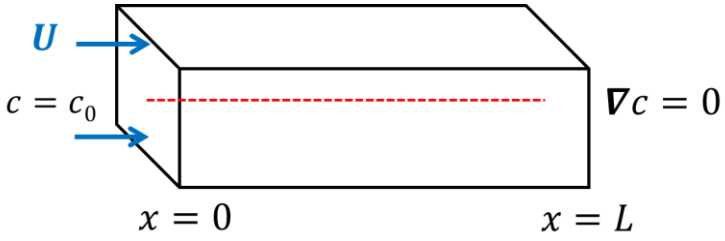

Figure 6.22: Schematic of the inhibition kinetics reaction test case. The red dashed line represents the direction along which the concentration data were gathered for the comparison.

The results were compared to those obtained with commercial COMSOL Multiphysics® software. As can been seen in Figure 6.23, very good agreement was found for the different kinetics parameters of k_1 and K.

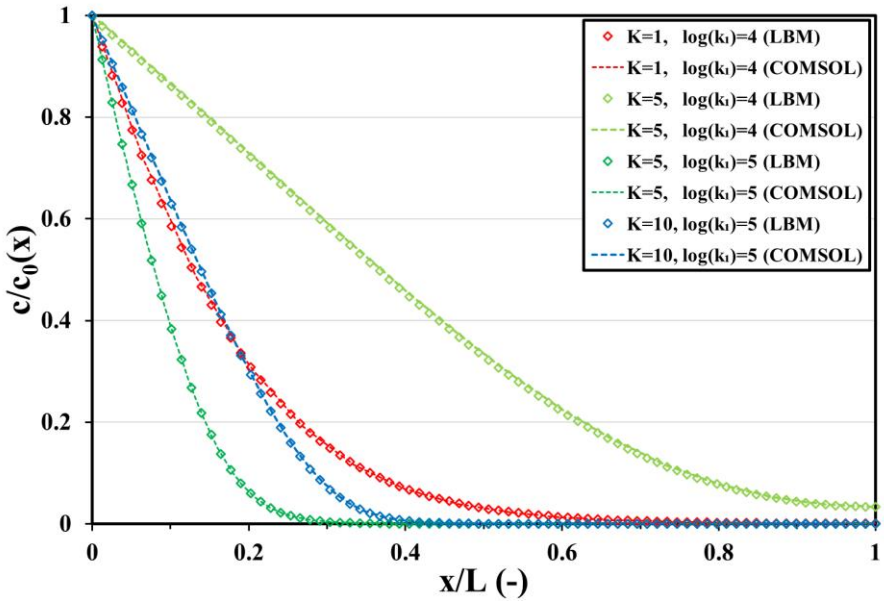

Figure 6.23: Concentration profile along the red dashed line of Figure 6.22 for different values of the kinetic and inhibition constants k_1 (in s^{-1}) and K (in m^3/mol) with the LBM code compared to the solutions obtained with COMSOL Multiphysics® software.

CHAPITRE 7 ARTICLE 3 : A 3D ADDITIVE MANUFACTURING APPROACH FOR THE VALIDATION OF A NUMERICAL WALL-SCALE MODEL OF CATALYTIC PARTICULATE FILTERS

Igor Belot, Yixun Sun, David Vidal, Martin Votsmeier, Philippe Causse, François Trochu and François Bertrand

Submitted to Chemical Engineering Journal

Abstract : The validation of a numerical model used to predict the permeability of the microporous wall of a coated gasoline particulate filer is arduous due to multiscale effects. To circumvent this, an experimental "magnified twin" approach based on kinematic similarity is proposed. It consists of (1) printing magnified porous wall sections by fused filament additive manufacturing; and (2) characterizing their permeability using a modified falling head permeability measurement device and testing procedure. A detailed approach is also proposed to select the appropriate scaling factor to produce the samples by 3D printing. Comparison between numerical, Blake-Kozeny, and experimental predictions of the impact of coating amount and degree of uniformity on wall permeability is presented. Despite the inherent sensitivity of permeability to pore space characteristics, a very good agreement is reported between simulations and experiments with a 19.3% mean discrepancy for the seven magnified structures tested. The proposed procedure is a relatively easy-to-implement and inexpensive method that may find many applications in the field of porous media.

7.1 Introduction

Porous media are ubiquitous at many different scales in a wide range of scientific fields, from soil chemistry (Baveye and Laba 2015) and lithium-ion power storage (Wu and Jiang 2013) to coal characterization (Nie et al. 2015), to name just a few. Predicting the transport phenomena that occur in such structures can be a challenging undertaking due to their typical multi-scale nature and complex geometry. Catalytic particulate filters for gasoline and diesel vehicles are no exception as they also make use of porous media to reduce noxious gas and soot emissions. Honeycomb ceramic-based structures coated with three-way catalysts are commonly used in coated gasoline particulate filters (c-GPF). A typical particulate filter (PF) device consists of a 20-cm-diameter

monolith made of an array of rectangular channels 10 cm in length and about 1 mm in width. These channels are alternatively plugged at the inlet and the outlet in a chessboard arrangement to force the passage of exhaust gases through their porous ceramic walls (Figure 7.1), and thus facilitate the capture and oxidation of soots as well as the conversion of gases.

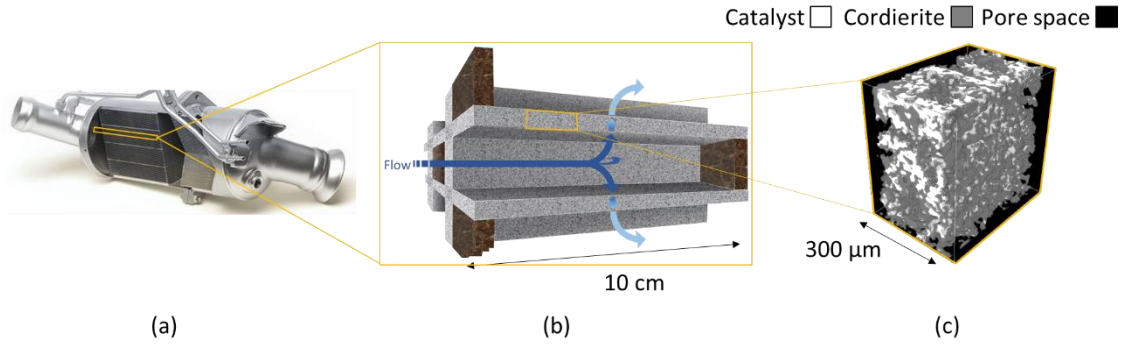

Figure 7.1: Representation of the different scales of a c-GPF: (a) whole filter scale, (b) channel scale, and (c) porous wall scale.

The substrate material making up the porous wall of GPFs is usually cordierite due to its geometrical properties that provide a large pore surface-to-volume ratio, its high thermal resistance, and its relatively low manufacturing cost (Guan et al. 2015). In addition, a three-way catalyst (TWC) coating (generally referred to as washcoat) is deposited on or within the porous walls of c-GPFs to reduce noxious emissions of nitrogen oxides (NO_X), carbon monoxide (CO), and hydrocarbons (HC) (Zhao, Lai, and Harrington 1999; Joshi and Johnson 2018; Thomas et al. 2019; Richter et al. 2012). Because of their multi-scale nature and multi-functionalities (i.e., soot capture and oxidation, and gas conversion), c-GPFs are very complex systems and their detailed behavior is not yet fully understood. The three main performance criteria of c-GPFs are (1) the pressure drop (ΔP), (2) the filtration efficiency (E_f), and (3) the catalyst conversion efficiency (η), the ultimate goal being to minimize ΔP while maximizing E_f and η. To help manufacturers design better c-GPFs, wall-scale numerical models are being developed to predict these performance criteria and thus provide guidelines on how to optimize the ceramic support and washcoat deposition, for instance. In a previous study (Belot, Vidal, Votsmeier, et al. 2020), the impact on the filtration performance of washcoat deposition uniformity inside the porous wall of a GPF was investigated. A uniform deposition was shown to improve filtration performance by up to 50% compared to a

non-uniform one. Another study that investigated the impact of in-wall vs. on-wall coatings showed that an in-wall coating provides better filter permeability than an on-wall coating (Kočí et al. 2019). In (Greiner et al. 2019), the catalyst distribution in the pore structure of a c-GPF was characterized by tomography and the reactive flow in the resulting pore network was simulated for a first-order reaction. It was shown that the efficiency of the catalytic reaction is governed by diffusion limitations in the catalyst domains. These studies typically used a three-step methodology to (1) reconstruct the porous wall based on tomography data or using reconstruction algorithms, and simulate therein (2) the flow field through computational fluid dynamics (CFD) and (3) mass transport using Lagrangian or Eulerian methods.

An essential step in the development of any numerical model consists in validating the model predictions using experimental measurements. Of the three performance criteria mentioned above, ΔP appears to be the most straightforward property to measure for validating wall-scale numerical models. Indeed, ΔP throughout the whole c-GPF is relatively easy to measure experimentally by simply running a test bench experiment with two pressure sensors, one upstream and one downstream from the filter (Mikulic et al. 2010; Tsuneyoshi, Takagi, and Yamamoto 2011; Swanson et al. 2013; George and Heibel 2016). The limitation of such an experimental approach is that it cannot on its own independently evaluate the contributions of the different parts of the GPF to the overall ΔP. With a clean c-GPF, ΔP can be mainly attributed to (1) friction loss along the channels, (2) flow expansion and contraction going in and coming out of the filter housing, (3) flow contraction and expansion going in and coming out of the monolith channels, and (4) pressure loss across the porous walls of every channel of the c-GPF (Koltsakis et al. 2013). The latter contribution is of interest for validating wall-scale models as it makes it possible to determine the wall permeability k using Darcy's law (Dullien 1979):

$$k = \frac{\mu U L}{\Delta P} \tag{7.1}$$

where U and μ are the superficial velocity and the dynamic viscosity of the fluid, respectively, and L is the length of the porous medium in the ΔP direction.

Wall permeability can be accurately assessed via simple mass and momentum balances with this experimental approach using high sensitivity sensors and certain assumptions such as a constant

flow rate in the radial direction and homogeneous characteristics of the porous material, for example (Masoudi, Heibel, and Then 2000; Konstandopoulos 2003). However, in the case of c-GPF applications, higher flow rates and fluctuating friction loss parameters along the channels makes it more complicated (Aleksandrova et al. 2018). For these reasons, determining the impact of washcoat deposition and the ceramic wall substrate on ΔP using such test bench experiments, for instance, is challenging in practice. In addition, these types of experiments require expensive laboratory resources such as a complete c-GPF system and a heavy set of compressors and pipes, which makes it difficult to perform ΔP measurements on real filter media. Other researchers have used wafers consisting of slices of single or multiple layers of PF channels, the permeability of which can be measured using a flow rig equipped with Pitot tubes (Aleksandrova et al. 2018; Lambert et al. 2017; Viswanathan et al. 2017). This procedure can be used to provide reasonably accurate measurements of the permeability of GPF walls, although it is not suitable for c-GPFs. In addition, not only does it require a flow rig, but the preparation of the wafer samples appears to be an essential but sensitive and complex step. A possible solution to overcome these difficulties would be to 3D print digital samples and measure their permeability.

3D printing has already been used in the manufacture of digitized rocks (Ishutov 2017), foams (Bracconi et al. 2019; Osei-Bonsu, Grassia, and Shokri 2018), and sandstones (Gomez, Chalaturnyk, and Zambrano-Narvaez 2018). Nowadays, numerous 3D printing processes are available. In the case of porous media manufacturing reported in the literature, the different printing techniques range from the classic additive manufacturing technique using the layer-by-layer deposition of a heated material (also known as Fused Deposition Modeling) to more advanced laser sintering, where a laser is used to sinter a powder (Otten et al. 2012; Rangel et al. 2013), or stereolithography, in which a resin in a pool is solidified layer-by-layer using a laser (Crandall et al. 2008). The last two techniques can achieve high-precision printing, stronger samples and shorter printing times, while the first method is more affordable and more readily available due to its maturity.

Very recently in the context of soil science, Ozelim and Cavalcante (2019) studied 3D additive manufacturing by laser sintering in combination with a falling head-based permeameter and numerical flow simulations as a valuable approach for building magnified representative porous structures with porosities ranging from 20% to 60% (Ozelim and Cavalcante 2019). However, the

computed and measured permeabilites differed on average by one order of magnitude. The authors attributed these dicrepancies to the magnification procedure used and the permeameter tests performed. In the study by (Bracconi et al. 2019), pressure losses through foams with porosities ranging from 70% to 90% were evaluated using CFD simulations combined with experiments on real stereolithography-printed foam structures. The authors reported very good agreement between numerical and experimental values. However, applying a similar methodology to the context of c-GPFs on structures with lower porosities but using a more affordable off-the-shelf printing technology remains to be demonstrated.

Several techniques have been proposed in the literature to directly measure the permeability of a manufactured porous sample while avoiding the need for cumbersome and expensive experimental setups (Nagy, Tabácks, and Huszák 2013). In practice, two experimental techniques are most often employed for relatively large sample sizes (~10 cm), namely the constant head and the falling head methods (Andres-Valeri et al. 2018; Hall 2004). The first technique measures permeability under constant inlet pressure whereas the second measures permeability under varying inlet pressures. The falling head technique is easier to set up. However, due to practical difficulties in measuring the flow rate, the range of measurable permeabilities for this technique is restricted to low values (at best ~10^{-10} m^2) (Zarandi, Pillai, and Barari 2018; Johnson, Arriaga, and Lowery 2005; Vardanega 2014). In the conventional falling head technique, a fluid is drained through the sample from a vertical standpipe placed on top of it, which provides the hydrostatic head. The set-up is usually cylindrical in shape with an expansion at the sample location such that the cross-section of the head pipe is smaller than that of the pipe containing the sample (Galvan et al. 2014; Pedescoll et al. 2011). The liquid interface position is recorded over time to assess the permeability of the sample using Darcy's law (see Eq. (7.1)). Some improvements have been made to this technique to broaden the range of achievable permeabilities such as, for example, by installing a strain gage to measure the fluid pressure and interface position automatically (Nightingale and Bianchi 1970; T., S., and C. 1998). More recently, (Sun et al. 2020) employed a modified falling head technique using a simpler set-up configuration and proposed a weighing procedure to assess sample permeability in the 10^{-8} - 10^{-7} m^2 range.

Based on the above, a twofold objective was pursued in the present study: (1) validate the impact of the washcoat amount and deposition uniformity on porous wall permeability as predicted by the

numerical wall-scale model of a c-GPF proposed by (Belot, Vidal, Votsmeier, et al. 2020), and (2) develop a quick-to-implement, reliable, and affordable experimental procedure based on 3D additive manufacturing of magnified porous structures using an off-the-shelf 3D printer (hereafter referred to as "magnified twins") and an easy-to-build modified falling head permeability measurement method. Essentially, this new experimental procedure aims to provide an alternative solution for validating CFD predictions of flows through small-scale porous media in the following situations: for screening porous structures (1) that only exist virtually and have not yet been manufactured and tested, (2) for which a direct experimental measurement would be difficult to carry out (e.g., because of the discrepancy between the sample characteristic lengths with respect to the requirements of permeability measurements), or (3) for research groups in need of an inexpensive and easily accessible permeability measurement technique. To the authors' knowledge, it is the first time that such a validation technique and detailed procedure is proposed, which is shown here to be effective in the context of particulate filters.

The remainder of this paper is organized as follows. In Section 2, the numerical and experimental methodologies used are explained in detail. In Section 3, after verifying the 3D printing procedure based on a porosity assessment, the agreement between numerical, semi-analytical and experimental permeability predictions of the investigated structures are assessed. Lastly, in Section 4, concluding remarks are provided and new opportunities for the validation and prediction of porous media permeability at the microscopic scale are discussed.

7.2 Methodology

This section is divided into two parts: (1) the numerical methodology used to study the impact of the washcoat distribution profile on Darcy's permeability of c-GPF porous walls is first recalled as it relies on a previous study (Belot, Vidal, Votsmeier, et al. 2020), and (2) the experimental procedure used to validate the permeability predictions obtained from this numerical study is carefully detailed.

7.2.1 Numerical model

To predict numerically the impact of the amount of catalyst deposited in the porous space of a c-GPF porous wall on permeability, a two-step procedure, which is a subset of a three-step

methodology established for the prediction of the overall filtration performance of c-GPFs in a previous study (Belot, Vidal, Votsmeier, et al. 2020), was used. Figure 7.2 summarizes this procedure. First, a set of porous walls was reconstructed from a tomographic image of a real filter, in which different catalyst amounts and distribution profiles were artificially deposited using numerical algorithms. Second, the flow field through the reconstructed structures using the Lattice Botzmann Method (LBM) was computed, making it possible to calculate the respective permeability of the samples. A brief overview of these two steps is presented next. For more details, the reader is referred to (Belot, Vidal, Votsmeier, et al. 2020).

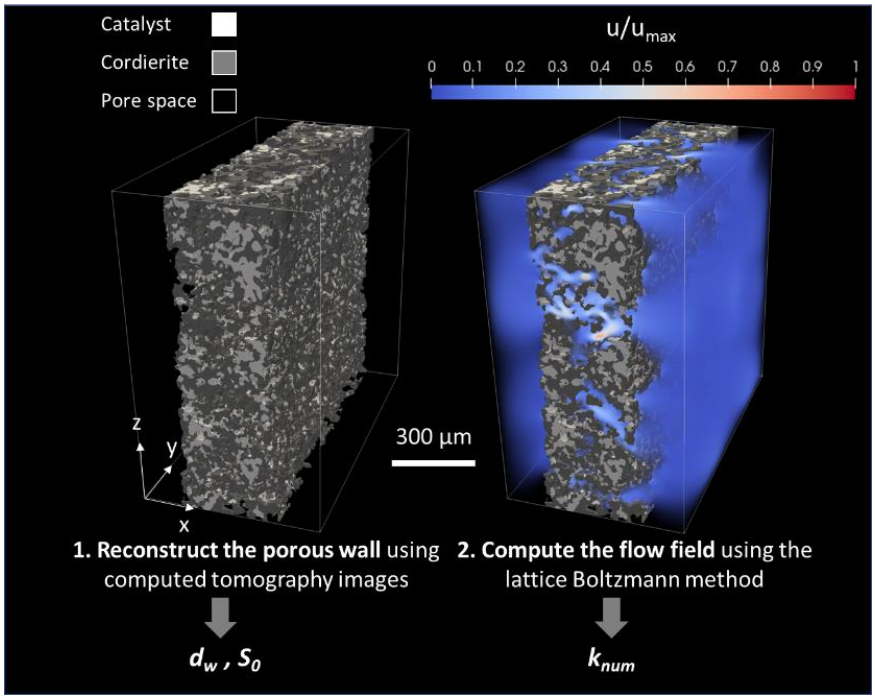

Figure 7.2: Representation of the two numerical steps used in the prediction of the permeability of a c-GPF porous wall at the microscopic scale.

7.2.1.1 Porous wall reconstruction

A 256×801×779-voxel domain was extracted from the raw data of the ~300-µm-thick channel wall starting from an X-ray CT scan image of a channel of a c-GPF acquired using a General Electric *Phoenix Nanotom M* at a resolution of 1.246 μm, the preparation of which is detailed in (Greiner

et al. 2019). The 8-bit grey scale image was then segmented into pore space, cordierite, and catalyst phases based on a thresholding algorithm developed in (Greiner et al. 2019). The catalyst coating of the original R&D sample was intentionally chosen for its non-uniform distribution. More precisely, this structure was digitally modified in a systematic way to create two series of artificial structures of various coat weights, with either uniform distribution or non-uniform distribution profiles. The latter series of profiles was generated by reducing or increasing the original washcoat non-uniformity and amount using catalyst phase erosion and dilation algorithms, respectively. Similarly, the uniform distribution series was generated by first erasing the catalyst phase of the original R&D sample and then, from the resulting structure, growing the catalyst phase uniformly using a dilation algorithm to create structures with various uniform coat weights.

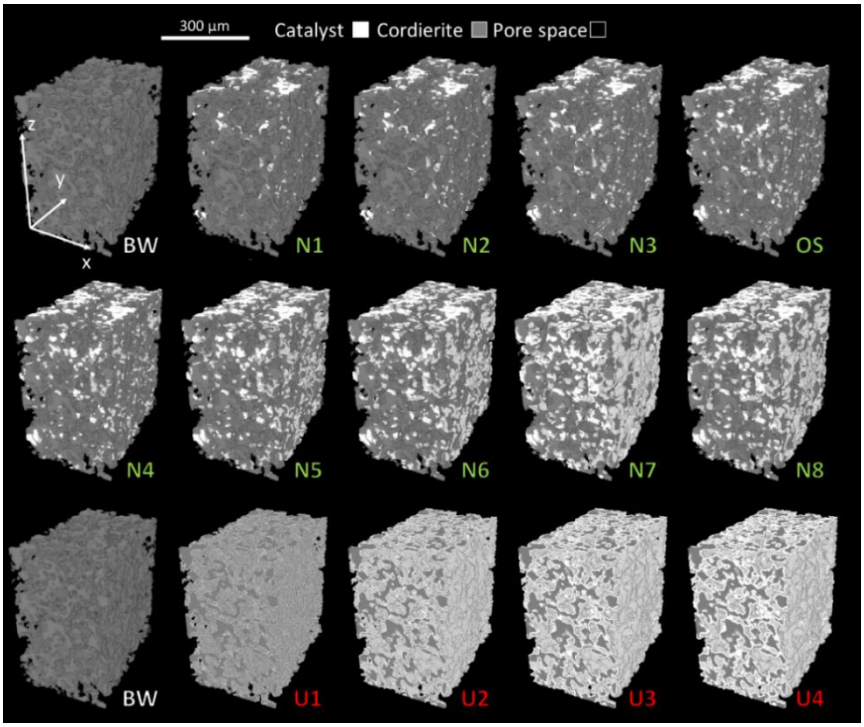

Figure 7.3: 3D visualizations of Subdomain 1 for each of the 14 different structures reconstructed. The structures labelled (in green) N1 to N8 and OS (for original structure) refer to non-uniform distribution profiles ordered in increasing amounts of washcoat. Similarly, the structures labelled U1 to U4 (in red) refer to uniform distribution profiles ordered in increasing amounts of washcoat. Lastly, the bare wall structure (identified as BW), which has no washcoat, is the lower bound limiting case for both distribution profiles.

More details about the erosion/dilation algorithms used here are given in (Belot, Vidal, Votsmeier, et al. 2020). As illustrated in Figure 7.3 for one sample (Subdomain 1), 9 non-uniformly coated structures (labelled N1 to N8, ordered in increasing amounts of washcoat, as well as the original R&D sample identified as OS) and 4 uniformly coated structures (labelled U1 to U4) were created using these procedures. In addition to these 13 structures, a bare wall structure (identified as BW), with no catalyst coating, was also generated, for a grand total of 14 structures. Lastly, each of the 14 structures was divided into four 256×400×389-voxel subdomains to speed up the flow computations by parallelization, bringing the number of flow simulations to 56. The size of the

subdomains was chosen to be representative of the elementary volumes of the porous media studied (Belot, Vidal, Votsmeier, et al. 2020).

Once the numerical structures were reconstructed, a variety of global descriptors could be used to characterize the geometrical properties of these media. The most commonly used one in a porous media context is porosity, defined as:

$$\varepsilon = \frac{V_{por}}{V_{tot}} \tag{7.2}$$

where V_{por} is the volume of the pore space and V_{tot} is the total volume of the structure. This value can be calculated by simply counting the number of pore voxels with respect to the total number of voxels in each structure. For this study, knowing the porosity of the 14 reconstructed structures, the fraction of pore volume filled with catalyst can be calculated in each case as follows:

$$f_w = 1 - \frac{\varepsilon}{\varepsilon_{BW}} \tag{7.3}$$

where ε_{BW} is the porosity of the bare wall structure. f_w will be used to report the permeability results in Section 3.2. Another very important global structural descriptor in the context of porous media is the specific surface area, which is defined as the interfacial area between the solid and the void phase S with respect to the volume of the solid phase (cordierite + washcoat) V_{sol} :

$$S_0 = \frac{S}{V_{sol}} \tag{7.4}$$

In this article, the specific surface area was calculated using the statistical method from (Ohser and Mücklich 2000). Lastly, knowing the specific surface area and the porosity of the porous medium, the mean pore diameter can be defined as (Dullien 1979):

$$d_w = \frac{2}{3}\frac{\varepsilon}{(1-\varepsilon)}\frac{6}{S_0} \tag{7.5}$$

These global structural descriptors are very useful for describing and characterizing porous media. For the sake of reproducibility, statistical structural descriptors of all these structures are also

provided in the form of two-point probability and lineal-path functions in (Belot, Vidal, Votsmeier, et al. 2020).

7.2.1.2 Flow field computation

The Lattice Boltzmann Method (LBM) is the numerical method of choice to compute fluid dynamics in porous media due to its ability to deal with complex geometries without the need for a meshing step since the computations take place on a Cartesian grid on which phases are encoded in a Boolean fashion (Vidal et al. 2009). Unlike traditional numerical methods such as the finite volume and element methods, which directly solve the Navier-Stokes equations (i.e., a macroscopic fluid flow description based on continuum mechanics), the LBM relies on the Boltzmann equation (i.e., a mesoscopic fluid flow description based on statistical mechanics). Using the LBM scheme, the Boltzmann equation, which describes the evolution of the probability distribution function of fluid molecules according to their microdynamic interactions, is discretized in the time, space, and velocity domains. The LBM scheme, which is derived from a finite difference approximation of the Boltzmann equation, marches in time *t* and propagates the probability distribution functions f_i in space $\boldsymbol{x}$ using a set of microscopic velocities $\boldsymbol{e_i}$, as follows:

$$f_i(\boldsymbol{x} + \boldsymbol{e_i}dt, t + dt) = f_i(\boldsymbol{x}, t) - \frac{1}{\tau}\left(f_i(\boldsymbol{x}, t) - {f_i}^{eq}(\boldsymbol{u}, \rho)\right) + \boldsymbol{F_i} \tag{7.6}$$

where $i \in \{1, 2, \dots, 15\}$ is one of the 15 velocity directions of the so-called D3Q15 lattice used here, dt is the time step, τ is a dimensionless relaxation time related to the fluid kinematic viscosity through $\nu = \frac{1}{3}\frac{dx^2}{dt}\left(\tau - \frac{1}{2}\right)$ (in which dx is the lattice spacing), and $\boldsymbol{F_i}$ is a body force such as, for instance, a pressure head. The middle term of the right-hand side of Eq. (7.6) is a collision operator that is approximated here using the so-called BGK operator, which was chosen for its simplicity and accuracy (Bhatnagar, Gross, and Krook 1954). The BGK operator approximates the collisions using a single relaxation procedure toward an equilibrium probability distribution function ${f_i}^{eq}(\boldsymbol{u}, \rho)$. The latter depends on the local macroscopic fluid velocity $\boldsymbol{u} = \boldsymbol{u}(\boldsymbol{x}, t)$ and density $\rho = \rho(\boldsymbol{x}, t)$, and is given by a second-order expansion in velocity of the Maxwell-Boltzmann distribution from the gas kinetic theory. More details can be found in (Krüger et al. 2017). Lastly,

taking the first and second moments of f_i with respect to the microscopic velocities $\boldsymbol{e_i}$, the pressure and velocity fields can be obtained, respectively, using the following equations:

$$p(\boldsymbol{x},t) = c_s^2 \rho(\boldsymbol{x},t) = \frac{1}{3}\left(\frac{dx}{dt}\right)^2 \rho(\boldsymbol{x},t) = \frac{1}{3}\left(\frac{dx}{dt}\right)^2 \sum_i f_i(\boldsymbol{x},t) \tag{7.7}$$

$$\boldsymbol{u}(\boldsymbol{x},t) = \frac{\sum_i \boldsymbol{e_i} f_i(\boldsymbol{x},t)}{\sum_i f_i(\boldsymbol{x},t)} \tag{7.8}$$

where c_s is the lattice speed of sound. Being explicit and local as it only involves the first layer of neighboring cells, the LBM scheme (Eq. (7.6)) is particularly well suited to parallelization on distributed memory computers for simulating transient flows in complex porous media, allowing large domain simulations and/or large numbers of simulations to be performed in a reasonable time frame. In the present study, the LBM code presented in (Vidal, Roy, and Bertrand 2010a, 2010b) was used with a unit single relaxation time ($\tau = 1$). For these calculations, a periodic boundary condition was applied in the direction of the flow (i.e., direction *x* in Figure 7.3), and the flow was driven using a body force related to ΔP, which was adjusted in such a way that the prescribed superficial velocity was recovered (see (Belot, Vidal, Votsmeier, et al. 2020) and (Bertrand et al. 2012)). Furthermore, symmetric boundary conditions were implemented in the perpendicular flow directions (i.e., *y* and *z*). At the interface between the fluid and solid cells, populations f_i were bounced back in the opposite direction following a classic half-way bounce back boundary condition (Vidal, Roy, and Bertrand 2010a). Lastly, two buffers of 100 fluid cells were added upstream and downstream from the porous structures in the flow direction in order to minimize the effect due to the use of periodic boundary condition in this direction.

Lastly, to compute the permeability of the 14 reconstructed structures, several assumptions were made. First, no flow passes through the cordierite and catalyst phases. The flow is thus exclusively contained in the pore space phase. As such, in these calculations, no distinction was made between the cordierite and the catalyst phases, and both were considered as a single solid phase as opposed to the pore space phase. Second, the fluid was assumed to be air at 650 K, and its flow was taken to be isothermal and incompressible. The physical parameters used for the LBM computations of the flow field are summarized in Table 7.1.

Table 7.1 : Physical parameters used for the simulations, considering air at 650 K.

Parameters	**Symbols**	**Values**
Fluid density (kg·m^{-3})	ρ	0.543
Fluid dynamic viscosity (Pa·s)	μ	3.18×10^{-5}
Superficial velocity (m·s^{-1})	U	0.055

The use of the parameters given in Table 7.1 gave a pore Reynolds number (Dullien 1979) for every one of the 56 structures studied in the range of:

$$0.03 \leq Re_p = \frac{\rho U d_p}{\mu(1-\varepsilon)} = \frac{3\rho U d_w}{2\mu\varepsilon} \leq 0.3 \tag{7.9}$$

with d_p being an equivalent particle diameter of the solid phase defined by the Sauter diameter (Dullien 1979):

$$d_p = \frac{6}{S_0} = \frac{3(1-\varepsilon)}{2\varepsilon} d_w \tag{7.10}$$

This range of Re_p was significantly lower than the upper limit of linear flows (i.e., $Re_p \leq \sim 10$ according to (Bird, Stewart, and Lightfoot 2007)), confirming that all the flow computations took place in the Darcy regime. In these conditions and despite some known limitations in terms of accuracy, the permeability of porous media is often approximated using the Blake-Kozeny equation, which defines the Blake-Kozeny permeability (k_{BK}) as (Blake 1922; Kozeny 1927):

$$k_{BK} = \frac{1}{4.16\,{S_0}^2} \frac{\varepsilon^3}{(1-\varepsilon)^2} = \frac{1}{150}\left(\frac{3}{2}\right)^2 d_w^2\,\varepsilon \tag{7.11}$$

This approximation will be used in Section 3.2 to compare the numerical and experimental permeability predictions.

7.2.2 Experimental procedure

For the purpose of the validation, seven out of the 14 digitally reconstructed porous structures were selected in such way that samples of both the uniform and non-uniform washcoat distribution profiles were represented and the selected washcoat amounts covered the range of coat weights investigated in the numerical study. Table 7.2 lists the seven structures selected and their respective washcoat amount, porosity, and mean pore diameter calculated using Eqs. (2) to (5). The experimental procedure employed to validate the corresponding numerical predictions about the impact of washcoat distribution and amount on permeability relied on the 3D additive manufacturing of the reconstructed porous structures followed by the measurement of their respective permeabilities using a permeability measurement device which will be hereafter referred to as a permeameter. However, because of the very small size of the samples involved and their pore space features (L ~ 300 µm and d_w ~ 20 µm) combined with the limited resolution of existing 3D printers, real-size printing of such structures was not technically feasible with current additive manufacturing technologies. A scaling procedure was thus required.

Table 7.2 : Properties of the numerical porous wall structures (256×801×779 voxels) selected for the experimental investigation.

Sample ID*	**BW**	**N1**	**OS**	**N6**	**N8**	**U2**	**U4**
Pore volume filled with washcoat (%)	0.00	14.0	23.2	35.6	49.5	26.4	52.1
Porosity (%)	68.3	58.7	52.4	44.0	34.5	50.2	32.7
Mean pore diameter (µm)	21.0	18.7	21.6	26.4	24.4	17.0	14.8

* BW: bare wall without washcoat, OS: original R&D sample, N: reconstructed non-uniform washcoat distribution profiles, U: reconstructed uniform washcoat distribution profiles.

The kinematic similarity between the real and magnified structures was thus established using an appropriate scaling factor conveniently but non-arbitrarily chosen as f_s=100. Appendix A reports all the constraints related to the 3D printer, permeameter, and flow conditions considered, which led to the choice of the scaling factor used for manufacturing the magnified 3D-printed twins. The most important constraint was that the scaled experiments had to be carried out in the same flow

regime, i.e., the linear flow regime, as in the real porous walls. A three-step methodology using this scaling procedure was devised to obtain the experimental permeability values (k_{exp}) that were compared to the corresponding numerical predictions (k_{num}). This is summarized in Figure 7.4. Each step of this methodology will be now detailed.

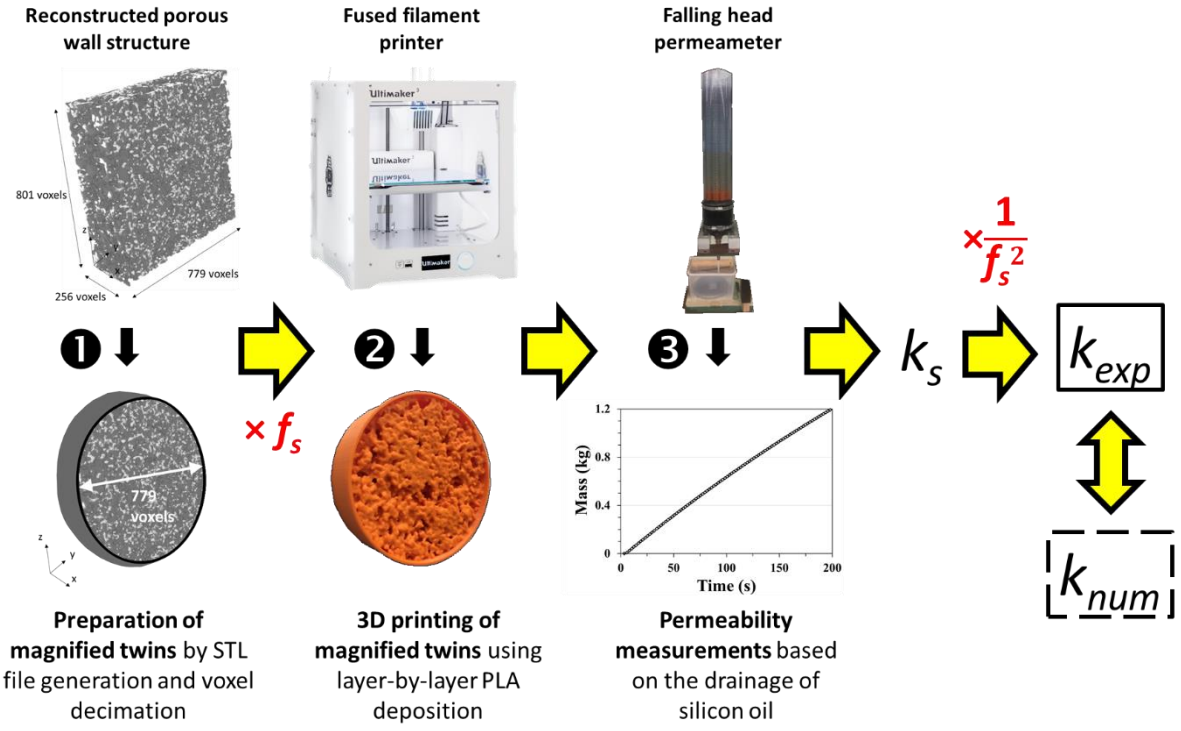

Figure 7.4: Experimental procedure for the determination of the experimental permeabilities (k_{exp}) used for the validation of the LBM permeability predictions (k_{num}), by means of a three-step methodology leading to the measurement of the permeability of the 3D-printed twins (k_s) magnified by a scaling factor f_s.

7.2.2.1 Magnified twin preparation

A preliminary sample preparation was required to provide the 3D printer with an instruction file containing a G-code, a numerical control programming language widely used to control additive manufacturing devices during the layer-by-layer deposition process of the 3D object to be built. These G-codes are created by 3D printing slicer software such as Cura, Simplify3D, and Slic3r 3D

(Šljivic et al. 2019), which take 3D models encoded in various formats, the most common being the stereolithography (STL) format, as an input file.

To create 3D models of the magnified twins in STL format in order for each magnified structure to be printed, a binary file containing the phase information of each 256×801×779-voxel domain was used as a starting point. The file was read by a MATLAB program specially designed to convert the information from the original phase into an STL file containing the structure to be printed. To achieve this, several sequential operations were performed on the phase data by the program, which are detailed in the following paragraphs.

First, the binary file data containing the phase information encoded as pore, ceramic substrate, and catalyst phases was converted into Boolean phase information by merging the substrate and catalyst phases into a single solid phase while retaining the pore phase, as was done for the numerical study.

Second, a cylindrical porous block was extracted from the original voxelization, as shown in Figure 7.5, in such way that it fit into the cylindrical chamber of the permeameter (see Section 2.2.3.1). For this, the phases of all voxels outside a 779-voxel diameter cylinder were set to pore phase. This number of voxels was chosen in order to take the largest and thus most representative section of the original domain into consideration (see Appendix A for more details).

Third, a 26-voxel-thick slice was removed from the bottom of the resulting cylindrical porous block in order to flatten one side of the printed structures and thus provide better stability and adhesion of the initial layers to the heated build plate of the printer. This operation resulted in a 230-voxel-thick cylindrical block.

Fourth, the program added a 12-voxel-thick cylindrical ring around the cylindrical porous block in order to avoid fragments not attached to the rest of the structure from being formed. This was performed by setting the phase of the corresponding voxels to the solid phase. The resolution of the original tomographic images being dx=1.246 µm, the dimensions of the resulting cylindrical porous blocks were (779+12) × 1.246 µm = 985.6 µm in diameter and 230×1.246 µm = 286.6 µm in thickness. The porosity of these cylindrical numerical structures was evaluated by calculating the ratio of pore voxels to the total number of voxels within a given block. These values will be compared in Section 3.1 to those obtained for the corresponding printed structures in order to verify the printing process.

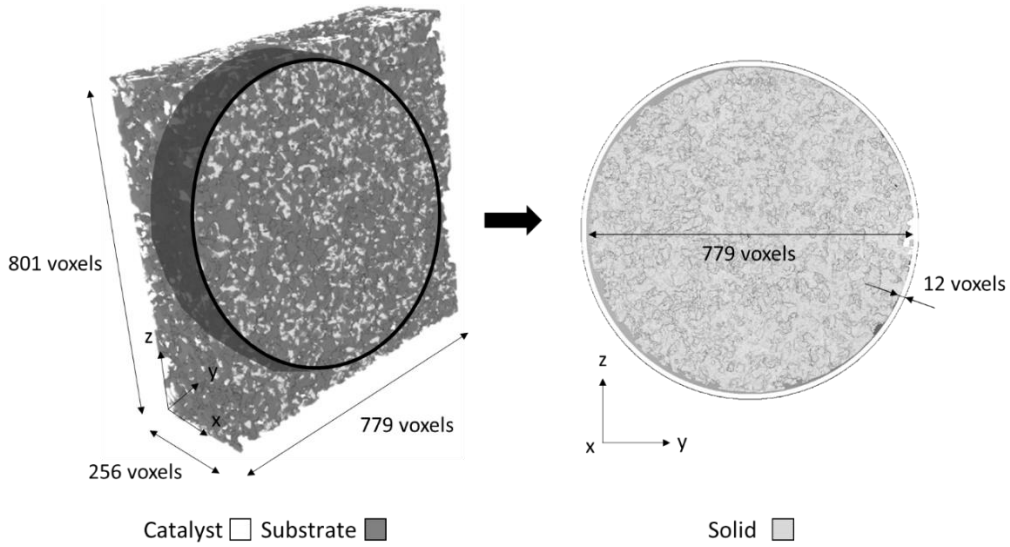

Figure 7.5: Illustration of the extraction of a cylindrical porous block combined with a 12-voxel-thick cylindrical solid ring (right) from the original voxelization (left).

Lastly, the MATLAB program converted the resulting voxelized object contained within the 3D Boolean array into an STL surface mesh using MATLAB routine "CONVERT_voxels_to_stl", which is available as an open source code on the MATLAB Central File Exchange (Aitkenhead 2010).

Because the STL conversion routine did not apply any smoothing to the surfaces represented by a large number of voxels (each voxel being represented by 6 faces, 12 edges, and 8 vertices), the size of the resulting STL file was much too large (~1-GB file for each structure) to be processed by the slicer software. To overcome this problem, a remeshing procedure leading to the simplification of the surface mesh contained in the STL file by means of a quadratic edge collapse decimation was applied to the original STL file. This post-treatment was performed using the open source software MeshLab® (version 2016.12) and the parameters reported in Table 7.3 for the "Quadratic Edge Collapse Decimation" function, which can be found in the "Remeshing, Simplification and Reconstruction" submenu from the "Filters" menu. Based on this procedure, the size of the resulting STL file was reduced to 1% of its original size (i.e., ~10 MB) while retaining the important surface details of the porous structures.

Table 7.3 : Parameters used for the quadratic edge collapse decimation procedure in MeshLab®.

Size reduction (-)	0.01
Quality threshold (-)	0.5
Preserve boundary of the mesh	Yes
Optimal position of simplified vertices	Yes
Post-simplification cleaning	Yes

7.2.2.2 3D printing

The final step before printing consisted in loading the resulting decimated STL file into the slicer software in order to create the G-code file containing the printing instructions for the corresponding structure. At this stage, the scaling factor f_s=100 was applied by setting the physical dimensions of the sample (d_s = 9.86 cm and L_s = 2.87 cm) in the slicer software. The software choice went to the open source 3D printer slicing application Cura® (version 4.0.0) for preparing the 3D printing instructions. The G-code file was then saved on a USB key, which was inserted into the corresponding port of a commercial Ultimaker 3® printer and its fused filament manufacturing technology. Unlike a recent study (Bracconi et al. 2019), which used stereolithography for printing magnified porous structures, we intentionally made a different choice to demonstrate the feasibility of the more widespread fused filament manufacturing technology for a similar purpose. This 3D printing technology consists in melting a filament of printing material from a motion-controlled heating nozzle. The fused filament is deposited layer by layer on a 197×215 mm^2 heated plate on the base of the Ultimaker 3® printing chamber. The printing resolution of each layer was 0.1 mm and was thus lower than the voxel resolution of the magnified structures to be printed (i.e., $dx \times f_s = 0.125$ mm). It should be noted that the resolution of the printer was considered as one criterion among five for choosing the scaling factor (see Appendix A). Polylactic acid (PLA) filaments of various colors (provided by Ultimaker®) were used to print the various magnified twins and easily distinguish among them, as shown in Figure 7.10. The main settings for the printing are reported in Table 7.4 and were preset in Cura® (default values were used for all other printer settings).

Table 7.4 : 3D printing conditions.

Printing temperature (°C)	140
Build plate temperature (°C)	60
Printing speed (mm/s)	40
Nozzle size (mm)	0.4

The printing time was more or less proportional to the sample porosity and generally varied from 48 to 90 h for all samples. Theoretically, the resulting cylindrical block diameter and thickness should be d_s = 9.86 cm and L_s = 2.87 cm, respectively. In practice, because of the object warping phenomenon (so-called elephant's foot effect), minor deviations in these dimensions in the order of 1 mm could be observed at the base of the blocks. In addition, a limited amount of surface defects in the form of small PLA strings sticking out, referred to as stringing in the 3D printing community, due to plastic oozing out of the nozzle while the extruder is moving to a new location (Devicharan and Garg 2019)), were present. A pressure air gun was used to blow most of them out of the PLA blocks. Lastly, to verify the quality of the 3D prints, the porosity of each cylindrical porous block was measured using a liquid immersion technique, which consisted in immersing the sample in a wetting liquid (water here) in a beaker and equating the differential volume to the solid fraction of the sample (see Appendix B for more details).

7.2.2.3 Permeability measurement

A modified falling head technique recently proposed by (Sun et al. 2020) was used to measure the permeability of the seven magnified porous wall twins. It consists in draining a column of a Newtonian liquid (usually a silicon oil with a carefully chosen kinematic viscosity) through a pipe containing the sample whose permeability is measured by recording the flow rate of the outgoing liquid over time. This method is particularly attractive because of the simplicity of its concept and the equipment required for its implementation, its low costs of installation and operation, and the speed of the measurements (one measurement took about two to three minutes for the samples tested). In addition, unlike the classic falling head permeability measurement procedure, the

modified technique can characterize permeabilities much larger than 10^{-10} m^2 (up to 10^{-7} m^2) (Sun et al. 2020), making it possible, with the current 3D printer resolutions, to directly manufacture porous objects with structural characteristics compatible with this range of permeability. More details on the method are given below regarding the experimental setup, the baseline test, the permeability measurements and the calculation procedure.

7.2.2.3.1 Experimental setup

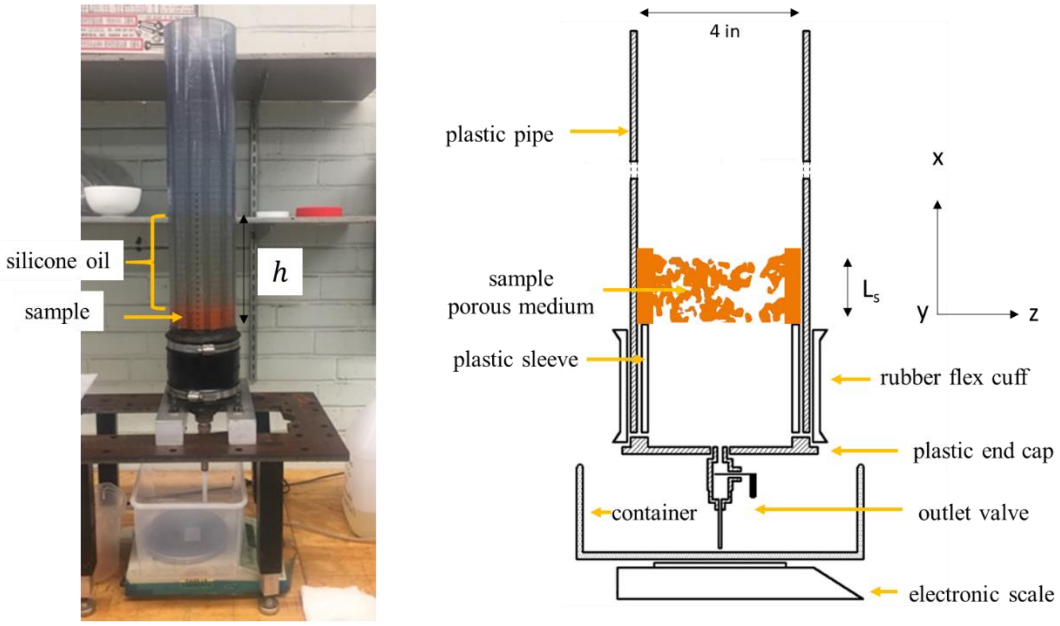

Figure 7.6: Image of the experimental setup (left) and its (not to scale) schematic (right).

The experimental setup used to measure the permeability of the 3D-printed samples is presented in Figure 7.6 and was inspired by the modified falling head technique proposed recently in the context of granular material by (Sun et al. 2020). To measure their permeability, each 3D-printed porous sample was placed in a vertical transparent plastic pipe with a 4-in inner diameter, which is slightly larger than the diameter of the printed samples (i.e., d_s = 9.86 cm). It theoretically left a very small gap of ~1.5 mm between the pipe and the sample so that typical printing defects such as an elephant's foot or print edge warping (Günaydın and Türkmen 2018) would not hinder the insertion of the sample into the pipe. Nonetheless, a long rod was required to help push the block close to the end of the pipe (placed just on top of a 4-in outer diameter plastic sleeve) as the samples all fit tightly inside the pipe. A plastic sleeve on which the samples were resting was added to

prevent the sample from being hidden by the rubber flex cuff that connects the pipe and the plastic end cap. It also prevented a channeling effect from taking place through possible gaps. The flex cuff was tightened and sealed around the main pipe and the end cap to prevent leakage. The outlet of the setup consisted of a valve and a small pipe, which were connected to the bottom cap. The outgoing liquid was collected in a container, and the amount of liquid collected over time was weighed using an electronic scale (SETRA EL-4100D) with a maximum capacity of 4.1 kg and a recording frequency of 5 Hz. In practice, the recorded mass data was averaged every 2 s to reduce signal fluctuations. The averaged data was recorded as a series of data points of mass over time (t_i, m_i) by a computer connected to the scale and equipped with Spyder® software, which is part of the Anaconda® Python/R Data Science platform (version 2019.07). Figure 7.7 gives a typical example of a mass over time recording. At time t_i, the volumetric flow rate $Q_{s,i}$, the fluid superficial velocity $U_{s,i,}$ and the liquid height $H_{s,i}$ above the sample were calculated as follows:

$$Q_{s,i} = \frac{m_i - m_{i-1}}{(t_i - t_{i-1})\,\rho_s} \tag{7.12}$$

$$U_{s,i} = -\frac{Q_{s,i}}{S} \tag{7.13}$$

$$H_{s,i} = H_{s,0} - \frac{m_i - m_0}{\rho_s S} \tag{7.14}$$

where m_0 and m_i are, respectively, the initial mass of fluid and the mass collected at time $t_{i,}$ ρ_s is the density of the test fluid, $S = 4\pi$ in^2 is the cross-sectional area of the pipe, and $H_{s,0}$ is the initial liquid height above the sample. To reproduce the linear regime of the air flow through the c-GPF porous wall, the dynamic viscosity of the test fluid in this experiment had to be relatively high. For this purpose, a XIAMETER™ PMX-200 calibrated silicon oil was selected in accordance with the first constraint reported in Appendix A and the experimental pore Reynolds number requiring that $Re_{p,s} \leq \sim 10$. The physical parameters used for these experiments are listed in Table 7.5. The $Re_{p,s}$ values of the seven magnified 3D-printed twins are given in Table 7.6.

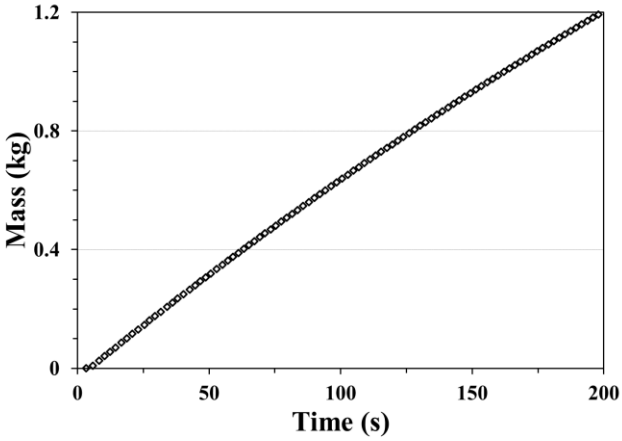

Figure 7.7: Typical two-second averaged mass recorded over time for the N6 structure.

Table 7.5 : Physical parameters used during the experiments.

Parameters	**Symbols**	**Values**
Silicon oil density (kg·m^{-3})	ρ_s	966
Silicon oil dynamic viscosity (Pa·s)	μ_s	0.1
Silicon oil initial height (m)	$H_{s,0}$	0.16
Room temperature (°C)	T	22

7.2.2.3.2 Baseline tests

In order to calculate the permeability of the samples from the measured flow rate over time, it was essential to determine the pressure gradient in the direction of the flow through the sample (see Eq. (7.1)). However, the pressure values at the top (P_1) and bottom (P_2) of the sample (Figure 7.8) were not measured directly. P_1 varied over time as the liquid height decreased but could be deduced from the hydrostatic pressure caused by the liquid column whose height $H_{s,i}$ was calculated at time t_i during the test using Eq. (7.14). The pressure loss due to friction in the pipe was not taken into consideration as it was much smaller than the pressure loss in the sample. At the bottom of the sample, P_2 was mainly generated by the change in cross-sectional area between the main pipe and the outlet valve. It can be regarded as an intrinsic pressure loss caused by the setup. Also, a 1.5-

mm-thick cylindrical ring similar in all ways to the ones added to each cylindrical porous block (see Section 2.2.1) was inserted in the setup in place of the sample in order to account for the impact of the ring on the pressure loss of the setup. An image of the 3D-printed cylindrical ring used for the baseline tests is shown in Figure 7.9 next to the cylindrical porous block.

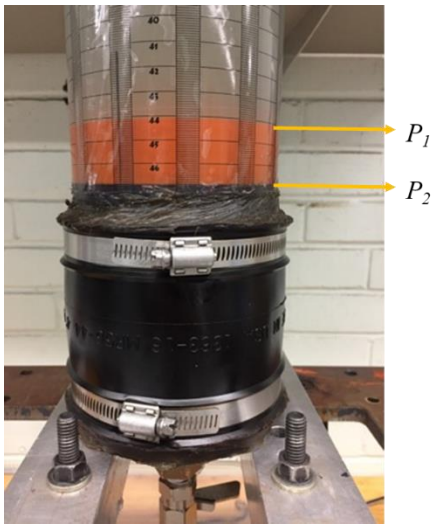

Figure 7.8: Close-up of the sample region and identification of the relevant pressure values.

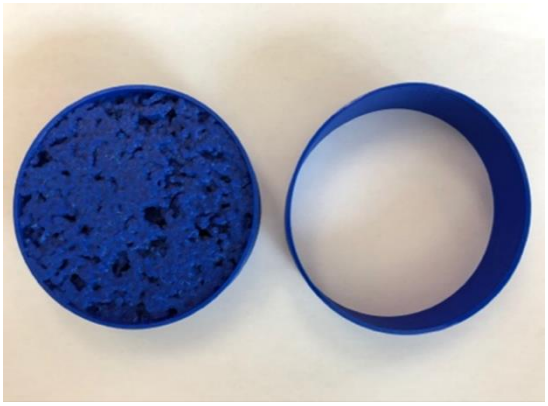

Figure 7.9: Image of a cylindrical porous block (left) and the 1.5-mm-thick cylindrical ring (right) used for the baseline tests.

To evaluate the pressure loss of the blank setup, silicon oil was drained through the empty setup four times, and the mean variation of the flow rate $Q_{s,i}$ as a function of the height of the silicon oil $H_{s,i}$ was obtained using Eqs. (12) and (14). In the absence of sample, the total pressure drop ΔP_s

through the setup can be approximated as $\Delta P_s = P_{out} - P_2 = -P_2$ if the pressure P_{out} at the outlet of the setup is set to zero and taken as a baseline. A linear relationship between the flow rate $Q_{s,i}$ and pressure drop ΔP_s (or simply P_2) can be written at any time t_i as (Sun et al. 2020):

$$P_2 = c_0\, Q_{s,i} + c_1 = \rho_s g (H_{s,i} + L_s) \tag{7.15}$$

where g is gravitational acceleration and $(H_{s,i} + L_s)$ is the total height of the liquid column above the location at which pressure P_2 is measured in the absence of sample. Fitting all the data points for the four baseline experiments by linear regression (with R^2=0.93) resulted in constant values of c_0 = 6.045×10^8 Pa·s·m^{-3} (with a *p*-value ≈ 0) and c_1 = –2571 Pa (with a *p*-value ≈ 0).

7.2.2.3.3 Measurement procedure

After performing the baseline tests, the seven magnified porous wall twins were characterized using the following experimental procedure. First, the outlet valve was closed, and the silicone oil was poured into the main pipe. With the silicone oil inside, the test sample was placed in the pipe from the top. To eliminate air bubbles entrapped inside the sample, several liters of fluid were allowed to pass through the sample several times before any measurements were taken. After reading the initial liquid level $H_{s,0}$, the data acquisition system was then launched, and the outlet valve was opened. Note that the test had to be stopped before the liquid level reached the top surface of the sample for the calculation of the permeability to be valid. To assess the experimental uncertainty of the method, the whole procedure was repeated four times for each sample. The calculation of the permeability of the samples from the recorded mass of fluid over time is presented in the next subsection.

7.2.2.3.4 Permeability calculation

Considering gravity, Darcy's law can be written in its general form as:

$$U_{s,i} = -\frac{Q_{s,i}}{S} = -\frac{k_s}{\mu_s}\left(\frac{\partial P_s}{\partial x} + \rho_s g\right) \tag{7.16}$$

where k_s is the permeability of the magnified twin and $\partial P_s/\partial x$ is the pressure gradient across the sample thickness, the direction of which is denoted by x, which can be developed as:

$$\frac{\partial P_s}{\partial x} = \frac{P_1 - P_2}{L_s} = \frac{\rho_s g H_{s,i} - c_0 Q_{s,i} - c_1}{L_s} \tag{7.17}$$

For an incompressible test fluid, the following equations are then considered:

$$H_s(t = 0) = H_{s,0}$$
$$U_{s,i} = \frac{dH_{s,i}}{dt} \tag{7.18}$$

Substituting Eqs. (17) and (18) into Eq. (7.16) leads to a differential equation over $H_{s,i}$ in time. The following analytical solution to this equation can be straightforwardly obtained:

$$ln\left(\frac{H_{s,i} + L_s - \frac{c_1}{\rho_s g}}{H_{s,0} + L_s - \frac{c_1}{\rho_s g}}\right) = -\frac{\rho_s\, g}{\frac{\mu_s L_s}{k_s} + c_0 S}\, t_i \tag{7.19}$$

A logarithmic relationship between liquid level $H_{s,i}$ and time t_i is thus described by Eq. (7.19). Using all the data points ($H_{s,i}$, t_i) measured in one test, a permeability value is obtained by fitting these data points to Eq. (7.19) using a least square regression.

Once the permeability values k_s for all the samples were measured, a downscaling operation was required to make them directly comparable to the numerical values (k_{num}) calculated with LBM. As permeability has length squared dimensions (see Eq. (7.11)), the experimental permeability k_{exp} was obtained using the following downscaling equation:

$$k_{exp} = \frac{1}{f_s^2} k_s \tag{7.20}$$

7.3 Results and discussion

In this section, the seven magnified 3D-printed twins are first verified against the corresponding digital structures to assess the print quality. Then, the numerical, analytical, and experimental predictions are compared in terms of the impact of washcoat amount and distribution profiles on porous wall permeability in order to validate both the numerical and experimental methodologies.

7.3.1 Printed structure verification

The resulting magnified 3D-printed twins are presented in Figure 7.10 along with their corresponding porosities measured using a liquid immersion technique. A close visual inspection of the printed porous blocks showed a very good definition of the pore space with only a limited number of remaining defects such as minor stringing and an elephant's foot effect.

Figure 7.10: Images of the seven magnified 3D-printed twins identified by their respective sample ID (see Table 7.2) and corresponding porosity.

As permeability is strongly related to porosity (see Eq. (7.11)), it was important here to assess the quality of the 3D prints by carefully comparing the porosities of the digital reconstructed structures and of the actual printed structures. Figure 7.11 shows very good agreement between the expected and actual porosities of each of the seven PLA blocks. The porosity values of the real printed samples were almost systematically slightly greater than those of the digital structures, likely due to a constant bias in the liquid immersion technique for measuring porosity, the digital sample preparation (e.g., the decimation step), and/or the printing process itself. Nevertheless, the overall result was very satisfactory, with a mean absolute discrepancy between the virtual and real samples of 1.5±2.4% in porosity and a maximum absolute discrepancy of 2.8±3.0% in porosity for the N6

structure. Moreover, there was no correlation between the magnitude of the discrepancy and the porosity level itself, meaning that the quality of the printing was independent of the porosity of the structure. In our opinion, these results qualify the 3D printing fused filament technique and demonstrates its accuracy in creating the digital porous structures studied in this investigation.

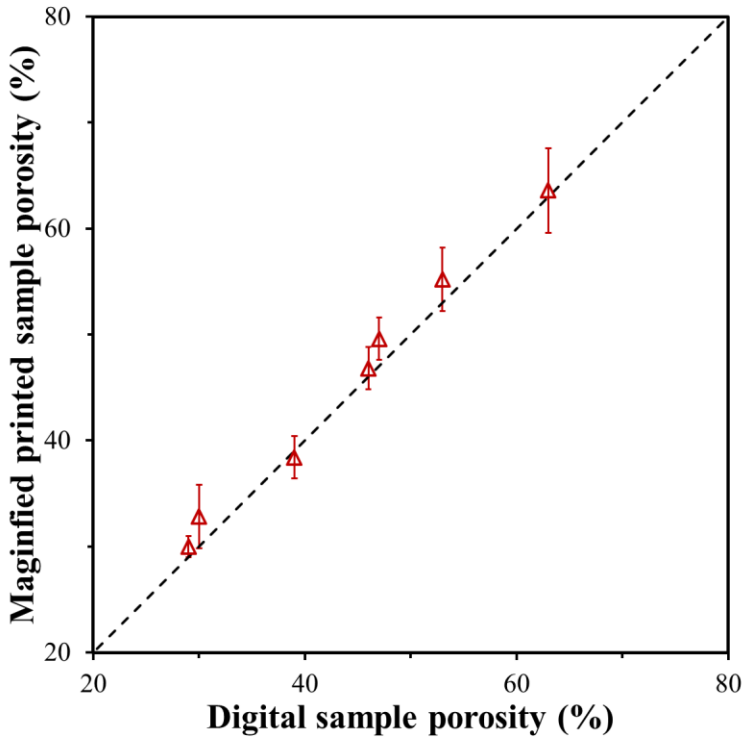

Figure 7.11: Comparison of the porosities of the digital porous wall structures (ε) and those of corresponding magnified 3D-printed twins (ε_s). The error bars represent the standard deviation of quadruplicate experiments.

7.3.2 Permeability validation

After verifying the quality of the 3D manufacturing fused filament technique by comparing the porosities, we compared the permeability values. At a practical level, this comparison was used to validate the numerical predictions of the impact of washcoat amount and distribution profiles on permeability in a previous study (Belot, Vidal, Votsmeier, et al. 2020). In addition, at the theoretical level, good agreement between numerical predictions and experiments serves as a way of validating

the numerical and experimental methodologies used. Indeed, when the numerical permeability values were compared to the Blake-Kozeny predictions as a function of washcoat amount (represented by the fraction of pore volume filled by the washcoat, see Figure 7.12 and Table 7.6), a significant discrepancy of 62.5% was obtained (considering only the seven experimentally tested structures). Given the extreme sensitivity of permeability to small variations in porosity and pore size, as evidenced by Eq. (7.11), this level of agreement could be considered as acceptable for many engineering applications as it gives a correct order of magnitude. However, the predictions about the exact impact of washcoat amount did not agree very well, particularly for the non-uniform washcoat distribution profiles. Both predicted a non-linear relationship between permeability and washcoat amount but, in the case of Blake-Kozeny predictions, this non-linearity was significantly more pronounced. However one should keep in mind that there is ample evidence in the literature that, despite its widespread use, the Blake-Kozeny equation is a correlation that should be used as a rough estimate in most cases (Torquato 1991; Øren and Bakke 2002; Dullien 1979). The Blake-Kozeny data points were added here for comparison and the fact that this correlation was used in a previous study (Belot, Vidal, Votsmeier, et al. 2020).

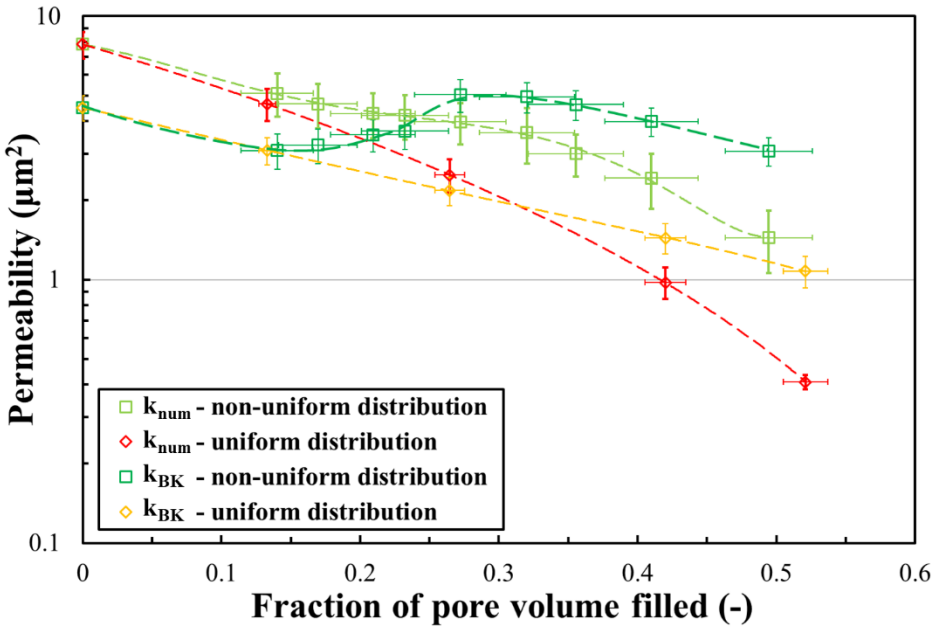

Figure 7.12: Permeability comparison between the LBM simulations (k_{num}) and the Blake-Kozeny equation (k_{BK}) for porous wall structures with various washcoat amounts and distribution profiles. High-order polynomial regressions (dashed lines) are used as guides for the eye, and the error bars represent the standard deviations of the reported mean values for the four wall subdomains.

Table 7.6 summarizes the permeability values for the seven structures obtained from the Blake-Kozeny equation, the LBM simulations, and the experiments. It is evident that there was much better agreement between the numerical and experimental data, with a mean relative discrepancy of 19.3%, than between the numerical and Blake-Kozeny data (62.5%) or the experimental and Blake-Kozeny data (83.4%).

Table 7.6 : Comparison of the permeability values obtained from the Blake-Kozeny equation (k_{BK}), the LBM simulations (k_{num}), and the falling head experiments (k_{exp}) for the seven reconstructed structures investigated.

Sample ID	BW	N1	OS	N6	N8	U2	U4	Mean
$f_{w,exp}$ (-)	0.000	0.132	0.220	0.396	0.484	0.264	0.528	
$10^2 \times Re_{p,s}$ (-)	1.48	1.54	1.99	2.90	3.41	1.64	2.19	
k_{exp} (µm^2)	9.45	6.08	5.02	3.39	1.25	3.21	0.30	
k_{BK} (µm^2)	4.50	3.35	3.76	4.13	3.28	2.17	1.04	
$\frac{\lvert k_{BK}-k_{exp}\rvert}{k_{exp}}$ (%)[a]	52.4	44.9	25.1	21.8	161	32.2	246	**83.4**
$f_{w,num}$ (-)	0.000	0.140	0.232	0.356	0.495	0.264	0.521	
k_{num} (µm^2)	7.82	5.10	4.20	3.01	1.44	2.50	0.41	
k_{BK} (µm^2)	4.50	3.09	3.67	4.62	3.08	2.18	1.07	
$\frac{\lvert k_{BK}-k_{num}\rvert}{k_{num}}$ (%)	42.4	39.3	12.7	53.8	113	12.7	163	**62.5**
$\frac{\lvert k_{num}-k_{exp}\rvert}{k_{nexp}}$ (%)[a]	17.2	14.8	15.2	24.0	17.1	21.8	25.3	**19.3**

[a] The relative differences were calculated as the fraction of pore volume filled measured experimentally ($f_{w,exp}$) for each structure using interpolations of the non-linear regressions of the data shown in Figure 7.12.

Figure 7.13 also presents the experimental data for the seven printed structures next to the LBM predictions for the 14 structures investigated in (Belot, Vidal, Votsmeier, et al. 2020). Unlike the Blake-Kozeny predictions in Figure 7.12, the experimental results agreed very well with the non-linear decreases in permeability as a function of washcoat amount for the uniform and non-uniform distribution profiles as predicted by the numerical simulations. Both the experimental and numerical data show a somewhat less pronounced decrease for the non-uniform washcoat distribution profiles than for the uniform profiles given that this type of deposition is inherently more prone to channeling effects. Overall, although the experiments tended to predict slightly higher permeability values than the simulations, except for the lowest porosities (i.e., the highest

fraction of pore volume filled), the agreement was considered to be very good given the extreme sensitivity of this property to minor differences in pore space characteristics. It is, however, worth noting that there was a somewhat higher uncertainty in the experimental values with the highest porosities.

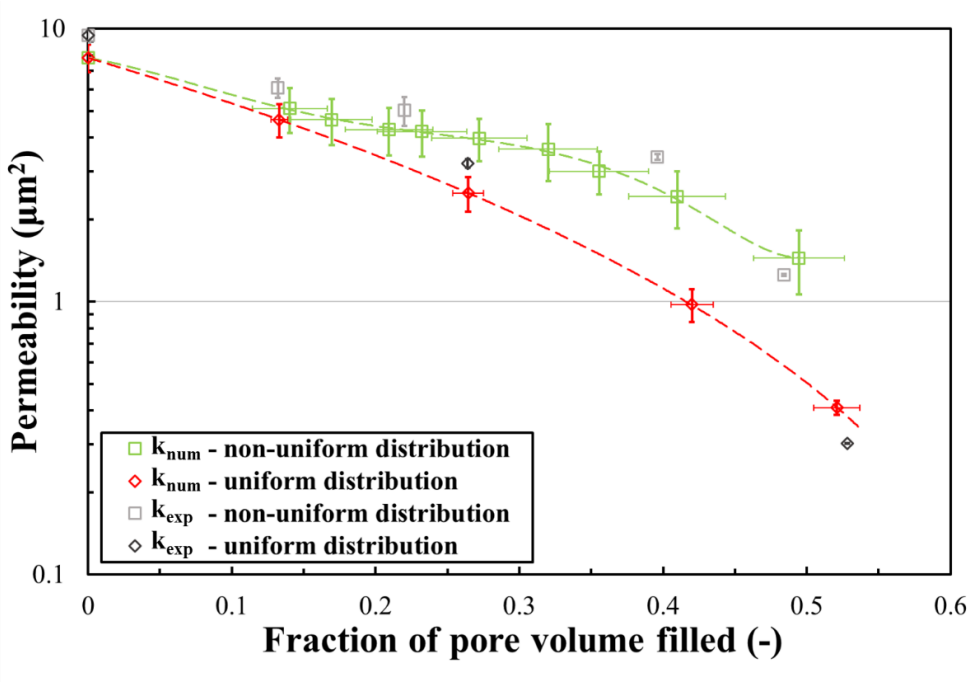

Figure 7.13: Permeability comparison between the LBM simulations and the falling head permeameter experiments for porous wall structures with various washcoat amounts and distribution profiles. For the numerical data (k_{num}), high-order polynomial regressions (dashed lines) are used as guides for the eye, and the error bars represent the standard deviations of the reported mean values for the four wall subdomains. For the experimental data (k_{exp}), the error bars represent the standard deviation of quadruplicate experiments.

No correlation was found between the level of porosity and the quality of the 3D prints, which can be attributed to the increasing proximity to the estimated upper limit of validity of the permeameter as mentioned in Section 2.2.3 (i.e., at the c-GPF scale, with $k_{exp} < \sim 10^{-7} \frac{1}{f_s^2} \approx 10^{-11}$ m^2). This result suggested that the modified falling head technique is precise and likely more accurate for

$k_s < \sim 4 \times 10^{-8}$ m^2. Nonetheless, the close adequacy obtained gave good confidence in both the numerical methodology and the experimental procedure employed in this comparison study. In addition, the very good overall agreement between the numerical and the experimental values validated the LBM model and its prediction about the impact of washcoat amount and distribution profiles on the permeability of the reconstructed c-GPF porous walls.

7.4 Conclusion

A numerical model based on the LBM was developed in a previous study (Belot, Vidal, Votsmeier, et al. 2020) to predict the impact on the filtration performance (i.e., the pressure drop and soot capture efficiency) of a three-way catalyst coating (washcoat) and its degree of uniformity within the porous ceramic (cordierite) wall of a coated gasoline particulate filter (c-GPF). The permeability predictions of the model were in fairly good qualitative agreement with classic theory such as the Blake-Kozeny equation. Nonetheless, more accurate validation work was required to precisely quantify the quality of the predictions of the model. However, due to the inherently small dimensions of cordierite walls, accurate measurements of ΔP generally require expensive experimental equipment that is often not readily available.

To overcome this limitation, an experimental method is proposed here that is an excellent alternative to existing conventional methods. It relies on the concept of kinematic similarity and the corresponding scale-up procedure of the porous wall structures. It makes use of a combination of fused filament additive manufacturing and a new falling head permeameter (Sun et al. 2020) to select a scaling factor that makes it possible to print structures with sufficient pore space resolution and appropriate permeability that can be easily and precisely measured. A detailed analysis that accounts for the flow regime, the structural characteristics of the porous media, and the printer and permeameter resolutions is proposed to help select the appropriate scaling factor. The proposed procedure is a relatively easy to implement and inexpensive method that may be of interest in many areas of science and engineering applications for which an understanding of the relationship between porous structures and fluid flow is important. It is thus particularly well suited as an experimental technique for validating the predictions of numerical models.

The proposed experimental procedure was used to validate the permeability predictions of a numerical wall-scale model of a c-GPF. Although permeability is very sensitive to small structural differences, the permeability measurements on seven magnified reconstructed wall structures with various washcoat amounts and degrees of uniformity were in very good agreement with the LBM model predictions. A specific non-linear reduction of permeability as the amount of washcoat in the pore space increased was observed for the uniform and non-uniform distribution profiles. In addition, with the same amount of washcoat, non-uniform profiles were shown both experimentally and numerically to create porous media with higher permeability values than the corresponding uniform profiles. This can be attributed to a greater propensity to flow channeling with non-uniform distribution profiles. Overall, these results give great confidence in both the numerical methodology and the experimental procedure proposed here, particularly in the context of c-GPFs. They also make it possible to precisely quantify the differences in ΔP between the washcoat deposits and can thus provide guidance to c-GPF manufacturers as well as insights into why specific catalyst coatings perform better than others. Lastly, this experimental methodology can be used as an affordable and easy to setup validation procedure in the general context of porous media permeability assessment.

7.5 Acknowledgements

The authors gratefully acknowledge the financial support of the Natural Sciences and Engineering Research Council of Canada (NSERC), support from the Simulation-Based Engineering Science (SBES) program funded through the CREATE program from NSERC, the Normand Brais PolyFab fabrication laboratory at Polytechnique Montreal for providing the 3D printers, and Calcul Québec and Compute Canada for the computational resource allocations. Lastly, a special thanks to Lenox-Antoine Vidal, the 14-year-old nephew of one of the co-authors, who first demonstrated the feasibility of using fused filament additive manufacturing for printing magnified porous ceramic structures.

7.6 Appendix A – Selection of a scaling factor for printing the magnified twins

Before selecting an appropriate scaling factor, we had to verify that the flows at the real and magnified scales would both take place within the continuum flow regime, i.e., at $Kn \leq 0.01$ (Nazari Moghaddam and Jamiolahmady 2016), where Kn is the Knudsen number, which is defined as the mean free path of molecules within the fluid divided by a characteristic length scale of the pore space. It thus characterizes the importance of the gas rarefaction effects. Although this condition can generally be easily guaranteed at the magnified scale, in practice this condition limits the lower bound of the scale of real porous structures that can be investigated with the proposed magnified twin approach. Under the actual operating conditions of reconstructed c-GPF porous structures (Belot, Vidal, Votsmeier, et al. 2020), it is possible to show that $0.0078 \leq Kn \leq 0.014$ (choosing the mean pore diameter as the characteristic length scale of the pore space). This range straddles the transition threshold between the continuum and slip flow regimes. However, it was assumed that gas rarefaction effects could be ignored as most of the flow should go through the largest capillaries, which exhibit Knudsen values below the threshold. This being settled, the choice of the scaling factor to be applied to the original digitally reconstructed structure was then dictated by the following five constraints:

1. The scaled pore Reynolds number ($Re_{p,s}$) has to be in the linear regime so that (Bird, Stewart, and Lightfoot 2007):

$$Re_{p,s} = \frac{3\rho_s U_s d_{w,s}}{2\mu_s \varepsilon_s} \leq \sim 10 \qquad (7.A1)$$

   where the s subscript is indicative of the properties measured for the scaled experiment with magnified porous wall structures. Note that as permeability is independent of the pore Reynolds number in the linear regime, the condition $Re_{p,s} = Re_p$ is not strictly required for a kinematic similarity to be obtained. As the structures are magnified by the scaling factor f_s, the following relationships between the properties of the magnified and real structures can be applied:

$$d_{w,s} = f_s\, d_w \text{ and } \varepsilon_s = \varepsilon \tag{7.A2}$$

From Eqs. (A1) and (A2), one can thus write that:

$$f_s \leq \sim \frac{20}{3} \frac{\mu_s \varepsilon}{\rho_s U_s d_w} \tag{7.A3}$$

Following Darcy's law (i.e., Eq(1)), one can show that:

$$U_s = k_s \frac{\Delta P_s}{\mu_s L_s} = \frac{1}{150} \left(\frac{3}{2}\right)^2 d_{w,s}^2 \varepsilon_s \frac{\rho_s g H_{s,0}}{\mu_s L_s} \tag{7.A4}$$

where the right-hand side of the equation results, in first approximations, from the substitution of ΔP and permeability by the pressure exerted by the initial column of fluid used and the expression of permeability obtained from the Blake-Kozeny equation, respectively. If Eq. (7.A4) is now introduced into Eq. (7.A3), we can obtain, after a few simple algebraic manipulations, the following:

$$f_s \leq \sim \frac{10}{\max(d_w)} \left(\frac{\mu_s^2 L_s}{9 \rho_s^2 g H_{s,0}}\right)^{\frac{1}{3}} \approx 103 \tag{7.A5}$$

Note that in the latter and following equations the maximum or the minimum of structural properties is introduced as an indication that the worst-case scenario among the seven structures investigated should be used, depending on the specific constraint considered.

2. The printer resolution (r_p) needs to be much smaller than the pore size for a good definition of the pore space, which can thus be translated into:

$$d_{w,s} \gg r_p \implies f_s \gg \frac{r_p}{\min(d_w)} \approx 4 \tag{7.A6}$$

Note that a good resolution for the largest pores through which the flow channeling occurs would probably be in fact sufficient.

3. The section of the magnified porous wall needs to be a Representative Elementary Volume (REV) of the pore space. For defining REV, it is a common practice to use the Brinkman's screening length criterion (Clague and Phillips 1997), which postulates that the domain characteristic length scale should be much larger than the square root of Darcy's permeability. Then, if it is assumed again that the permeability can be approximated through the Blake-Kozeny correlation, one can thus write that:

$$D_s \gg \sqrt{k_s} = \frac{3}{10\sqrt{6}} d_{w,s}\sqrt{\varepsilon_s} \implies f_s \ll \frac{10\sqrt{6}}{3}\frac{D_s}{\max(d_w\sqrt{\varepsilon})} \approx 4 \times 10^4 \tag{7.A7}$$

where D_s, the diameter of the cylindrical chamber of the permeameter that contains the magnified 3D-printed twin, is used as a domain characteristic length scale.

4. The measured permeability values must be between the lower ($k_{\min}$) and upper ($k_{\max}$) permeability sensitivity limits of the falling head permeameter used, which results in:

$$\begin{gathered} \sim 10^{-10} < k_s = \frac{1}{150}\left(\frac{3}{2}\right)^2 d_{w,s}^2 \varepsilon_s < \sim 10^{-7} \\ \implies \frac{10\sqrt{6}}{3}\frac{\sqrt{k_{min}}}{\min(d_w\sqrt{\varepsilon})} \approx 6 < f_s < \frac{10\sqrt{6}}{3}\frac{\sqrt{k_{max}}}{\max(d_w\sqrt{\varepsilon})} \approx 140 \end{gathered} \tag{7.A8}$$

where $k_{\min}$ and $k_{\max}$ are evaluated to be $\sim 10^{-10}$ m^2 and $\sim 10^{-7}$ m^2, respectively. Note that for a classic falling head permeameter with $k_{\min} = \sim 10^{-14}$ m^2 and $k_{\max} = \sim 10^{-10}$ m^2 (Sun et al. 2020), Eq. (7.A8) would give $0.06 < f_s < 5$, which would be in contradiction with the constraint related to the printer's resolution (Eq. (7.A6)). As such, a technique other than the falling head would be required.

5. Lastly, the diameter of the printed cylindrical structures must be smaller than the smallest in-plane dimension of the original porous wall voxelization magnified at the printing scale, which is written as:

$$D_s \leq \min(n_y, n_z)\ dx\ f_s \Longrightarrow f_s \geq \frac{D_s}{\min(n_y, n_z)\ dx} \approx 100 \qquad (7.A9)$$

where $n_y = 801$ and $n_z = 779$ for the porous wall voxelization extracted from the tomographic image in the present study. In other words, this constraint states that the magnification must not be too small, otherwise the dimensions of the available voxelization will not be large enough to provide structures that can completely fill the cylindrical chamber of the permeameter. The largest possible section of the original voxelization should be used, in practice, to avoid large-scale heterogeneity of the porous wall structures, which could affect the measured permeability. Indeed, as mentioned in (Belot, Vidal, Votsmeier, et al. 2020), the third constraint related to the Brinkman screening length criterion is a necessary but often not sufficient condition for cordierite structures that present long-scale heterogeneity. Therefore, a small as possible f_s should be chosen, within the prescribed limits determined by all the constraints.

Of all the constraints, the first constraint can be met by carefully selecting the fluid used (e.g., a silicon oil) in the falling head permeability measurement procedure. All the other constraints depend either on the features of the measuring or printing devices used and the size of the available voxelization or structural characteristics of the porous media, which are harder to control. If the fluid is carefully selected, the five constraints (Eqs. (A5)-(A9)) should, in theory, define a range of appropriate scaling factors with which the experiments could be performed. However, the lower limit should be preferred to avoid large scale heterogeneity of the porous media. Nonetheless, for the silicon oil used for the present study, a close inspection of the five constraints revealed a very narrow range to choose from, i.e., $100 \leq f_s \leq 103$. To use the largest possible section of the original voxelization and also for convenience, we thus selected f_s=100 as the scaling factor.

7.7 Appendix B – Porosity measurements using a liquid immersion technique

The samples were immerged in a 200-mL beaker filled with water, as shown in Figure 7.14. The water level height was measured before and after immersing the sample using a ruler with a 1 mm/graduation precision. The air bubbles trapped in the samples, once immerged, were removed by carefully tapping the sample using a metallic rod, making sure no water escaped from the beaker.

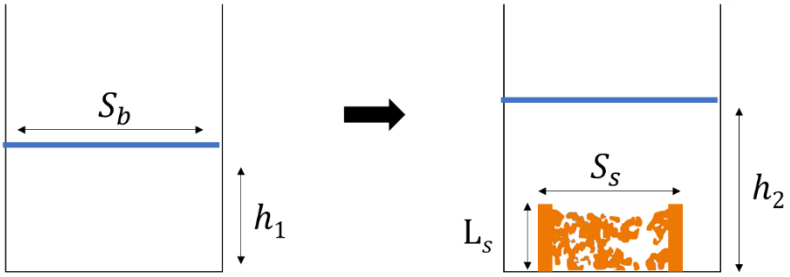

Figure 7.14: Schematics of the liquid immersion technique for measuring porosity showing the empty beaker (left) and the beaker containing the immerged sample (right).

To retrieve the porosity ε_s of the sample, the following equation was used:

$$\varepsilon_s = 1 - \frac{S_b(h_2 - h_1)}{S_s \times L_s} \tag{7.B1}$$

where h_1 is the water level height in the beaker without a sample, h_2 is the water level height with an immerged sample, $S_s = \frac{\pi}{4} d_s^2$ and L_s are, respectively, the cross-sectional area and the height of the cylindrical sample (these values are given in Section 2.2.3.1), and S_b is the cross-sectional area of the beaker.

CHAPITRE 8 DISCUSSION GÉNÉRALE

L'objectif général de cette thèse a été formulé ainsi : évaluer l'impact de la distribution d'un dépôt de catalyseur sur les performances globales des FAPC à l'échelle microscopique.

Afin de mener à bien cet objectif, un modèle en quatre étapes de prédiction des performances globales des filtres à particules catalytiques (FAPC) a été développé. Les performances globales d'un FAPC à l'échelle microscopique sont résumées par : (1) la perte de charge à travers le mur poreux composant ses canaux (ΔP), (2) son efficacité de capture (E_f) et (3) sa conversion catalytique (X).

Dans un premier temps, un modèle de prédiction des performances en filtration des FAPC a été assemblé. Celui-ci est présenté dans l'Article 1 (Chapitre 5). Cette partie du modèle permet le calcul de la perte de charge et de l'efficacité de capture d'une structure représentative du mur de céramique composant les canaux d'un FAPC. À l'aide de ce modèle, une étude comparative a été réalisée entre les performances en filtration de plusieurs structures poreuses représentatives du mur poreux d'un FAPC pour moteur EID, présentant différents profils de distribution de catalyseur. Ainsi deux profils de distribution sont étudiés : (1) un profil de distribution non uniforme à différentes quantités de catalyseur et (2) un profil uniforme à différentes quantités de catalyseur. Malgré une plus grande perte de charge générée, une distribution uniforme de catalyseur entraine des performances en filtration nettement meilleures qu'une distribution non uniforme en termes d'efficacité de capture des particules de suie (jusqu'à 100 % d'amélioration) et de facteur de qualité (jusqu'à 50% d'amélioration) pour une fraction du volume de pores rempli de catalyseur pouvant atteindre 40%. En plus de ce résultat, de façon non intuitive, il a été montré que pour un dépôt non uniforme de catalyseur, l'efficacité de capture diminue lorsque la quantité de catalyseur est augmentée. Ce phénomène, bien que n'étant pas le cas général, a déjà été reporté dans la littérature (Liu et al. 2018; Joshi and Johnson 2018), et peut s'expliquer par un temps de résidence diminué des particules de suie dans le filtre, à mesure que la quantité de catalyseur augmente. Cet effet a pu être expliqué par des visualisations de champs d'écoulement qui montrent un renardage de l'écoulement vers les plus gros pores du milieu filtrant dans le cas d'une augmentation du volume de dépôt de catalyseur non uniforme. Toutefois, il n'a pas été prouvé que ce résultat pouvait se

généraliser à tous les types de céramiques et toutes les dépositions de catalyseur. D'autres simulations seraient nécessaires pour amener à cette généralisation.

Dans un deuxième temps, un modèle de prédiction des performances catalytiques des FAPC a été développé dans l'Article 2 (Chapitre 6). Il consiste en (1) la reconstruction de volumes élémentaires représentatifs des parois poreuses du FAPC à l'aide d'images tomographiques, et (2) à calculer le champ d'écoulement et (3) le champ de concentration d'une espèce chimique hypothétique en considérant une réaction rapide de premier ordre à l'intérieur de la paroi du FAPC à l'aide de deux programmes basés sur la MBR. Bien que ne pouvant généraliser les résultats à tous les dépôts de catalyseurs et à tous les substrats de FAPC, les conclusions qui suivent ont pu être tirées. Pour le substrat de cordiérite étudié, la conversion catalytique augmente nettement pour les deux distributions de catalyseur, lorsque la quantité de catalyseur est augmentée jusqu'à occuper 30 % du volume des pores. La distribution uniforme de catalyseur permet une meilleure conversion jusqu'à ~20% pour une réaction rapide de premier ordre. La différence de conversion catalytique entre les deux types d'uniformité de distribution du catalyseur est principalement apparente dans le régime transitoire, c'est-à-dire entre le régime limité par la réaction et le régime limité par le transport des espèces chimiques. Cette différence peut s'expliquer par la plus faible surface spécifique entre le catalyseur et les pores dans le cas de la distribution non uniforme, qui résulte de l'obstruction préférentielle des petits pores, rendant une grande partie du volume du catalyseur indisponible pour la réaction. L'efficacité du catalyseur, pour une réaction de premier ordre à cinétique rapide, diminue progressivement à mesure que la quantité de catalyseur augmente pour une distribution uniforme, mais diminue fortement pour une distribution non uniforme de catalyseur à faible quantité. Cette tendance peut s'expliquer par le fait que pour une distribution non uniforme, à mesure que la quantité de catalyseur augmente, le volume du catalyseur devient de moins en moins accessible en raison de sa plus faible surface spécifique et des limitations en transport des espèces chimiques. En calculant le module de Thiele via une longueur caractéristique définie comme le rapport du volume de la phase catalytique divisé par la surface ouverte du catalyseur, l'efficacité du catalyseur peut être prédite presque quantitativement pour différentes géométries de dépôt catalytique, en utilisant une formule analytique à un seul paramètre. De cette façon, l'efficacité du catalyseur peut être déterminée directement à partir de la géométrie du dépôt catalytique, sans qu'il soit nécessaire de procéder à une simulation 3D à l'échelle microscopique.

En combinant les résultats des Articles 1 et 2 (Chapitres 5 et 6), il a été montré que le modèle numérique proposé peut être une approche quantitative permettant de déterminer si certains dépôts catalytiques sont plus performants que d'autres en termes de filtration et de catalyse, et ainsi fournir des orientations aux chercheurs et aux fabricants de FAPC pour améliorer les dispositifs de traitement des gaz d'échappement. Cette étude de cas a montré qu'une distribution uniforme de catalyseur est plus performante que la distribution non uniforme étudiée, tant en termes de filtration que de fonctionnalités catalytiques. Bien que ce résultat aurait pu être anticipé, le modèle proposé permet de quantifier les améliorations qui peuvent être attendues.

Une fois ces résultats obtenus, il est important de pouvoir vérifier et valider le modèle utilisé. Dans ce but, une procédure de validation des résultats de l'Article 1 a été développée et est présentée dans l'Article 3 (Chapitre 7). En effet, les prédictions en perméabilité du modèle présenté dans l'Article 1 étaient en assez bon accord qualitatif avec la théorie classique telle que l'équation de Blake-Kozeny, comme montré en Section 5.3.2.1. Néanmoins, un travail de validation plus précis était nécessaire pour quantifier avec précision la qualité des prédictions du modèle. Cependant, en raison des dimensions intrinsèquement petites des murs de cordiérite, les mesures précises de ΔP nécessitent généralement un équipement expérimental coûteux qui n'est souvent pas facilement disponible. Pour pallier cette limitation, une méthode expérimentale a été proposée. Elle repose sur le concept de similitude cinématique et sur une procédure de mise à l'échelle des structures poreuses de cordiérite recouvertes de catalyseur. Elle utilise une combinaison de fabrication additive à l'aide de filaments fondus et d'un nouveau perméamètre à pression variable développé par (Sun et al. 2020), pour sélectionner un facteur de mise à l'échelle permettant d'imprimer des structures avec une résolution suffisante de l'espace poreux et une perméabilité appropriée qui peuvent être facilement et précisément mesurées. Une analyse détaillée qui tient compte du régime d'écoulement, des caractéristiques structurelles du milieu poreux et des résolutions de l'imprimante 3D et du perméamètre est proposée afin de sélectionner le facteur d'échelle approprié. La procédure expérimentale ainsi proposée est une méthode relativement facile à mettre en œuvre et peu coûteuse, qui peut être intéressante pour de nombreux domaines des sciences et de l'ingénierie pour lesquels il est important de comprendre la relation entre les caractéristiques géométriques de structures poreuses et l'écoulement de fluides à leur travers. Elle est donc particulièrement bien adaptée pour valider les prévisions des modèles numériques. Bien que la perméabilité soit très

sensible aux petites caractéristiques structurelles, les mesures de perméabilité sur sept structures de paroi reconstruites agrandies avec des quantités de catalyseur et des degrés d'uniformité différents sont en très bon accord avec les prévisions du modèle MBR. Dans l'ensemble, ces résultats donnent une grande confiance à la fois dans la méthodologie numérique et dans la procédure expérimentale proposée, en particulier dans le contexte des FAPC.

Ainsi les Articles 1, 2 et 3 (Chapitres 5, 6 et 7 respectivement), ont permis d’atteindre l’objectif principal de prédiction de l’impact de la distribution de catalyseur sur les performances globales des FAPC. En plus de cela, les phénomènes physiques étant responsables de ce lien de cause à effet ont pu être décrits par une analyse détaillée des résultats de simulation.

CHAPITRE 9 CONCLUSION ET RECOMMANDATIONS

Afin de conclure cette thèse, une synthèse des travaux proposée sera présentée. Additionnellement, les limites de la méthode proposée ainsi que les nouvelles voies de recherche entrouvertes dans ce travail seront résumées. L'amélioration des systèmes tels que les FAPC par la modélisation numérique est un vaste sujet qui lie beaucoup de domaines de la recherche : physique et chimie à plusieurs échelles, techniques d'imagerie, algorithmes mathématiques, mécanique des fluides numérique, etc.

9.1 Synthèse des travaux présentés

Dans cette thèse, un modèle numérique de prédiction des performances des filtres à particules catalytiques (FAPC) à l'échelle microscopique a été développé. Il consiste en quatre étapes : (1) la reconstruction de milieux poreux digitaux représentant la céramique recouverte de catalyseur d'un FAPC pour moteur EID, (2) le calcul des propriétés d'écoulement de ces milieux par la méthode de Boltzmann sur réseau (MBR), (3) le calcul des trajectoires des particules de suie à travers ces milieux par la résolution de l'équation de Langevin et (4) le calcul des propriétés catalytiques de ces milieux par la MBR. Une fois ce modèle développé, il a été utilisé pour mener une étude comparative entre deux dépôts de catalyseur présentant différentes uniformités dans l'espace poreux de la céramique constituant les canaux du FAPC étudié. Cette étude avait pour but de déterminer l'impact de la distribution du catalyseur sur les performances globales du FAPC. Pour cela, les performances en filtration, définies par la perte de charge et l'efficacité de capture du mur poreux, ainsi que les performances catalytiques définies par la conversion des espèces chimiques à travers le mur poreux recouvert de catalyseur, ont été systématiquement calculées pour deux séries de structures. Une série de structures représentative du mur poreux original du FAPC présentant un dépôt non uniforme de catalyseur et une série présentant un dépôt uniforme de catalyseur. L'avantage en termes de performances globales, d'une distribution uniforme de catalyseur par rapport à une distribution non uniforme, a ainsi pu être quantifié. Ayant ces données entre leurs mains, les industriels travaillant à l'amélioration continue des systèmes de traitement des gaz d'échappement tels que les FAPC, vont pouvoir prendre des décisions quant à l'investissement à mettre dans l'uniformisation du dépôt de catalyseur au sein des canaux poreux

des FAPC. Pour cela, les techniques de déposition du catalyseur, qui consistent à injecter sous pression une suspension de catalyseur et à en enlever l'excès par succion et séchage, devront être améliorées à travers l'optimisation des paramètres expérimentaux comme la pression d'injection ou les propriétés physiques du catalyseur.

Tout au long de ce travail, une attention particulière a été portée à la vérification et la validation de chacune des étapes de la méthodologie numérique employée. Cela a permis de bâtir un modèle robuste et fiable. Les résultats obtenus sont donc utiles à l'industrie et vont servir à l'amélioration des systèmes de traitement des gaz d'échappement développés pour les véhicules modernes. Ce travail constitue donc une étape vers des véhicules plus propres et un environnement moins pollué. Il peut avoir un impact direct sur notre qualité de vie.

9.2 Limites de la méthode proposée

Bien que le modèle numérique développé dans ce travail se soit montré performant dans l'étude de l'impact de la distribution de catalyseur sur les performances des FAPC, et qu'il ait été vérifié et validé à l'aide de plusieurs cas tests, il est important de lui admettre des limites. Ses principales limites peuvent être résumées par les points suivants :

- Le modèle numérique est dépendant de la qualité des images qui servent à reconstruire une structure représentative du milieu poreux. Cette première étape est donc primordiale. Si le milieu reconstruit n'est pas assez représentatif de la géométrie réelle du FAPC, alors tous les calculs qui s'en suivent seront biaisés. Il est donc important de vérifier la première étape du modèle. Dans le cas de données de mauvaise qualité, des méthodes de reconstruction moins dépendantes aux données peuvent être toutefois envisagées. Une telle méthode est présentée en Annexe C.
- Le modèle ne prend pour l'instant pas en compte l'accumulation des particules de suie au sein du milieu poreux. Cependant, il est facilement possible d'ajouter cette prédiction au modèle en complétant l'étape (3). En effet le logiciel GeoDict® permet de telles simulations. Pour cela, le champ d'écoulement est d'abord calculé, les trajectoires des particules de suies sont alors résolues. Chaque position finale des particules est enregistrée et la géométrie est modifiée en fonction de la fraction de particules qu'elle contient. Les équations de

Brinkman-Navier-Stokes, qui sont une variante des équations de Navier-Stokes qui prennent en compte de la perméabilité via un terme source, sont alors résolues. De nouvelles trajectoires de particules sont calculées et ainsi de suite, jusqu'à un critère d'arrêt portant sur la perte de charge atteinte ou la masse de particules accumulées par exemple.

- Une seule réaction hypothétique est pour l'instant simulée par le modèle. Or la MBR est une méthode de calcul intrinsèquement transitoire et hautement parallélisable. L'approche proposée serait donc bien adaptée pour étudier l'évolution temporelle de nombreuses réactions concurrentes dans des conditions variables, comme pour étudier l'impact du stockage de l'oxygène du catalyseur sur les émissions de NOx, CO et HC. Il faudrait pour cela résoudre autant de problèmes d'ADR qu'il y a d'espèces impliquées dans ces réactions et déployer les calculs couplés résultants sur un cluster GPU haute performance, une solution capable d'accélérer considérablement les calculs.
- Un travail de validation est encore nécessaire, notamment pour les calculs de l'efficacité de capture et la résolution du champ de concentration. En effet pour ces deux étapes, le cas de V&V proposé n'est pas encore assez proche de la réalité. Une campagne d'expériences de validation sur des FAPC réels serait donc idéale pour compléter la validation du modèle. Cependant, ces expériences pourraient être compliquées et nécessiter du matériel onéreux. Les ressources de l'entreprise Umicore ou du groupe de recherche du professeur Robert E. Hayes à l'université d'Alberta, pourraient être mises à contribution.

9.3 Nouvelles voies de recherche

L'une des principales voies de recherche ouverte dans la conclusion de ce travail est le développement de modèles réduits de calcul des performances des FAPC. En effet, comme le disent François Bertrand et David Vidal, le but d'un ingénieur en simulation « n'est pas de faire rouler des simulations indéfiniment, mais d'en extraire la substantifique moelle ». Ainsi, à travers les résultats obtenus grâce aux étapes (2)-(4) du modèle numérique présenté en Section 4.1, des corrélations peuvent être tirées afin de réduire le modèle 3D à des modèles 1D voir 0D. Ces modèles peuvent être développés :

- En perméabilité, à l'aide de corrélations similaires à celle de Blake-Kozeny ou Carman-Kozeny pour lesquelles un nouveau coefficient d'ajustement pourrait être trouvé, comme montré en Section 2.2.1.3.
- En efficacité de capture, à partir des corrélations similaires à celles utilisées pour les entassements de sphères, comme détaillé en Section 2.2.1.4.
- En catalyse, à l'aide du module de Thiele, défini en Section 2.2.2.3, et dont un modèle analytique est développé dans le cadre des profils de distribution étudiés dans ce travail en Section 6.4.4.

Afin de généraliser les résultats obtenus dans ce travail et parce qu'il existe une infinité de non-uniformités pour le dépôt de catalyseur, il est nécessaire de compléter cette étude sur un plus grand nombre de structures avec un plus grand panel de non-uniformités. Il est également possible de changer la nature du substrat. En effet, bien que la cordiérite étudiée dans ce travail, soit la céramique la plus largement répandue pour la fabrication des FAPC pour moteurs EID, d'autres céramiques telles que le SiC peuvent être mises à l'étude.

De plus, il serait intéressant de lier des paramètres géométriques du dépôt, à la fois aux critères de performances, et aux paramètres expérimentaux de déposition du catalyseur, afin de permettre une étude d'optimisation de ces derniers. Ainsi un modèle réduit global à quelques paramètres pourrait être bâti pour mener à la distribution de catalyseur optimale, pour un substrat donné.

Enfin, le modèle numérique développé dans cette thèse a pour l'instant été utilisé à l'étude d'un seul cas, dans le contexte particulier des FAPC. Cependant, sa généralisation à des contextes de la recherche en lien avec les milieux poreux, la catalyse ou la filtration est envisageable : masques fibreux pour les épidémies, filtres pour cheminées d'usines, etc... Cependant ces nouvelles applications pourraient nécessiter une mise à l'échelle des simulations.

RÉFÉRENCES

Abell, A. B., K. L. Willis, and D. A. Lange. 1999. 'Mercury Intrusion Porosimetry and Image Analysis of Cement-Based Materials', *Journal of Colloid and Interface Science*, 211: 39-44.

Aderhold, Dirk, Alan Haynes, Georges, Michael Spencer, Leonard, William, and Duncan Winterbourn, John, William. 1999. "Monolith Coating Apparatus and Method Therefor." In *International Search Report.*: Wishart, Ian, Carmichael.

Ahmadinejad, Mehrdad, Jonathan E. Etheridge, Timothy C. Watling, Åsa Johansson, and Gareth John. 2015. 'Computer Simulation of Automotive Emission Control Systems', *Johnson Matthey Technology Review*, 59: 152-65.

Aitkenhead, Adam H. 2010. "Converting a 3D logical array into an STL surface mesh " In. MATLAB Central File Exchange.

Aleksandrova, Svetlana, Jonathan Saul, Humberto Medina, Oscar Garcia-Alfonso, Chunxing Lin, Jose Martin Herreros, Mark Bevan, and Stephen F. Benjamin. 2018. 'Gasoline Particulate Filter Wall Permeability Testing', *SAE Int. J. Engines*, 11.

Allouche, Mohamed Hatem, Romain Enjalbert, Federico Alberini, Mostapha Ariane, and Alessio Alexiadis. 2017. 'Development of a combined solver to model transport and chemical reactions in catalytic wall-flow filters', *Chemical Engineering Research and Design*, 117: 681-87.

"Ambient air pollution: A global assessment of exposure and burden of disease." In. 2016. *WHO Press*. Geneva, Switzerland World Health Organization

Andres-Valeri, Valerio, Luis Juli-Gandara, Daniel Jato-Espino, and Jorge Rodriguez-Hernandez. 2018. 'Characterization of the Infiltration Capacity of Porous Concrete Pavements with Low Constant Head Permeability Tests', *Water*, 10.

Aris, R. 1957. 'On shape factors for irregular particles-I. The steady-state problem. Diffusion and reaction', *Chem. Engng. Sci.*, 6: 262-68.

Azimian, Mehdi, Liping Cheng, and Andreas Wiegmann. 2017. "Simulation of soot filtration in diesel particulate filter with GeoDict." In *15th FAD-Conference "Challenge- Exhaust Aftertreatment for Diesel Engines"*. Dresden, Germany.

Baltzopoulou, Penelope, Margaritis Kostoglou, Eleni Papaioannou, and Athanasios G. Konstandopoulos. 2018. 'On the Effective Density and Fractal–Like Dimension of Diesel Soot Aggregates as a Function of Mobility Diameter', *Emission Control Science and Technology*, 4: 240-46.

Baveye, Philippe C., and Magdeline Laba. 2015. 'Moving away from the geostatistical lamppost: Why, where, and how does the spatial heterogeneity of soils matter?', *Ecological Modelling*, 298: 24-38.

Becker, Jürgen, Liping Cheng, Cornelia Kronsbein, and Andreas Wiegmann. 2016. 'Simulation of Cake Filtration for Polydisperse Particles', *Chemical Engineering & Technology*, 39: 559-66.

Belot, Igor, Yixun Sun, David Vidal, Martin Votsmeier, Philippe Causse, Robert Hayes, François Trochu, and François Bertrand. Submitted (2020). 'A 3D Additive Manufacturing Approach for the Validation of a Numerical Wall-Scale Model of Catalytic Particulate Filters', *Chemical Engineering Journal*.

Belot, Igor, David Vidal, Robert Greiner, Martin Votsmeier, Robert Hayes, and François Bertrand. 2020. 'Impact of Washcoat Distribution on the Catalytic Performance of Gasoline Particulate Filters as predicted by Lattice Boltzmann Simulations ', *submitted to Chemical Engineering Journal*.

Belot, Igor, David Vidal, Martin Votsmeier, Robert Hayes, and François Bertrand. 2020. 'Numerical Investigation of the Impact of Washcoat Distribution on the Filtration Performace of Gasoline Particulate Filters', *Chemical Engineering Science*, 221.

Benjamin, S. F., Z. Liu, and C. A. Roberts. 2004. 'Automotive catalyst design for uniform conversion efficiency', *Applied Mathematical Modelling*, 28: 559-72.

Benjamin, S. F., and C. A. Roberts. 2014. 'Methodology for Modelling a Combined DPF and SCR Catalyst with the Porous Medium Approach in CFD', *SAE International Journal of Engines*, 7: 1997-2011.

Bensaid, S., D. L. Marchisio, D. Fino, G. Saracco, and V. Specchia. 2009. 'Modelling of diesel particulate filtration in wall-flow traps', *Chemical Engineering Journal*, 154: 211-18.

Bensaid, Samir, Daniele L. Marchisio, and Debora Fino. 2010. 'Numerical simulation of soot filtration and combustion within diesel particulate filters', *Chemical Engineering Science*, 65: 357-63.

Bertrand, François, Christophe Devals, David Vidal, Cyrille Séguineau de Préval, and Robert E. Hayes. 2012. 'Towards the simulation of the catalytic monolith converter using discrete channel-scale models', *Catalysis Today*, 188: 80-86.

Bhatnagar, PL, EP Gross, and M Krook. 1954. 'A model for collision processes in gases. I. Small amplitude processes in charged and neutral one-component systems', *Phys Rev*, 94:511–25.

Bird, R. Byron, Warren E. Stewart, and Edwin N. Lightfoot. 2007. *Transport Phenomena* (John Wiley & Sons, Inc.).

Bissett, E. J., and Farhang Shadman. 1985. 'Thermal Regeneration of Diesel-Particulate Monolithic Filters', *AICHE Journal*, 31: 753-58.

Blake, F. C. 1922. *Trans. Amer. Inst. Chem. Engrs.*, 14: 415-21.

Blazek, Jiri. 2005. *COMPUTATIONAL FLUID DYNAMICS : Principles and Applications* (Elsevier Ltd.).

Bogarra, Maria, Jose Martin Herreros, Cruz Hergueta, Athanasios Tsolakis, Andrew P. E. York, and Paul J. Millington. 2017. 'Influence of Three-Way Catalyst on Gaseous and Particulate Matter Emissions During Gasoline Direct Injection Engine Cold-start', *Johnson Matthey Technology Review*, 61: 329-41.

Bracconi, Mauro, Matteo Ambrosetti, Obinna Okafor, Victor Sans, Xun Zhang, Xiaoxia Ou, Claudio Pereira Da Fonte, Xiaolei Fan, Matteo Maestri, Gianpiero Groppi, and Enrico

Tronconi. 2019. 'Investigation of pressure drop in 3D replicated open-cell foams: Coupling CFD with experimental data on additively manufactured foams', *Chemical Engineering Journal*, 377.

Braisher, Mike, Richard Stone, and Phil Price. 2010. 'Particle Number Emissions from a Range of European Vehicles', *SAE International*.

Brandstätter, W., J. Leixnering, P. Faraldi, E. Merlone Borla, M. Ranalli, N. Vlachos, and A. G. Konstandopoulos. 2005. 'The STYFF-DEXA Project: Advanced Simulation Tools for Ceramic Foam Diesel Particulate Filters'.

Burtscher, H. 2005. 'Physical characterization of particulate emissions from diesel engines: a review', *Journal of Aerosol Science*, 36: 896-932.

Calore, E., A. Gabbana, J. Kraus, E. Pellegrini, S. F. Schifano, and R. Tripiccione. 2016. 'Massively parallel lattice–Boltzmann codes on large GPU clusters', *Parallel Computing*, 58: 1-24.

Chang, X., S. Wang, B. Zhao, J. Xing, X. Liu, L. Wei, Y. Song, W. Wu, S. Cai, H. Zheng, D. Ding, and M. Zheng. 2019. 'Contributions of inter-city and regional transport to PM2.5 concentrations in the Beijing-Tianjin-Hebei region and its implications on regional joint air pollution control', *Sci Total Environ*, 660: 1191-200.

Charbonnel, Sylvain, and Cornelius N. Opris. 2009. 'Fundamental Diesel Particulate Filter (DPF) Pressure Drop Model', *SAE International*.

Chen, Ding-Jun, Chung-Yeol Lee, Cheol-Hoon Park, and Pedro Mendes. 2007. 'Parallelizing simulated annealing algorithms based on high-performance computer', *Journal of Global Optimization*, 39: 261-89.

Clague, David S., and Ronald J. Phillips. 1997. 'A numerical calculation of the hydraulic permeability of three-dimensional disordered fibrous media', *Phys. Fluids*, 9.

Cornejo, Ivan, Petr Nikrityuk, and Robert E. Hayes. 2020. 'The influence of channel geometry on the pressure drop in automotive catalytic converters: Model development and validation', *Chemical Engineering Science*, 212.

Crandall, D., G. Ahmadi, D. Leonard, M. Ferer, and D. H. Smith. 2008. 'A new stereolithography experimental porous flow device', *Rev Sci Instrum*, 79: 044501.

Crowe, Clayton T. 2005. *Multiphase Flow Handbook* (Taylor & Francis Group: Boca Raton).

Czerwinski, Jan, Yan Zimmerli, Andreas Mayer, Giovani D'Urbano, and Daniel Zürcher. 2015. 'Emission Reduction with Diesel Particle Filter with SCR Coating (SDPF)', *Emission Control Science and Technology*, 1: 152-66.

Davis, S.C., S.E. Williams, R.G. Boundy, and S Moore. 2016. "Vehicle Technologies Market Report." In.: Oak Ridge National Lab, ORNL.

Deutschmann, Olaf. 2014. 'Modeling of the Interactions Between Catalytic Surfaces and Gas-Phase', *Catalysis Letters*, 145: 272-89.

Devicharan, R., and R. Garg. 2019. 'Optimization of the Print Quality by Controlling the Process Parameters on 3D Printing Machine.' in, *Kumar L., Pandey P., Wimpenny D. (eds) 3D Printing and Additive Manufacturing Technologies* (Springer: Singapore).

Doran, Pauline M. 2013. *Bioprocess Engineering Principles* (Academic Press).

Dražić, Slobodan, Nataša Sladoje, and Joakim Lindblad. 2016. 'Estimation of Feret's diameter from pixel coverage representation of a shape', *Pattern Recognition Letters*, 80: 37-45.

Dudák, Michal, Vladimír Novák, Petr Kočí, Miloš Marek, Patricia Blanco-García, and Glenn Jones. 2014. 'Prediction of diffusivity and conversion of n-decane and CO in coated Pt/γ-Al2O3 catalyst depending on porous layer morphology', *Applied Catalysis B: Environmental*, 150-151: 446-58.

Dullien, F. A. L. 1979. *Porous media – fluid transport and pore structure* (Academic Press: New York, NY, USA).

Ferziger, Joel H., and Milovan Peric. 2002. *Computational Methods for Fluid Dynamics - 3rd edition* (Springer).

Fiano, Angela. 2017. 'A model for soot load estimation in a Gasoline Particulate Filter using a Radio Frequency sensor"', University of Windsor.

Foerster, Martin, Ewald Dittrich, Gerhard Birtigh, Walter Leibold, Bernd Mergner, Michael Hoffmann, Wolfgang Hasselmann, and Robert Schafer. 2000. "Process for the coating of the flow channels of a honeycomb form catalytic converter carrier with a dispersion coating." In.: Degussa-Huls Aktiengesellschaft.

Fuller, Edward N., Paul D. Schettler, and J. Calvin Giddings. 1966. 'A new method for prediction of binary gas-phase diffusion coefficients', *Industrial And Engineering Chemistry*, 58.

Galvan, S., C. Pla, N. Cueto, J. Martínez-Martínez, M. A. García-del-Cura, and D. Benavente. 2014. 'A comparison of experimental methods for measuring water permeability of porous building rocks', *Materiales de Construcción*, 64.

"GeoDict." In. 2018. www.geodict.com: Math2Market GmbH.

George, Sam, and Achim Heibel. 2016. "Next Generation Cordierite Thin Wall DPF for Improved Pressure Drop and Lifetime Pressure Drop Solution." In *SAE Technical Paper Series*.

Gervais, P. C., S. Bourrous, F. Dany, L. Bouilloux, and L. Ricciardi. 2015. 'Simulations of filter media performances from microtomography-based computational domain. Experimental and analytical comparison', *Computers & Fluids*, 116: 118-28.

Gomez, J. S., R. J. Chalaturnyk, and G. Zambrano-Narvaez. 2018. 'Experimental Investigation of the Mechanical Behavior and Permeability of 3D Printed Sandstone Analogues Under Triaxial Conditions', *Transport in Porous Media*.

Gonçalves-e-Silva, Kayo, Daniel Aloise, and Samuel Xavier-de-Souza. 2018. 'Parallel synchronous and asynchronous coupled simulated annealing', *The Journal of Supercomputing*, 74: 2841-69.

Gong, J., S. Viswanathan, D. A. Rothamer, D. E. Foster, and C. J. Rutland. 2017. 'Dynamic Heterogeneous Multiscale Filtration Model: Probing Micro- and Macroscopic Filtration Characteristics of Gasoline Particulate Filters', *Environ Sci Technol*, 51: 11196-204.

Gong, Jian, Mark L. Stewart, Alla Zelenyuk, Andrea Strzelec, Sandeep Viswanathan, David A. Rothamer, David E. Foster, and Christopher J. Rutland. 2018. 'Importance of filter's microstructure in dynamic filtration modeling of gasoline particulate filters (GPFs): Inhomogeneous porosity and pore size distribution', *Chemical Engineering Journal*, 338: 15-26.

Graves, Brian Mackenzie, Charles Robert Koch, and Jason Scott Olfert. 2017. 'Morphology and volatility of particulate matter emitted from a gasoline direct injection engine fuelled on gasoline and ethanol blends', *Journal of Aerosol Science*, 105: 166-78.

Greiner, Robert, Torben Prill, Oleg Iliev, Barry A. A. L. van Setten, and Martin Votsmeier. 2019. 'Tomography based simulation of reactive flow at the micro-scale: Particulate filters with wall integrated catalyst', *Chemical Engineering Journal*, 378.

Guan, B., R. Zhan, H. Lin, and Z. Huang. 2015. 'Review of the state-of-the-art of exhaust particulate filter technology in internal combustion engines', *J Environ Manage*, 154: 225-58.

Günaydın, Kadir, and Halit Süleyman Türkmen. 2018. "COMMON FDM 3D PRINTING DEFECTS." In *International Congress on 3D Printing (Additive Manufacturing) Technologies and Digital Industry*.

Guo, Zhaoli, and Chang Shu. 2013. *Lattice Boltzmann Method and Its Applications in Engineering* (World Scientific: Singapore).

Haile, J. M., C. Massobrio, and S. Torquato. 1985. 'Two-point matrix probability function for two-phase random media: Computer simulation results for impenetrable spheres', *J. Chern. Phys.*, 83.

Hajireza, S, LT Johannesen, T Wolff, GC Koltsakis, ZC Samaras, and OA Haralampous. 2010. 'A modeling and experimental investigation on an innovative substrate for DPF applications', *SAE Int. J. Engines*, 01.

Hall, K. D. 2004. 'Comparison of falling-head and constant-head techniques: Estimating field permeability of hot-mix asphalt pavements', *Transportation research record*, 1891: 23-31.

Harry, Karen G., and Allen Johnson. 2004. 'A non-destructive technique for measuring ceramic porosity using liquid nitrogen', *Journal of Archaeological Science*, 31: 1567-75.

Havelka, Jan, Anna Kucerova, and Jan Sykora. 2016. 'Compression and Reconstruction of Random Microstructures using Accelerated Lineal Path Function', *arXiv:1601.04359 [cond-mat.mtrl-sci]*.

Hayashi, Hidemitsu, and Shuichi Kubo. 2008. 'Computer simulation study on filtration of soot particles in diesel particulate filter', *Computers & Mathematics with Applications*, 55: 1450-60.

Hayes, R. E., B. Liu, and M. Votsmeier. 2005. 'Calculating effectiveness factors in non-uniform washcoat shapes', *Chemical Engineering Science*, 60: 2037-50.

Hayes, R. E., and J. P. Mmbaga. 2012. 'Chapter 9 : Transport Processes In Catalysis.' in Hoboken : CRC Press. (ed.), *Introduction to Chemical Reactor Analysis, Second Edition.*

Hayes, R. E., P. K. Mok, J. Mmbaga, and M. Votsmeier. 2007. 'A fast approximation method for computing effectiveness factors with non-linear kinetics', *Chemical Engineering Science*, 62: 2209-15.

Hekmatzadeh, Ali, Hatef Keshavarzi, Nasser Talebbeydokhti, and Ali Torabi Haghighi. 2018. 'Lattice Boltzmann solution of advection-dominated mass transport problem: a comparison', *Scientia Iranica*: -.

Hinds, William C. 1999. *Aerosol Technology : Properties, Behavior, and Measurement of Airborne Particles - 2nd ed.* (John Wiley & sons, Inc.).

Hosseini, Seyed Ali, Nasser Darabiha, Dominique Thévenin, and Amir Eshghinejadfard. 2018. 'Stability limits of the single relaxation-time advection–diffusion lattice Boltzmann scheme', *International Journal of Modern Physics C*, 28.

Howitt, J., and M. Montierth. 1981. 'Cellular Ceramic Diesel Particulate Filter', *SAE Technical Paper*, 810114: 12.

Inoda, Satoru, Yasutaka Nomura, Hirotaka Ori, and Yuji Yabuzaki. 2017. "Development of New Coating Technology Optimized for Each Function of Coated GPF." In *SAE Technical Paper Series*.

Ishutov, Sergey. 2017. '3D printing porous proxies as a new tool for laboratory and numerical analyses of sedimentary rocks', Iowa State University.

Johnson, D. O., F. J. Arriaga, and Birl Lowery. 2005. 'Automation of a Falling Head Permeameter for Rapid Determination of Hydraulic Conductivity of Multiple Samples', *Soil Science Society of America Journal*, 69.

Johnson, Timothy V. 2004. 'Diesel Emission Control Technology – 2003 in Review', *SAE Technical Paper Series*, 2004-01-0070.

Joshi, Ameya, and Timothy V. Johnson. 2018. 'Gasoline Particulate Filters—a Review', *Emission Control Science and Technology*, 4: 219-39.

Karakaya, Canan, Peter J. Weddle, Justin M. Blasi, David R. Diercks, and Robert J. Kee. 2016. 'Modeling reaction–diffusion processes within catalyst washcoats: I. Microscale processes based on three-dimensional reconstructions', *Chemical Engineering Science*, 145: 299-307.

Karamitros, Dimitrios, and Grigorios Koltsakis. 2017. 'Model-based optimization of catalyst zoning on SCR-coated particulate filters', *Chemical Engineering Science*, 173: 514-24.

Karani, H., and C. Huber. 2015. 'Lattice Boltzmann formulation for conjugate heat transfer in heterogeneous media', *Phys Rev E Stat Nonlin Soft Matter Phys*, 91: 023304.

Kazemimanesh, Mohsen, Alireza Moallemi, Kevin Thomson, Greg Smallwood, Prem Lobo, and Jason S. Olfert. 2018. 'A novel miniature inverted-flame burner for the generation of soot nanoparticles', *Aerosol Science and Technology*, 53: 184-95.

Keskinen, Jorma, Annele Virtanen, Peter Ahlvik, and Leonidas Ntziachrstos. 1998. 'Estimation of effective Density of Diesel Particles', *J. Aerosol Sci.*, 29: S1007-S08.

Khalek, Imad A, Thomas L Bougher, and Jeff J. Jetter. 2010. 'Particle Emissions from a 2009 Gasoline Direct Injection Engine Using Different Commercially Available Fuels', *SAE Int. J. Engines*, 3: 623-37.

Khan, M. R., and T. Shamim. 2008. 'A numerical investigation of the regeneration characteristics of diesel particulate filters under simulated transient exhaust conditions', *Proceedings of the Institution of Mechanical Engineers, Part D: Journal of Automobile Engineering*, 222: 2469-85.

Kikkinides, E. S., and V. N. Burganos. 2000. 'Permeation properties of three-dimensional self-affine reconstructions of porous materials', *Physical Review E*, 62.

Kinoshita, Kentaro, Atsushi Sakaguchi, Akinori Harada, Hiroki Yamaoka, Satoru Kishida, Yukinobu Fukaya, Toshiki Nokami, and Toshiyuki Itoh. 2017. 'Improvement of switching endurance of conducting-bridge random access memory by addition of metal-ion-containing ionic liquid', *Japanese Journal of Applied Physics*, 56.

Kittelson, David B. 1998. 'Engines and Nanoparticles: a Review', *J. Aerosol Sci.*, 29: 575—88.

Kočí, P., F. Štěpánek, M. Kubíček, and M. Marek. 2007. 'Modelling of micro/nano-scale concentration and temperature gradients in porous supported catalysts', *Chemical Engineering Science*, 62: 5380-85.

Kočí, Petr. 2019. "Multi-scale modeling of catalytic particulate filtes for gasoline engines (GPF)." In *International Symposium on Modeling of Exhaust-Gas After-Treatment (MODEGAT VI)*. Bad Herrenalb/Karlsrue , Germany.

Kočí, Petr, Martin Isoz, Marie Plachá, Adéla Arvajová, Marek Václavík, Miloš Svoboda, Emily Price, Vladimír Novák, and David Thompsett. 2019. '3D reconstruction and pore-scale modeling of coated catalytic filters for automotive exhaust gas aftertreatment', *Catalysis Today*, 320: 165-74.

Kočí, Petr, Vladimír Novák, František Štěpánek, Miloš Marek, and Milan Kubíček. 2010. 'Multi-scale modelling of reaction and transport in porous catalysts', *Chemical Engineering Science*, 65: 412-19.

Kočí, Petr, František Štěpánek, Milan Kubíček, and Miloš Marek. 2006. 'Meso-scale modelling of CO oxidation in digitally reconstructed porous catalyst', *Chemical Engineering Science*, 61: 3240-49.

Koltsakis, Grigorios, Onoufrios Haralampous, Christopher Depcik, and J. Colter Ragone. 2013. 'Catalyzed diesel particulate filter modeling', *Reviews in Chemical Engineering*, 29: 1-61.

Kong, Hyeonoh, and Kazuhiro Yamamoto. 2018. 'Simulation on soot deposition in in-wall and on-wall catalyzed diesel particulate filters', *Catalysis Today*.

Konstandopoulos, A. G., M. Kostoglou, S. Lorentzou, and N. Vlachos. 2012. 'Aspects of multifunctional diesel particulate filters and their efficient simulation', *Catalysis Today*, 188: 2-13.

Konstandopoulos, A., and J. Johnson. 1989. 'Wall-Flow Diesel Particulate Filters—Their Pressure Drop and Collection Efficiency', *SAE Technical Paper*, 890405: 23.

Konstandopoulos, A.G., M. Kostoglou, and N. Vlachos. 2006. 'The multiscale nature of diesel particulate filter simulation', *Int. J. Vehicle Design*, 41: 256-84.

Konstandopoulos, Athanasios G. 2000. 'Fundamental Studies of Diesel Particulate Filters: Transient Loading, Regeneration and Aging', *SAE Int. J. Engines*.

Konstandopoulos, Athanasios G. 2003. "Flow Resistance Descriptors for Diesel Particulate Filters: Definitions, Measurements and Testing." In.: SAE International.

Konstandopoulos, Athanasios G., Margaritis Kostoglou, Nickolas Vlachos, and Evdoxia Kladopoulou. 2005. 'Progress in Diesel Particulate Filter Simulation', *SAE International*.

Konstandopoulos, Athanasios G., and Eleni Papaioannou. 2008. 'Update on The Science and Technology of Diesel Particulate Filters', *KONA Powder and Particle Journal*, 26.

Kozeny, J. 1927. *Sitzungsber. Akad. Wiss. Wien, Abt. IIa*, 136: 271-306.

Krüger, Timm, Halim Kusumaatmaja, Alexandr Kuzmin, Orest Shardt, Goncalo Silva, and Erlend Magnus Viggen. 2017. *The Lattice Boltzmann: Method Principles and Practice* (Springer International Publishing).

Krupp, H. 1967. 'Particle adhesion, theory and experiment', *Advances in Colloid and Interface Sci.*, 1: 111.

Lambert, Christine, Timothy Chanko, Douglas Dobson, Xin Liu, and James Pakko. 2017. 'Gasoline Particle Filter Development', *Emission Control Science and Technology*, 3: 105-11.

Lambert, Christine K., Mira Bumbaroska, Douglas Dobson, Jon Hangas, James Pakko, and Paul Tennison. 2016. 'Analysis of High Mileage Gasoline Exhaust Particle Filters', *SAE Int. J. Engines*, 01.

Larson, Mats G., and Fredrik Bengzon. 2013. *The Finite Element Method: Theory, Implementation, and Applications.* (Springer Heidelberg New York Dordrecht London).

Leclaire, Sébastien, David Vidal, Louis Fradette, and François Bertrand. 2018. "Lattice Boltzmann Modeling of Immiscible Liquid-Liquid Flows in Static Mixers." In *Mixing XXVI*. San Juan, Porto Rico, USA.

Lee, Da Young, Gi Wook Lee, Kyu Yoon, Byoungjin Chun, and Hyun Wook Jung. 2018. 'Lattice Boltzmann simulations for wall-flow dynamics in porous ceramic diesel particulate filters', *Applied Surface Science*, 429: 72-80.

Lee, Jungkuk, Joseph R. Theis, and Eleni A. Kyriakidou. 2019. 'Vehicle emissions trapping materials: Successes, challenges, and the path forward', *Applied Catalysis B: Environmental*, 243: 397-414.

Lee, K. W., and B. Y. H. Liu. 1981. 'Experimental Study of Aerosol Filtration by Fibrous Filters', *Aerosol Science and Technology*, 1: 35-46.

Lee, KW, and JA Gieseke. 1979a. 'Collection of aerosol particles by packed beds', *Environ Sci Technol*, 13: 466-70.

Lee, Kyoo Won, and James A. Gieseke. 1979b. 'Collection of Aerosol Particles by Packed Beds', *Environmental Science & Technology*, 13: 466-70.

Leung, D., and R. E. Hayes. 1996. 'Diffusion Limitation Effects in the Washcoat of a Catalytic Monolith Reactor', *The Canadian Journal of Chemical Engineering*, 74.

Levitz, P. 1998. 'Off-lattice reconstruction of porous media: critical evaluation, geometrical confinement and molecular transport', *Advances in Colloid and Interface Science*, 76-77: 71-106.

Lewtas, J. 2007. 'Air pollution combustion emissions: characterization of causative agents and mechanisms associated with cancer, reproductive, and cardiovascular effects', *Mutat Res*, 636: 95-133.

Lindquist, W. B., and A. Venkatarangan. 1999. 'Investigating 3D Geometry of Porous Media from High Resolution Images', *Phys. Chem. Earth (A)*, 25: 593-99.

Liu, Shijie. 2017. *Bioprocess Engineering : Kinetics, Sustainability, and Reactor Design* (Elsevier).

Liu, Xin, Timothy Chanko, Christine Lambert, and Matti Maricq. 2018. "Gasoline Particulate Filter Efficiency and Backpressure at Very Low Mileage." In *SAE Technical Paper Series*.

Lopez-Gonzalez, D., M. N. Tsampas, A. Boréave, L. Retailleau-Mevel, M. Klotz, C. Tardivat, B. Cartoixa, K. Pajot, and P. Vernoux. 2015. 'Mixed Ionic–Electronic Conducting Catalysts for Catalysed Gasoline Particulate Filters', *Topics in Catalysis*, 58: 1242-55.

Lorentzou, Souzana, Chrysa Pagkoura, Athanasios G. Konstandopoulos, and Joerg Boettcher. 2008. 'Advanced Catalyst Coatings for Diesel Particulate Filters', *SAE Int. J. Engines*, 01.

Lorentzou, Souzana, Chrysa Pagkoura, Alexandra Zygogianni, Georgia Kastrinaki, and Athanasios G. Konstandopoulos. 2008. 'Catalytic Nano-structured Materials for Next Generation Diesel Particulate Filters', *SAE Technical Paper Series*, 01.

Lupše, Janez, Marina Campolo, and Alfredo Soldati. 2016. 'Modelling soot deposition and monolith regeneration for optimal design of automotive DPFs', *Chemical Engineering Science*, 151: 36-50.

Maricq, M. M., J. J. Szente, J. Adams, P. Tennison, and T. Rumpsa. 2013. 'Influence of mileage accumulation on the particle mass and number emissions of two gasoline direct injection vehicles', *Environ Sci Technol*, 47: 11890-6.

Maricq, M. Matti, Diane H Podsiadlik, Diana D Brehob, and Mohammad Haghgooie. 1999. 'Particulate Emissions from a Direct-Injection Spark-Ignition (DISI) Engine ', *Society of Automotive Engineers, Inc.*

Maricq, M. Matti, Diane H. Podsiadlik, and Richard E. Chase. 1999. 'Gasoline Vehicle Particle Size Distributions: Comparison of Steady State, FTP, and US06 Measurements', *Environmental Science & Technology*, 33.

Martinet, S., Y. Liu, C. Louis, P. Tassel, P. Perret, A. Chaumond, and M. Andre. 2017. 'Euro 6 Unregulated Pollutant Characterization and Statistical Analysis of After-Treatment Device and Driving-Condition Impact on Recent Passenger-Car Emissions', *Environ Sci Technol*, 51: 5847-55.

Masoudi, Mansour. 2005. "Pressure Drop of Segmented Diesel Particulate Filters." In *SAE Technical Paper Series*.

Masoudi, Mansour, Achim Heibel, and Paul M. Then. 2000. "Predicting Pressure Drop of Wall-Flow Diesel Particulate Filters - Theory and Experiment." In.: SAE International.

Matte-Deschênes, Guillaume, David Vidal, François Bertrand, and Robert E. Hayes. 2016. 'Numerical investigation of the impact of thermophoresis on the capture efficiency of diesel particulate filters', *The Canadian Journal of Chemical Engineering*, 94: 291-303.

Mikulic, Dr.-Ing. Ingo, Hein Koelman, Steve Majkowski, and Paul Vosejpka. 2010. "A Study about Particle Filter Application on a State-of-the-Art Homogeneous Turbocharged 2L DI Gasoline Engine." In *Aachener Kolloquium Fahrzeug- und Motorentechnik 2010*.

Mitsouridis, M. A., D. Karamitros, and G. Koltsakis. 2019. 'Model-Based Analysis of TWC-Coated Filters Performance', *Emission Control Science and Technology*, 5: 238-52.

Mock, P. 2017. "European Vehicle Market Statistics." In *Pocketbook 2017/18*. Berlin: International Council on Clean Transportation.

Moore, Gordon E. 1965. 'Cramming more components onto integrated circuits', *Electronics*, 38.

Mosser, L., O. Dubrule, and M. J. Blunt. 2017. 'Reconstruction of three-dimensional porous media using generative adversarial neural networks', *Phys Rev E*, 96: 043309.

Nagy, L., A. Tabácks, and T. Huszák. 2013. 'Comparison of permeability testing methods', *Proceedings of the 18th International Conference on Soil Mechanics and Geotechnical Engineering, Paris*: 399-402.

Nazari Moghaddam, Rasoul, and Mahmoud Jamiolahmady. 2016. 'Slip flow in porous media', *Fuel*, 173: 298-310.

Nie, Baisheng, Xianfeng Liu, Longlong Yang, Junqing Meng, and Xiangchun Li. 2015. 'Pore structure characterization of different rank coals using gas adsorption and scanning electron microscopy', *Fuel*, 158: 908-17.

Nightingale, H., and W. Bianchi. 1970. 'Rapid measurement of hydraulic conductivity changes in slowly permeable soils', *Soil Science*, 110: 221-28.

Ohser, J., and F. Mücklich. 2000. *Statistical Analysis of Microstructures in Materials Science* (Wiley and Sons).

Olfert, Jason, and Steven Rogak. 2019. 'Universal relations between soot effective density and primary particle size for common combustion sources', *Aerosol Science and Technology*, 53: 485-92.

Olowojebutu, Seun, and Thomas Steffen. 2017. "A Review of the Literature on Modelling of Integrated SCR-in-DPF Systems." In *SAE Technical Paper Series*.

"OpenFOAM." In.

Opitz, B., and M. Votsmeier. 2016. 'A simulation study on the conversion efficiency of catalytically active particulate filters', *Chemical Engineering Science*, 149: 117-28.

Øren, Pal-Eric, and Stig Bakke. 2002. 'Process Based Reconstruction of Sandstones and Prediction of Transport Properties', *Transport in Porous Media*, 46: 311-43.

Osei-Bonsu, Kofi, Paul Grassia, and Nima Shokri. 2018. 'Effects of Pore Geometry on Flowing Foam Dynamics in 3D-Printed Porous Media', *Transport in Porous Media*, 124: 903-17.

Otsu, Nobuyuki. 1979. 'A Threshold Selection Method from Gray-Level Histograms', *IEEE Transactions on Systems, Man, and Cybernetics*, SMC-9, NO. 1.

Otten, W., R. Pajor, S. Schmidt, P. C. Baveye, R. Hague, and R. E. Falconer. 2012. 'Combining X-ray CT and 3D printing technology to produce microcosms with replicable, complex pore geometries', *Soil Biology and Biochemistry*, 51: 53-55.

Ozelim, Luan C. de S. M., and André L. B. Cavalcante. 2019. 'Combining Microtomography, 3D Printing, and Numerical Simulations to Study Scale Effects on the Permeability of Porous Media', *International Journal of Geomechanics*, 19.

Ozhan, Cansu, Daniel Fuster, and Patrick Da Costa. 2014. 'Multi-scale flow simulation of automotive catalytic converters', *Chemical Engineering Science*, 116: 161-71.

Palmaa, Vincenzo, Paolo Ciambellia, Eugenio Melonia, and Agusti Sinb. 2013. 'Optimal CuFe2O4 Load for MW Susceptible Catalysed DPF', *Chemical Engineering Transactions*, 35.

Papadias, D., L. Edsberg, and P. BjoKrnbom. 2000. 'Simplified method for effectiveness factor calculations in irregular geometries of washcoats', *Chemical Engineering Science*, 55: 1447-59.

Park, Kihong, David B. Kittelson, and Peter H. McMurry. 2004. 'Structural Properties of Diesel Exhaust Particles Measured by Transmission Electron Microscopy (TEM): Relationships to Particle Mass and Mobility', *Aerosol Science and Technology*, 38: 881-89.

Patelli, Edoardo, and Gerhart Schuëller. 2009. 'On optimization techniques to reconstruct microstructures of random heterogeneous media', *Computational Materials Science*, 45: 536-49.

Pedescoll, A., P. R. Knowles, P. Davies, J. García, and J. Puigagut. 2011. 'A Comparison of In Situ Constant and Falling Head Permeameter Tests to Assess the Distribution of Clogging Within Horizontal Subsurface Flow Constructed Wetlands', *Water, Air, & Soil Pollution*, 223: 2263-75.

Penner, J. E., C. C. Chuang, and K. Grant. 1998. 'Climate forcing by carbonaceous and sulfate aerosols', *Climate Dynamics*, 14: 839—51.

Platt, S. M., I. El Haddad, S. M. Pieber, A. A. Zardini, R. Suarez-Bertoa, M. Clairotte, K. R. Daellenbach, R. J. Huang, J. G. Slowik, S. Hellebust, B. Temime-Roussel, N. Marchand, J. de Gouw, J. L. Jimenez, P. L. Hayes, A. L. Robinson, U. Baltensperger, C. Astorga, and A. S. H. Prevot. 2017. 'Gasoline cars produce more carbonaceous particulate matter than modern filter-equipped diesel cars', *Sci Rep*, 7: 4926.

Premchand, Kiran C. 2013. 'Development of a 1-D Catalyzed Diesel Particulate Filter Model for Simulation of the Performance and the Oxidation of Particulate Matter and Nitrogen Oxides Using Passive Oxidation and Active Regeneration Engine Experimental Data', Michigan Technological University.

Quintanilla, J., and S. Torquato. 1997. 'Microstructure functions for a model of statistically inhomogeneous random media', *Phys Rev E*, 55.

Rangel, David P., Claire Superak, Mayra Bielschowsky, Katie Farris, Ruth E. Falconer, and Philippe C. Baveye. 2013. 'Rapid Prototyping and 3-D Printing of Experimental Equipment in Soil Science Research', *Soil Science Society of America Journal*, 77.

Rappé, Kenneth G. 2014. 'Integrated Selective Catalytic Reduction–Diesel Particulate Filter Aftertreatment: Insights into Pressure Drop, NOx Conversion, and Passive Soot Oxidation Behavior', *Industrial & Engineering Chemistry Research*, 53: 17547-57.

Raza, Mohsin, Longfei Chen, Felix Leach, and Shiting Ding. 2018. 'A Review of Particulate Number (PN) Emissions from Gasoline Direct Injection (GDI) Engines and Their Control Techniques', *Energies*, 11.

Ricca, Antonio, Vincenzo Palma, Marco Martino, and Eugenio Meloni. 2017. 'Innovative catalyst design for methane steam reforming intensification', *Fuel*, 198: 175-82.

Richter, Joerg Michael, Raoul Klingmann, Stephanie Spiess, and Ka-Fai Wong. 2012. 'Application of Catalyzed Gasoline Particulate Filters to GDI Vehicules ', *SAE Int. J. Engines*, 5.

Rosner, Daniel E., and Pushkar Tandon. 1995. 'Rational Prediction of Inertially Induced Particle Deposition Rates for a Cylindrical Target in a Dust-Laden Stream ', *Chemical Engineering Science*, 50: 3409-31.

Rouquerol, Jean, Gino Baron, Renaud Denoyel, Herbert Giesche, Johan Groen, Peter Klobes, Pierre Levitz, Alexander V. Neimark, Sean Rigby, Romas Skudas, Kenneth Sing, Matthias Thommes, and Klaus Unger. 2011. 'Liquid intrusion and alternative methods for the characterization of macroporous materials (IUPAC Technical Report)', *Pure and Applied Chemistry*, 84: 107-36.

Seong, Heeje, Seungmok Choi, Katarzyna E. Matusik, Alan L. Kastengren, and Christopher F. Powell. 2019. '3D pore analysis of gasoline particulate filters using X-ray tomography: impact of coating and ash loading', *Journal of Materials Science*, 54: 6053-65.

Serrano, José Ramón, Héctor Climent, Pedro Piqueras, and Emanuele Angiolini. 2016. 'Filtration modelling in wall-flow particulate filters of low soot penetration thickness', *Energy*, 112: 883-98.

Shen, Peiliang, Linnu Lu, Fazhou Wang, Yongjia He, Shuguang Hu, Jianxin Lu, and Haibing Zheng. 2020. 'Water desorption characteristics of saturated lightweight fine aggregate in ultra-high performance concrete', *Cement and Concrete Composites*, 106.

Shimrock, Thomas, R. Dirk Taylor, and Jr. John M. Collins. 1985. "Method of Impregnating Ceramic Monolithic Structures with Predetermined Amounts of Catalyst." In.: Engelhard Corporation

Šljivic, M., A. Pavlovic, M. Kraišnik, and J. Ilić. 2019. 'Comparing the accuracy of 3D slicer software in printed enduse parts', *IOP Conference Series: Materials Science and Engineering*, 659.

Smekens, A., R. H. M. Godoi, M. Vervoort, P. Van Espen, S. S. Potgieter-Vermaak, and R. Van Grieken. 2007. 'Characterization of Individual Soot Aggregates from Different Sources using Image Analysis', *J Atmos Chem*, 56: 211–23.

Soille, Pierre. 1999. *Morphological Image Analysis, Principles and Applications* (Springer: Berlin).

Stewart, M., TR Gallant, DH Kim, GD Maupin, and A Zelenyuk. 2010. 'Fuel Efficient Diesel Particulate Filter (DPF) Modeling and Development', *Pacific Northwest National Laboratory*.

Stewart, Mark , David Rector, George Muntean, and Gary Maupin. 2004. 'A Mechanistic Model for Particle Deposition in Diesel Particluate Filters using the Lattice-Boltzmann Technique', *Ceramic Engineering and Science Proceedings*.

Suga, S. 2009. 'Stability and accuracy of lattice Boltzmann schemes for anisotropic advection-diffusion equations', *International Journal of Modern Physics C*, 20: 633-50.

Sun, Y., P. Causse, B. Benmokrane, and F. Trochu. 2020. 'Permeability Measurement of Granular Porous Materials by a Modified Falling Head Method', *Journal of Engineering Mechanics*.

Swanson, J., W. Watts, D. Kittelson, R. Newman, and R. Ziebarth. 2013. 'Filtration Efficiency and Pressure Drop of Miniature Diesel Particulate Filters', *Aerosol Science and Technology*, 47: 452-61.

T., Fwa, Tan S., and Chuai C. 1998. 'Permeability measurement of base materials using falling-head test apparatus', *Transportation Research Record: Journal of the Transportation Research Board*, 16: 81-87.

Tanaka, Atsushi, Naoto Miyoshi, and Akemi Sato. 2018. "Development of Low Pressure and High Performance GPF Catalyst." In *SAE Technical Paper Series*.

Tandon, P., Khamonchat Thiengkaew, Vivan Khongsup, Ekathai Wirojsakunchai, and M. Guo. 2015. 'Sensitivities Of Diesel Particulate Filter Clean And Loading Models', *MATEC Web of Conferences*, 34.

Tandon, Pushkar, Achim Heibel, Jeanni Whitmore, Naveen Kekre, and Kranthi Chithapragada. 2010. 'Measurement and prediction of filtration efficiency evolution of soot loaded diesel particulate filters', *Chemical Engineering Science*, 65: 4751-60.

Tavakoli, Farzan, Sushanta K. Mitra, and Jason S. Olfert. 2011. 'Aerosol penetration in microchannels', *Journal of Aerosol Science*, 42: 321-28.

Tavakoli, Farzan, and Jason S. Olfert. 2014. 'Determination of particle mass, effective density, mass–mobility exponent, and dynamic shape factor using an aerodynamic aerosol classifier and a differential mobility analyzer in tandem', *Journal of Aerosol Science*, 75: 35-42.

Tessier, Lynn P., Harry F. Sullivan, Gordon M. Bragg, and Clark E. Hermance. 1980. 'The Development of a High Efficiency Diesel Exhaust Particulate Filter', *Society of Automotive Engineers, Inc.*: 80-86.

Thomas, C. R., J. A. Pihl, M. J. Lance, T. J. Toops, J. E. Parks, and J. Lauterbach. 2019. 'Effects of four-mode hydrothermal aging on three-way catalysts for passive selective catalytic reduction to control emissions from lean-burn gasoline engine', *Applied Catalysis B: Environmental*, 244: 284-94.

Thomas, Dominique, Augustin Charvet, Nathalie Bardin-Monnier, and Jean-Christophe Appert-Collin. 2017. *Aerosol Filtration* (Elsevier Science).

Tien, Chi, and B.V. Ramarao. 2007. *Granular Filtration of Aerosols and Hydrosols* (Elsevier Science).

Toffoli, Tommaso, and Norman H. Margolus. 1990. 'Invertible cellular automata: A review', *Physica D*, 45: 229-53.

Tomašić, V., and Z. Gomzi. 2004. 'Experimental and theoretical study of NO decomposition in a catalytic monolith reactor', *Chemical Engineering and Processing: Process Intensification*, 43: 765-74.

Torquato, S. 1991. 'Random heterogeneous media: Hicrosttucture and improwed bounds on effective properties', *Appl Mech Rev*, 44.

Torquato, S. 2002. *Random Heterogeneous Materials Microstructure and Macroscopic Properties* (Springer).

Torregrosa, A. J., J. R. Serrano, F. J. Arnau, and P. Piqueras. 2011. 'A fluid dynamic model for unsteady compressible flow in wall-flow diesel particulate filters', *Energy*, 36: 671-84.

Tronconi, E., I. Nova, F. Marchitti, G. Koltsakis, D. Karamitros, B. Maletic, N. Markert, D. Chatterjee, and M. Hehle. 2015. 'Interaction of NO x Reduction and Soot Oxidation in a DPF with Cu-Zeolite SCR Coating', *Emission Control Science and Technology*, 1: 134-51.

Tsuneyoshi, K., O. Takagi, and K. Yamamoto. 2011. 'Effects of Washcoat on Initial PM Filtration Efficiency and Pressure Drop in SiC DPF', *SAE Technical Paper*, 01: 10.

Tsushima, Shohji, Issei Nakamura, Satoshi Sakashita, Shuichiro Hirai, and Daisuke Kitayama. 2010. 'Lattice Boltzmann Simulation on Particle Transport and Captured Behaviors in a 3D-Reconstructed Micro Porous DPF', *SAE International*.

Václavík, Marek, Marie Plachá, Petr Kočí, Miloš Svoboda, Thomas Hotchkiss, Vladimír Novák, and David Thompsett. 2017. 'Structure characterisation of catalytic particulate filters for automotive exhaust gas aftertreatment', *Materials Characterization*, 134: 311-18.

Vadeiko, I., and F. Drolet. 2009. 'A fourth-order algorithm for solving the multi- dimensional Kramers equation in Langevin form', *Journal of Physics A: Mathematical and Theoretical*, 42.

van Setten, Barry A. A. L., Michiel Makkee, and Jacob A. Moulijn. 2001. 'Science and technology of catalytic diesel particulate filters', *Catalysis Reviews*, 43: 489-564.

Vardanega, P. J. 2014. 'State of the Art: Permeability of Asphalt Concrete', *Journal of Materials in Civil Engineering*, 26: 54-64.

Vidal, David Jean-Emmanuel. 2008. 'Developpement d'Algorithmes Paralleles pour la Simulation d'Ecoulements de Fluides dans les Milieux Poreux', Universite de Montreal.

Vidal, David, Cathy Ridgway, Grégoire Pianet, Joachim Schoelkopf, Robert Roy, and François Bertrand. 2009. 'Effect of particle size distribution and packing compression on fluid permeability as predicted by lattice-Boltzmann simulations', *Computers & Chemical Engineering*, 33: 256-66.

Vidal, David, Robert Roy, and François Bertrand. 2010a. 'On improving the performance of large parallel lattice Boltzmann flow simulations in heterogeneous porous media', *Computers & Fluids*, 39: 324-37.

Vidal, David, Robert Roy, and François Bertrand. 2010b. 'A parallel workload balanced and memory efficient lattice-Boltzmann algorithm with single unit BGK relaxation time for laminar Newtonian flows', *Computers & Fluids*, 39: 1411-23.

Viswanathan, Sandeep, David Rothamer, Alla Zelenyuk, Mark Stewart, and David Bell. 2017. 'Experimental investigation of the effect of inlet particle properties on the capture efficiency in an exhaust particulate filter', *Journal of Aerosol Science*, 113: 250-64.

Vollz, Sterling E., Charles R. Morgan, David Liederman, and Solomon M. Jacob. 1973. 'Kinetic Study of Carbon Monoxide and Propylene Oxidation on Platinum Catalysts', *Ind. Eng. Chem, Prod. Res. Develop.*, 12.

Wang, Jihui, Hong Chen, Zhicheng Hu, Mingfa Yao, and Yongdan Li. 2014. 'A Review on the Pd-Based Three-Way Catalyst', *Catalysis Reviews*, 57: 79-144.

Wang, Yuzhu, Christoph H. Arns, Sheik S. Rahman, and Ji-Youn Arns. 2018. 'Porous Structure Reconstruction Using Convolutional Neural Networks', *Mathematical Geosciences*, 50: 781-99.

Wang, Zhoukai, Yinliang Zhao, Yang Liu, and Cuocuo Lv. 2018. 'A speculative parallel simulated annealing algorithm based on Apache Spark', *Concurrency and Computation: Practice and Experience*, 30.

Wanker, R., J. C. Wurzenberger, B. Peters, and R. Tatschl. 2004. "Integrated 1D and 3D Modeling of Exhaust-Gas Aftertreatment Devices." In *International Multidimensional Engine Modeling User's Group Meeting*.

Watling, Timothy C., Maya R. Ravenscroft, Jason P. E. Cleeton, Ian D. Rees, and David A. R. Wilkins. 2017. 'Development of a Particulate Filter Model for the Prediction of

Backpressure: Improved Momentum Balance and Entrance and Exit Effect Equations', *SAE International Journal of Engines*, 10.

Weichenthal, S., E. Lavigne, M. F. Valois, M. Hatzopoulou, K. Van Ryswyk, M. Shekarrizfard, P. J. Villeneuve, M. S. Goldberg, and M. E. Parent. 2017. 'Spatial variations in ambient ultrafine particle concentrations and the risk of incident prostate cancer: A case-control study', *Environ Res*, 156: 374-80.

Weichenthal, Scott, Toyib Olaniyan, Tanya Christidis, Eric Lavigne, Marianne Hatzopoulou, Keith Van Ryswyk, Michael Tjepkema, and Rick Burnett. 2019. 'Within-City Spatial Variations in Ambient Ultrafine Particle Concentrations and Incident Brain Tumors in Adults', *Epidemiology*, Publish Ahead of Print.

Wiegmann, Andreas, Stefan Rief, and Arnulf Latz. 2006. "Soot Filtration Simulation – Generation of Porous Media on the Micro Scale from Soot Deposition on the Nano Scale." In *2nd European Conference on Filtration and Separation* Compiegne, France

Wu, Wei, and Fangming Jiang. 2013. 'Simulated annealing reconstruction and characterization of the three-dimensional microstructure of a LiCoO2 Lithium-ion battery cathode', *Materials Characterization*, 80: 62-68.

Wurzenberger, Johann C., Sophie Bardubitzki, Susanne Kutschi, Robert Fairbrother, and Christoph Poetsch. 2016. 'Modeling of Catalyzed Particulate Filters - Concept Phase Simulation and Real-Time Plant Modeling on HiL', *SAE International Journal of Engines*, 9.

Xie, Luke. 2014. "3D structuring element (sphere)." In. MATLAB Central File Exchange.

Xu, A., T. S. Zhao, L. Shi, and J. B. Xu. 2018. 'Lattice Boltzmann Simulation of Mass Transfer Coefficients for Chemically Reactive Flows in Porous Media', *Journal of Heat Transfer*, 140.

Xuereb, Emilio, and Mario Farrugia. 2016. "Review and Validation of Models of Pressure Drop Across Diesel Particulate Filter and Particulate Loading Quantity." In *SAE Technical Paper Series*.

Yamamoto, K., S. Oohori, H. Yamashita, and S. Daido. 2009. 'Simulation on soot deposition and combustion in diesel particulate filter', *Proceedings of the Combustion Institute*, 32: 1965-72.

Yamamoto, Kazuhiro, and Masamichi Nakamura. 2011. 'Simulation on Flow and Heat Transfer in Diesel Particulate Filter', *Journal of Heat Transfer*, 133.

Yamamoto, Kazuhiro, Masamichi Nakamura, Hiroyoshi Yane, and Hiroshi Yamashita. 2010. 'Simulation on catalytic reaction in diesel particulate filter', *Catalysis Today*, 153: 118-24.

Yamamoto, Kazuhiro, and Shinya Ohori. 2012. 'Simulations on flow and soot deposition in diesel particulate filters', *International Journal of Engine Research*, 14: 333-40.

Yamamoto, Kazuhiro, and Tatsuya Sakai. 2015. 'Simulation of continuously regenerating trap with catalyzed DPF', *Catalysis Today*, 242: 357-62.

Yamamoto, Kazuhiro, Shingo Satake, Hiroshi Yamashita, Naoki Takada, and Masaki Misawa. 2006. 'Lattice Boltzmann simulation on porous structure and soot accumulation', *Mathematics and Computers in Simulation*, 72: 257-63.

Yamamoto, Kazuhiro, and Kazuki Yamauchi. 2013. 'Numerical simulation of continuously regenerating diesel particulate filter', *Proceedings of the Combustion Institute*, 34: 3083-90.

Yang, Juan, Mark Stewart, Gary Maupin, Darrell Herling, and Alla Zelenyuk. 2009. 'Single wall diesel particulate filter (DPF) filtration efficiency studies using laboratory generated particles', *Chemical Engineering Science*, 64: 1625-34.

Yang, Shichun, Cheng Deng, Yanfei Gao, and Yongling He. 2016. 'Diesel particulate filter design simulation: A review', *Advances in Mechanical Engineering*, 8.

Yeong, C. L. Y., and S. Torquato. 1998a. 'Reconstructing random media', *Physical Review E*, 57.

Yeong, C. L. Y., and S. Torquato. 1998b. 'Reconstructing random media. II. Three-dimensional media from two-dimensional cuts', *Physical Review E*, 58.

You, Yonghua, Zhongda Wu, Weidong Zeng, Zhuang Zhang, Sheng Wang, Fangqin Dai, and Zhengming Yi. 2019. 'CFD modeling of unsteady SCR deNOx coupled with regenerative heat transfer in honeycomb regenerators partly coated by Vanadium catalysts', *Chemical Engineering Research and Design*, 150: 234-45.

Young, Ian T. 1983. 'Image analysis and mathematical morphology, by J. Serra. Academic Press, London, 1982, xviii + 610 p. $90.00', *Cytometry*, 4: 184-85.

Zarandi, M. Amin F., Krishna M. Pillai, and Bamdad Barari. 2018. 'Flow along and across glass-fiber wicks: Testing of permeability models through experiments and simulations', *AICHE Journal*, 64: 3491-501.

Zhang, F., R. E. Hayes, and S. T. Kolaczkowski. 2004. 'A New Technique to Measure the Effective Diffusivity in a Catalytic Monolith Washcoat', *Chemical Engineering Research and Design*, 82: 481-89.

Zhang, K., and S. Batterman. 2013. 'Air pollution and health risks due to vehicle traffic', *Sci Total Environ*, 450-451: 307-16.

Zhao, F., M.-C. Lai, and D.L. Harrington. 1999. 'Automotive spark-ignited direct-injection gasoline engines', *Progress in Energy and Combustion Science*, 25: 437–562.

Zinola, Stéphane, Mickaël Leblanc, Antoinette Boreave, Badr R'Mili, Bruno Cartoixa, Philippe Vernoux, and Stéphane Raux. 2013. "The Particulate Number Emissions from GDI Engines: Advanced Characterization and Reduction through a Gasoline Particulate Filter with Membrane Technology." In *SIA International Conference : The spark Ignition Engine of the Future, At Strasbourg*.

Zou, Ying, and Jürgen Malzbender. 2016. 'Development and optimization of porosity measurement techniques', *Ceramics International*, 42: 2861-70.

Zuberi, Bilal, James J. Liu, Sunilkumar C. Pillai, Jerry G. Weinstein, Athanasios G. Konstandopoulos, Souzana Lorentzou, and Chrysa Pagoura. 2008. 'Advanced High Porosity Ceramic Honeycomb Wall Flow Filters', *SAE Technical Paper*, 01.

ANNEXE A LIMITE EN PECLET DU CODE MBR POUR LA RÉSOLUTION DE L'ADR

La MBR, comme d'autres méthodes numériques utilisant des schémas centrés pour approximer les dérivées partielles des équations à résoudre, présente des limites dans les valeurs atteignables des nombres de Péclet dans le cas de la résolution d'un problème d'advection-diffusion. Ceci s'explique par la limite de la vitesse à laquelle l'information peut être transporté sur le maillage du domaine de simulation, par rapport à la vitesse physique à laquelle l'information doit réellement être transportée.

Un cas de vérification a été réalisé afin d'évaluer le nombre de Péclet maximal pouvant être atteint avec le code MBR utilisé dans ce travail. Comme mentionné en Section 6.2.3, cette limite est de l'ordre de O(1) dans la littérature. Un canal carré d'un matériau hypothétique est utilisé, comme présenté dans la Figure A.1. La vitesse est uniforme dans le canal et fixée à $U=L/t_1$ *m/s*, avec $t_1=1$ *s*. Une condition limite de Dirichlet est fixée à l'entrée et une condition limite de flux diffusif nul est fixée à la sortie. Le coefficient de diffusion du matériau hypothétique est $D_1=L_2/t_2$ avec $t_2=t_1/20$.

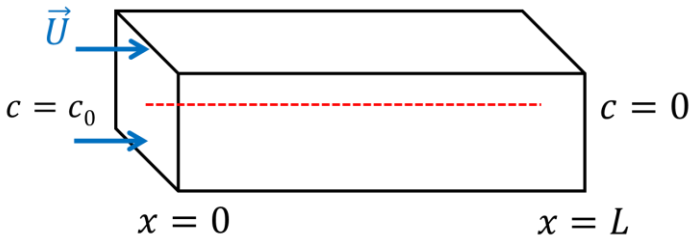

Figure A.1: Schéma de la géométrie utilisée pour évaluer le nombre de Péclet maximal atteignable par le code MBR utilisé dans ce travail. La ligne rouge en pointillés représente la position selon laquelle les données de concentration sont recueillies.

Les résultats sont présentés en Figure A.2. Des instabilités dans le champ de concentration des espèces chimiques apparaissent pour des nombres de Péclet plus grands que 5. Ce résultat est donc en accord avec les données de la littérature.

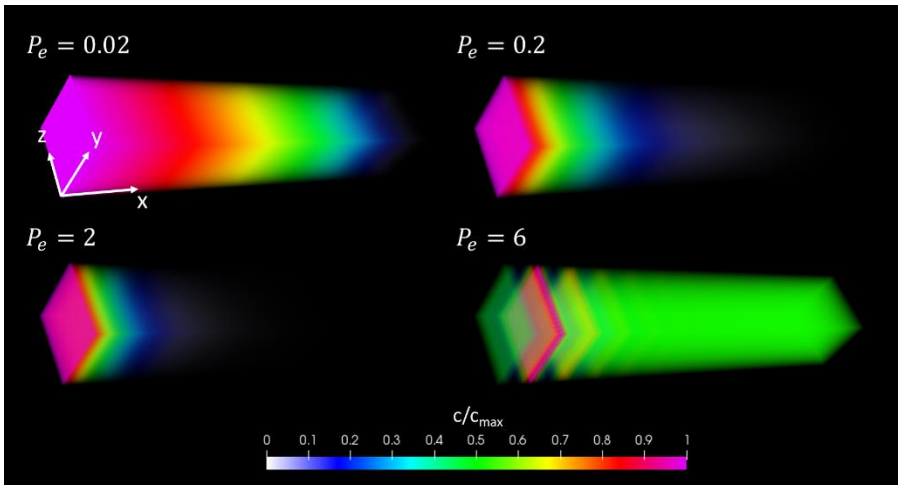

Figure A.2: Visualisation des champs de concentration du cas test présenté en Figure A.1.

ANNEXE B SEGMENTATION D'IMAGES TOMOGRAPHIQUES

Il a été évoqué plusieurs fois dans ce document, que l'étape (1) du modèle développé, consistant à la reconstruction de milieux digitaux représentatifs des FAPC, est très dépendante des données de départ. Cela peut alors avoir un gros impact sur les résultats des prédictions faites aux étapes (2)-(4). Dans l'Article 1 (Chapitre 5), les images tomographiques à disposition étaient de bonne qualité, leur traitement a été relativement facile. Elles ont permis la reconstruction de milieux représentatifs de la géométrie réelle de la céramique des FAPC. La résolution, de $dx = 1.25\ \mu m$, aurait pu toutefois être nettement amélioré par des techniques d'imageries encore plus avancées que la tomographie, comme le microscope électronique à balayage (MEB). Cependant les images acquises avec ce type de technologie ne peuvent être que 2D. Dans d'autres cas, la segmentation des images tomographiques, c'est-à-dire le passage de l'image en niveaux de gris à une image qui distingue les différentes phases de façon déterministe, est rendue beaucoup plus compliqué à cause de la mauvaise qualité de l'acquisition. C'est dans ce cas de configuration qu'il faut se placer pour cette étude.

Afin de combiner la résolution plus élevée des images MEB, avec le caractère 3D des images tomographiques, une technique de recuit simulé utilisant les informations des deux méthodes d'acquisition d'images a été développée. Le principe de l'algorithme est présenté en Figure B.1. Le principe de la méthode se base sur le recuit simulé. Cet algorithme qui rentre dans la catégorie des méthodes de Monte Carlo, se base sur la minimalisation d'une fonction de pseudo-énergie. Cette fonction est construite comme la somme des écarts aux carrés entre des descripteurs géométriques décrivant la structure cible et ces mêmes descripteurs pour la structure reconstruite. Théoriquement, n'importe quel descripteur de la géométrie peut être pris en compte dans la fonction de pseudo-énergie. En pratique, deux descripteurs sont le plus souvent utilisés. La probabilité que *n* points aux positions $(x_1, x_2, \ldots, x_n)$ dans le milieu soient contenus dans la phase *i* est notée ${S_n}^i$. Ici, seulement deux phases sont considérées : la phase solide (cordiérite + catalyseur, $i = 1$) et la phase poreuse ($i = 0$). Basé sur cette définition, pour un milieu isotrope, le *two-point-probability function* est donné par:

$$ {S_2}^i(r) = \frac{n_i(r)}{n_t(r)} \tag{B.1} $$

où $n_i(r)$ et $n_t(r)$ sont, respectivement, le nombre de paires de voxels de phase i et le nombre total de paires de voxels de toute phases séparées par la distance *r*. Cette fonction est calculée sur la phase de catalyseur (descripteur f_1) Cette fonction peut également être calculée entre deux phases : le catalyseur et la cordiérite par exemple (descripteur f_2).

En plus des fonctions de probabilité à deux points, une autre fonction de corrélation spatiale très utile pour caractériser les milieux poreux est le *lineal-path* donnée par (Torquato 2002):

$$L^i(r) = \frac{m_i(r)}{m_t(r)} \tag{B.2}$$

où $m_i(r)$ et $m_t(r)$ sont respectivement le nombre de segments de longueur r s'ajustant totalement à la phase i lorsqu'ils sont lancés au hasard dans l'échantillon et le nombre total de tentatives d'ajustement. Cette fonction est calculée sur la phase de catalyseur (descripteur f_3). Dans ce travail, ${S_2}^i(r)$ et $L^i(r)$ ont été calculés à l'aide d'un programme personnalisé basé sur une procédure décrite dans la littérature (Torquato 2002). Dans ce cas, les fonctions de corrélation (f_1, f_2, f_3) sont calculées sur une image MEB du FAPC.

En plus de ces deux fonctions utilisées classiquement dans la littérature, calculées sur une image MEB 2D d'un morceau de mur de cordiérite recouvert de catalyseur, l'information de niveau de gris de l'image tomographique 3D est utilisée (descripteur f_4). Pour cela, pour chaque voxel du milieu poreux à reconstruire en 3D, l'écart est calculé entre la valeur du niveau de gris, sur une échelle de 0 à 255, et la valeur attribuée à la structure reconstruite : 0 pour un voxel de cordiérite et 255 pour un voxel de catalyseur. Finalement, la fonction de pseudo-énergie est décrite par :

$$E(f_i) = \sum_{i=1}^{4} \gamma_i \left(f_i - f_{i,target}\right)^2 \tag{B.3}$$

où les f_i sont les descripteurs géométriques utilisés, pondérés par des coefficients γ_i. Les résultats sont présentés en Figure B.2.

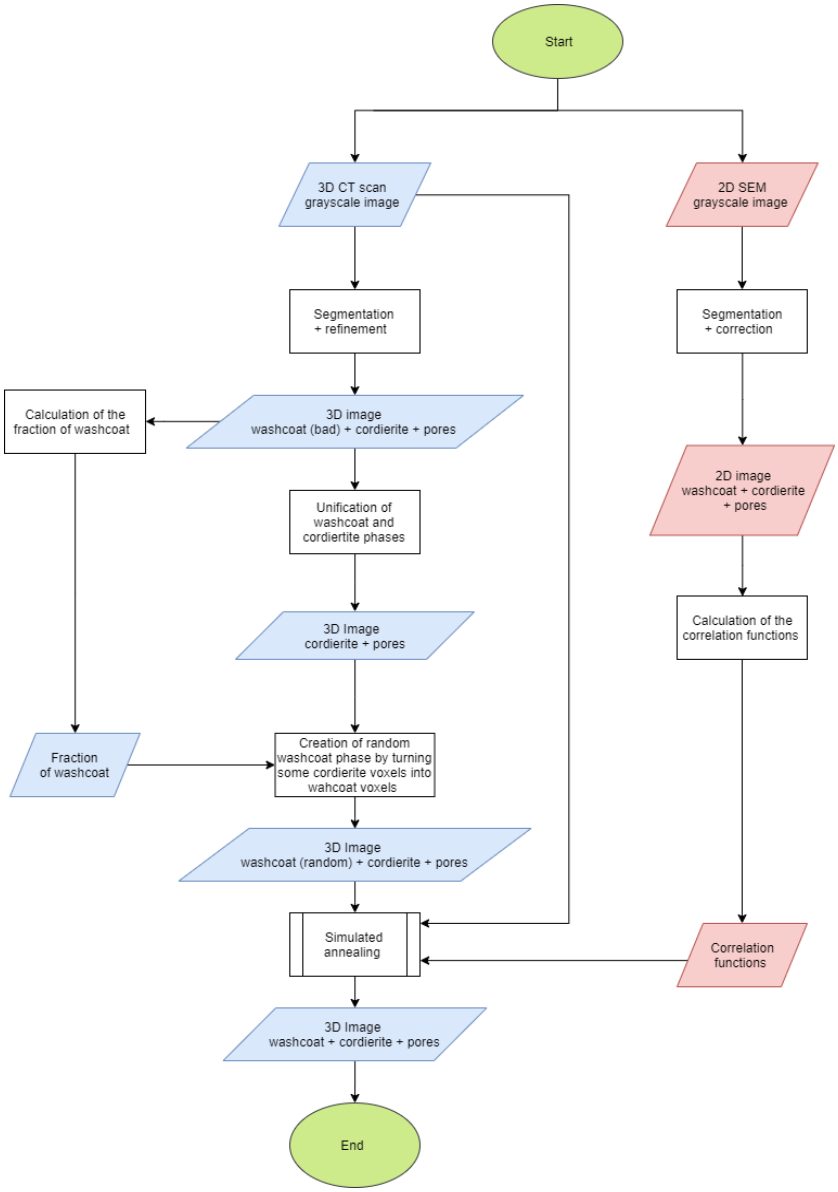

Figure B.1: Schéma de l'algorithme utilisé pour la segmentation d'images tomographiques d'un FAPC supporté par une méthode de recuit simulé se basant sur des fonctions de corrélation calculées sur une image MEB d'une section différente du même FAPC.

Les résultats sont présentés en Figure B.2, sous la forme de 6 images 2D représentant différentes étapes du processus décrit plus haut et dont l'algorithme est illustré en Figure B.1. Le résultat final, illustré en Figure B.2 (4), semble présenter une représentation beaucoup plus réaliste de la phase de catalyseur, comparée à l'image (6), par rapport au résultat obtenu à l'aide d'une segmentation classique montrée en image (5).

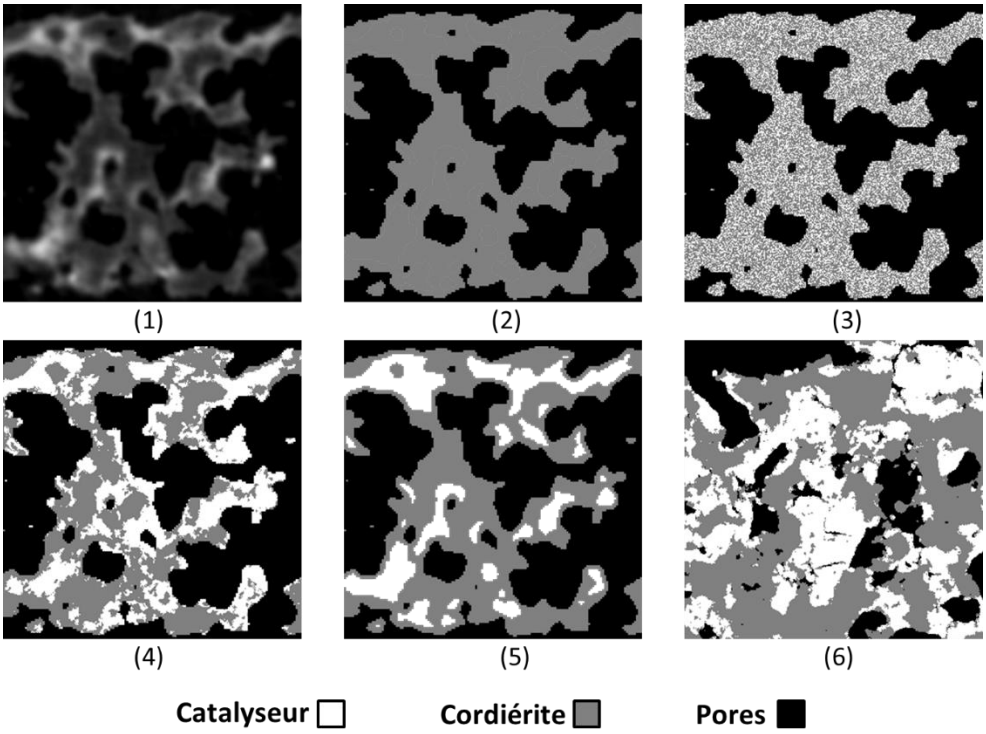

Figure B.2 : (1) Section 2D de l'image tomographique de départ en niveaux de gris, (2) Section 2D de l'image tomographique de départ segmenté entre phase solide et phase poreuse, (3) Section (2) à laquelle à été ajouté des voxels de catalyseur de façon aléatoire, (4) Section 2D de l'image reconstruite, (5) Section 2D de l'image tomographique de départ segmenté de façon classique, (6) Image MEB servant à calculer les descripteurs (f_1, f_2, f_3).

Cette méthode est encore l'objet d'amélioration, notamment dans le choix de la pondération de chaque descripteur par rapport aux autres. Enfin, un critère de performance doit être développé afin de quantifier la qualité de la segmentation.

ANNEXE C VERIFICATION DE LA DEPOSITION ARTIFICIELLE DE CATALYSEUR

Pour s'assurer que le point d'inflexion dans le profil de perméabilité obtenu à la Figure 5.13, n'est pas dû aux algorithmes de dépôt utilisés dans cette étude, 3 structures supplémentaires ont été créées, suivant la méthode décrite dans la Section 5.2.1. En partant du profil de distribution de la structure N5, présentant une fraction du volume des pores remplie de catalyseur de 0.32, en utilisant une sphère d'érosion de diamètre croissant, 3 structures présentant une fraction du volume des pores remplie inférieure à 0.32 ont été obtenues. Les nouveaux points de données sont ajoutés aux données vues dans la Figure 5.13 et tracés dans la Figure C.1. Les résultats montrent un très bon accord avec les points de données précédemment tracés pour un dépôt non uniformément distribué, ce qui prouve que les algorithmes de dépôt utilisés dans ce travail n'ont aucun impact sur la forme de la courbe de perméabilité sur la quantité de catalyseur.

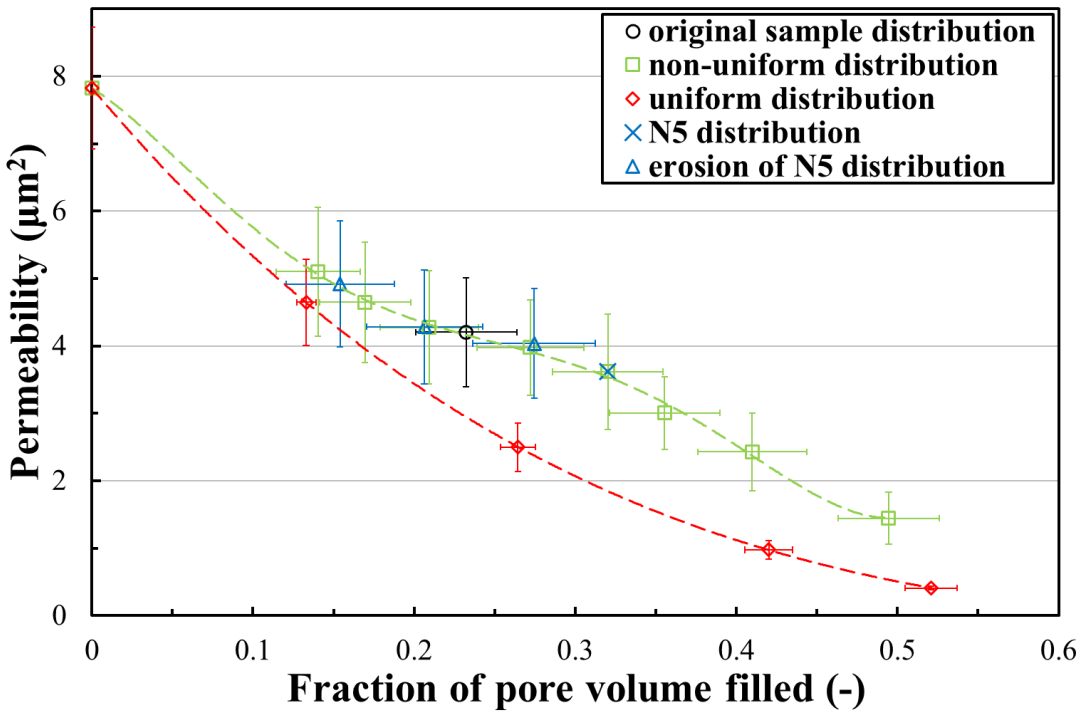

Figure C.1: Vérification de la procédure de déposition artificielle de catalyseur.

ANNEXE D VALIDATION DES CALCULS D'EFFICACITÉ DE CAPTURE DES PARTICULES DE SUIE

Afin de valider l'étape (3) du modèle développé dans ce travail, qui consiste à calculer la trajectoire des particules de suie à travers le milieu poreux du FAPC, afin de calculer son efficacité de capture, une série d'expériences à été réalisé à l'Université d'Alberta. La principale difficulté dans la validation de calculs d'efficacité de captures fait à l'échelle microscopique est la nature multi-échelle du FAPC. En effet le mur de céramique recouvert de catalyseur n'est pas le seul contributeur à la capture totale du FAPC. En plus de par la céramique, les particules peuvent être capturées par effet d'entrée dans le monolithe et le long des canaux rectangulaires par diffusion brownienne. Cette dernière contribution a été prise en compte à l'aide de formules analytiques de la littérature et superposé aux résultats numériques. L'accord obtenu, présenté en Figure D.1, entre simulation et expérience est très bon dans le régime de diffusion, pour des diamètres de particule faibles, mais un écart important est obtenu pour de plus larges particules pour lesquelles l'impaction inertielle joue un plus grand rôle. Plus de recherches et d'expériences sont nécessaires à l'explication de cet écart.

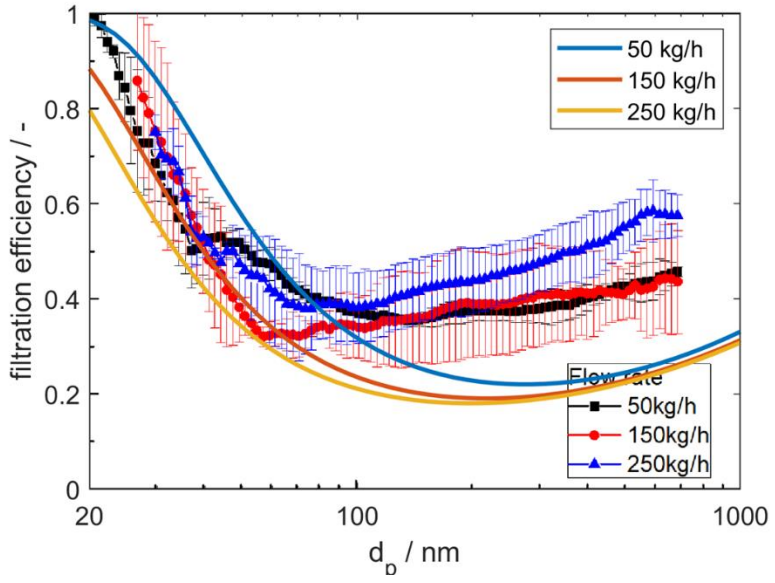

Figure D.1: Courbes d'efficacité de capture mesurée et calculée à l'aide de la MBR, pour trois débits de gas d'échappement. Les expériences sont les séries de points (bleue, rouge et noir) et les simulations sont les courbes continues (bleue, orange et jaune)